Design and operation of a harmonic gyrotron based on a cusp electron gun

Fengping Li

(BSc University of Science and Technology, China)
(MSc Post-Graduate School of CAEP, China)

Department of Physics, SUPA

University of Strathclyde

Thesis submitted for degree of Ph.D

September 2010

Copyright

Dedication

I would like to dedicate this thesis to my father Xiu’an, my mother, Xizhi and my brother Yongbo for their support, endless love and encouragement.

Table of Content

Chapter 1

Chapter 2

Chapter 3

Chapter 4

Chapter 5

Chapter 6

Chapter 7

Chapter 8

Acknowledgements

To all the people who helped me during my work to produce this dissertation, I would like to express my gratitude. First and foremost, I'd like to acknowledge my supervisor Dr. W. He and Dr. Adrian Cross and Prof. A. D. R. Phelps for introduce me into the field of gyrotrons and providing me the opportunity to work on this thesis. They not only provided much needed guidance, encouragement and support through the course of this PhD, but also the help for me to enjoy this period while living in UK and working with them. I really appreciate how much I've learned and been inspirited from them, thanks for their kindness to provide me this opportunity of studying under these talented people.

I would also like to acknowledge my fellow colleagues Dr. C. Donaldson, and Mr. L. Zhang who have both been directly involved with the experimental side of the work, Thanks them for their hard work and many valuable discussions.

I would also express my gratitude to Dr. K. Ronald, Dr. I. Konoplev, Dr. P. MacInnes, Dr. C. G. Whyte and Dr. C. W. Robertson for their help in the experiment and also for their kind suggestions during the whole PhD. Mr. D. Constable and Mr. D. Bowes must been thanked for their help with the VNA measurement.

I would like to offer my sincerest thanks to Mr. D. Barclay for his technical skill and advices in constructing varies challenging parts for the gyrotron experiment.

I am indebted to all my colleagues at the RELD group, Thanks them for all the help that I received during these years and thanks for their kindness and all the happy time we spend together. The RELD group is more than a peer research group but also a big family.

Finally, I would like to thank my friends and family for their support I have received without whom I would have never reached to this level. Specially, I can never thank enough my parents, who have been a source of encouragement and inspiration to me throughout my journey so far as a human being and as a researcher, and sacrificed so much to make me what I am today.

Abstract

This thesis presents the results of successful operation of a 2nd harmonic gyrotron based on a cusp electron gun. The numerical and experimental results agreed well with the gyrotron design parameters. Two gyrotrons based on a cusp electron gun were designed: the first gyrotron operated at the 2nd harmonic and the second gyrotron was studied to look at the scaling of this concept for operation at the 7th harmonic at a frequency of 390 GHz. The cusp electron gun was used to produce the electron beam in the gyrotron which was annular in shape. The electron beam had a voltage of 40 kV, a current of 1.5A and a velocity ratio (perpendicular component to horizontal component) of 1.5. The experimental results from the first cusp electron gun and measurements of the high quality electron beam with ~8% velocity spread and ~10% alpha spread are presented.

Analytical, numerical and experimental results of a DC harmonic gyrotron are presented. The 3D PIC code MAGIC was used to simulate the interaction of the harmonic gyrotron such as the TE71 mode at the 7th cyclotron harmonic with the large orbit electron beam with the beam thickness and beam spread introduced into the simulation. The interaction cavity of both gyrotrons was in the form of a smooth cylindrical waveguide. The relationship between the cavity dimensions and cavity Q values has been studied for optimized output at the design mode with the aim of suppressing other competing modes. A linear output taper was designed with low mode conversion at the gyrotron output. A Vector Network Analyzer with high frequency millmetre wave heads was used to measure the millimeter wave properties of the gyrotron cavity.

Experiments were conducted using the electron gun for the harmonic gyrotron. The gyrotron and electron gun were built as well as the interlock and safety system, pulsed power supply and magnet, the cooling and vacuum system. Millimetre wave radiation was measured for the 2.6 mm diameter cavity gyrotron operating at the 2nd harmonic at a magnetic field of 2.08 T. Experiments demonstrated that the harmonic gyrotron was sensitive to the magnetic field and electron beam parameters. Millimetre wave radiation from 108GHz to 110GHz was measured with the use of a W-band rectifying crystal detector and high pass cut off filters. The frequency of the measured millimeter wave radiation agreed very well with the design and predictions of theory.

Abbreviation & Symbols List

EM	Electromagnetic
THz	Terahertz
RF	Radio Frequency
UHF	Ultra High Frequency
NMR	Nuclear Magnetic Resonance
DNP	Dynamic Nuclear Polarization
COBE	Cosmic Background Explorer
TDS	Time Domain Spectroscopy
FET	Field Effect Transistor
AC	Alternating-current
BWO	Backward Wave Oscillator
TWT	Travelling Wave Tube
MVED	Micro-fabrication Microwave Vacuum Electronic Devices
FEA	Field Emission Array
HPM	High Power Microwave
EIK	Extended Interaction Klystron
QO	Quasi-optical
ITER	International Thermonuclear Experimental Reactor
FEL	Free Electron Lasers
Gyro-BWO	Gyrotron Backward Wave Oscillator
Gyro-TWT	Gyrotron Travelling Wave Tube
Gyro-TWA	Gyrotron Travelling Wave Amplifier
CW	Continuous Wave
ECM	Electron Cyclotron Maser
CRM	Cyclotron Resonance Maser
TE	Transverse Electric
TM	Transverse Magnetic
TEM	Transverse Electric and Magnetic

SEM	Scanning Electron Microscope
OFHC	Oxygen Free High Conductivity
SNA	Scalar Network Analyzer
VNA	Vector Network Analyzer
MIG	Magnetic Injection Gun
ESR	Electron Spin Resonance
EPR	Electron Paramagnetic Resonance
CC-TWT	Coupled-Cavity Travelling Wave Tube
CFA	Crossed-Field Amplifier
PPM	Periodic Permanent Magnets
PIC	Particle In Cell
PFL	Pulse Forming Line
DUT	Device Under Test
EIR	Extended Interaction Region

A	Vector potential.
A	Cross-sectional area of a conductor.
A_{CF}	Area correction factor.
A_e	Area of emitter.
A_{k_z}	Constant multiplier that differs depending on electromagnetic mode.
A_θ	Magnetic vector potential in the θ direction.
a_+	Amplitude of the co-rotating mode A inside the helical waveguide.
a_-	Amplitude of the counter-rotating mode A inside the helical waveguide.
a_w , a_n	Radius of waveguide w and n respectively.
B	Magnetic field flux density.
b_+	Amplitude of the co-rotating mode B inside the helical waveguide.
B_0	Cavity magnetic field.
B_1	The magnetic field of the electromagnetic wave.
B_c	Magnetic field at cathode side of the electron gun.
B_x , B_y , B_z	Magnetic field flux density in the x, y and z direction respectively.
B_{z_0}	Cavity magnetic field.

B_θ	Magnetic field flux density in the θ direction.
c	Speed of EM wave in free-space, c = 3 x 10^8 ms^{-1}.
C	Pierce parameter.
C_d	Diode capacitance.
D	Electric displacement field.
D_{ant}	Diameter of antenna.
d_{ac}	Distance between anode and cathode.
E	Electric field.
E_c	Electric field in a conductor.
$E_{k_{\max}}$	Kinetic energy of electrons ejected by absorption of photon.
E_x, E_y, E_z	Electric field component in the *x*, *y* and *z* direction respectively.
E_0	Amplitude of the electromagnetic wave.
E_{0x}, E_{0y}, E_{0z}	The amplitude of the electromagnetic wave in the *x*, *y* and *z* direction respectively.
E_t	Transverse electric field.
E_{0t}	Initial transverse electric field.

E_T	Electric field at the thermionic cathode surface.
E_r	Radial electric field.
e	Charge on the electron, e = 1.602 x 10^{-19} C.
e_x, e_y	The *x* and *y* direction unit vector respectively.
f	Frequency.
F	Force.
F_r	Radial force.
G	Transverse spatial function.
H	Magnetic field.
H_t	Transverse magnetic field.
H_{0t}	Initial transverse magnetic field.
H_z	Magnetic field in *z* direction.
$\bar{h}$	Axial index of Bragg periodicity.
h_A	Axial wavenumber of mode A.
h_B	Axial wavenumber of mode B.
H	Hamiltonian.
H_s	Coupling coefficient.

I	Current.
I_d	Displacement current.
I_o	Incident energy of light.
j	Volume current density.
J	Current density.
J_e	Emission current density.
J_m	Bessel function of order *m*.
J_s	Bessel function of order *s*.
k	Wavenumber.
k_c	Cut-off wavenumber.
$\hat{k}$	Unit vector.
k_n	nth nonzero root of $J_1(x) = 0$.
k_0	Cut-off wavenumber for the A mode.
k_{0_B}	Cut-off wavenumber for the B mode.
k_{z_1}	Axial wavenumber at lowest measurement frequency.
k_{z_2}	Axial wavenumber at highest measurement frequency.

k_t	Transverse wavenumber.
k_x, k_y, k_z	Wavenumber in the x, y and z direction respectively.
l	Amplitude of the corrugation in a helically corrugated waveguide.
l_{cab}	Length of cable.
L	Length.
L	Lagrangian.
n_0	Electron beam density.
n	Mode number in the x direction.
m	Mode number in the y direction.
m	Particle mass.
m_e	Mass of an electron.
$\bar{m}$	Azimuthal index of the helical waveguide.
N	Turn density.
P	Power.
P	Perviance.
$P_{canonical}$	Canonical angular momentum.
P_i	Transmitting antenna power

P_r	Receiving antenna power
P_r , P_z , P_θ	Canonical moment in the r, z and θ directions respectively.
q	Charge of a particle.
r	Radius.
r_a	Anode aperture radius.
r_0	Mean radius of corrugation in a helically corrugated waveguide.
r_{0L}	Initial Larmor radius.
r_L	Larmor radius.
r_{inj}	Injected electron radius.
r_{cath}	Average radius of the cathode.
r_W	Waveguide radius.
r_c	Average radius of cathode.
r_g	Guiding centre of electrons.
r_{cy}	Cyclotron radius.
R	Resistance.
R_{ant}	Separation distance between transmitter and receiver antenna.

R_m	A function that satisfies the Bessel equation.
R_{SWS}	Radius of the helical slow-wave structure.
R_1, R_2	Resistance.
R_{e1}, R_{e2}	Inner and outer radii of the emitting strip respectively.
s	Harmonic number.
t	Time.
T	Temperature.
T	Kinetic energy.
T_c	Temperature of cathode surface.
u	Heaviside unit step function.
v_p	Phase velocity.
v_g	Group velocity.
$\mathrm{v}_{\parallel}$	Axial velocity of electrons.
$\mathrm{v}_{\perp}$	Perpendicular velocity of electrons.
$\mathrm{v}_{0\perp}$	Initial perpendicular velocity of electrons.
v_c	Charging voltage.

v_t	Transverse velocity.
$\mathrm{v_x}$, $\mathrm{v_y}$, $\mathrm{v_z}$	Velocity in the *x*, *y* and *z* direction respectively.
V	Voltage.
V	Scalar potential.
V_{out}	Output voltage from a cable Blumlein or PFL.
V	Potential Energy.
V_{ac}	Accelerating voltage.
V_o	Electron velocity.
v_c	Speed of an electromagnetic wave through a cable.
$\mathrm{v_{z,av}}$	Average axial velocity.
v_{crit}	Minimum velocity of particle that passes the cusped magnetic field.
v_{z1}	Velocity upstream of the cusp transition.
v_{z2}	Velocity downstream of the cusp transition.
v_{zth}	Threshold velocity for electrons passing a cusped magnetic field.
x	*x* coordinate in a Cartesian coordinate system.
y	*y* coordinate in a Cartesian coordinate system.
z	*z* coordinate in a Cartesian coordinate system.

Z_L	Load impedance.
Z_0, Z_1, Z_2	Impedance of a cable.
z_{opt}	Optical path length.

Greek:

α	Attenuation constant.
α	Velocity ratio, alpha.
α_c	Absorption coefficient.
β	Relativistic velocity factor.
$\beta_{\perp_0}$	Relative transverse velocity.
β_{z_0}	Relative longitudinal velocity.
γ, γ_0	Lorentz relativistic factor.
$\gamma_{0\perp}$	Initial transverse Lorentz relativistic factor.
Δ_g	Geometrical mismatch.
Δ_H	Relative frequency mismatch.
δ	Frequency mismatch.
δ_s	Skin depth.

$\delta(z)$	Dirac delta function.
ε	Permittivity of a medium.
ε_0	Permittivity of a free space, $\varepsilon_0 = 8.854 \times 10^{-12}$ Fm^{-1}.
ε_r	Relative permittivity of a medium.
$\tilde{\varepsilon}$	Corrugation in permittivity of a medium.
ξ_{mn}	The nth zero of the mth Bessel function.
ξ'_{mn}	The nth zero of the differential of the mth Bessel function.
ζ_{scale}	Scaling factor.
η	Electron charge-to-mass ratio.
θ_2, θ_1	Phase with and without the device under test respectively.
λ	Wavelength.
λ_c	Cut-off wavelength.
λ_g	Guide waveguide.
λ_0	Free space wavelength.
μ	Permeability of a medium.
μ_r	Relative permeability of a medium.

μ_0	Permeability of free space, $\mu_0 = 4\pi \times 10^{-7}$ Hm^{-1}.
ν	Frequency of a photon.
ρ	Charge density.
ρ	Electrical resistivity of a conductor.
ρ_P	Power density.
σ	Coupling coefficient.
σ_c	Conductivity of the conductor.
σ_m	Conductivity of the medium.
τ	Time of voltage pulse.
Φ	Magnetic flux.
ϕ	Polar coordinate, angle.
ϕ_w	Material work function.
ψ	Effective potential.
$\psi_{\min}$	Minimum electron energy to pass through the cusped magnetic field.
ψ	Phase shift.
ψ_w , ψ_n , ψ_e	Phase shift of wave E_1 and E_2 through the ellipse respectively.
Ω	Cyclotron frequency.

Figure List

Table List

Chapter 1

Introduction

1.1 **Terahertz**

James Clerk Maxwell's equations postulated in 1865 [1], were used to describe the experimental results of Michael Faraday [2] as well as to explain the propagation of electromagnetic waves in free space which was later confirmed by Heinrich Hertz in 1887 [3]. The electromagnetic (EM) spectrum extends from below the frequencies used for modern radio communication to gamma radiation covering wavelengths from thousands of kilometres down to sub-nanometre. Physicists and engineers have progressively explored and conquered most of EM spectrum in terms of generation. This has resulted in a range of technologies for producing and detecting the EM radiation at both high (gamma and X-rays) and low frequencies (microwave) and its exploitation in every aspect of daily life. But there is one part of the electromagnetic spectrum: the THz frequency band (0.1THz to 10THz), that despite a lot of scientific effort in this area since the 1920s [4] it still lags behind what has been achieved in the other parts of the EM spectrum such as the radio, UHF, TV and microwave Radar [5] bands. This is due mainly to the lack of available high power continuous wave sources in the THz frequency range which has resulted in one of the least tapped regions of the electromagnetic spectrum [6].

Terahertz corresponds to a wavelength range between about 3 and 0.03 mm (100 GHz to 10 THz) [7] of the electromagnetic spectrum. At lower frequencies lies the electronic regime of millimetre-wave radiation, used for applications such as wireless telecommunication. At higher frequencies lies the optical regime, where active optical devices like semiconductor lasers and light-emitting diodes generate near-infrared and visible light for fibre-optic transmission and data storage. So there are two dramatically different groups—ultra-fast time-domain spectroscopists who work with EM radiation at wavelengths produced by conventional solid-state optical technologies, and scientist such as radio astronomers who work at longer wavelengths using EM sources based on electronic devices. But neither can have a very good coverage that is why terahertz radiation is also known as the "Terahertz Gap" in the electromagnetic spectrum as shown in Figure 1-1.

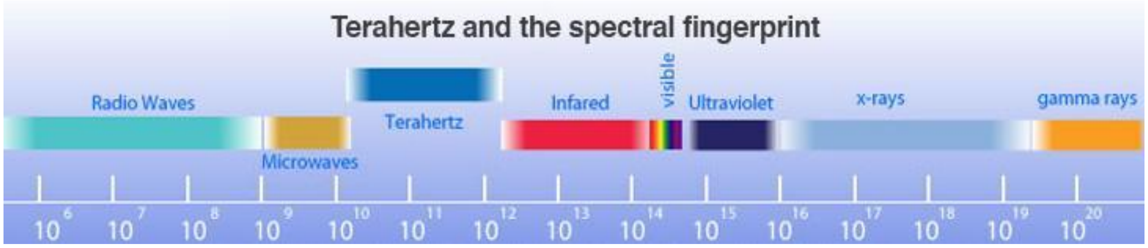

Figure 1-1 Electromagnetic Spectrum and Terahertz Gap

Terahertz radiation can penetrate a wide variety of materials, and it is non-ionizing due to its lower photon energy (1THz = 0.41 MeV) which makes it much safer than X-rays. It can also be focused (unlike X-rays) and steered easily (unlike radio frequency radiation) by quasi-optical mirrors with enhanced spatial resolution. This makes the THz radiation a perfect probe for non-invasive and non-destructive inspection using various spectroscopic and imaging techniques.

Terahertz radiation can also penetrate many visually opaque materials, and as its wavelength is very close to bio-molecular vibrations, spectroscopic techniques can be used to obtain greater understanding of such systems. It interacts strongly with water but passes through biological tissue allowing the imaging of biological tissue. It can also be used to enhance the signal-to-noise ratio of Nuclear Magnetic Resonance (NMR), with its use in the new expanding field known as Dynamic Nuclear Polarization (DNP) [8, 9, 10]. DNP can increase the resolution of NMR by orders of magnitude, and the unique vibration, rotational, and translational response of materials within the THz range can provide information generally absent by the use of optical, X-ray or NMR techniques. Also due to its capability of penetrating many visually opaque materials, it can also be used in security scanning for concealed weapons, narcotics, explosives, or biological agents such as anthrax, skin cancer imaging and dental imagining [11].

Also, as terahertz radiation is readily absorbed by water, it can be used to distinguish between materials with varying water content, for example, fat versus lean meat. Because terahertz radiation can be focused, this makes it capable of producing images with signature or fingerprint (functional) [12,13] of the molecular structure of the material. This fingerprinting will allow THz radiation to be used to detect harmful biological or chemical agents [14], and to differentiate between different tissue types.

Terahertz radiation can also be used in plasma diagnostics [15] and to help scientists understand the complex dynamics involved in condensed-matter physics. In plasma diagnostics most of the measurements involve determination of the electron density profile as a function of position and time in the plasma core [16], and Thomson scattering [17] or detection of synchrotron radiation can be used to identify the power spectrum.

Terahertz technology can even help people to understand the universe as demonstrated by results from the NASA Cosmic Background Explorer (COBE) Diffuse Infrared Background Experiments (DIRBE) where examination of the spectral energy distributions in observable galaxies, showed that approximately one-half of the total luminosity and 98% of the photons emitted since the Big Bang fall into the sub-millimetre and far-infrared [18] part of the EM spectrum. Therefore Continuous Wave (CW) THz sources are required for space based applications [6].

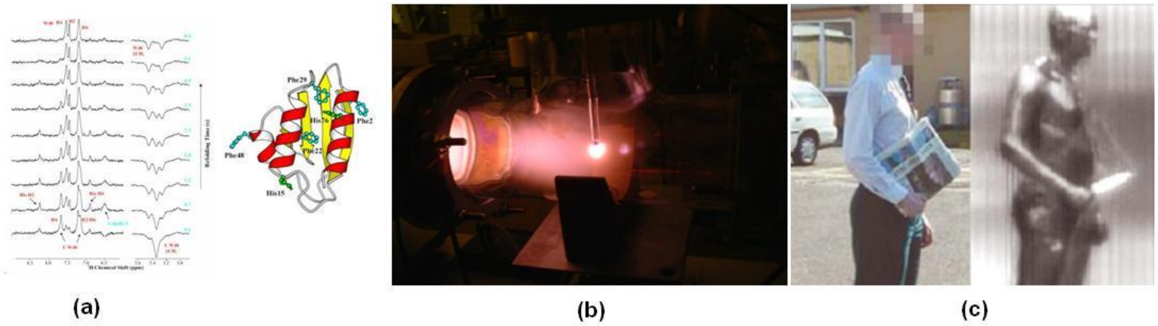

Figure 1-2 Some Application of Terahertz Radiation

(a) DNP [19], (b) Plasma Diagnostic [20], (c) Security Check [21];

Another major application for terahertz radiation is in planetary and small-body observations. Because terahertz radiation can interact with abundant molecules, such as water, oxygen, carbon monoxide, nitrogen, etc., surface based or orbital remote terahertz sensing observations can be used as an atmospheric sensor and to help understand our atmosphere or other solar planets' and gaseous species such as the composition, temperature, pressure, and the dynamics of the atmosphere. This can help gain insight into the formation and evolution of the solar system [22]. There are also a lot of other important applications of terahertz radiation, such as communication and high resolution radar. Potential applications are continuously increasing as fundamental scientific research and various advanced technologies are developed some of which are summarised in Figure 1-3.

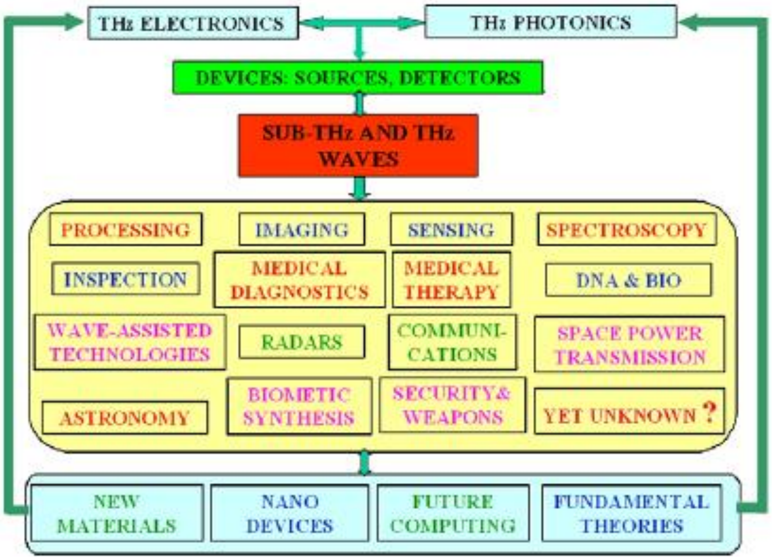

Figure 1-3 Fields of application of the THz Radiation [23]

1.2 Terahertz Sources

It is because of the properties of THz radiation and its potential applications, that it is considered by Technology Review [24] to be one of the 10 most important areas that will change our world in the 21st century. Though, due to the lack of reliable terahertz sources, the practical applications of terahertz radiation are still in its infancy. As mentioned before, the two dramatically different groups: (a) ultra-fast time domain spectroscopists and (b) long-wavelength radio astronomers are developing very different technologies to try and realize reliable terahertz radiation sources.

1.2.1 **Photonic Devices**

Types of terahertz sources to be discussed first are lasers and optical devices that use downward frequency conversion techniques to produce THz radiation. Optical pumped terahertz lasers (OPTL) are probably the most widely employed optical technique for producing terahertz energy [25]. It is one type of CW or pulsed terahertz source, which is used around the world for astronomical and environmental monitoring, and plasma diagnostics, etc. An OPTL system normally consists of a grating-tuned carbon dioxide pump laser and a far-infrared gas cell mounted in a laser resonator. This technique can produce a power level of 1-20 mW with the power output dependent on the chosen emission line, with discrete frequency coverage in the terahertz range achieved by using different molecular gases each having their own spectrum of available lines. The lasers can also be used with harmonic generators to make sideband sources [25] which can provide more flexible tuning.

Quantum Cascade Lasers [26,27] (QCL) is another very competitive optical terahertz radiation source. Unlike other typical interband semiconductor lasers, QCLs are unipolar and laser emission is achieved through the use of intersubband transitions in a repeated stack of superlattices formed by a periodic series of thin varying semiconductor layers. An advantage of QCLs over other semiconductor mid and far infrared lasers is that the optical power can be higher. It is currently the only solid-state source of coherent Terahertz radiation capable of delivering more than 1 mW of average power at frequencies above ~ 2 THz [28]. It can be operated in CW mode at room temperature and can be tuned from one wavelength to the other externally [29,30]. QCLs are very compact and have become commercially available [31]. However, several challenges still need to be overcome before QCLs become practical THz sources, such as the decrease in power as the operation temperature increases, and the highly divergent and non-Gaussian free space output beam makes it difficult to use in practical applications.

Another widely used terahertz source is the down-conversion from the optical regime especially for time domain spectroscopy (TDS) [32] which is achieved by using fast photoconductive switches with can create broad band short-pulse terahertz radiation. In this method, an ultra-short pump-laser (femtosecond optical laser) pulse is focused to a split antenna which is fabricated on a semiconductor substrate (e.g. Silicon-on-sapphire or LTG GaAs), and a dc bias is placed across the antenna. The laser pulse generated carriers in these photoconductors, and these carriers are accelerated by the bias voltage and the resulting current is coupled with the antenna and produces terahertz radiation waves. The terahertz radiation pulses' repetition frequency is the same as the femtosecond pump lasers'. This pulse frequency is typically centred at about 1 to 2 THz with a bandwidth spread of over 500 GHz and an average power of a few microwatts [7].

Another method to produce terahertz radiation is by using lasers and photoconductors, in the technique known as photomixing [33]. Two CW lasers with identical polarisation and different frequency ω_1 and ω_2 are required. The co-linear laser beams are mixed and focused on to a small piece of ultra-fast (<1 ps carrier lifetime) semiconductor material, the photons are absorbed and the short charge carrier lifetime results in the modulation of the conductivity at the desired terahertz frequency ($\omega=\omega_1-\omega_2$). So, photomixing can produce narrow-band phase lockable terahertz radiation in the entire terahertz band by slightly shifting the optical frequencies of the two lasers. But as the efficiency of conversion from optical to terahertz radiation is very low (typically below 10^{-5} for a single device [34]), the output power falls to around a microwatt, however new developments have reached milliwatt levels of power recently [35].

1.2.2 **Solid State Electron Devices**

The second type of THz radiation source is based on electron devices including solid state oscillators and vacuum electron devices which are trying to increase their frequency range of operation to cover the terahertz region of the electromagnetic spectrum. All microwave power electronics operate on the principle of converting the kinetic energy of an electron stream to coherent electromagnetic radiation.

In solid-state microwave electronics, the electron stream is sustained by applying a voltage between the emitter and collector electrodes (junction transistor) or the source and drain electrodes (field effect transistor or “FET”) at the two extreme ends of the device. This electron stream diffusively drifts through a solid medium (semiconductor). The drifting electrons experience many collisions with the atoms of the semiconductor lattice, and inevitably the electron stream converts a significant fraction of its kinetic energy into waste heat directly inside the device.

In a solid-state transistor amplifier, a microwave frequency, alternating-current (AC) voltage at low current is applied to the base or gate (FET) electrode. The corresponding microwave frequency modulations on the large emitter-base or source-drain current equates to a net current and power gain for the microwave signal. The RF performance of a solid state device is fundamentally related to the speed at which charge carriers, generally electrons, can move through the material. So the frequencies of electronic solid state sources are generally bounded below by the limits of the carriers’ velocity, which limits the transit time of the carriers through the semiconductor junctions. This limit and the resistance-capacitance effects cause high frequency roll-off.

Microwave and mm-wave solid state devices can be fabricated from two-terminal diode or three-terminal transistor structures. Three terminal devices, such as bipolar transistor [36,37] and field-effect transistors, although they have replaced most of the two terminal devices in the microwave band, especially in the lower frequency range of this band, their performance at sub-millimetre wavelengths are not so good, the record performance in terms of power generation capability are still held by the two terminal device. Two terminal devices such as high frequency Gunn, resonant tunnelling devices (RTDs) [38], IMPATT and TUNNEL diodes are being developed by several research groups [39]. For these sources the output power decreases rapidly when the frequency is increased. As shown in Figure 1-4, normally about 100 mW CW output power can be obtained around 100 GHz, which falls off as $1/f^2$ or even $1/f^3$ as the frequency is increased. Frequency multipliers with two or more diodes can be employed to extend the frequency range of operation up to 1 THz, with an average power level 0.1 to 1 mW achievable in the region of around 400 GHz. By using superconducting material, the frequency bounded from above can be extended to approximately to 2 THz, and a value of 0.5 microwatts at frequencies up to 0.85 THz has been observed at ~50 Kelvin [40]. But the characteristics of these devices make them undesirable for many applications due to difficulties arising in providing suitable isolation and biasing etc.

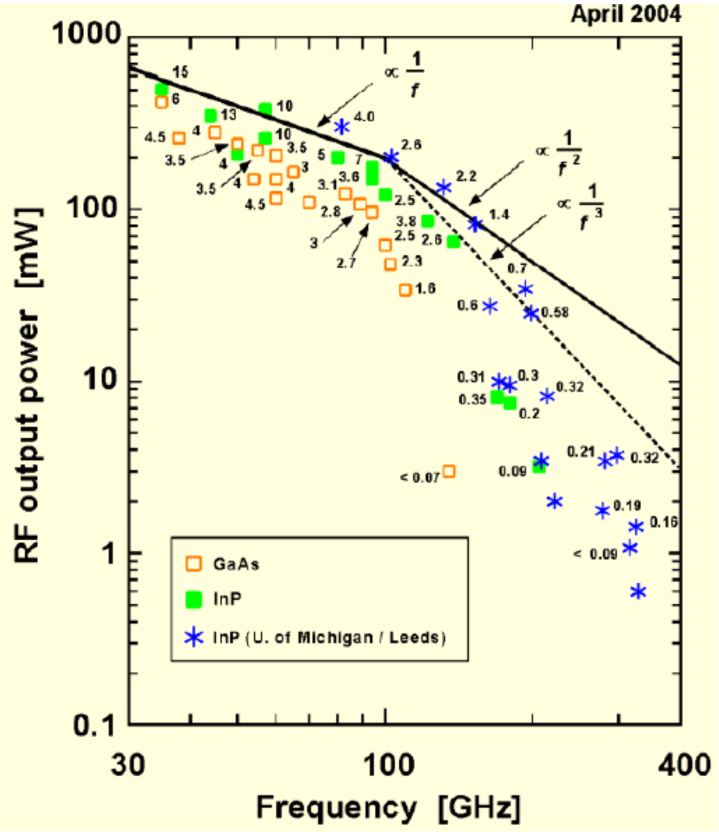

Figure 1-4 RF performance vs Frequency from GaAs & InP Gunn Diodes [41]

New technologies have been employed in recent years involving advanced materials such as Graphene [42], which is a layer of dense honeycomb crystal lattice formed by 2-D carbon atoms. The charge carriers in this material can be transported much faster as compared to other materials using new charge carriers, known as plasmons [43] which have velocities in the semiconductor channel 10 times higher than the electron velocities. All these methods can overcome the limitation dictated by the transit time of the electrons in the material, and the combination of these technologies brings new hope for operation of these devices at terahertz frequencies. The response in various forms of plasmonic transistors has recently been observed at THz frequencies.

1.2.3 **Vacuum Electron Devices**

Vacuum electron devices are by far the most common source for producing high power, frequency tuneable radiation at millimetre and sub-millimetre wavelengths. It played and still plays a very important role in the generation of microwave and millimetre wave radiation. Vacuum electron devices are the only high power radiation sources available for use throughout the entire microwave and millimetre wave part of the EM spectrum. Vacuum tubes were pioneered in the early 20th century when the diodes and triodes were invented. This led the way to the first steps in signal processing, transmission, and detection, and the advent of wireless communication, broadcasting and other applications which were developed and extended rapidly all over the world. The magnetron was known for two decades before the World War II, but its development and application accelerated in the early 1940's when the higher power capability of the resonant cavity version became recognised [44,45]. The klystron was invented in the 1930's and the travelling wave tube (TWT) and backward wave oscillator (BWO) in the 1940's. These electron devices have been extensively studied during World War II for use in radar. Since then inventors, physicist and engineers have combined to extend considerably the performance of the tube installed in the overall system.

Numerous other microwave tube types and configurations were invented, and most did not find application for any of several reasons such as low efficiency, low gain and complexity [46,47]. However the range of vacuum electron devices has now largely expanded mainly into three different groups 1). Conventional slow wave tubes (gridded tubes, klystrons, travelling wave tubes, crossed-field tubes, hybrid tubes, etc.), 2). Fast-wave tubes (gyrotrons and various gyro-devices), and 3). Accelerator-based sources (free electron lasers and coherent synchrotron sources).

1.2.3.1 Slow Wave Devices

Conventional microwave tubes are commonly referred to as slow-wave tubes [48]. There are two ways to slow down the microwave phase velocity: by dielectrically loading the waveguide or by the use of periodic boundary conditions. In the first case, a waveguide is partially filled with dielectric material and, if properly designed, only a single wave may propagate through. In the other case, which also is the more widely used way to generate radiation, is by exciting a very large number of spatial harmonics for a given frequency; each harmonic having a different phase velocity. The system is designed so that the harmonic which is synchronous with the electrons is dominant. The microwave tube as gridded tubes [49], travelling wave tubes (TWT) [50], magnetrons [51] and crossed field amplifiers [52] all belong to this type of electron beam wave interaction. There are advantages and disadvantages to both systems but the interaction process is always the same. The main slow wave devices for microwave generation in use today can be categorized as shown in Figure 1-5.

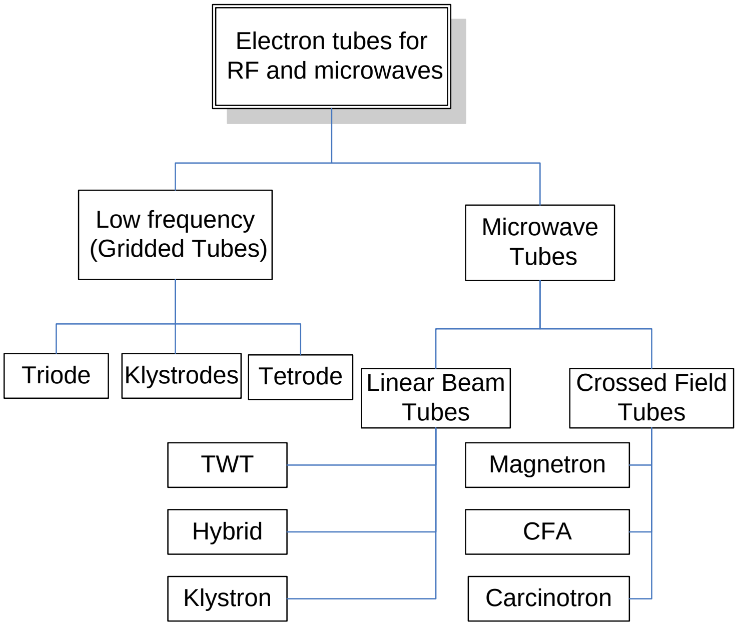

Figure 1-5 Family tree of microwave power tubes [53]

Slow wave devices are very mature technology in the microwave band and have been widely used in daily life. Various types of pulsed or CW slow wave devices have been invented in the past century and covers a very wide band throughout the HF (3MHz to 30MHz) to W-band (75GHz to 110GHz) with output powers from Milli-Watts to Giga Watts[54,55,56,57,58,59,66, 60]. New technology and new schemes have been applied in slow wave structures to extend its frequency coverage to G band (140GHz to 220GHz) and even into the terahertz band [63]. But for slow wave structures the RF circuit dimensions are typically a fraction of the wavelength, so in order to extend application of slow wave structures to the Terahertz region, most of them are micro-fabrication microwave vacuum electronic devices (MVEDs) [61]. Klystron, BWO and TWT MVEDs are very activity being pursued as possible sources of THz radiation.

Klystron

The klystron invented by the Varian brothers in the late 1930s was the first practical microwave tube to enter service. The first klystron was based on two cavities as shown in Figure 1-6, the input signal is coupled into the input cavity and the RF voltage developed across the cavity gap velocity modulates the electron beam. The output cavity is separated by a drift tube whose length is designed to provide optimum bunching of electrons at the output cavity. These bunches of electrons induce an RF current in the output cavity which is then coupled out. Various types of klystron have been invented, such as: (a) multi-cavity klystron [62] which can greatly increase the efficiency and output power by the addition of intermediate cavities between the input and output cavities of the basic two cavity klystron configuration; (b) multiple-beam klystron [63] which was introduced shortly after the invention of the single-beam klystron; and (c) relativistic klystron which use high energy electrons that the relativistic effects need to be taken into account and modification of the formulas is required to describe the klystron bunching.

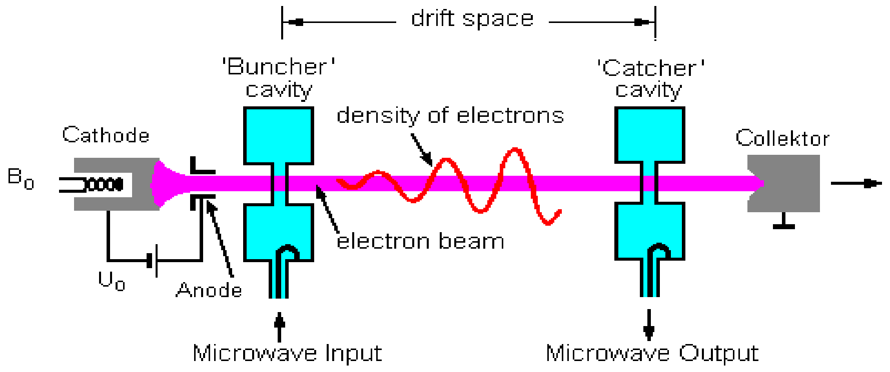

Figure 1-6 Typical two-cavity klystron

In order to improve the power available for sensors, Jet Propulsion Laboratory (JPL) researchers investigated alternative source technologies. They chose to combine two new technologies together with a reflex klystron design to provide power levels in the milliwatt range. Combining MEMs-based circuit fabrication with a carbon nanotube field emission cathode they produced a simple, low voltage device called a "nanoklystron" [64]. Estimated using simple beam analysis the anticipated performance characteristics are as follows: Highest frequency of operation 1.2 THz; test frequencies 0.3, 0.6, and 1.2 THz; Power generated about 3 mW; estimated Q 207; operating voltage 500 V; operating current 3mA. Similar research has been carried out by a research group at the University of Leeds who have developed a 1.2 THz micro-fabrication reflex klystron with a Spindt-type FEA cathode [65].

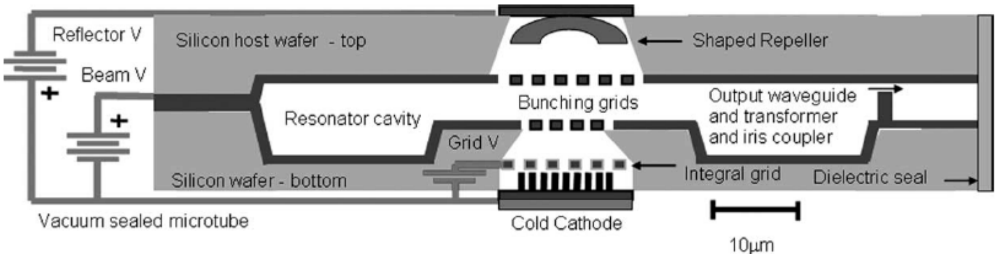

Figure 1-7 Schematic cross section of the proposed JPL nanoklystron

Backward wave oscillator

A Backward Wave Oscillator (BWO) is a device that is used to generate microwaves and terahertz radiation. It has two main subtypes, the M-type (M-BWO) and O-type (O-BWO). The OBWO is a microwave-frequency, velocity-modulated tube that operates on the same principle as the TWT. However, a travelling wave that moves from the electron gun end of the tube toward the collector is not used in the BWO; instead, it extracts energy from the electron beam by using a backward wave that travels from the collector toward the electron gun (cathode). Otherwise, the electron bunching action and energy extraction from the electron beam is very similar to the actions in a TWT. Two fundamental backward-wave circuits are commonly used. In each of these, apertures are used to couple the fields from one cavity to the next.

If the coupling loops of the forward-wave circuit are reversed (called aligned slot), then fundamental backward-wave coupling occurs. The magnetic field in a cavity induces a current in the coupling loops to the cavity on the right. That current then induces a field in the adjacent cavity, which is 180° out of phase with the cavity on the left, plus an additional phase shift of roughly 90°. If the beam velocity is high enough so that the electron transit angle is about 90°, then backward-wave oscillation is possible.

The BWO was the first microwave device driven by a high-current relativistic electron beam to demonstrate efficient, coherent high power microwave (HPM) radiation pioneered by the Institute of Applied Physics (IAP) Nizhny Novgorod, Russia and the Institute of High Current Electronics (Tomsk), Russia. An X-band (8.4GHz to 12GHz) tube generated 0.5 GW of microwave power in single 5-ns pulses from a 500-keV, 10 kA electron beam, with the power dropping to 100 MW per pulse as the pulse repetition frequency was increased to 100 Hz [66]. Later, a 1 GW power-level with more than 30% efficiency in 1-2 ns pulses with a repetition frequency of about 10 Hz and 400 MW at 100 Hz repetition was achieved. The BWO is still being developed for the generation of millimetre wavelength radiation. A series of experiments was performed, and at wavelengths from 8.8 mm down to 0.9 mm, power was radiated at levels from 50 MW to 0.5 MW, respectively. Correspondingly, the efficiency went down from 6% to 0.1%. Later, a series of experiments was carried out with millimetre-wave relativistic diffractive generators (RDGs) driven by a 2 MV, 20 KA microsecond electron beam pulses. Using an RDG multi-GW level millimetre wave radiation with about 30% efficiency was reported by Bugaev et al [67].

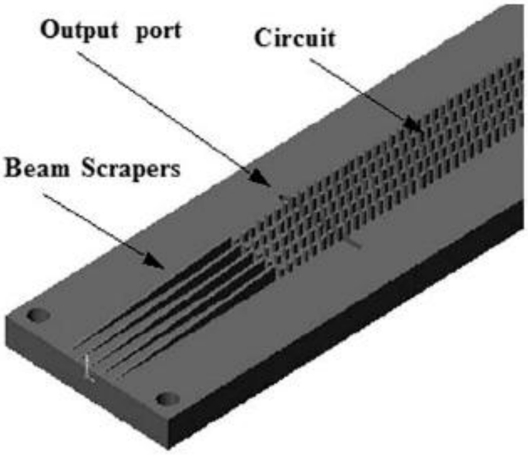

Figure 1-8 Front end of 600-700 GHz BWO circuit, showing beam scraper and output coupling port

For continues wave generation, the BWO is suitable for producing high frequency (millimetre and sub-millimetre wave) radiation with high tunability. It can provide 0.5 mW to 40 mW of power at a range of 36 GHz to 1.4 THz [63,68]. Carcinotrons are used as powerful and stable microwave sources, and due to the good quality wave front they produce, they find use as illuminators in terahertz imaging. Calabazas Creek Research is developing micro-fabricated backward-wave oscillators (BWO) in the 300 GHz to 1.5 THz range [69] to use as a local oscillator source in heterodyne receivers for ground, air, and space applications, as the existing sources at these frequencies are inefficient and use large heavy solenoids for beam focusing.

The second structure uses a staggered slot which can also be defined as a folded waveguide [70]. The wave propagates upward in one cavity, through the slot and down ward in the adjacent cavity (Figure 1-9), where the direction of the electric field reverses. Thus, there is basically a 180° phase shift from cavity to cavity plus an additional phase delay associated with the time that it takes the wave to propagate from one gap to the next. The fixed spacing of the folded waveguide limits the bandwidth of the BWO. Since the frequency of a given waveguide is constant, the frequency of the BWO is controlled by the transit time of the electron beam. The transit time is controlled by the collector potential. Thus, the output frequency can be changed by varying the collector voltage, which is a definite advantage.

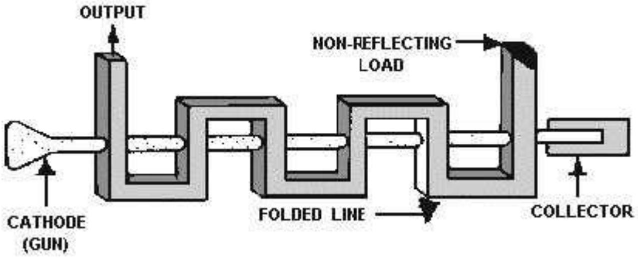

Figure 1-9 the Folded wave guide structure in BWO [71]

Folded wave guide is one of the alternative candidates for robust and high power mm-wave sources with the advantages of a simpler coupling structure, and reasonably wide bandwidth [72]. It has high thermal capacity due to the all-metal structure, a high Q, high efficiency and has no periodic reactive load; therefore, the dispersion relations of space harmonics can be easily estimated by a simple transform to that of a rectangular waveguide. Folded waveguide tubes are capable of operating at a very broad band from VHF [30MHz to 300 MHz] to W-band, at low frequency high power density larger than $2kW/cm^2$ have been achieved. At high frequency as in millimetre wavelengths, higher

RF power folded waveguides are capable of RF powers of 1000 W at 35 GHz and 100s of Watts at frequencies up to 100 GHz. Litton [73] has successfully developed a PPM (Periodic Permanent Magnet) focused folded waveguide radiation source with more than 1000 W average output power at around 35 GHz. This device has greater than 10% bandwidth and operates below 20 kV. High efficiency is achieved using a multi-stage depressed collector. By using a linear electron beam in folded rectangular waveguide, Dohler et al, observed a 30-dB saturated gain (100W output power) with a bandwidth in excess of 25% in the 40- 54 GHz frequency range [74]. J. H. Booske etc are designing a micro-fabricated folded waveguide TWT to operate in the range from 0.2 to 1 THz to achieve relatively high power (> 1 *mW* in CW). Simulation has achieved 56 mW, CW output at 560 GHz with 1% (intrinsic) efficiency for the oscillator [75].

Hybrid Tubes

In hybrid tubes, klystron and coupled-cavity TWT technologies are combined to achieve enhanced bandwidth, power capability, or operation at high frequencies. As linear-beam amplifier tubes can be considered to consist of a driver section and an output section, and the output section must have a bandwidth at least as wide as that of the driver section. There are two main types of hybrid tubes (1) the extended interaction klystron (EIK) and (2) the twystron, the main difference between these two hybrid tubes is shown in Figure 1-10(c) and (d).

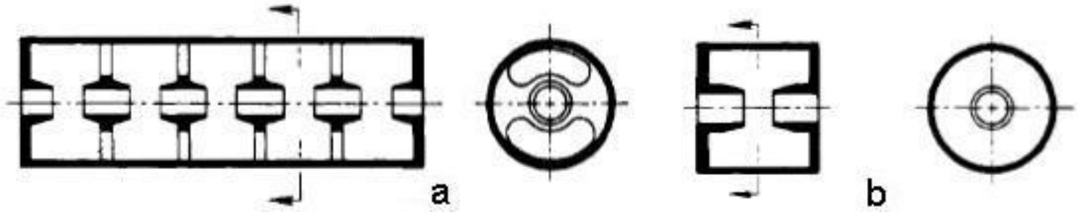

Figure 1-10 Comparison of a five-gap EIK cavity (a) to a single-gap klystron cavity (b).

As with most klystrons and TWTs, EIOs are designed for minimum interception of the electron beam on the RF structure. At high frequencies, these devices are capable of operation at higher power levels than reflex klystrons or magnetrons. EIOs are available for operation at frequencies up to 260 GHz. The high power capability of the EIK can achieve 1 MW average power in X-band with a bandwidth over 10%, and an efficiency of nearly 40%. For pulsed EIKs, it can achieve 100 kW at 40 GHz, and several hundreds of watts over 200 GHz. For CW EIKs, it can achieve several hundreds of watts at 40 GHz, and several watts over 200 GHz. Pulsed EIOs are capable of power outputs of several kilowatts at 40 GHz varying down to 100 W at over 200 GHz [53].

Surface-Wave Microwave Oscillator [76]

In order to increase the power-handling capabilities of HPM devices, one method is to increase the transverse diameter D to several times the free-space wavelength λ thereby reducing the internal field stress for the same power flow. By using this method, microwave-generating structures can be designed with internal microwave electric fields below the breakdown levels. An overmoded interaction cavity will support surface waves that synchronous the electron beam even with a modest voltage. In order to avoid mode competition, the surface waves are crucial and large values of coupling impedance is required to achieve an efficient interaction. These can be both satisfied with the use of a periodic structure.

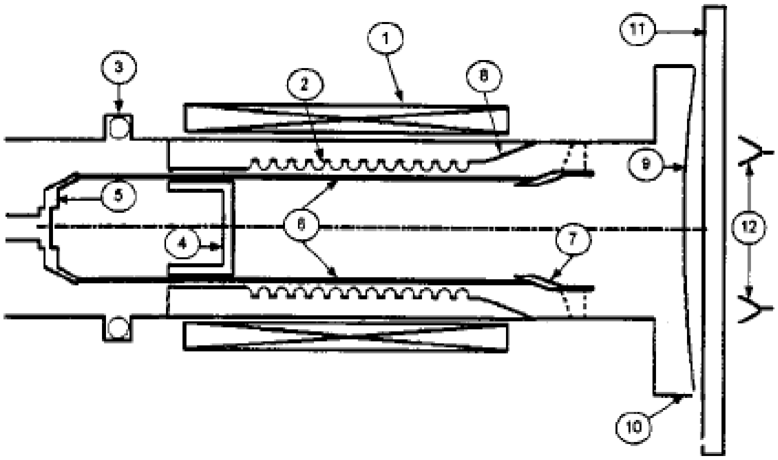

Figure 1-11 A schametic diagram of a large diameter surface-wave generator; 1) solenoid, 2) slow wave overmoded structure, 3) Rogowski current monitor, 4) adjustable RF reflector, 5) explosive cathode, 6) electron beam, 7) coaxial collector, 8) output up-taper, 9) output window, 10) vacuum jacket, 11) wide band calorimeter, 12) receiving horns, connected to hot carrier detectors.

Oversized slow wave generators have produced record levels of multi-GW microwave radiation. The Relativistic Diffraction Generator demonstrated a peak output power of 4.5 *GW* in the 9-11.3 *mm* wavelength range and the Multi-wave Cerenkov

Generator (MWCG) has produced 15 GW at a wavelength of 3 cm. These results were achieved by using a high-voltage electron beam (in the range of 1.5-2 *MV*). For practical devices, operation at reduced voltages, possibly no more than 500 *kV* is preferable. So far the maximum power achieved in a slightly oversized backward wave oscillator with D/λ~ 1.8 operating at 550 *kV* is about 0.8 GW at 10 GHz frequency. Recently, 60 MWs of pulsed microwave radiation at 37.5GHz has been obtained through the use of overmoded 1D or 2D periodic structures, and MWs of simulated output power have been predicted at several hundred GHz [77,78,79].

1.2.3.2 Fast wave devices

In fast-wave tubes, the RF structure is usually a smooth waveguide or a large resonator in which no attempt is made to reduce the velocity of the wave. The electron beam is injected into the electromagnetic field in a manner such that interaction can take place. In fast-wave tubes, the electron beam is normally placed well away from the RF structure which can both relax the size limitations as compared to conventional microwave tubes and significantly increases the power handling capability.

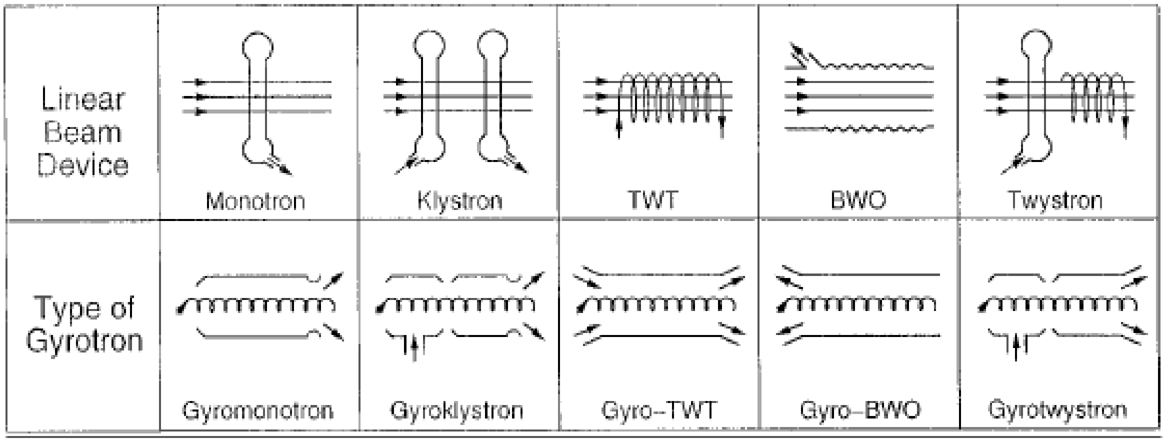

Figure 1-12 Overview of gyro-devices and comparison with corresponding conventional O-type devices.[80]

The gyrotron was originally used by the Russians for a single-cavity oscillator, the definition of which now has been expanded to include both oscillators and amplifiers. Gyrotrons are well recognized as high-power sources of coherent electromagnetic radiation in the millimetre and sub-millimetre wavelength regions. Gyrotrons can produce microwaves in continuous-wave and long-pulse regimes with powers which exceed the power of classical microwave tubes by many orders of magnitude. It is one of the most promising vacuum electronic devices for producing both high average power and high peak power at millimetre and sub millimetre wavelengths.

In a gyrotron, the electron beam which is normally in the shape of a thin hollow cylinder, is injected into a strong axial magnetic field and passed through a circular cavity or waveguide containing an electromagnetic wave with a circular electric field pattern. The rotational velocities of the electrons are normally 1.5 to 2 times the axial velocity so that most of the electron energy is rotational. Because the magnetic field is very large, the orbit diameter for the electrons is small. As a result, the thickness of the hollow electron beam may be several times the diameter of the electron orbit.

Although the processes of electron energy modulation, phase bunching in cyclotron orbits and energy extraction by transverse deceleration are common to all gyrotrons, a variety of circuit configurations are applied. Normally, it can be divided into such basic types: gyro-klystron, gyro-twystron, gyro-monotron, gyro-TWT, and gyro-BWO.

The gyromonotron is an oscillator with a single resonant cavity and is characterized by high efficiency (~40%) and high average-power output at fixed frequency. The gyro-TWT is an amplifier in which the interaction circuit is typically a hollow pipe waveguide of constant cross-section; it is characterized by a bandwidth of several percent. The tapered two-stage gyro-TWT varies both the waveguide cross-section and the magnetic field, B_0 along the axis to achieve wider bandwidth; a bandwidth of 20% has been demonstrated in this configuration. The Gyro-klystron amplifier consists of a number of resonant cavities separated by cut-off drift tubes. Gyroklystrons are generally more efficient than gyro-TWTs but have a narrower bandwidth, typically a fraction of 1%. Gyro-twystron is similar to a gyro-klystron except that the output cavity has been replaced by a travelling wave section (waveguide); the properties of the gyro-twystron are a compromise between the higher efficiency of

Gyro-klystrons and the wider bandwidth of gyro-TWTs. An inverted version of the gyro-twystron is where the input section is a waveguide and the output section is a resonant cavity.

Gyro-Klystron

A Gyro-klystron is a narrow-band amplifier, it's transverse and axial cavity dimensions can be much larger than the wavelength, allowing these devices to scale to higher frequencies and significantly greater power-handling capability than conventional klystrons. But the efficiency of gyro-klystrons is generally lower than the klystron, as only the transverse electron energy is available for RF power generation. Multiple cavities are commonly employed to increase the gain; however the principle can be illustrated with a two-cavity model.

The operation of a gyro-klystron is similar to the conventional klystron except the electron bunching occurs in the azimuthal direction rather than in the axial direction. In a gyro-klystron, the signal to be amplified is fed into the input cavity where the cyclotron bunching process is initiated and the bunching continues while drifting to the output cavity.

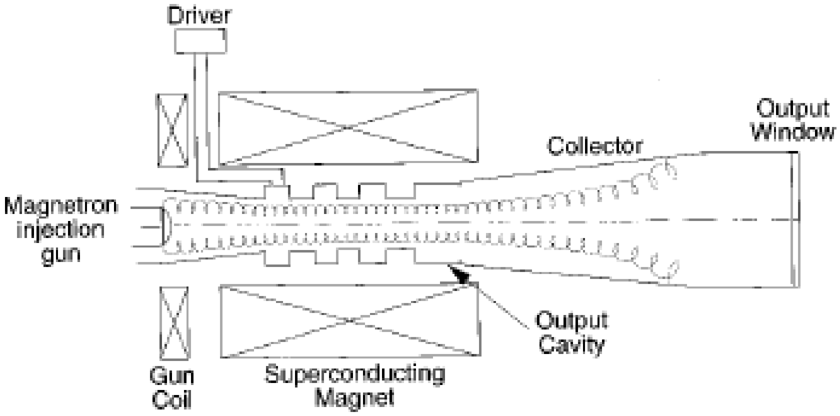

Figure 1-13 Schematic diagram of a relativistic gyro-klystron.

Gyro-klystrons can achieve high power from X-band to even W-band which are normally aimed at radar applications and accelerators. Such as the 75 MW peak power achieved in the X-band and 50-MW at 30GHz in the Ka-band [81], and the 94 GHz W-band gyro-klystrons capable of 100-kW peak power at a 10% duty factor developed and integrated into the NRL WARLC radar system [82].

Gyrotwystrons and inverted gyrotwystrons [83]

Just like twystrons derived from the klystron, which changes the output cavity to the travelling wave structure, the gyrotwystrons is derived from the gyroklystron by extending the length of the drift section and replacing the output cavity with a slightly tapered waveguide section like in a gyro-TWT. The output waveguide section is excited by the beam of electrons that are bunched because of modulation in the input cavity. Thus the gyrotwystron configuration can mitigate the problem of microwave breakdown at high power levels, since the microwave energy density in the output waveguide can be much smaller than in an output cavity and can offer a higher bandwidth than the gyro-klystron and the gain-bandwidth product can be increased by more than three times as well.

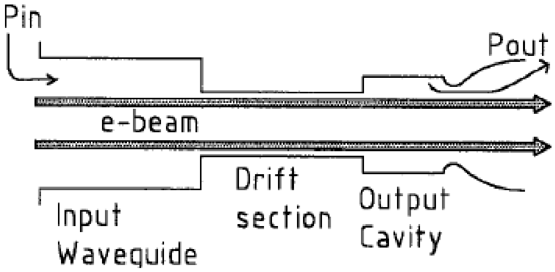

Figure 1-14 The scheme of the inverted grotwystron.

The inverted gyrotwystron is a device consisting of the input waveguide, drift section, and output cavity. The travelling signal wave in the input waveguide may induce a higher harmonic content in the electron current density. Then the pre-bunched electron beam can excite phase-locked oscillations in the cavity at a harmonic of the signal frequency.

The development of W-band gyrotwystrons for radar applications was started at NRL in 1996. In the first experiments (94 GHz), a low-duty prototype was developed and tested. This device produced 50 kW of peak power in a 0.925 GHz bandwidth that represented a substantial improvement in the power-bandwidth product over that previously demonstrated gyroklystrons (56.25 kW-GHz versus maximum 38.4 kW-GHz in gyroklystrons) [84]. Joint work by NRL-CPI has achieved a power level of 60 kW peak and a measured bandwidth of 1.8 GHz centred at 94 GHz in 2002 [85]. In the relativistic gyrotwystrons that have been developed for accelerator applications, at fundamental harmonics peak powers above 20 MW were achieved with an efficiency exceeding 22% and a large-signal gain of 24 dB [86].

Gyro-TWT

When very wide bandwidth is required, one must resort to devices based on beam interactions with travelling waves. Certainly this is the same in gyro-devices and the Gyro-TWT serves as a good example of the transformation of an electron cyclotron maser. However, early attempts at building such amplifier tubes were plagued by oscillation due to both absolute and convective instabilities. Later, a better understanding of these instabilities and how to avoid them has allowed considerable experimental progress to be made, resulting in the development of high performance gyro-TWT amplifiers. Operation of the gyro-TWT is based on a convective instability. The input wave is amplified while propagating forward with the beam. The gyro-TWT utilizes a moderately relativistic electron beam to interact with a fast wave guide mode near the grazing intersection of the frequency versus wave-number plot where the resonance line is tangent to the electromagnetic mode. A gyro-TWT can also oscillate as a gyro-BWO at the Doppler downshifted cyclotron frequency and its harmonics.

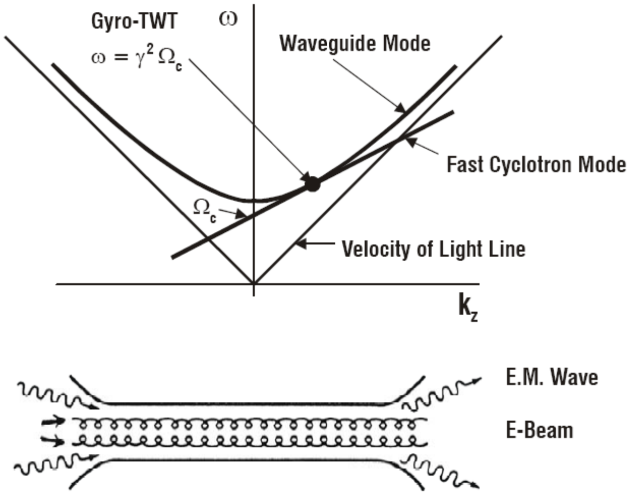

Figure 1-15 Dispersion diagram and scheme of interaction circuit of Gyro-TWT amplifier.

Significant progress has been achieved in gyro-TWT research since 1995, and has been developed as a dependable, high power and high gain millimetre wave amplifier. It has been stabilized by heavily loading the interaction circuit with distributed loss. Researchers at the National Tsing Hua University in Taiwan were the first to show that extremely high gain as well as excellent stability could be achieved by loading the interaction waveguide with a substantial amount of distributed loss. The required attenuation was achieved by coating the wall of the circuit with a thin layer of Aquadag of depth corresponding to approximately one skin depth. At optimum operation a peak power of 93 kW with an efficiency of 26.5% and a saturated bandwidth of 8.6% with a saturated gain of 70 dB in the fundamental TE_{11} mode was achieved.

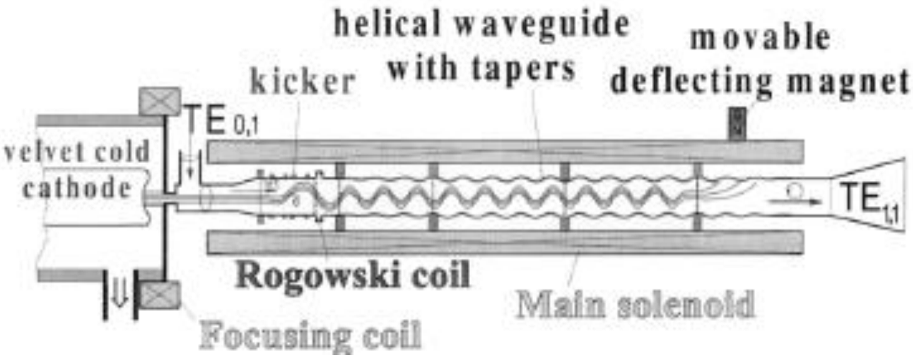

Figure 1-16 Schematic of the gyro-TWT with a helically corrugated waveguide. [87]

A new concept of large-bandwidth gyro-TWTs has actively been studied jointly since 1997 by a group of researchers from the University of Strathclyde (Glasgow, Scotland) and the Institute of Applied Physics (Nizhny Novgorod, Russia) [88,89]. The concept is based on the use of a microwave structure, which can simultaneously provide the cyclotron resonance condition between electrons and the forward wave over a large bandwidth and makes the beam-wave interaction insensitive to electron velocity spread. Such characteristics can be realized in a cylindrical helically corrugated waveguide as shown in Figure 1-16. About 1MW output power and over 20% 3-dB bandwidth were obtained at around a centre frequency of 9.4GHz from a helically corrugated TWT experiment that was carried out at the University of Strhaclyde[90]. In the linear gain region 137 kW of output power at 47-dB gain and 17% efficiency was found in this second harmonic gyro-TWT experiment. Power levels of up to 180 kW at 30 dB gain and 10% bandwidth were generated at 35 GHz using a gyro-TWT based on a helically corrugated cylindrical interaction region by S.V. Samsonov et al at the IAP, Nizhny Novgorod, Russia.

Gyro-BWO

The gyro–BWO employs a waveguide structure like the gyro-TWT but operated at a point in the $w - k_z$ diagram where the group velocity is opposite to the beam velocity as shown in Figure 1-17. The oscillation is based on the backward waveguide mode which takes place as the forward moving electron beam and the backward wave form a feedback loop, thus the beam power must exceed a certain threshold to start the oscillation. In the noise fields, the electron beam will be weakly bunched by a resonant backward wave. The bunched electrons impart energy to the wave, which propagates backward toward the beam entrance to generate tighter electron bunches. More and more energy is thus fed to the wave until an equilibrium state is reached. Since the beam and the wave constitute a closed loop, no reflections are required in the build-up process.

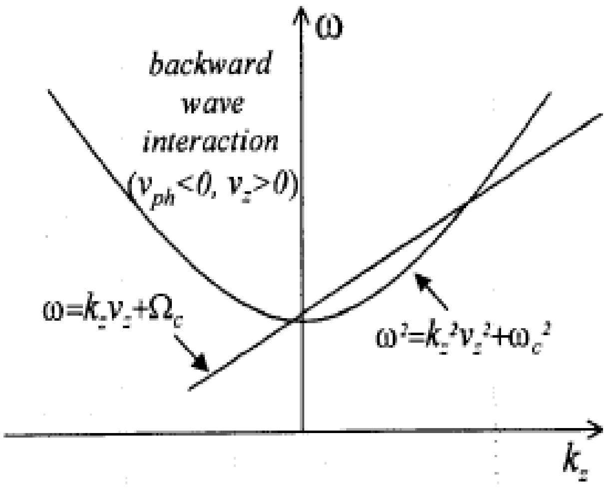

Figure 1-17 The ω-k_z diagram of the operation point of the gyro-BWO.

In the gyro-BWO the frequency of operation is governed by the slope of the line, which is a function of v_z, and thus of the beam acceleration voltage V_0. As there is a Doppler down shift in frequency ($\Omega_c/2 < \omega < \Omega_c$), so that very high magnetic fields are required for high frequency operation. For the gyro BWO frequency tuning can be achieved by voltage adjustment as in the case for the conventional BWO, but it can also be tuned through variation of the magnetic field.

As the wave frequency in the gyroklystron and gyrotron is fixed by the cavity resonance, the magnetic field can be adjusted to achieve optimum detuning. However, it is difficult to control the detuning factor for waveguide-based devices. The gyro-BWO oscillation frequency varies with the magnetic field to maintain a synchronous interaction. The gyro-TWT gain diminishes with too large a detuning factor. There are also other factors that adversely affect the efficiency of the gyro-TWT and gyro-BWO. The gyro-TWT operates at a frequency farthest away from the cutoff and thus is most sensitive to beam velocity spread. The gyro-BWO field is at a high level at the beam entrance, which results in abrupt electron bunching unfavourable for efficient interaction. Largely for these reasons, the interaction efficiency is generally higher for the gyromonotron and gyroklystron (30%~50%) than for the gyro-TWT and gyro-BWO (10%~30%). The gyro-BWO delivers a power ranging from tens of watts at ~1000 GHz to nearly 100 MW at 10 GHz [91]. Low-voltage and small-size BWOs are capable of providing an output power of several milliwatts in the CW regime at a frequency of up to 1.4 THz [92].

Gyromonotron

In the gyromonotron self-oscillation in a single cavity by the distributed interaction forms the bases of high-average-power devices. To build up and sustain the oscillation, a feedback loop is required. In the gyromonotron, it is provided by end reflections, which means that the forward wave turns into a backward wave upon reflection at one end, while the backward wave reverses to a forward wave at the other end. This results in continuous wave circulation in a closed loop.

If the power gained from the beam exceeds the power lost, the circulating wave will be repetitively pumped by the electron beam from the noise level to equilibrium amplitude. This feed-back process results in fresh electrons interacting with a wave, while the gyro-TWT is based on a single-path process. As the electron beam deposits energy into the cavity fields, there are also power losses through output coupling and wall dissipation. The field amplitude grows as long as the deposit of power is larger than the loss of power, an equilibrium state will be reached when the power deposited equals the power lost.

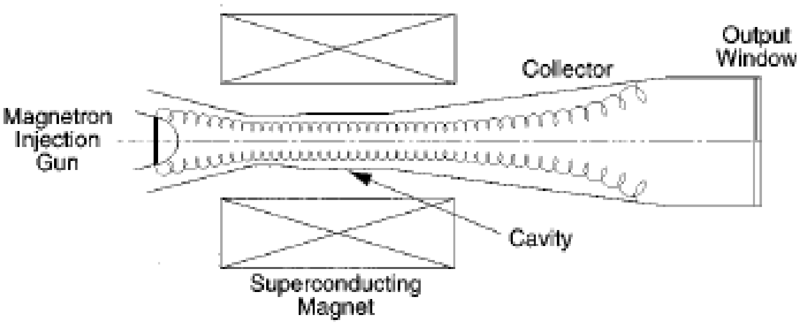

Figure 1-18 Schematic diagram of a gyromonotron.

The gyromonotron oscillator is the most mature type of gyrotron. High-lights of early accomplishments included CW operation at the second cyclotron harmonic which could produce 1.5 kW at 326 GHz [93] and 10kW at 34 GHz [94]. Gyromonotrons are now commercially available sources. These devices can produce megawatt output power in long-pulse or CW operation in the frequency range 75-170 GHz[6], which represents an advance of more than three orders of magnitude beyond the capability of other tube types. In step-tunable gyromonotrons, as the magnetic field can vary over a broad range, the oscillation frequency can jump from mode to mode, thus generating a broad and usually discrete radiation spectrum. Contemporary step-tunable gyrotrons have achieved hundreds of watts of CW power at 190 GHz and tens of watts CW radiation at 860 GHz [95]. With strong pulsed magnetic fields, kilowatts of output power have been achieved at a frequency of up to 1.3 THz [96].

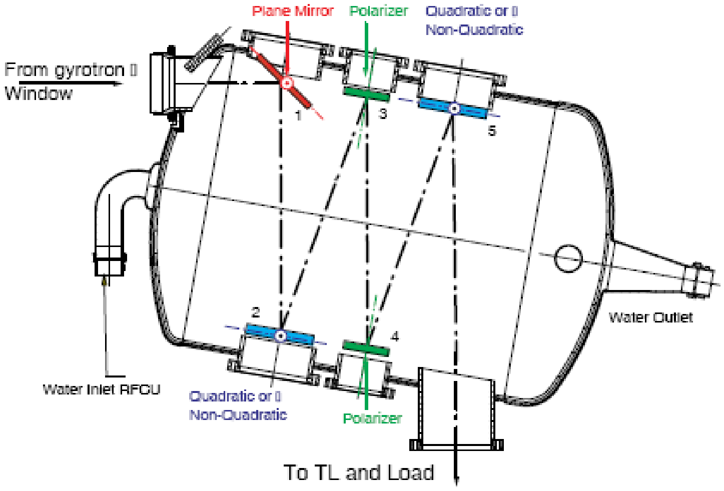

Figure 1-19 The RF coupling unit of the 170 GHz Gyrotron.

Quasi-optic gyro-amplifiers operate in the middle ground between geometric optics and diffraction dominated propagation. In this regime, the dimensions of the system elements are larger than the wavelength but the diffraction effects are still important. Quasi-optical techniques of wave propagation are very important in the millimetre and sub-millimetre wave regime. The wavelength in this region of the spectrum is still not small enough when compared to the size of the system elements to permit the use of geometric optics techniques. At the same time, however, the propagation losses in single-mode waveguides are not small enough to use standard microwave techniques for wave propagation.

A Quasi-optical (QO) gyroklystron was demonstrated using two resonators transverse to the beam propagation direction at NRL in 1994. Phase-locked oscillator operation was obtained, as was amplifier operation at 30 kW of output power and 18 dB of gain at 85GHz with an efficiency of 10%. More recently, a novel geometry for a QO resonator has been implemented in a gyro-TWT operated at 140 GHz, which was designed to operate in a higher-order HE_{06} mode with an unsaturated 3-dB bandwidth of 2 GHz [97]. The European research centre and the Thales Electron Devices under the auspices of the European Fusion Development Agreement are developing a 170 GHz, 2 MW and CW coaxial QO gyrotron for the electron cyclotron heating system of ITER after they achieved an output power of 1 MW [98,99].

Frequency-multiplying Gyro-Amplifiers

Frequency multiplication [100] is another very straight forward and attractive way to obtain a practical source of THz radiation based on the nonlinear properties of the electron beam medium. This nonlinearity means that, after initial modulation of the beam in the input stage by the RF field at the signal frequency ω_s, not only does the electron current density possess an RF component at ω_s, but components at its harmonics also appear. Subsequently, one of these harmonics can be used for exciting other stages of the device at correspondingly higher frequencies. This frequency multiplication mechanism is known and used in both linear-beam klystrons and TWTs. Also single-cavity gyro-multiplier schemes have been studied when both the lower harmonic and higher harmonic waves in a gyro-multiplier are radiated by the same electron beam in a single cavity which can enable high harmonic radiation to be generated [101]. An azimuthal corrugated cavity has also been considered in order to improve the efficiency of the gyro-multiplier and demonstration experiments are under preparation at the Institute of Applied Physics [102].

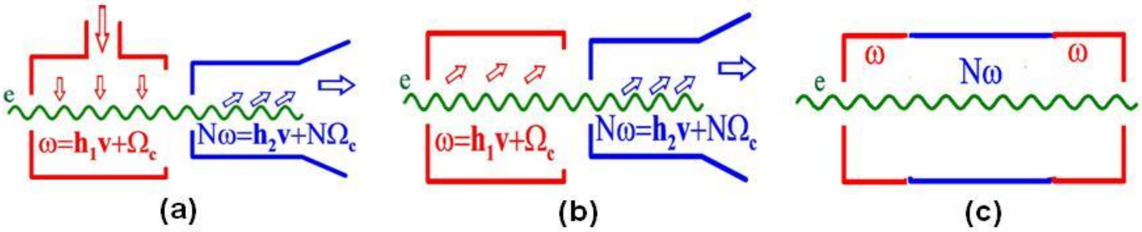

Figure 1-20 Frequency multiplier schemes:

(a) Klystron-type with LF input, (b) self-exciting Klystron-type; (c) single cavity scheme.

Free Electron Laser

The most common devices based on radiation from electrons oscillating in periodic external fields are free-electron lasers (FELs). They are quite different from the other high-power microwave sources that have been discussed. FELs can generate output over a range of frequencies extending far beyond the microwave spectrum, well into the visible and ultraviolet range. The term “free electron laser” or “FEL” is generally used to describe devices that generate coherent radiation (light) by means of a fast-wave interaction in which a beam of relativistic “free” electrons is induced to radiate coherently by passage through a periodic wiggler field. Perhaps another name by R. M. Phillips is more descriptive: UBITRON (Undulated Beam Interaction elecTRON) [103]. There is another type of wiggler using an electrostatic instead of magnetostatic fields to provide electron undulation, which is called the scattron. In 1971, Madey initiated an important step by proposing that an undulator structure working as an amplifier at optical wavelengths could replace the active medium between the mirrors of a laser optical cavity, he called such a device a free-electron laser. While some researchers seek to extend the operation of modern descendants of the undulator called free-electron lasers to lower and lower wavelengths, other modern descendants of the ubitron (which are also called free electron lasers) can produce higher and higher microwave power outputs from mildly relativistic electron beams.

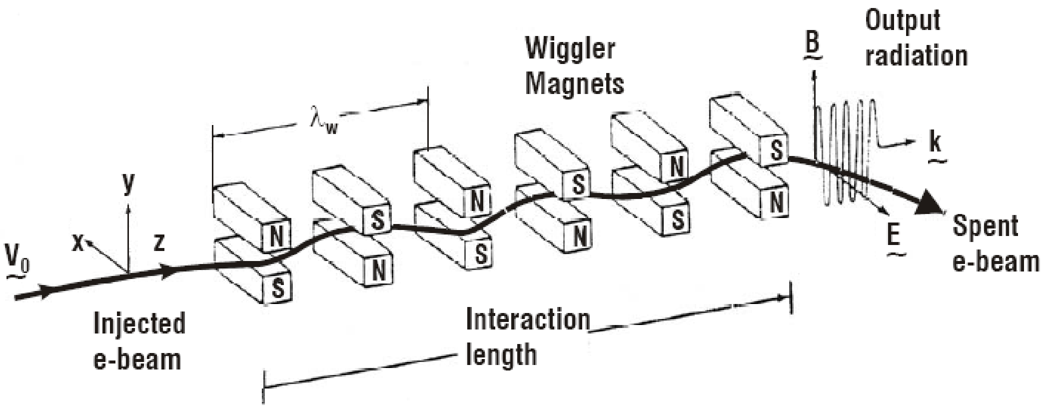

Figure 1-21 The basic FEM configuration.

As the electrons vibrating by the spatially periodic wiggler field they will radiate, if the electron beam is highly relativistic then the radiation will have a much shorter wavelength than in the laboratory frame ($\lambda \cong \lambda_{\omega}/2\gamma^2$ so that $\omega \cong 2\gamma^2\Omega_b$). Therefore, FEMs are capable of generating electromagnetic waves of very short wavelength determined by the relativistic Doppler Effect. The bunching of the electrons in the FEM is due to the perturbation of the beam electrons by the ponderomotive potential well which is caused by “beating” of the electromagnetic wave with the spatially periodic wiggler field. It is this bunching that enforces the coherence of the emitted radiation. As the radiation wavelength is not determined by the characteristic size of the interaction region, such fast-wave devices require no periodically rippled walls or dielectric loading and can instead use a simple hollow-pipe oversized waveguide as the circuit. These devices are capable of producing very high power radiation at cm-, mm-, and sub-millimetre wavelengths since the use of a large waveguide or cavity cross sections reduces wall losses and breakdown restrictions, as well as permitting the passage of larger size, higher power electron beams. It also relaxes the constraint that the electron beam in a single cavity can only remain in a favourable RF phase for half of a RF period (as in klystrons and other devices employing transition radiation).

Free electron lasers appear to be potentially capable of fulfilling all the requirements for a frequency tunable high-power mm-wave source. It has achieved more than 1 MW output power in the entire frequency range of 130-260 GHz, and even higher frequencies are quite feasible. A disadvantage of FELs is that they often require high energy ~(500keV and above) electron beams for optimum operation which results in a large size electrode beam source to ensure adequate voltage hold off as well as the generation of high energy X-rays which needs to be adequately shielded.

1.3 **Thesis Project**

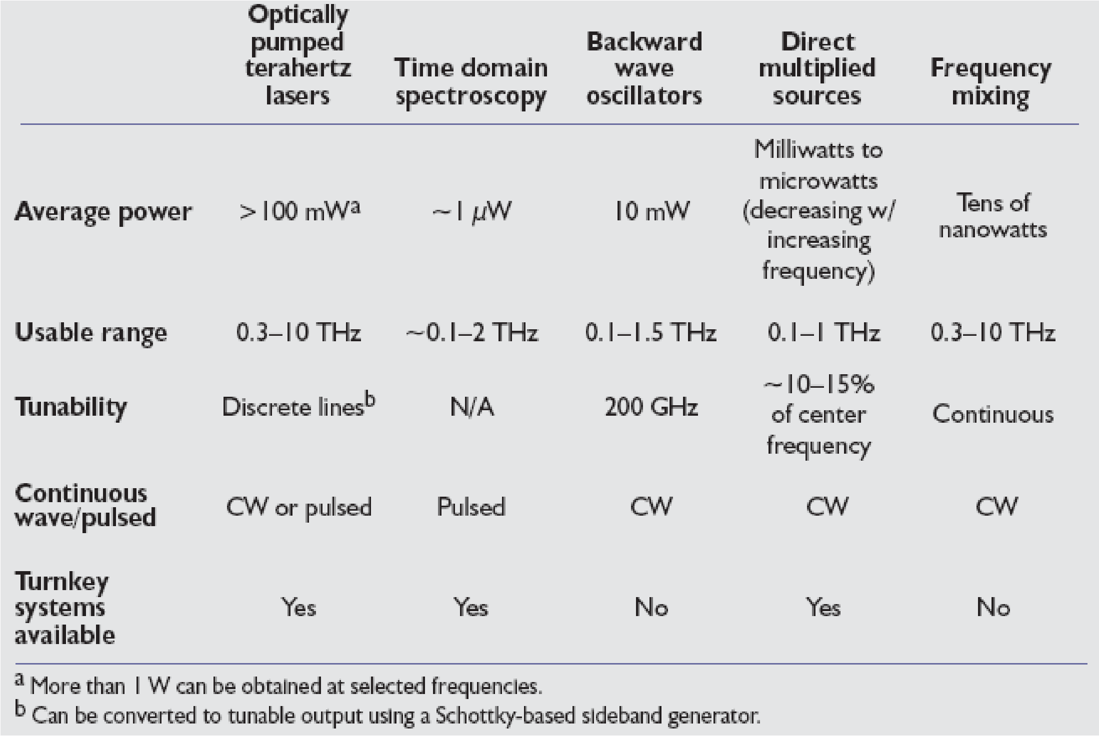

	Optically pumped terahertz lasers	Time domain spectroscopy	Backward wave oscillators	Direct multiplied sources	Frequency mixing
Average power	>100 mW[a]	~1 μW	10 mW	Milliwatts to microwatts (decreasing w/ increasing frequency)	Tens of nanowatts
Usable range	0.3–10 THz	~0.1–2 THz	0.1–1.5 THz	0.1–1 THz	0.3–10 THz
Tunability	Discrete lines[b]	N/A	200 GHz	~10–15% of center frequency	Continuous
Continuous wave/pulsed	CW or pulsed	Pulsed	CW	CW	CW
Turnkey systems available	Yes	Yes	No	Yes	No

[a] More than 1 W can be obtained at selected frequencies.
[b] Can be converted to tunable output using a Schottky-based sideband generator.

Figure 1-22 Some Techniques for Generating Terahertz Radiation. [7]

Many other terahertz source technologies have been investigated in the past, such as Direct Multiplied (DM) sources and p-Germanium Lasers. Some of the techniques for generating terahertz radiation are shown in Figure 1-22. Though there are already several types of systems commercially available none of them can fully satisfy the requirement in practical applications. Nevertheless, the impetus to develop an economically feasible THz technology has arguably never been greater than it is now [104] to satisfy the market requirement for more reliable, powerful and compact terahertz sources at an economically viable cost.

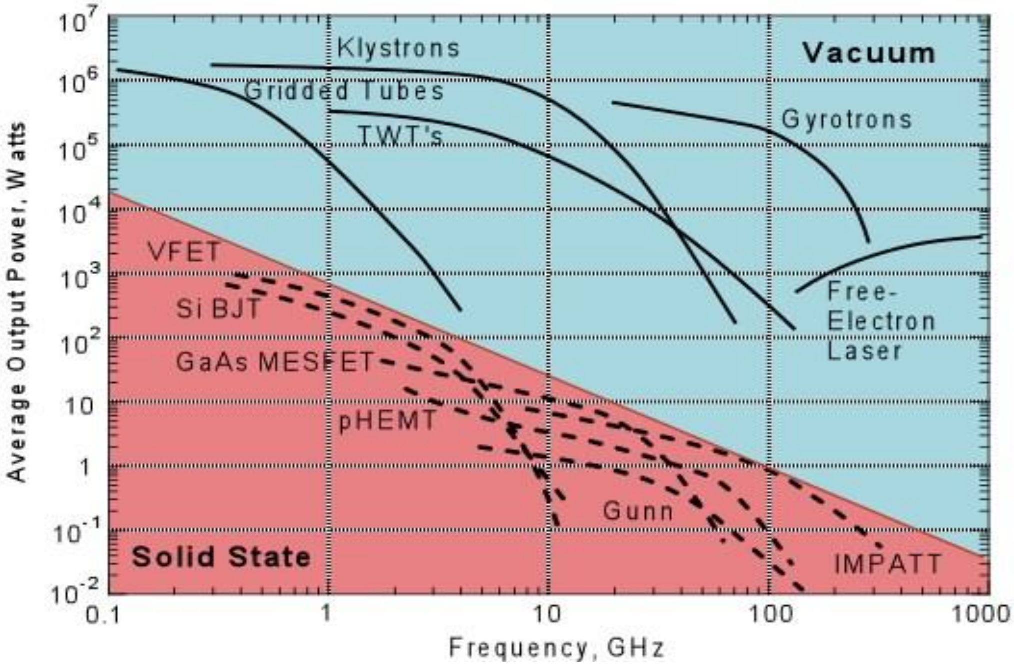

Figure 1-23 The capability of microwave sources.

The PhD project is to design a harmonic oscillator at a frequency in the hundreds of GHz frequency range. According to the radiation sources introduced above, it was decided to build an oscillator based on a cusp gun and a harmonic gyrotron interaction. A cusp electron gun works by using a non-adiabatic magnetic field, reversed initially at negative amplitude changing to positive amplitude, invariance of the magnetic moment results in a large orbit, annular electron beam. In a harmonic gyrotron, the cusp gun has a lot of advantages over other conventional electron guns, as it can create an annular axis encircling electron beam that the interaction and resonance with the TE_{nmq} mode can be maintained for $\omega = n\Omega$ over the entire electron orbit and hence high efficiencies can be realized. It also has the advantage of not requiring a kicker magnet, can operate in CW mode, and the beam trajectories are more suitable for energy recovery as well as enabling better mode selection. Successful operation of a cusp electron gun will be a major achievement as very few microwave sources based on this novel electron beam source have been successfully operated. Two successful gyro-TWA sources based on a cusp electron gun were a 35GHz experiment at the Institute of Applied Physics, Nizhny Novgorod, Russia, 2005 and a 9.4GHz experiment at the Department of Physics, University of Strathclyde, UK, 2006. The cusp gun parameters were beam energy 40keV, beam current of 1.5A, a pitch alpha of 1.6 with minimum beam velocity spread and scalloping in the beam trajectory.

In principle, vacuum electronics allows production of coherent Terahertz radiation practically to operate at any power level. However, in practice there are a lot of problems which has limited the development of high power, high frequency radiation sources, such as the high magnetic field, voltage breakdown and manufacture of small size microwave waveguides at high frequency. The most widespread electron devices in this frequency range are low-voltage Backward Wave Oscillators which can generate CW radiation with output powers of $1-10^{-3}$ W at frequencies of 0.1~1.0 THz with broad frequency tuning. Gyrotrons can produce high powers up to 1 MW at the frequency of 0.17 THz in the quasi-CW regime. Gyrotrons with strong pulse magnetic field have demonstrated tens of kWs output power at frequencies up to 0.65 THz. The highest frequency achieved in gyrotrons is over 1.0 THz with power of several watts. Free electron lasers demonstrate very high pulsed and average power along with a possibility of broadband frequency tuning within the entire Terahertz range and even at many times higher frequencies. Gyrotron operation at THz frequencies requires a very strong magnetic field: 36 T at the frequency of 1 THz when operating at the fundamental cyclotron resonance. This is possible in the pulse regime of operation only. An alternative way is to generate high cyclotron harmonics is via the so called gyro-multiplier concept. Gyro-multipliers can operate at low-voltages and be compact while at the same time requiring a magnetic field of 5-12 T to provide $1-10^{4}$ watts at the frequencies of up to 1 THz. As for Terahertz FELs, they use basically very high energy electron beams (2-12 MeV) that can only be produced by large accelerators. So the most probable way of achieving hundreds of GHz millimetre wave radiation is to use a harmonic gyro-device or frequency multiplication, such as a high harmonic QO-gyro source, gyromonotron, gyro-BWO, or large orbit gyrotron. Micro-fabrication MEVDs can also be used to achieve about tens of milliwatt of output power at 400 GHz, but the size limits on the beam-wave interaction region limits the output power and it is incredibly difficult to fabricate.

Chapter 2

Beam Physics

2.1 Introduction

An electron beam is a group of electrons that are moving in almost the same direction with approximately the same kinetic energy which is usually much larger than the thermal kinetic motion at normal room temperature.

If the electrons kinetic energy of the electron beam approaches or exceeds its rest energy, in this situation one must use a relativistic equation of motion, and the Newtonian equations of motion are approximately correct for the electron beams with kinetic energy below 30 (keV).

A very useful parameter is the ratio of the electron speed to the speed of light in free space(c).

$$\beta = v / c \tag{2.1}$$

And the apparent mass of the electron which is moving at a speed of v:

$$m = \frac{m_0}{\sqrt{1-(v/c)^2}} = m_0(1-\beta^2)^{-1/2} = \gamma \cdot m_0 \tag{2.2}$$

Here $\gamma = (1-\beta^2)^{-(1/2)}$, and the quantity of γ is always greater than unity because the observed speed of a particle can never be equal or exceed c.

Electron beams are widely used in scientific, industrial, and even domestic apparatus. The high kinetic energy and good directionality of electron beams make them ideal for use in pulsed RF linacs, induction linac injectors, electron cyclotron maser (ECMs) and free electron lasers (FELs). Electron beams have continually expanding applications in many branches of research and technology, such as flat-screen cathode-ray tubes, synchrotron light sources, beam lithography for microcircuits, thin-film technology, production of short-lived medical isotopes, radiation processing of food and free-electron lasers. Finely focused electron beams are also employed in electron microscopy analysis such as transmission electron microscopes (TEM) and scanning electron microscope (SEM).

2.2 Electron beam parameters

To characterize an electron beam, several quantities are normally used, including average kinetic energy and its spread, current, power, pulse length, transverse dimension and parallelism. The first four parameters are quite obvious and easy to measure. The quantitative description of the transverse dimension and parallelism of an electron beam is based on the concepts of 'phase space' and its modification 'trace space'. The emittance and brightness describe the quality of an electron beam when defined in phase-space or trace-space.

2.2.1 Particle trajectories in phase space

As mentioned before, the motion of electrons or charged particles in general is usually portrayed in 3-D Geometric space, or in configuration space. The motion of an electron in an electromagnetic field can be described in the equation(2.3).

$$\frac{d}{dt}\vec{P} = \vec{F} = q\left(\vec{E} + \vec{v} \times \vec{B}\right) \tag{2.3}$$

when replacing $\vec{P}$ with position vector:

$$\frac{d}{dt}\gamma m_0 \dot{\vec{r}} = \vec{F} = q(\vec{E} + \vec{v} \times \vec{B}) \tag{2.4}$$

here "$\dot{\vec{r}}$" represents "$\frac{d\vec{r}}{dt}$", as the kinetic energy of the electron is:

$$W = \frac{1}{2}\gamma m_0 v^2 = \frac{1}{2}\gamma m_0 (\dot{x}^2 + \dot{y}^2 + \dot{z}^2) \tag{2.5}$$

if define:

$$L(x, y, z, \dot{x}, \dot{y}, \dot{z}, t) = W - Q = \frac{1}{2}\gamma m_0 (\dot{x}^2 + \dot{y}^2 + \dot{z}^2) - qV + q(xA_x + yA_y + zA_z) \tag{2.6}$$

then electron motion can been solved by the Lagrange equations:

$$\begin{cases} \frac{d}{dt}\left(\frac{\partial L}{\partial \dot{x}}\right) - \frac{\partial L}{\partial x} = 0 \\ \frac{d}{dt}\left(\frac{\partial L}{\partial \dot{y}}\right) - \frac{\partial L}{\partial y} = 0 \\ \frac{d}{dt}\left(\frac{\partial L}{\partial \dot{z}}\right) - \frac{\partial L}{\partial z} = 0 \end{cases} \tag{2.7}$$

The electron orbit can be determined entirely by the external electromagnetic field and the position vector (*x(t), y(t), z(t)),* the velocity vector (*vx(t), vy(t), vz(t)),* will respond to the action of the applied forces. Because it is not an effective way to describe beams that contain a large number of charged particles in configuration trajectories the model can be improved by representing particle trajectories in a 6-D (six-dimensional) space with axes in both space and velocity (*x, y, z, vx, vy, vz*). This mathematical space is called phase space.

Each particle in a beam represents a single point in phase space at a particular time. For an electron beam, all the beam electrons together consist of a group of points in phase space; it is obvious that the trajectories of the electrons will not cross in phase space because no two electrons can have the same velocity at the same point in space. Therefore the neighbouring electrons will always be neighbours in phase space as there are no interactions between these electrons, and the phase-space volume occupied by the beam electrons is an invariant of motion according to Liouville's theorem [105].

2.2.2 **Beam Emittance**

Emittance is a measure both of the size and parallelism of the beam electrons and is used to compare the quality of electron beams. For a practical beam in phase space, the volume (or area) occupied by beam electrons in 2-D trace-space $(x, x'), (y, y')$ can always be calculated as below:

$$\begin{cases} S_x = \iint dx dx' / \pi \\ S_y = \iint dy dy' / \pi \end{cases} \tag{2.8}$$

for an axisymmetric system: $S_x = S_y = S_r$

the transverse hyper phase volume in 4-D is:

$$V_4 = \iint\iint dx dx' dy dy' \tag{2.9}$$

Therefore, emittance was defined as equation(2.10) and is a quantity to characterizes the effective phase volume (or area) of a beam distribution.

$$\begin{cases} \varepsilon_x = S_x / \pi \\ \varepsilon_y = S_y / \pi \end{cases} \tag{2.10}$$

For an axisymmetric system: $\varepsilon_x = \varepsilon_y = \varepsilon_r$, and the unit of ε here is $m \cdot rad$. In 4-D trace space (x, x', y, y'), the hyperemittance is defined as:

$$\varepsilon_4 = \frac{1}{\pi^2} \iint\iint dx dx' dy dy' = \frac{1}{\pi^2} V_4 \tag{2.11}$$

If the particle motions in the x and y directions are independent, the hyper-emittance could be expressed as:

$$\varepsilon_4 = \varepsilon_x \varepsilon_y \tag{2.12}$$

Normalized emittance ε_{nx} is defined in the phase space (x, p_x). For a relativistic paraxial beam it is given by the equation

$$\begin{cases} \varepsilon_{nx} = \dfrac{1}{\pi m_0 c} \iint dx dp_x = \dfrac{1}{\pi} \beta\gamma \iint dx dx' = (\beta\gamma) \varepsilon_x \\ \varepsilon_{ny} = \dfrac{1}{\pi m_0 c} \iint dy dp_y = \dfrac{1}{\pi} \beta\gamma \iint dy dy' = (\beta\gamma) \varepsilon_y \end{cases} \tag{2.13}$$

Liouville's Theorem tells us that the beams volume Ω_4 in phase space (x, p_x, y, p_y) is conserved when the particle motions in the x and y directions are independent.

A third form of the emittance is the root-mean-square (RMS) emittance ε_{rms} [106]:

$$\varepsilon_{rms} = 4[< x^2 >< x'^2 > - < xx' >^2]^{1/2} \tag{2.14}$$

The symbol < > indicates that x and x' have been averaged over the trace-space for a specific electron distribution function. The RMS emittance provides a more meaningful quantitative measure of the effective emittance of a beam.

2.2.3 **Beam Brightness**

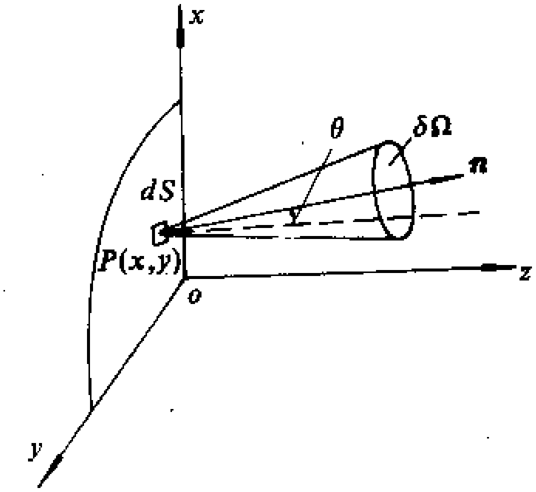

Figure 2-1 The first type of definition of the microscopic brightness

The brightness was defined as the current that pass through the unit area of unit spatial angle. As shown in Figure 2-1, the dI current element from the area element ds round point $p(x,y)$ in the section area S of the beam, and the angle of dI and the normal direction of area element ds is θ, and the spatial angle is $\delta\Omega$, thus the microscopic brightness was defined as the current per unit area per unit solid angle:

$$dB = \frac{dI}{\delta\Omega dS \cos\theta} \tag{2.15}$$

Normally, to a paraxial system, the transverse angle is very small and we can take $\theta = 0$ approximately. Then:

$$dB = \frac{dI}{\delta\Omega dS} \tag{2.16}$$

Because the density distribution of the beam in phase space is not uniform, the microscopic brightness is different at different points across the cross section of the beam with the average brightness (or brightness) given by:

$$B = \frac{I}{\iint d\Omega dS} \tag{2.17}$$

The microscopic brightness was defined in the transverse 4-D phase space, and is the current divided by the transverse 4-D unit phase space volume:

$$dB = \frac{dI}{dV_4} \tag{2.18}$$

And the average brightness of a beam is:

$$B = \frac{I}{V_4} = \frac{I}{\iint\iint dx dx' dy dy'} \tag{2.19}$$

As:

$$d\Omega = \frac{dA}{h^2} = dx' dy' \tag{2.20}$$

Equation (2.20) substituted into equation(2.17), we obtain:

$$B = \frac{I}{\iint [\iint dx' dy'] ds} = \frac{I}{\iint\iint dx dx' dy dy'} \tag{2.21}$$

So these two definitions are same, and the unit of brightness is: $A \cdot m^{-2} \cdot rad^{-2}$. The transverse emittance is closely related to the ‘brightness’ concept used in electron optics. When beams have Cartesian symmetry in the transverse direction, we can write an expression for brightness in terms of the emittances as:

$$B = \frac{I}{\pi^2 \varepsilon_x \varepsilon_y} \tag{2.22}$$

And the normalized brightness is given by:

$$B = \frac{B}{(\beta_c \gamma_c)^2} = \frac{I}{V_4 (\beta_c \gamma_c)^2} \tag{2.23}$$

2.3 **Electron Beam Diagnostics**

The electron beam diagnostics are often used to measure the parameters of an electron beam such as the beam emittance, beam current, beam energy, beam velocity and its spread as well as the beam cross section.

2.3.1 **Voltage Measurement**

High voltage signals are needed in accelerating electron beams, so it is necessary to measure the high voltages applied to the experiments. But most of these high voltage signals are too high for the measuring instrument and hence some form of voltage divider is required. Voltage dividers are widely used in high voltage measurement (DC, AC, or pulsed voltages). It can be classified into one of the three types: a capacitive voltage divider, a resistive voltage divider and a combination of both resistive and capacitive voltage dividers. But there is never purely resistive R, inductive L, or capacitive C voltage dividers in real situations, but always some mixture of these three basic parameters due to the existence of stray capacitance and inductance. These distribution parameters become important for the measurement of fast rising pulsed high voltages, the rise time of the pulse to be measured often approaches the transient time through the divider elements, and in this case the divider reaches an absolute upper limit of its bandwidth of the pulse response.

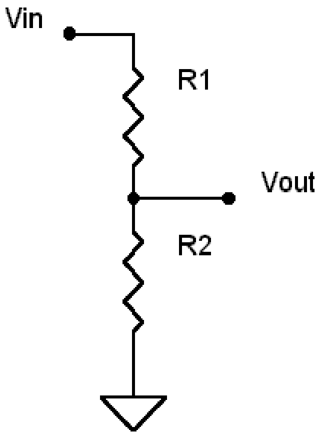

Figure 2-2 Resistance divider

To the simplest situation: two resistances R_1 and R_2 are connected in series as shown in Figure 2-2 and the out voltage V_{out} is related to the input voltage V_{in} as below:

$$V_{out} = \frac{R_2}{R_1 + R_2} \cdot V_{in} \tag{2.24}$$

this rule only works if the divider is unloaded, if it is loaded and then the loaded resistance is R_L and equation (2.24) should be changed to:

$$V_{out} = \frac{R_2 \,||\, R_L}{R_1 + R_2 \,||\, R_L} \cdot V_{in} = \frac{R_2}{R_1 + R_2 + \frac{R_1 R_2}{R_L}} \cdot V_{in} \tag{2.25}$$

Taking into account the capacitance and the inductance parameters, Z can be used to replace R in equation(2.25) as below:

$$V_{out} = \frac{Z_2 \parallel Z_L}{Z_1 + Z_2 \parallel Z_L} \cdot V_{in} = \frac{Z_2}{Z_1 + Z_2 + \frac{Z_1 Z_2}{Z_L}} \cdot V_{in} \tag{2.26}$$

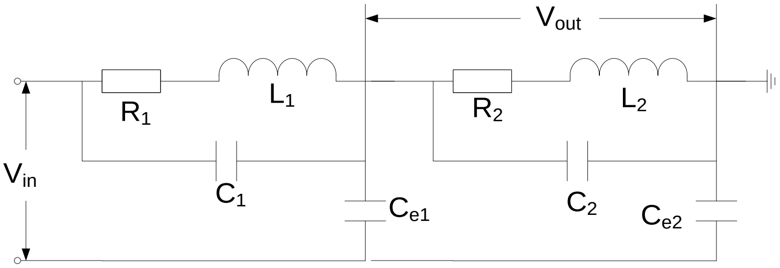

Figure 2-3 The Equivalent circuit for resistor voltage divider

Figure 2-3 shows the equivalent circuit for the resistor voltage divider, R is the resistance, and L is the self-inductance of each R component, C is the self-capacitance and is due to the structure of the resistor, and the stray capacitance C_e represent the capacitance between the resistor and the earth.

To make problems simple, three simple situations were analyzed:

(1) Self capacitance; only the self-capacitance will be consider in this situation, and the output voltage can be given as:

$$V_{out} = \frac{R_2}{R_1 + R_2} V_{in} [1 + \frac{R_1 C_1 - R_2 C_2}{R_2 (C_1 + C_2)} \exp(-t/\tau_e)] \tag{2.27}$$

where $\tau_e = R_1 R_2 (C_1 + C_2)/(R_1 + R_2)$. When $R_1 C_1 = R_2 C_2$, the divider will output a pulse with a pulse shape exactly the same as that of the input voltage. Otherwise, the output signal of the divider will have an overshoot or undershoot at the beginning of the pulse.

(2) Self-inductance: in this situation, only the self-inductance of the voltage divider will be considered, and the output voltage is given by:

$$V_{out} = \frac{R_2}{R_1 + R_2} V_{in} [1 - e^{-\frac{R_1 + R_2}{L_1 + L_2} t}] \tag{2.28}$$

Which means the self-inductance of the resistors slows down the input pulse which results in a rise time $\tau_L = 2.2(L_1 + L_2)/(R_1 + R_2)$.

(3) Stray capacitance: which means only the effect of the stray capacitance will be considered, then the total stray capacitance is $C_e = C_{e1} + C_{e2}$, and the voltage output pulse is:

$$V_{out} = \frac{R_2}{R_1 + R_2} V_{in} [1 + 2 \sum (-1)^k \exp\left(-\frac{k^2 \pi^2}{RC_e} t \right)] \tag{2.29}$$

and the corresponding rise time $\tau_{C_e} \approx (R_1 + R_2) C_e / 3$.

2.3.2 **Current measurement**

There are three basic ways to measure a pulsed current that can be recorded using an oscilloscope: (1) a magnetic probe (including a Rogowski coil), (2) a current shunt [107] and (3) a Faraday Cylinder. A magnetic probe is just a coil of wire which is used to pick up the magnetic flux produced by the electrons as they flow through the centre of the coil. This electron current diagnostic was first developed by Rogowski and is very suitable way to measure high frequency current signals. A current shunt is a non-inductive resistor connected into the circuit, where the current to be measured is passed through the resistor, which can also measure the position of the beam at the same time. A Faraday Cup normally captures the electrons, and is a destructive method to measure electron beam current. The Faraday Cup is a little complicated but suitable for current signal measurements at both high and low frequencies. Therefore the magnetic probe and current shunt methods are the most commonly used methods for measurement of high current electron beam pulses. Usually magnetic probes can achieve nanosecond or less rise times.

(1) Rogowski Coil

The most convenient method of beam current measurement is by means of a current transformer: called a Rogowski coil named following Rogowski's paper in 1912 [108]. The beam current is normally measured by using a compact Rogowski coil upstream from the interaction region and the transported beam current measured using another compact Rogowski coil downstream from the interaction region.

A Rogowski coil is a special magnetic pickup probe which measures pulsed currents. It is a multi-turn solenoid winding around a torus which encircles the current to be measured. The changing magnetic field which is produced by the pulsed current to be measured will cause an electro motive force- $d\psi/dt$ in the Rogowski coil. A measure of the electromotive induced output voltage in the electric circuit of the probe (either differential or self-integration type) will result in a measurement of the magnetic field induction in the probe and thus the measurement of the pulsed current. In principle a Rogowski coil is a current transformer. Its primary is the current to be measured and the secondary often consisting of many turns depending on the attenuating ratio expected is used to increase the signal to be measured. This method is suitable for high frequency current measurement. However when the frequency is less than several kilohertz, this configuration will result in large errors.

A Rogowski coil current transducer has many features, which gives them an advantage over current transformers in several applications. It is linear; has no core saturation effects and has a wide bandwidth and wide measurement range [109,110]. Thus it was widely used for the detection and measurement of electric currents.

The theory of a Rogowski coil illustrates very well how a coil can be considered as an embodiment of Ampere's Law. It senses the magnetic field in the space around the conductor and Ampere's Law provides the relationship between the current flowing and the magnetic field around it. According to Ampere's Law, the line integral of the magnetic field around the loop is equal to the current enclosed by it no matter what path the loop takes, if the loop encloses no net current then the line integral is zero. This can be expressed as:

$$\oint H \cos\alpha dl = i \tag{2.30}$$

As in Figure 2-4 (a), a long, thin helical coil, with n turns per meter and cross-sectional area A which encircles a current i and the flux linking with the length of dl is given by:

$$d\Phi = \mu_0 H \cdot A \cdot ndl \cos\alpha \tag{2.31}$$

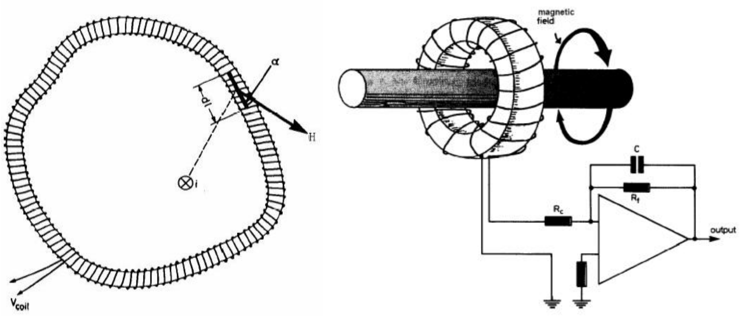

(a) (b)

Figure 2-4 The principle of Rogowski Coil [109]

Where H is the magnetic field and α is the angle between the direction of H and the axis of the coil section. The flux linking the entire coil is given by integrating along the coil:

$$\Phi = \mu_0 nA \int H \cos\alpha dl = \mu_0 nAi \tag{2.32}$$

For an alternating current, the voltage output from the coil is given by the rate of change of flux:

$$V_{coil} = -\frac{d\Phi}{dt} = \mu_0 nA \frac{di}{dt} = -M \frac{di}{dt} \tag{2.33}$$

Where $M = \mu_0 nA$ is named as the mutual inductance, and this makes a thin Rogowski coil ideal for use as a transducer for alternating currents since it responds only to currents which thread the loop and rejects currents and fields from external sources. Also the output of the transducer is independent of the exact path taken by the loop.

The Rogowski coil's output voltage is a differential signal and to obtain a measure of current, the coil's output voltage must be integrated. The addition of an integrator to the coil completes the transducer to provide a voltage which reproduces the current waveform.

Figure 2-4 (b) shows a typical active system using an inverting integrator. It is usually to be integrated with a passive RC network [111] or by terminating the coil with a very low resistance, thereby making the coil "self integrating" [112]. There are two types of Rogowski coils which are categorized according to their operating circuit. One is the self-integration Rogowski coil. The other is the differential Rogowski coil with an external integration network.

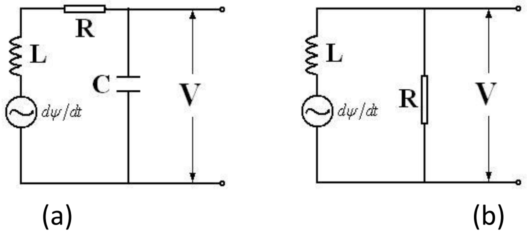

Figure 2-5 Equivalent circuit for Rogowski coils (a) differential type with and external integration network and (b) self-integration type

The equivalent circuits for the two types of Rogowski coils are shown in Figure 2-5 (a) and (b) respectively. Other integrator designs, including passive integrators, can be used depending on the circumstances.

The circuit equations for the external integration type of Rogowski coil is given as:

$$\frac{d\psi}{dt} = L\frac{di}{dt} + iR + \frac{1}{C}\int_0^t idt \tag{2.34}$$

Where *i* is the current flowing in the Rogowski coil, ψ is the magnetic flux in the cross section of the Rogowski coil, *L* is the inductance of the coil, and *R* and *C* are the resistance and capacitance of the external integration network. If the operating conditions described in equation (2.34) are satisfied:

$$R \gg L\omega_h ; RC \gg \tau \tag{2.35}$$

Where ω_h and τ are the highest significant frequency components of ψ and pulse duration of the current respectively, then equation (2.34) becomes:

$$i \approx \frac{1}{R}\frac{d\psi}{dt} \tag{2.36}$$

Thus the output voltage V_0 is given as:

$$V_0(t) = \frac{1}{C}\int_0^t idt = \frac{\psi(t)}{RC} \tag{2.37}$$

If we assume that $\psi(0)=0$, the magnetic flux ψ is proportional to the number of the coil turns n_R and current amplitude I. Suppose the proportionality constant is κ, then:

$$V_0(t)=\frac{\kappa n_R}{RC}I(t) \tag{2.38}$$

For a Rogowski coil of cross sectional area A, mean circumference length l and permeability of the coil material μ, assuming that the thickness of the coil is much less than the radius of the coil such that the B field inside of the torus solenoid is approximately uniform, then it is possible to show that:

$$\kappa=\frac{\mu A}{l} \tag{2.39}$$

The equation for a self-integration Rogowski coil is given as below:

$$\frac{d\psi}{dt}=L\frac{di}{dt}+iR \tag{2.40}$$

When $R \ll L\omega_1$ (ω_1 is the lowest significant frequency component of ψ). From equation (2.40) it is found that:

$$V_0(t)=iR=\frac{\psi}{L}R=\frac{\kappa n_R R}{L}I(t) \tag{2.41}$$

The inductance of the Rogowski coil L is equal to ${n_R}^2\kappa$ with Rogowski coil parameters identical to those used in equation(2.40).

The design and application of the Rogowski coil varies with different circumstances according to the different currents to be measured. As it can be seen from equation(2.33), the sensitivity of the Rogowski Coil is determined by the mutual inductance $M=\mu_0 nA$. So we can increase the coil section area A and the number of turns of the coil per unit length in order to measure relatively low current. To increase the area A it will introduce a systematic departure from the simple theory because the measured flux-density is no-uniform over the turn area. The coil would therefore require calibrating in a fixed position, and if it is disturbed then it can greatly affect the accuracy of measurement. Thus it is more helpful to increase the density n_R. But the wire can't be too thin as it will easily break and be difficult to achieve mechanical stability. But in the fabrication of a multiple-layer Rogowski coil, the windings are layered one on top of the other. The value of the mutual inductance can be largely increased in this way. But the disadvantage of multiple-layer Rogowski coils is poorer performance with increasing frequency. The shunt capacitance of the multilayer coil increases approximately linearly with the number of turns, and the series self-inductance of the coil, however, increases with the square of the number of turns. Both of these and other factors can degrade the coil's frequency and phase response [113].

Sometimes people make several coils, which have the same size in series, the distributed capacitance decreases approximately linearly with the number of coils while the series-inductance increases approximately linearly with it. So the frequency response of the Rogowski coil will not be affected in theory. But in practice, between the coils, there exists distributed capacitance and inductance, so the frequency response's characteristic can decrease. Experiments shows that if two coils are connected in series, the range of frequency response characteristics will decrease 10%, and when the numbers of coils connected is increased, the range of frequency response will decrease. In practice the use of a central return conductor was introduced to the Rogowski coil design, which conveniently brings both terminals to the same end and eliminates spurious signals due to the whole coil acting as a one-turn search coil114. As shown in Figure 2-6, a co-axial cable with its shield ground removed was used as the core of a Rogowski coil.

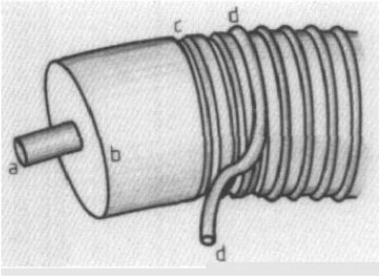

Figure 2-6 Rogowski coil based on co-axial cable core; a. core for return path; b. insulation stripped of braid; c cut threads for location; d. helix laid into threads

High-frequency response is obviously very important in some transient measurements. At frequencies up to a few tens of kilohertz the coil behaves as a simple mutual inductor and measurement is straight forward. At higher frequencies the self-inductance and self-capacitance of the coil become significant. If the inductive impedance of the coil is comparable with the input resistance of the integrator there can be amplitude and phase errors which depend on the coil design. For most cases the effect is small at low frequencies. A compensation circuit can be added in the integrator for high frequency applications.

The self-capacitance and self-inductance of the Rogowski coil can cause a resonance, and this resonance frequency is a very important parameter in designing Rogowski Coils and it is crucial to understand its high-frequency behaviour. There will be a damping effect and the resonance can be under damped, over-damped or critically-damped.

At very high frequencies the coil behaves as a transmission line and correct termination of both ends of the coil is important. The induced voltage distribution along the length of the coil also becomes significant because of propagation time delays and this makes the output of the coil dependent on conductor position.

(2) Faraday Cylinder

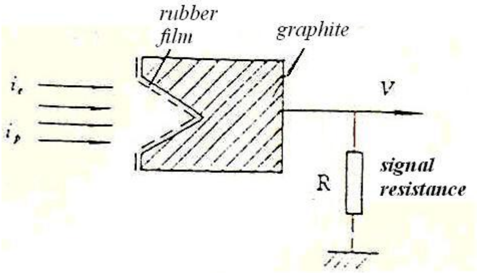

Figure 2-7 the Scheme of Faraday Cylinder

Faraday Cylinders act as electrons absorbers while being used to measure the electron beam current. As shown in Figure 2-7: when the electrons in the electron beam to be measured incident on the Faraday Cylinder, they will interact with the detector material (graphite is the material usually used for the collector of the Faraday cup) and will be absorbed. The electron charges absorbed in the Faraday Cylinder will produce a voltage which is proportional to the beam current via a low inductance signal resistance, which can be recorded by an oscilloscope, thus building up a real time beam current measurement.

To make accurate measurement, the faraday cylinder needs to be a highly efficient absorbing material, and have a low inductance hence they are usually structured in co-axial geometry to reduce the inductance. All conducting joints need to have a good conducting contact with low distributed inductance.

Electrons interact with material normally in 3 different methods:

$$\left.\begin{aligned} -\left(\frac{dE}{dx}\right)_{ion-loss} &\propto \frac{Z}{A} \\ -\left(\frac{dE}{dx}\right)_{rad-loss} &\propto Z^2 \\ -\left(\frac{dE}{dx}\right)_{scat-loss} &\propto \frac{Z^2}{A^2} \end{aligned}\right\} \tag{2.42}$$

So the absorber material should be a low Z material, usually graphite or aluminium. Aluminium is compatible with vacuum and is easily machined as compared to graphite. There are two main factors that affect the absorbing efficiencies: secondary electrons and ion current. The entrance of the Faraday Cylinder can be made in the shape of a horn to reduce the effect of secondary electrons', and cover a thin rubber film over the entrance which allows only high energy electrons to pass through to decrease the effect of ion current, and it can also form a potential barrier to stop the escape of the secondary electrons. For very high energy electrons, the cross section of the secondary electrons is very narrow, and the effect of the secondary electrons can be ignored. If the beam current is not strong enough to produce an ion current, the rubber film can be removed.

(3) Current Shunt

A current shunt is another important diagnostic developed for electron beams especially in electron accelerators. It is a device that monitors the beam current and position in the accelerator and associated beam transport lines. A current shunt is capable of measuring kilo-ampere beam currents and beam position with rise times of less than $0.2\,ns$ and relative position resolutions of less than $100\,\mu m$. The current shunt can be formed by placing the resistors in series with the inner wall of the beam transport lines and detecting the currents induced in the wall by the passage of the beam.

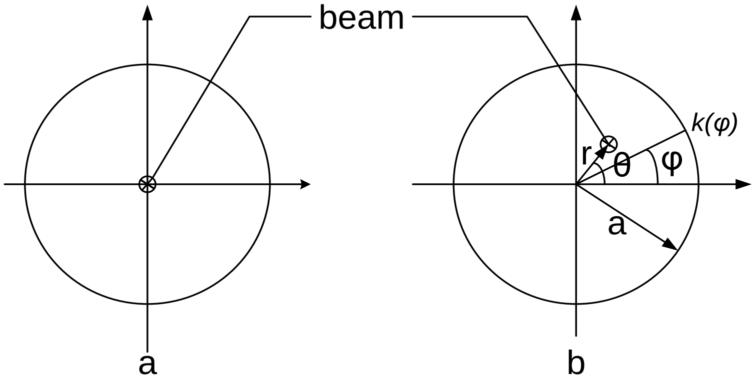

Figure 2-8 The scheme of a current shunt; (a) beam at the axis; (b) beam off axis

The principle of the current shunt is shown in Figure 2-8. As the current I flowing within a tube of radius a at a distance r off axis causes a surface current to flow on the inner tube wall in the opposite direction (sometimes called return current). The induced current in the inner wall of the tube per unit length along the circumference is given as below:

$$k(\varphi) = \frac{I}{2\pi a} \frac{\rho^2 - 1}{1 + \rho^2 - 2\rho \cos(\varphi - \theta)} \tag{2.43}$$

Where $\rho = r/a$ is the normalized beam displacement, and θ and φ were defined in Figure 2-8. If it is assumed that n pieces of resistors with the value of *R* are placed in series and are uniformly distributed along the circumference of the inner tube wall, and the radius of the resistance band is equal to the inner tube wall radius with a surface current passing through the resistors then a voltage will developed or initiated along the resistors. The voltage can be expressed as:

$$V(\varphi) = k(\varphi) \frac{2\pi a \cdot R}{n} = \frac{RI}{n} \frac{\rho^2 - 1}{1 + \rho^2 - 2\rho \cos(\varphi - \theta)} \tag{2.44}$$

From equation (2.44) we can find that the voltage in different positions on the circumference can be different, and with 3 typical voltage values at different positions around the circumference, the current I and normalized beam displacement ρ and angle θ can be calculated.

2.3.3 **Beam Cross Section Measurement**

The cross sectional physical geometry of the electron beam, such as beam position, size, shape and even electron beam density distribution, i.e., profiles, is a fundamental property of any electron beam. Monitoring of these quantities of an electron beam is important for understanding and studying the electron beam physics, such as beam production, beam transport and beam quality, it could also be used to check possible problems in the beam production and transport, such as asymmetry and misalignment of the device fabrication, magnet formation and any alignment or matching problems of different device components which may affect the motion of the electron beam. These factors are also important when one comes to study the motion of the electron beam and beam wave interaction properties in the cavity.

The most common method used to obtain beam cross sectional information such as position, size, shape and profile is through the use of a witness plate techniques. This is done by inserting some kind of special sheet material into and normal to the beam propagation. The electron beam will interact with the sheet and sometimes will leave a deposit on the inserted diagnostic. These special materials will change in appearance such as colour or will produce some detectable effects such as light or x-ray radiation, which can be recorded by monitoring these property changes to reveal beam cross sectional information. Usually these sheets are Mylar sheets, films or scintillators. Scintillators disk were used to record the electron beam position, size, shape and profile. The scintillators disk were made by painting a scintillator powder on a copper disk, this powder had a light emitting response time of 1 ns and a persistence time of ~ 10 ms. The light radiation emitted was detected using a CCTV (closed-circle TV) enabling the real time beam cross section to be measured .

When relativistic electrons pass through the materials, there are several types of light emitting mechanisms, and the optical radiation emitted can be used to measure the beam cross section. As the electrons interact with materials, due to the particle force, the molecule and atom are excited, and when they go back to their ground state, a photon will be emitted. In cross section diagnostics the radiation mechanism used:

(1) Cerenkov Radiation

When the particles moving in the material with a speed larger than the light speed in this medium as $v > c/\sqrt{\varepsilon}$ (ε present the dielectric coefficient of this material), Cerenkov radiation[115] is emitted. As a charged particle travels, it disrupts the local electromagnetic field (EM) in its medium. Electrons in the atoms of the medium will be displaced and polarized by the passing EM field of a charged particle. Photons are emitted as the insulator's electrons restore themselves to equilibrium after the disruption has passed. (In a conductor, the EM disruption can be restored without emitting a photon.) In normal circumstances, these photons destructively interfere with each other and no radiation is detected. However, when the disruption travels faster than the photons themselves, the photons constructively interfere and radiation is observed.

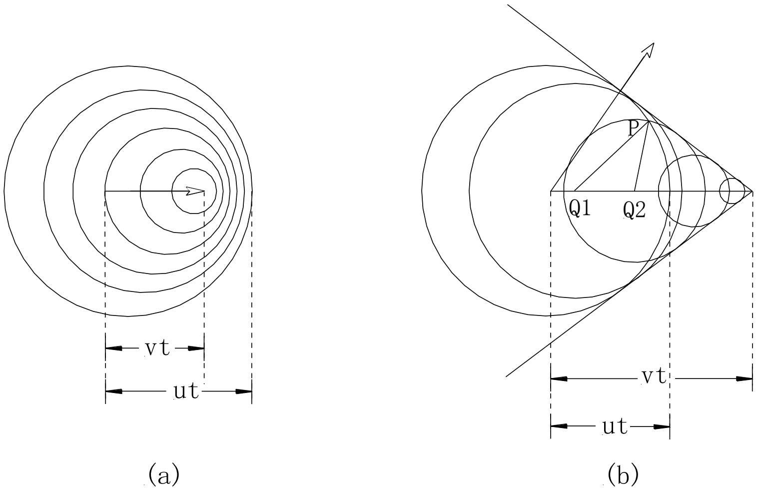

Figure 2-9 the Scheme of Cerenkov radiation

As shown in Figure 2-9, electrically charged particles have electric fields around them as a result of their charge. When such a charged particle is moving, the electric field moves along with the particle. However, since the electrical field is carried by photons, it can only travel at the speed of light. If the particle is travelling faster than the speed of light in a certain medium (such as water), then it, in a sense, out-runs its electrical field.

The electric field that is left behind forms a shock front and this manifests itself in the form of light. Thus the radiation angle is:

$$\cos\theta = \frac{ut}{vt} = \frac{\frac{c}{\sqrt{\varepsilon}}}{c\beta} = \frac{1}{\beta\sqrt{\varepsilon}} \tag{2.45}$$

where $\beta = v/c$. The directional property of Cerenkov radiation makes it possible to detect the energy of the particles by measuring the radiation deflection. The overall intensity of Cherenkov radiation is proportional to the velocity of the incident charged particle and to the number of such particles. Unlike fluorescence or emission spectra that have characteristic spectral peaks, Cherenkov radiation is continuous. The relative intensity of one frequency is proportional to the frequency that is, higher frequencies (shorter wavelengths) are more intense in Cherenkov radiation. This is why visible Cherenkov radiation is observed to be brilliant blue. In fact, most Cherenkov radiation is in the ultraviolet spectrum; it is only with sufficiently accelerated charges that it even becomes visible.

(2) Optical Transition Radiation (OTR) [116]

Transition radiation is produced when a relativistic particle traverses an inhomogeneous medium, in particular the boundary between materials of different electrical properties. The emitted radiation is the homogeneous difference between the two inhomogeneous solutions of Maxwell's equations of the electric and magnetic fields of the moving particle in each medium separately. In other words, since the electric field of the particle is different in each medium, the particle has to "shake off" the difference when it crosses the boundary. The total energy loss of a charged particle on the transition depends on its Lorentz factor $\gamma = E/mc^2$ and is mostly directed forward, peaking at an angle of the order of $1/\gamma$ relative to the particle's path. The intensity of the emitted radiation is roughly proportional to the particle's energy E.

Optical transition radiation is emitted both in the forward direction and the reflected direction by the interface surface. As shown in Figure 2-10, in case of a foil having an angle at 45° with respect to the particle beam, the shape of the particle beam can be visually seen at an angle of 90°. More elaborate analysis of the emitted visual radiation may allow for the determination of γ and emittance. The radiation production is very low compared to Cerenkov radiation, especially for low energy charged particle beams (typical lower than 30 MeV). This radiation hence offers the possibility of particle identification at highly relativistic energies, where Cherenkov radiation or ionization measurements no longer provide useful particle discrimination, particularly of electrons and hadrons in the momentum range between $1\,GeV/c$ and $100\,GeV/c$ or higher, the upper limit being determined not only by particles reaching the Fermi plateau, but also by the radiation of highly relativistic particles. The peak transition radiation photons produced by electrons having wavelengths in the X-ray range, with energies typically in the range from 10 keV to 30 keV. To make real time detection, a very thin foil target is required, normally several micrometres to tens of micrometres.

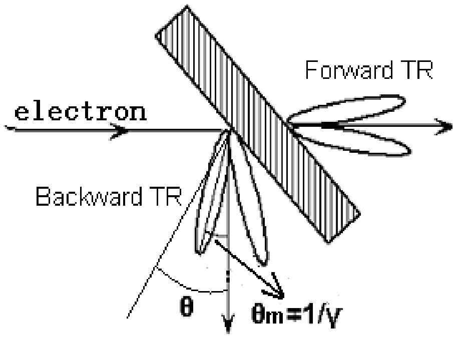

Figure 2-10 The Scheme of Transition radiation

(3) Synchrotron Radiation

Synchrotron radiation is electromagnetic radiation, similar to cyclotron radiation, but generated by the acceleration of relativistic electrons through magnetic fields. This may be achieved artificially by storage rings in a synchrotron, or naturally by fast moving electrons moving through magnetic fields in space. The radiation angle is $\theta \simeq 1/\gamma$, and the characteristic wave length is:

$$\lambda_c = \frac{18.6}{BE^2} \tag{2.46}$$

The unit of λ is nanometres, and B is the magnetic flux with unit of T, and E is the energy of the electrons with unit of GeV. The radiation typically includes infrared, optical, ultraviolet and X-rays. Synchrotron radiation has a high brightness and high intensity, many orders of magnitude more than with X-rays produced in conventional X-ray tubes; high brilliance, exceeding other natural and artificial light sources by many orders of magnitude; high collimation, i.e. small angular divergence of the beam; Low emittance, i.e. the product of source cross section and solid angle of emission is small; widely tuneable in energy/wavelength by monochromatization and possess a high level of polarization (linear or elliptical).

The particles in a bunch travelling on a curved trajectory in free space emit synchrotron radiation with a broad spectrum of wavelengths. At wavelengths comparable to the bunch length or larger, the radiation from various particles is coherent, giving a radiated power proportional to N^2, which was mainly polarized in the orbital plane [117,118]. As the spectrum of coherent Synchrotron Radiation is dominated by the bunch length of the electron beam, thus the bunch shape can be estimated using Fourier analysis of this spectrum.

(4) Bremsstrahlung Radiation

Bremsstrahlung Radiation is electromagnetic radiation produced by the acceleration of a charged particle, such as an electron, when deflected by another charged particle, such as an atomic nucleus. The term is also used to refer to the process of producing the radiation. The phenomenon was discovered by Nikola Tesla during high frequency research he conducted between 1888 and 1897. Bremsstrahlung has a continuous spectrum. The characteristic angle of the Bremsstrahlung is $\gamma^{-1} = m_e / E_e$, where m_e is the rest mass of the electron and E_e is the energy of the radiating electron. At a wavelength $\lambda = 1.24/E_e\ nm$, it is normally in the X-ray region or γ region, and has good directionality when the electrons have a high energy. Now this radiation is widely used for collider luminosity measurement. Bremsstrahlung photons distribution can be used also for measurement of electron beam divergence at the interaction point as the photons carries information about the geometric parameters of the electron beam at the interaction point such as the angular spread, position and orientation of the beam axis.

Chapter 3

Harmonic Gyrotron

3.1 Introduction

As mentioned previously, gyrotrons are the most developed type of high power, high frequency radiation sources in the millimetre and sub-millimetre wavelength range which are also extendable to the Terahertz (THz) frequency region. The Institute of Applied Physics (IAP) of Russian Academy of Sciences pioneered the development of the gyrotron and have produced about 1.5 kW at 326 GHz [119]. Gyrotrons are now commercial available devices that can produce megawatt output power in long pulse or continue wave (CW) operation in the frequency range up to 200 GHz. Recently a gyrotron achieved kilowatts of output power operated at a fundamental electron cyclotron frequency of 1 THz [96] by using a pulsed coil. However CW operation at such a frequency is a formidable task because of the large magnetic field (~40 T) that is required. As the output frequency increases, both larger magnetic fields and reduced size interaction regions are needed when operating at the fundamental cyclotron mode. An alternative approach to generate CW high frequency radiation is to work at higher cyclotron harmonics [120,121,122] which allow the use of larger cavity sizes and smaller magnetic fields by a factor of *s*, where *s* is the harmonic number.

3.2 CRM Instability

Gyrotrons are based on the Cyclotron Resonance Maser (CRM) [123] instability using relativistic electrons gyrating in an external magnetic field. The gyrotron extracts the transverse energy of the electrons in the beam instead of axial beam energy as is the case in most other conventional linear tubes such as klystrons and TWTs. An alternative definition describing the bunching process in a gyrotron is known as the Electron Cyclotron Maser (ECM) instability which is a relativistic effect due to the energy dependence of the electron cyclotron frequency. Figure 3-1 is a schematic cross section diagram of a gyrotron, showing the particle trajectories with the electrons initially uniformly distributed along the gyro orbit.

These electrons are rotating in the counter clockwise direction in a uniform and constant magnetic field $B_z\hat{e}_z$, so the initial Larmor radius and gyrating frequency are given by equation (3.1) and (3.2):

$$\Omega = \frac{|e|B_0}{m_0\gamma} \tag{3.1}$$

$$R_l = \frac{v_{0\perp}}{\Omega} \tag{3.2}$$

A small constant amplitude electric field $E_y = \varepsilon_0\, cos(\omega_0 t)\hat{e}_y$ was introduced which gyrating at a frequency ω in the same direction as the electrons as shown in Figure 3-1 (a).

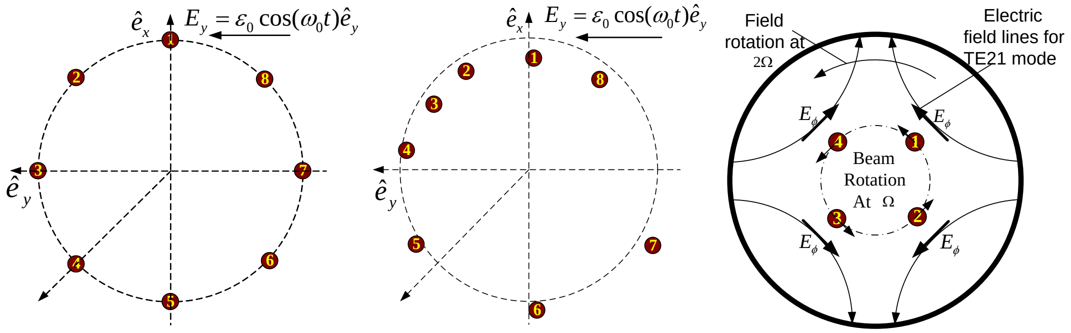

(a) (b) (c)

Figure 3-1 CRM bunching process illustrated by gyrating electrons in phase space in the presence of a small external field (a) Initial electron positions. (b) Bunched electrons after several cycles. (c) two bunches formed in a 2nd harmonic gyrotron

Electrons 1, 2, 8 will lose energy as their y component speed is in the same direction as E_y thus from equation (3.1) we can see the relativistic cyclotron frequency of these particles will increase and tend to spiral inward as γ decreases. Particles 4, 5 and 6, on the other hand, will gain energy and their relativistic cyclotron frequency will decrease and tend to spiral outward as γ increases. So the phase of the particles 1, 2, 8 will tend to slip ahead of the wave and particles 4, 5, 6 will tend to slip behind the wave. After an integral number of wave periods, the particles will become bunched around the positive y axis as shown in Figure 3-1 (b). To obtain energy from the particles, ω_0 must be slightly greater than Ω, as the electrons will rotate as a whole in a clockwise sense while the bunch is being formed; hence the centre of the bunch will gradually slip behind the wave to the right half of the half-circle, and give energy to the wave. So at this fundamental mode, there will be one bunch at the beam cross section view. When operating with a high harmonic mode, the electron beam gyrates at a frequency of Ω, and the electro-magnetic wave rotates at a frequency of $s\Omega$, where s is harmonic number. In this case there will be more than one bunch formed with the bunch numbers equal to the harmonic number. Figure 3-1 (c) shows how the electron beam interacts with the electro-magnetic wave for the 2nd harmonic situation. As we can see the TE_{21} wave is rotating at $\omega = 2\Omega$ frequency, and particles 2 and 4 are moving against the electric field, so they will gain energy and spin back ward and inward. On the other hand particles 1 and 3 will loose energy and spin forward and inward, so 2 bunches will formed at the position between 4 and 2, 3 and 1 respectively.

Table 3-1 Gyrotron requirement for different harmonic number at 390 GHz

Harmonic number	Mode	B(T)	Cavity Radius(mm)	Larmor Radius(mm)
1	TE_{11}	14.6	0.225	0.040
2	TE_{21}	7.34	0.374	0.083
3	TE_{31}	4.84	0.514	0.120
4	TE_{41}	3.63	0.651	0.161
5	TE_{51}	2.91	0.785	0.202
6	TE_{61}	2.42	0.918	0.241
7	TE_{71}	2.07	1.062	0.281

As a high frequency gyrotron operated at the fundamental mode requires a very high magnetic field it is very attractive to use harmonic interactions and take advantage of the magnetic field reduction by a factor of s. As show in Table 3-1, the B field requirement decreases significantly when the harmonic number increases. It can also be found that the resonance cavity radius increases as the harmonic number increases, and this leads to another advantage of the harmonic gyrotron in that it can handle much more power than gyrotrons operating with the fundamental mode. However, because the electrons in the phase bunches typically continue to spread in phase faster than the energy that can be extracted from the electron bunches, the saturated efficiency of the harmonic interactions decreases rapidly with increasing harmonic number, typically falling below 10% at the third or fourth harmonic.

Gyrotrons operate through a fast cyclotron wave interaction, which takes place in the fast-wave region near the cut off frequency, where the gyrotrons inherit the advantage of being insensitive to the electron beam spread. The electron beam interacts with the transverse electron field of a TE type mode and the energy exchange takes place through the transverse motion of the electrons interacting with the transverse electric field. For the general situation, it is assumed that the electron beam is guided by a constant confining magnetic field B_0 and is injected into an open ended smooth cylindrical cavity. The cylindrical cavity has a radius of r_w, and the electron is grating at a radius of $r_L = P_\perp / eB_0$ which known as Larmor radius, and $P_\perp = \gamma m_0 v_\perp$ is the transverse momentum of the electron beam. $\gamma = 1 + eU/m_0c^2$ is the Lorentz factor and U is the electron accelerating beam voltage.

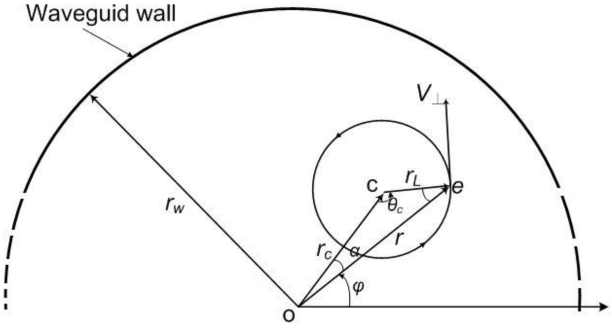

Figure 3-2 Projection of the electron orbits on the cross section of a smooth cylindrical waveguide

The gyrating centre located at a radius of r_c is known as guiding centre radius and is shown in Figure 3-2. The transverse component of the electric field of this TE_{mn} (m,n are integers) wave can be written as:

$$E_\varphi = \frac{-i\omega\mu}{k_{mn}} A J'_m(x_{mn} r/r_w) e^{-i(\omega t - k_\parallel z - m\varphi)} \tag{3.3}$$

$$E_r = \frac{-\omega\mu}{k_{mn}^2 r} A J'_m(x_{mn} r/r_w) e^{-i(\omega t - k_\parallel z - m\varphi)} \tag{3.4}$$

The magnetic field of this TE_{mn} wave not only has a transverse component but also an axial component and these components can be written as:

$$B_r = \frac{-ik_\parallel}{k_{mn} r} A J'_m(x_{mn} r/r_w) e^{-i(\omega t - k_\parallel z - m\varphi)} \tag{3.5}$$

$$B_\varphi = \frac{-ik_\parallel}{k_{mn}^2 r} A J'_m(x_{mn} r/r_w) e^{-i(\omega t - k_\parallel z - m\varphi)} \tag{3.6}$$

$$B_z = \frac{-ik_\parallel}{k_{mn}^2 r} A J_m(x_{mn} r/r_w) e^{-i(\omega t - k_\parallel z - m\varphi)} \tag{3.7}$$

Where x_{mn} is the nth root of $J'_m(x) = 0$, $k_\parallel = \sqrt{(\omega/c)^2 - k_\perp^2}$ is the propagation constant parallel with the axis direction, and $k_\perp = x_{mn}/r_w$. A is a complex constant. μ is the magnetic permeability.

When an electron beam is introduced into this system, the source current is J, and Maxwell's equations need to be satisfied as follows:

$$\nabla^2 \vec{B} - \frac{1}{c^2}\frac{\partial^2}{\partial t^2}\vec{B} = -\frac{4\pi}{c}\nabla \times \vec{J} \tag{3.8}$$

Where $\vec{B}$ is the wave magnetic field. By taking the z component of equation (3.8) and combining with equation (3.3)~(3.7), we obtain [124]:

$$\left(\frac{\omega^2}{c^2} - k_\parallel^2 - k_\perp^2\right) B_0 \vec{e}_z = -\frac{4\pi}{c}\left[\frac{1}{r}\frac{\partial}{\partial r}(rJ_\theta) - \frac{im}{r} J_r\right] \tag{3.9}$$

The dynamics of the electron beam can be described by the linear relativistic Vlasov equation:

$$\left(\frac{\partial}{\partial t} + \vec{v}\cdot\frac{\partial}{\partial \vec{x}} - e\vec{v}\times B_0\vec{e}_z\cdot\frac{\partial}{\partial \vec{P}}\right) f_1 = e[\vec{E}^{(1)} + \vec{v}\times B^{(1)})]\cdot\frac{\partial}{\partial \vec{P}} f_0 \tag{3.10}$$

Where $B_0\vec{e}_z$ is the applied uniform magnetic field, $\boldsymbol{E}^{(1)}$ and $\boldsymbol{B}^{(1)}$ are the wave fields of the TE_{mn} wave given by equation (3.3) ~ (3.7). f_0 and f_1 are the initial and perturbed distribution functions of the electron beam. We assume that $f_1 \ll f_0$ and $E^{(1)}, B^{(1)} \ll B_0$ so as to satisfy the linear theory requirement. It is assumed that the cylindrical waveguide is lossless and in vacuum, so the circularly TE_{mn} mode dispersion relation in this wave guide can be written as:

$$\omega^2 - k_{\parallel}^2 c^2 - k_{\perp}^2 c^2 = 0 \tag{3.11}$$

Due to the triangular relationship in Figure 3-2, r can be replaced by the equation 3.12:

$$r = [r_c^2 + r_L^2 - 2 r_c r_L cos\theta_c]^{1/2} \tag{3.12}$$

Combining equation (3.9)~(3.12), the dispersion relation can be obtained [125]:

$$\omega^2 - \left(k_{\parallel}^2 + {x_{mn}^2}\big/{r_w^2} \right) c^2 = - \frac{4c^2 N_e \mu_0 e^2/(4\pi m_0)}{\gamma_0 r_w^2 J_m^2(x_{mn})[1-m^2/x_{mn}^2]}$$

$$\left[\frac{(\omega^2 - k_{\parallel}^2 c^2)\beta_{\perp}^2 H_{sm}(x_{mn} r_c/r_w,\ x_{mn} r_L/r_w)}{(\omega - k_{\parallel} v_{\parallel} - s\Omega)^2} - \frac{(\omega - k_{\parallel} v_{\parallel}) Q_{sm}(x_{mn} r_c/r_w,\ x_{mn} r_L/r_w)}{\omega - k_{\parallel} v_{\parallel} - s\Omega}\right] \tag{3.13}$$

Here function H_{sm} and Q_{sm} are defined as:

$$H_{sm}(x, y) = [J_{s-m}(x) J_s'(y)]^2 \tag{3.14}$$

$$Q_{sm}(x, y) = 2H_{sm}(x, y) + y\{J_{s-m}^2(x) J_s'(y) J_s''(y) +$$

$$\tfrac{1}{2}[J_{s-m-1}^2(x) J_s'(y) J_{s-1}'(y) - J_{s-m+1}^2(x) J_s'(y) J_{s+1}'(y)]\} \tag{3.15}$$

In the situation of an axis encircling beam r_c=0 and the interaction occurs near the cut-off frequency, so the equation can be simplified as below:

$$\omega^2 - k_z^2 c^2 {}^2 = - \frac{4\beta_{\perp}^2}{(x_{mn}^2 - m^2)(\omega - k_z v_z - s\Omega)^2} \left(\frac{I}{I_A}\right) \left(\frac{x_{mn} c}{r_w}\right)^4 \left(\frac{J_m'(x_{mn} r_L/r_w)}{J_m(x_{mn})}\right)^2 \tag{3.16}$$

Where I is beam current in amps, and $I_A = 4\pi\epsilon_0 m_0 c^3/e \approx 17\ kA$ is the Alfven current. The dispersion diagram can be gained through equation(3.16), which gives a lot useful information about the interaction as shown in Figure 3-3.

The beam parameters and cavity parameters are set to enable the interaction with the harmonic operating mode at the design frequency to take place. Information about the interaction frequency, mode, wave-numbers, and magnetic field are also determined. In the diagram the TE_{71} cylindrical waveguide mode is interacting with the 7th harmonic of the electron cyclotron mode of a beam of voltage 40 *kV* and current 1.5 *A* with a velocity ratio α=2 at a magnetic field of 2.10 *T*. The diameter of the cylindrical waveguide is 2.11 *mm*, and the cavity interaction range length is 50 *mm*.

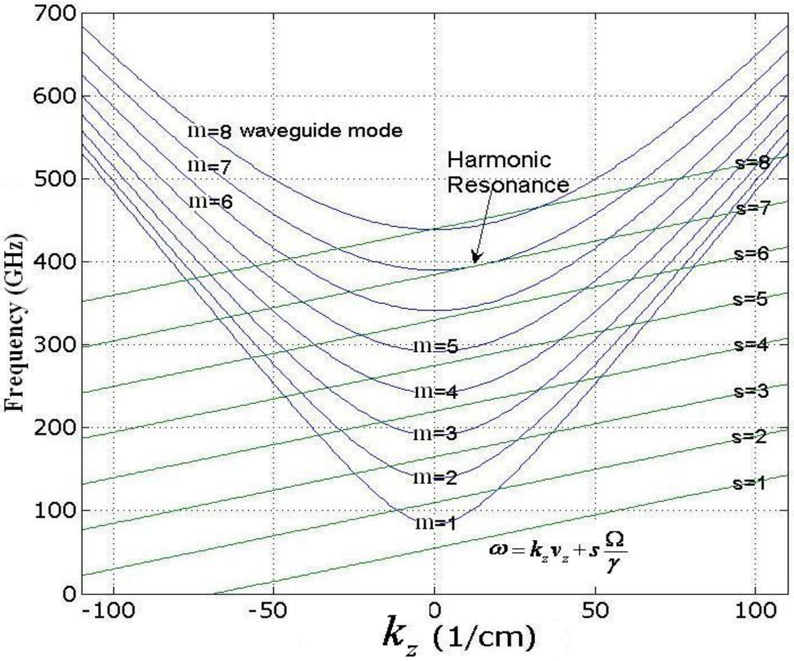

Figure 3-3 Dispersion of the TEm1 waveguide modes (m = 1-8) and beam-wave resonances at different harmonics.

The dispersion diagram is shown in Figure 3-3 illustrating the beam-wave (harmonic number s>1) interaction with high order waveguide modes TE_{mn} which satisfy the requirement $s = m$, as well as all the other possible interactions. From the diagram, all the possible interactions below the designed TE$_{61}$ mode are eliminated because the electron cyclotron lines are below their corresponding transverse electric mode. The only possible parasitic interactions might be from higher modes, i.e., TE_{61} with $s = 6$, TE_{81} with $s = 8$ and TE_{91} with $s = 9$, etc. However the most dangerous competing interaction are with the neighbouring TE$_{81}$ and TE_{61} interaction as the starting current increases as the mode index increases. The competing TE_{81} interaction has a starting current that is higher than the beam current that has been designed to be produced from the Cusp electron gun, and the TE_{61} interaction requires a higher magnetic field. By properly designing the interaction cavity *Q*, these two competing interactions as well as other parasitic interactions of other modes can be minimised.

In order to maintain the self-oscillation in a single cavity, a feedback loop is required in the gyrotron oscillator, provided by the reflectors at both ends of the cavity. A reflector will reflect the front wave and turn it into a backward wave and when this backward wave reaches the other end of the cavity it reverses to a forward wave again. Thus continuous wave circulation in the cavity is formed. If the power that the wave gained from the beam exceeds the power been lost while propagating and reflecting, the wave will be repetitively pumped by the electron beam from the noise level to equilibrium amplitude. In a gyrotron oscillator, this means the electromagnetic wave generated by the initial early electrons will grow and then interact with later electrons to form a stable oscillation, with the growth time limited by the wave transit time.

As mentioned before, some of the electron beam energy is transferred into the wave energy of the cavity electromagnet waveguide mode. There are also power losses while the wave field propagates and reflects in the cavity. Some of the power will propagate through the cavity end and form the output power (P_{out}), some of the power will be dissipated in the wall (P_{ohm}). The power that the electron beam deposits into the cavity wave is ηP_b, where η is the interaction efficiency and P_b is the electron beam power, and P_b are assumed to be constant during the cavity wave build up.

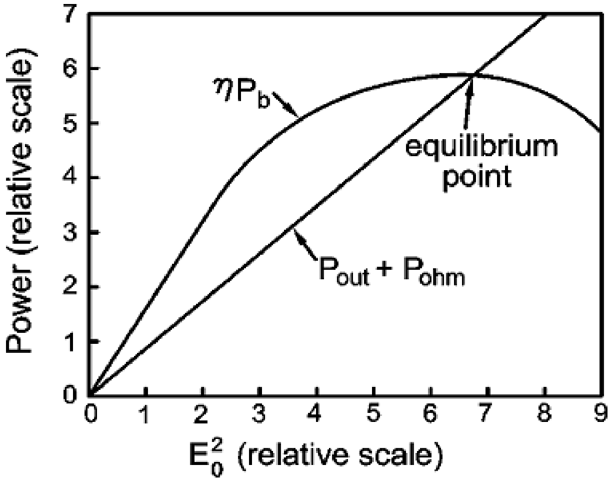

Figure 3-4 Schematic illustration of the beam-generated wave power (ηP_b) and the sum of output and Ohmic power ($P_{out} + P_{ohm}$) as functions of the square of the field amplitude (E_0^2), E_0 increase when $\eta P_b > P_{out} + P_{ohm}$ and decrease when $\eta P_b < P_{out} + P_{ohm}$. Hence a stable equilibrium is maintained at the intersection of the two curves, which is usually designed to occur at or near the maximum efficiency point [126]

Figure 3-4 demonstrates the existence of this threshold situation for gyrotron oscillation. In this diagram, both P_{out} and P_{ohm} are scaled as E_0^2, and so the sum appears to be a straight line in the linear stage with a slope proportional to the cavity quality factor. Thus the ηP_b curve appears to be linear too at the linear stage and the slope is proportional to η. When these two slopes are equal, the beam threshold power is reached. If the beam power exceeds the threshold value, there will be more energy deposited in to the field than it lost, and consequently E_0 starts to grow. It can also be seen from the diagram that this growth cannot continue indefinitely. As the field amplitude increases, the linear interaction requirement will be broken and the interaction becomes nonlinear, the efficiency will level off and eventually decrease. So the ηP_b curve will bend downwards and meet the $P_{out} + P_{ohm}$ line where $\eta P_b = P_{out} + P_{ohm}$. Thus the equilibrium state is established and the cavity field will no longer increase.

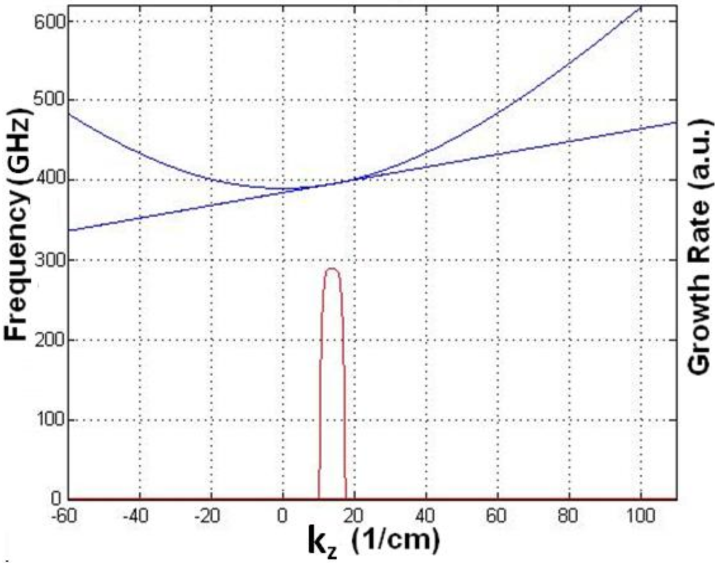

Figure 3-5 The growth rate at the 7th harmonic interaction

The growth rate of this interaction can be obtained by solving the imaginary part of ω in equation (3.16) as a function of axial wave-number k_z and is shown in Figure 3-5. In the diagram the TE_{71} cylindrical waveguide mode is interacting with the 7^{th} harmonic of the electron cyclotron mode of a beam with a velocity ratio α=3 at a magnetic field of 2.10 *T*. The radius of the cylindrical waveguide is 1.055 *mm*, and the cavity interaction length is 50 *mm*.

3.3 **Cavity Design**

Since the cavity field energy losses due to the power output from the cavity and the ohmic losses at the cavity wall, two quality factors will be introduced in cavity design, i.e., the diffraction quality factor Q_d and the ohmic quality factor Q_Ω respectively. They are governed by the equations below:

$$Q_d = 4\pi \frac{(L/\lambda)^2}{1-|R_1 R_2|} \tag{3.17}$$

$$\frac{1}{Q_\Omega} = (\frac{\delta}{r_w})[\frac{c^2}{\omega^2}\frac{x_{mn}^2}{r_w^2} + (\frac{x_{mn}^2}{x_{mn}^2 - m^2})] \tag{3.18}$$

Where $\delta = \sqrt{\frac{2}{\omega\mu\sigma}}$ is the skin depth of cavity wall, σ is the conductivity of cavity material, μ is absolute permeability. R_1 and R_2 are the reflection index at both ends of the cavity interaction region. The total Q of the resonant cavity is given by:

$$\frac{1}{Q} = \frac{1}{Q_d} + \frac{1}{Q_\Omega} \tag{3.19}$$

The cavity scheme used in the experiment is shown in Figure 3-6. The cavity interaction length and the taper angle were optimized for a reasonably high *Q* which is a very important parameter in harmonic gyrotron design as the cavity Q is inversely proportional to the starting current (please refer to section 3.4). The reflection index was gained through the use of simulation codes Cascade and CST Microwave Studio.

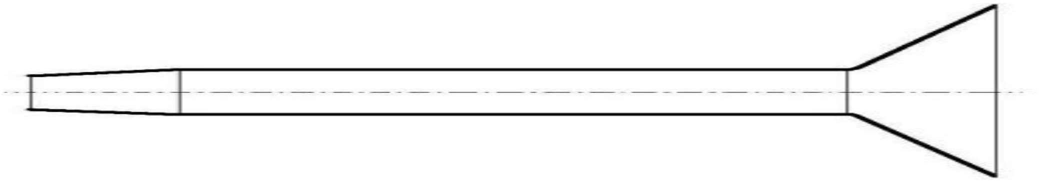

Figure 3-6 The Gyrotron Geometry

Figure 3-7 curve shows the reflect ratio changes against the output taper angle at 390 GHz. In this simulation code, the cavity is a 40 mm long smooth cylindrical cavity with a diameter of 2.11 mm, the output taper is 10 mm in length and the input taper is a cut-off taper with an input diameter of 1.6 mm and a length of 20 mm. All the cavity materials are OFHC (Oxygen Free High Conductivity) copper.

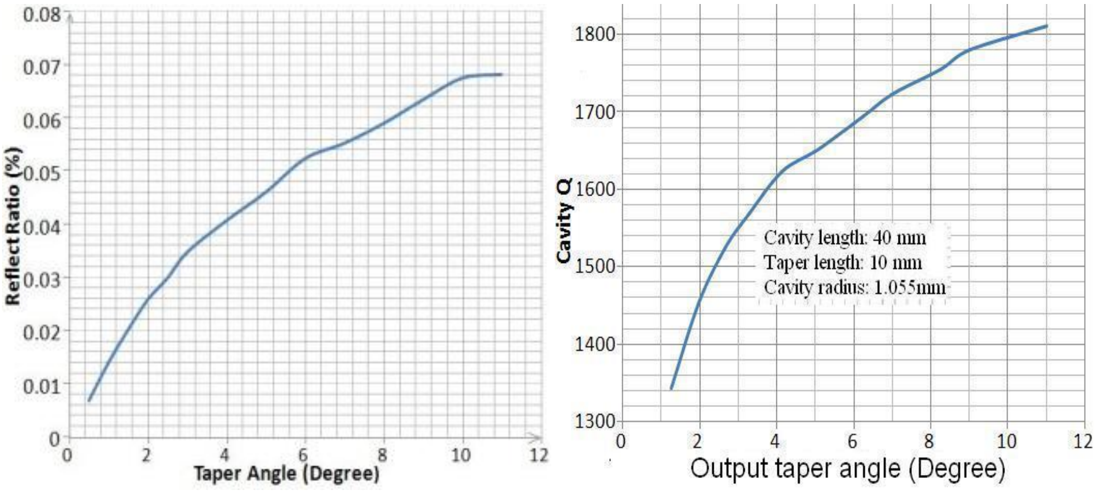

Figure 3-7 Reflect radio (L) and Cavity Q (R) against taper angle

From the diagram we can see the reflection factor increases as the angle increases as well as the cavity Q. But in order to sustain enough output power and decrease the heat load [127], the reflection ratio needs to be limited. Taking into account all of these factors a 6 degree taper was chosen for the cavity design.

Also by changing the length of the resonance cavity a curve showing the change in the cavity Q with respect to its length is shown in Figure 3-8. In this case the input end is a 20 mm long cut-off taper with an input diameter of 1.6mm. The cavity diameter is 2.11 mm and the output end of the cavity was defined by a 6 degree output horn. Though in real situation the tolerance of the cavity surface [128] and the purity of materials will affect the value of ohmic losses at high frequency range, ideal OFHC copper was used as the metal conductivity in the calculations.

As can be seen in figure 3.8 , Q_d increases with the length of the cavity as $\mathrm{Q_d} \propto (\frac{L}{\lambda})^2$, but the increase in the length leads to an increase in the ohmic losses of the cavity which is governed by [129]:

$$\eta \propto \frac{Q_\Omega}{Q_\Omega+Q_d} \tag{3.20}$$

The cavity in an overmoded gyrotron needs to be designed to minimise mode competition. One way to suppress undesired modes is to set the beam current to be below the start oscillation threshold.

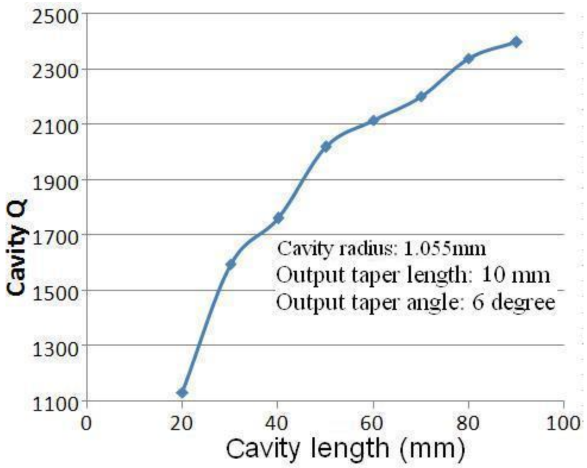

Figure 3-8 Cavity Q against cavity length

3.4 Starting Current

As shown in Figure 3-4, in order to obtain stable electromagnetic radiation (C) from a gyrotron, the beam generated power (ηP_b) must be larger than the power that has been lost in the cavity wall as well as been reflected back both of which are set by the cavity Q as discussed in previous paragraph. This is set by the starting oscillation threshold, and the threshold beam current is defined as the starting current below which the oscillation will not start. It is the minimum current required to overcome the dissipative process in the cavity for which $dP_{out}/dt > 0$ in the limit $P_{out} \rightarrow 0$. The value of the start current depends on the beam properties, magnetic field, resonator geometry, resonator frequency and mode etc., and can be obtained from the energy balance equation:

$$\frac{dW}{dt} = \eta(t)U(t)I(t) - \frac{\omega W}{Q} \tag{3.21}$$

Where W is the stored energy of the mode, $\eta(t)$ is the efficiency, it is a function of the field amplitude which is equivalent to the output power P_{out}. $U(t), I(t)$ are the beam voltage and beam current respectively, and for a first approximation we can assume they are constant. If the transit time of the electrons is smaller than the rise time of the electric field in the cavity, the electrons will experience approximately a constant field. Thus equation (3.21) can be rewritten as [130]:

$$\frac{Q}{\omega}\frac{dP_{out}}{dt} = \eta(P_{out})UI - P_{out} \tag{3.22}$$

and:

$$I_{start} = (U\frac{d\eta}{dP}|_{p=0})^{-1} \tag{3.23}$$

So the analytical starting current for the TE_{mnq} mode at m_{th} Harmonic resonance can be given as follows [131]:

$$I_s = (\frac{I_A}{Q})(\frac{\omega}{m\Omega_c})(\frac{\gamma L r_w^2 k_{\|}^2 \beta_{\|}^2}{16c})(1-\frac{m^2}{x_{mn}^2})(\frac{J_m(x_{mn})}{J'_m(x_{mn}\beta_{\perp}c/(r_w\Omega_c))})^2 R(x)^{-1} \tag{3.24}$$

Where I_A is the Alfven current given by $I_A = 4\pi\varepsilon_0 mc^3/c \simeq 17kA$. Q is the cavity quality factor,

$$\begin{aligned} R(x) = \{&2 - 2x(\frac{\beta_{\perp}^2}{\beta_{\|}})(\frac{\omega}{m\Omega_c})(\frac{k_{\|}c}{\omega}) + [(\frac{r_w m\Omega_c}{\beta_{\perp}cx_{mn}})^2 - 1](\frac{J_m(x_{mn}\beta_{\perp}c/(r_w\Omega_c))}{J'_m(x_{mn}\beta_{\perp}c/(r_w\Omega_c))}) \\ &+(\frac{2x_{mn}\beta_{\perp}c}{r_w\Omega_c})(\frac{J''_m(x_{mn}\beta_{\perp}c/(r_w\Omega_c))}{J'_m(x_{mn}\beta_{\perp}c/(r_w\Omega_c))})\}G(x) \\ &+((\frac{\beta_{\perp}^2}{\beta_{\|}})(\frac{\omega}{N\Omega_c})[(\frac{\omega}{ck_{\|}}) - x^2(\frac{ck_{\|}}{\omega})]G'(x) \end{aligned} \tag{3.25}$$

where $x = (\omega - m\Omega_c)\gamma m_0/k_{\|}\vec{p}_{\|}$, and $\vec{p}_{\|} = \gamma m_0 \vec{v}_{\|}$.

$$G(x) = \begin{cases} [\cos(\pi qx/2)/(1-x^2)]^2 & (where \quad q \quad is \quad odd) \\ [\sin(\pi qx/2)/(1-x^2)]^2 & (where \quad q \quad is \quad even) \end{cases} \tag{3.26}$$

and q is the related to the axial wave- number $k_{\|} = q\pi/L$ and L is the cavity length. So the starting oscillating current for this cavity in the designed mode and its competition modes can be acquired some of which are shown in Figure 3-9.

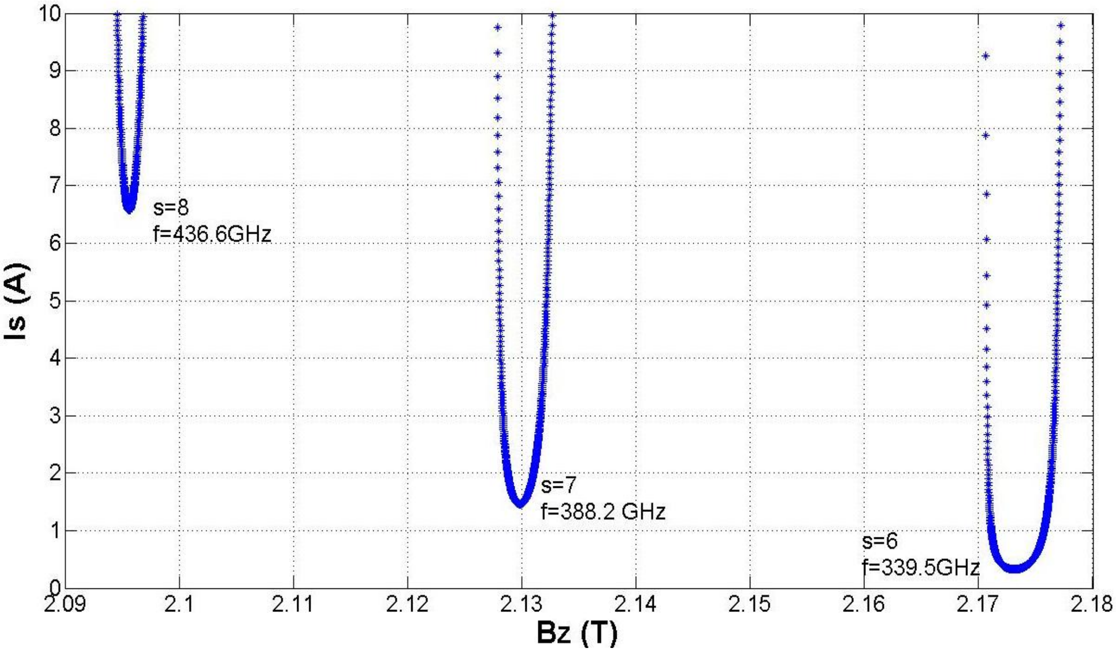

Figure 3-9 Start-oscillation current for 3 different harmonic number interaction as a function of magnetic field (harmonic number: S =6, S=7 and S =8)

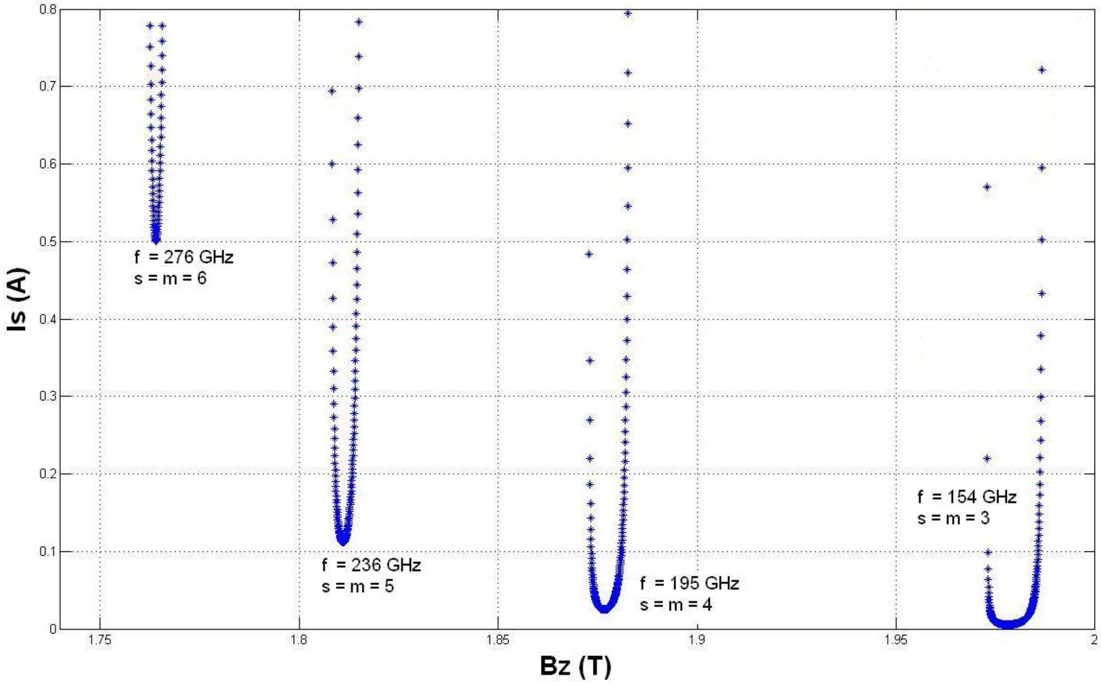

Figure 3-10 Starting current for 4 different harmonic number interaction as a function of the magnetic field (harmonic number: s =3, s=4, s=5, s=6, cavity radius r_w = 1.3 mm)

As the gyrotron works near cut-off frequency, using a large orbit electron beam the interaction requires $s=m$, so once the frequency and operation harmonic number are decided, both the cavity size as well as the wave transverse mode index can be determined. When the cavity size is set other modes and frequencies can be obtained by tuning the magnetic field at the interaction region

Through the same equation used previously, the start oscillation threshold requirement can be calculated. Two different sizes of cavities were studied: one with the interaction cavity radius 1.055 mm, and another one with the interaction cavity radius of 1.3 mm. The starting oscillation current for the radius 1.3 mm cavity were calculated by the same equation (3.24) as used in Figure 3-10. The results are shown in Table 3-2 with all the possible interactions highlighted in the gray rows.

Table 3-2 All the possible gyrotron interaction modes and starting oscillation threshold

Harmonic Number	Cavity Size Diameter (mm)	Magnetic field B (T)	Starting Current I (A)	Frequency (GHz)
2	**2.60**	**2.09**	**0.004**	**112**
3	2.11	2.44	0.0043	190
3	**2.60**	**1.98**	**0.006**	**154**
4	2.11	2.31	0.017	240
4	**2.60**	**1.88**	**0.03**	**195**
5	2.11	2.23	0.08	290
5	**2.60**	**1.812**	**0.11**	**236**
6	2.11	2.174	0.38	340
6	**2.60**	**1.77**	**0.51**	**276**
7	**2.11**	**2.13**	**1.50**	**389**
7	2.60	1.73	2.33	315
8	2.11	2.097	6.75	436
8	2.60	1.7	10.2	354

3.5 Output Taper Design

Due to the cavity Q requirement, the output taper is chosen to be a taper with a large taper angle of a certain length. This is a strong, linear up-taper which may lead to the excitation of parasitic modes. In order to study the mode conversion due to this output taper, simulations were carried out using CST Microwave Studio.

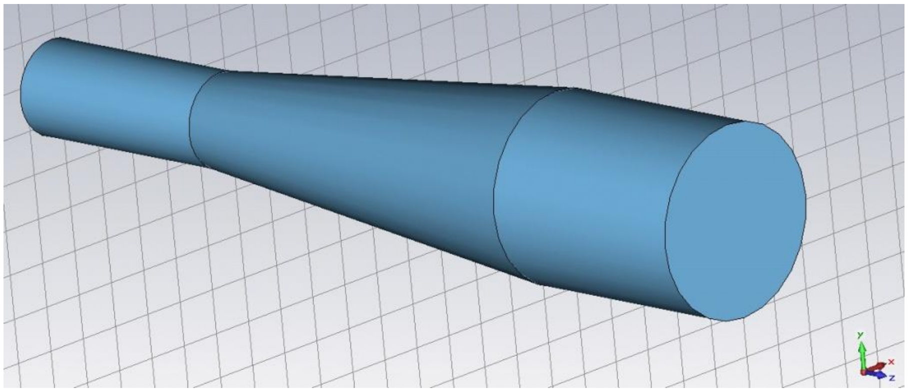

Figure 3-11 The Geometry of the output taper used in CST Microwave Studio simulation

The geometry of the output taper used in the CST Microwave Studio is shown in Figure 3-11. Two short pieces of straight cylindrical waveguide were added at both ends of the output to make the configuration used in the simulation more close to real situation. A TE_{71} 390 GHz microwave signal was introduced into port 1 which lies at the end of the small cavity. The input microwave E-field pattern is shown in Figure 3-12. The energy and port mode at the output were monitored during the simulation.

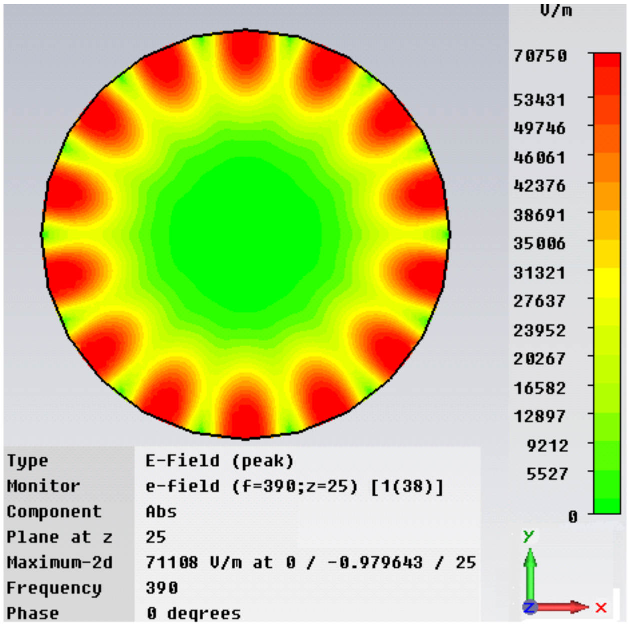

```
Type          E-Field (peak)
Monitor       e-field (f=390;z=25) [1(38)]
Component     Abs
Plane at z    25
Maximum-2d    71108 V/m at 0 / -0.979643 / 25
Frequency     390
Phase         0 degrees
```

Figure 3-12 The incident microwave signal e-field pattern at port 1

When the taper angle is 6 degree and 20 mm in length, the simulation results shows more than 70% output power was converted to the TM_{52} mode. The percentage of output power in the TM_{52} mode and the H-plane pattern at the output are displayed in Figure 3-13. In CST Microwave studio, the output profiles were given in volts/m in percentage to the input microwave amplitude, so the results shown below have been squared to enable the power percentage of this mode to be presented.

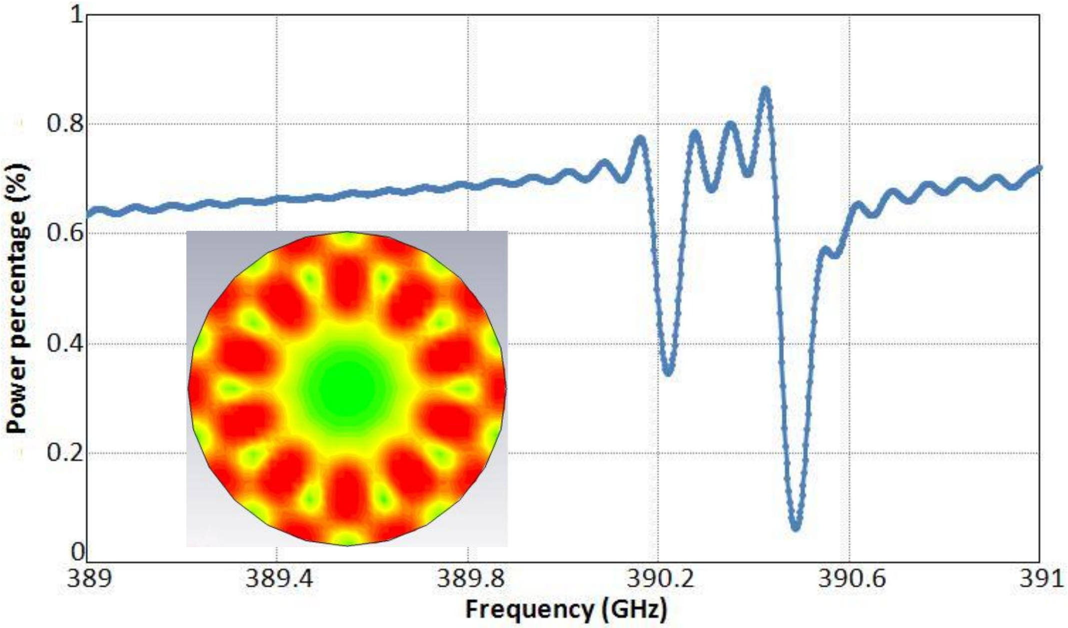

Figure 3-13 The output power of TM_{52} mode at port 2

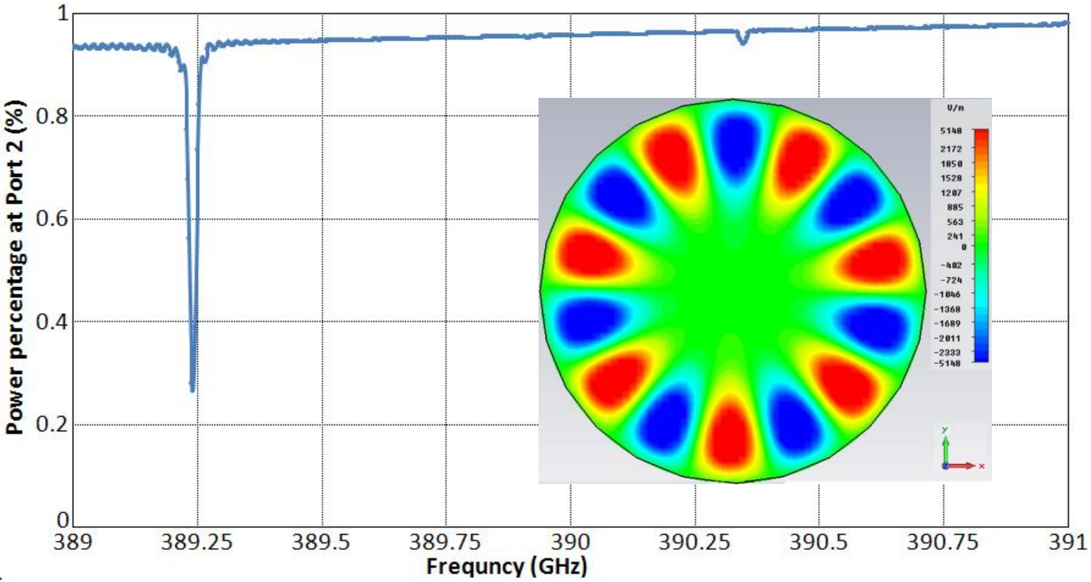

Figure 3-14 The output power of the TE_{71} mode at port 2 of the 4 °output taper

As there is significant mode conversion in this taper, a change of the taper parameter was necessary. One approach is to use a smaller taper angle. When a 4 degree taper was used in the simulation, the results can be seen in Figure 3-14. There is very little energy converted to other modes and more than 95 percent of the energy stays in TE_{71} mode. But when the taped angle is reduced the cavity Q was also reduced making it difficult to satisfy the staring oscillation threshold. Another approach is to shorten the output taper length. When a 6 degree output taper of 10 mm length was used in the simulation the results are shown in Figure 3-15.

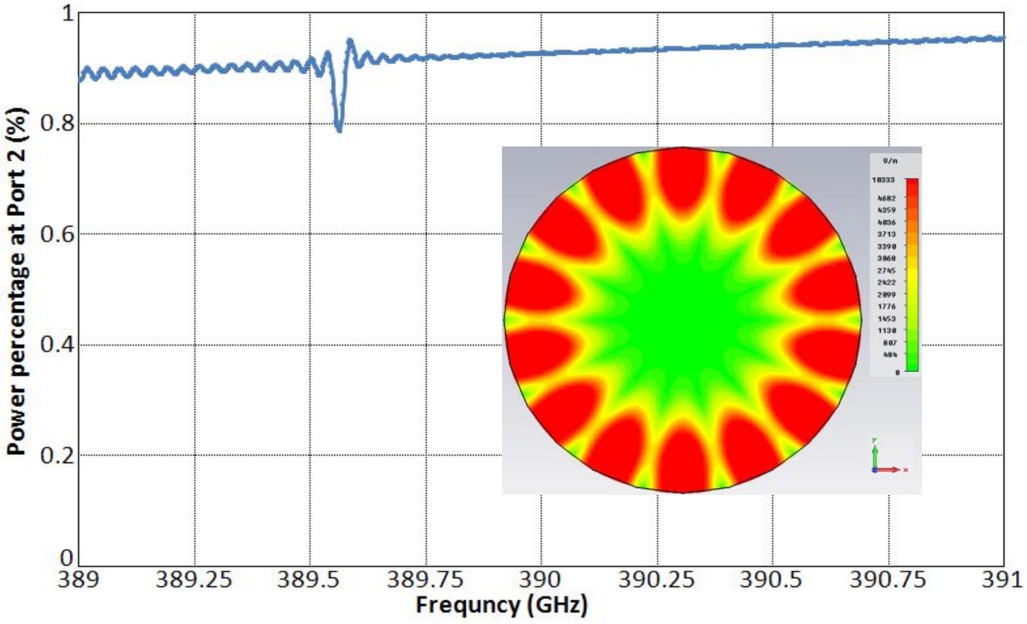

Figure 3-15 The output power of the TE_{71} mode at port 2 of the 10 mm 6 degree output taper

From the simulation results, there is little mode conversion at the end of the output taper, only less than 10% power being converted to other modes. Thus this output taper is suitable for the gyrotron design, and the shorter output taper length makes very little difference to the cavity Q calculated. It was decided to use this very simple cavity design in the high harmonic gyrotron experiments as it will enable the physics of the interaction to be studied while being less complicated to manufacture. A more complex non-linear output taper with less mode conversion and having a high cavity Q will be the subject of future work.

3.6 **PIC Code Simulation**

The 3D PIC (Particle in Cell) code MAGIC was used to simulate the harmonic gyrotron interaction. MAGIC is a finite-difference, time-domain electromagnetic particle-in cell code which can be used to simulate interactions between space charged particles and electromagnetic fields.

The MAGIC code divides the time and space into a finite grid from the known initial state, then as the time increases by a single time step, and at each new value of time, Maxwell’s equations will be solved throughout the space and updating the electromagnetic fields in time. Using these new field values, the Lorentz equation will be solved to map charges and current densities onto the grids and these results will then be used as sources for Maxwell’s equations on the next time step. This provides self-consistent interaction between the fields and particles. In addition, the code has been provided with powerful algorithms to represent structural geometries, material properties, incoming and outgoing waves, particle emission process, and so forth. As a result, the code is applicable to a broad class of plasma physics problems.

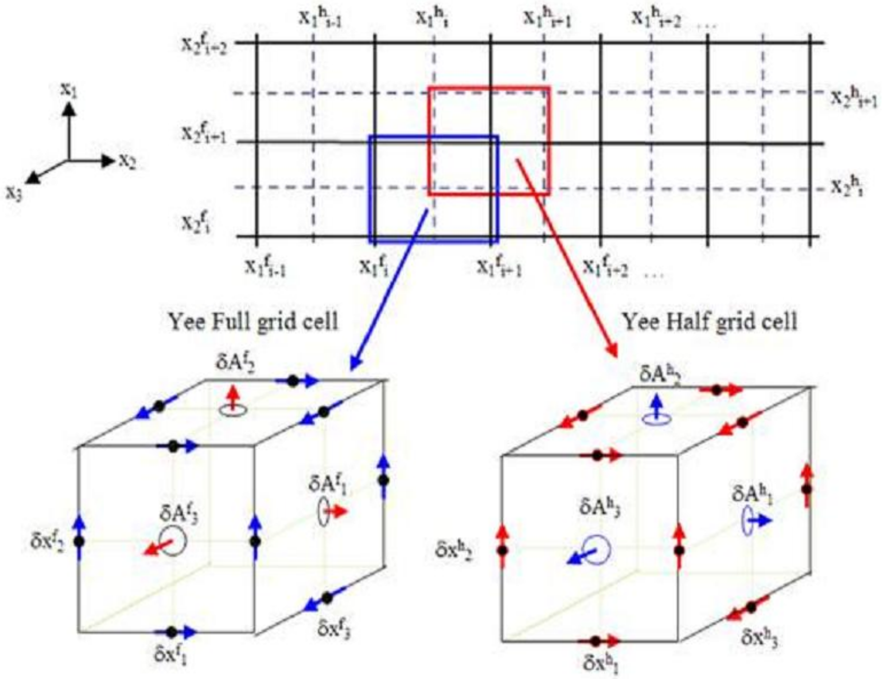

Figure 3-16 The full grid and half grid of "Yee Cell" [132]

The finite-difference Maxwell solvers are based on a discrete formulation of the conventional equations. This discrete foundation begins with the so-called “Yee Cell [132]”, of which the formulations have essential properties that the full-grid and half-grid placement of field elements, results in perfect curl-grad =0 and div-curl=0 in the finite difference representation. All derivatives, both “∇x” and “∂t” become matrices of 0, ±1. Figure 3-16 illustrates the full grid and half grid assignments and the “Yee Cell” for both the full grid and half grid.

In the simulation a smooth cylindrical cavity was built with the parameter that were designed, the structure of the cavity is shown in Figure 3-17. The interaction region of the cavity has a length of 30 mm and a diameter of 2.11 mm. This length is short than the designed cavity length because in MAGIC code, the omega loss is not concerned and shorten the cavity length can save much computation time. At both ends of the cavity were two taper sections to create the resonant cavity in the interaction region. A solenoid was built outside the cavity to produce the magnetic field that was needed in our simulation as shown in Figure 3-17, represented by the dark block with the crossed line through it. Two extra layers of coils were built at both ends of the solenoid to profile of the magnetic field. The magnetic field profile produced by the solenoid is shown in Figure 3-17.

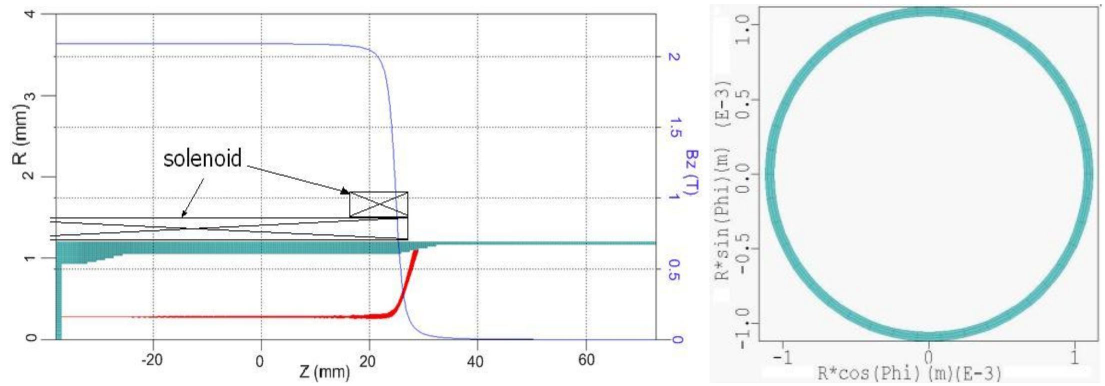

Figure 3-17 The gyrotron geometries with simulated electron beam trajectories

In MAGIC simulation, the electron beam was generated using an electron beam command. In this simulation, a large orbit annular shape electron beam with a voltage of 40 *kV*, current of 1.5 *A* was produced and injected into the cavity. Different beam velocity ratios α were applied in the simulations, where the beam velocity ratio α is defined as the vertical velocity of the electrons over the horizontal velocity. Due to the axis symmetrical geometry a cylindrical coordinate system was used in MAGIC simulation.

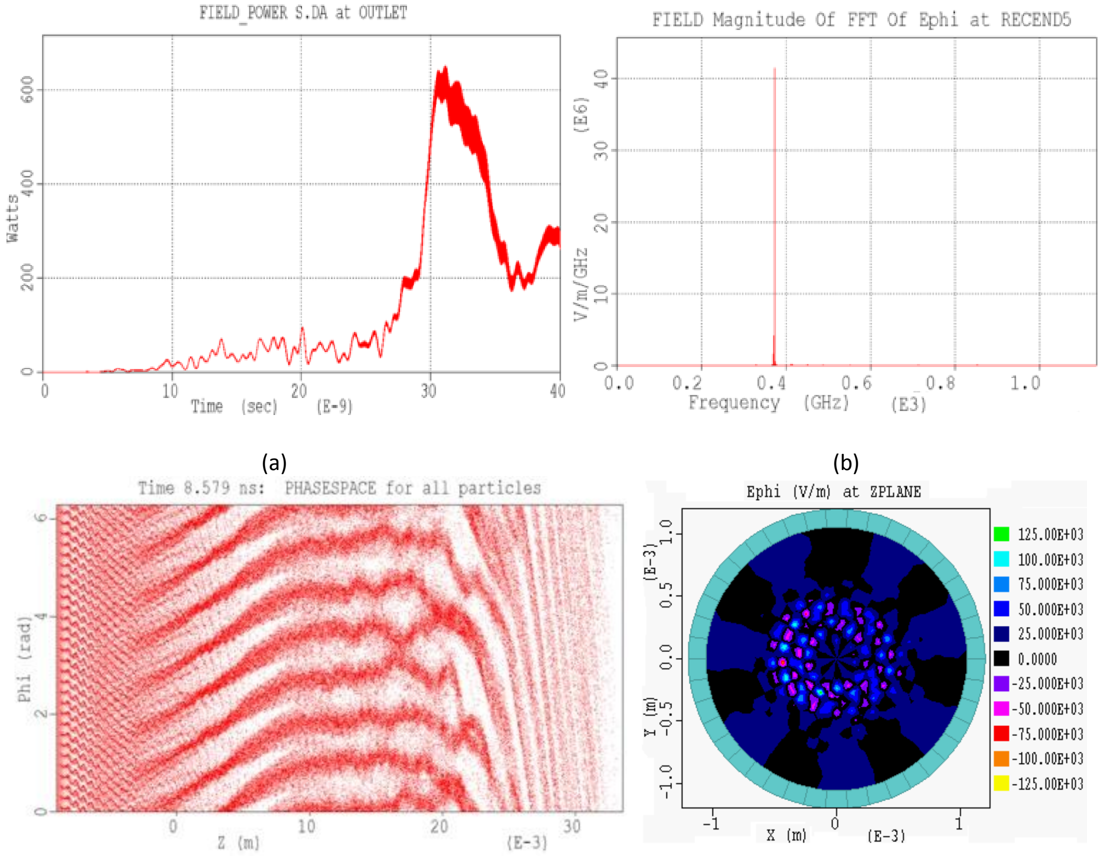

(a) (b)

(c) (d)

Figure 3-18 Simulation results of the 7th harmonic gyrotron in a smooth cavity: (a) output power, (b) output spectrum and (c) electron distribution in phase space and (d) microwave E_{Φ} field pattern at resonance

One of the simulation results is shown in Figure 3-18, the electron distribution in the phase space (Figure 3-18 (c) and the magnet field pattern at the resonance cavity Figure 3-18 (d) indicates the interaction occurred at the 7th harmonic of the electron cyclotron mode. Very pure radiation output at a frequency of 384 GHz was observed in the simulation as shown in Figure 3-18 (b) and more than 600 W of output power was achieved in this simulation as shown in Figure 3-18 (a). In this simulation the interaction region of the cavity has a length of 30 mm and the magnetic field applied in the cavity was 2.10 T. The reduction in power observed after ~30 ns arises due to the cavity of 30 mm in length being sufficiently long in the absence of wall loss, for the interaction to enter phase trapped saturation resulting in re-absorption of the wave energy—this can be seen in Figure 3-18 (c), where the electron distribution in phase angle illustrates the trapping occurring.

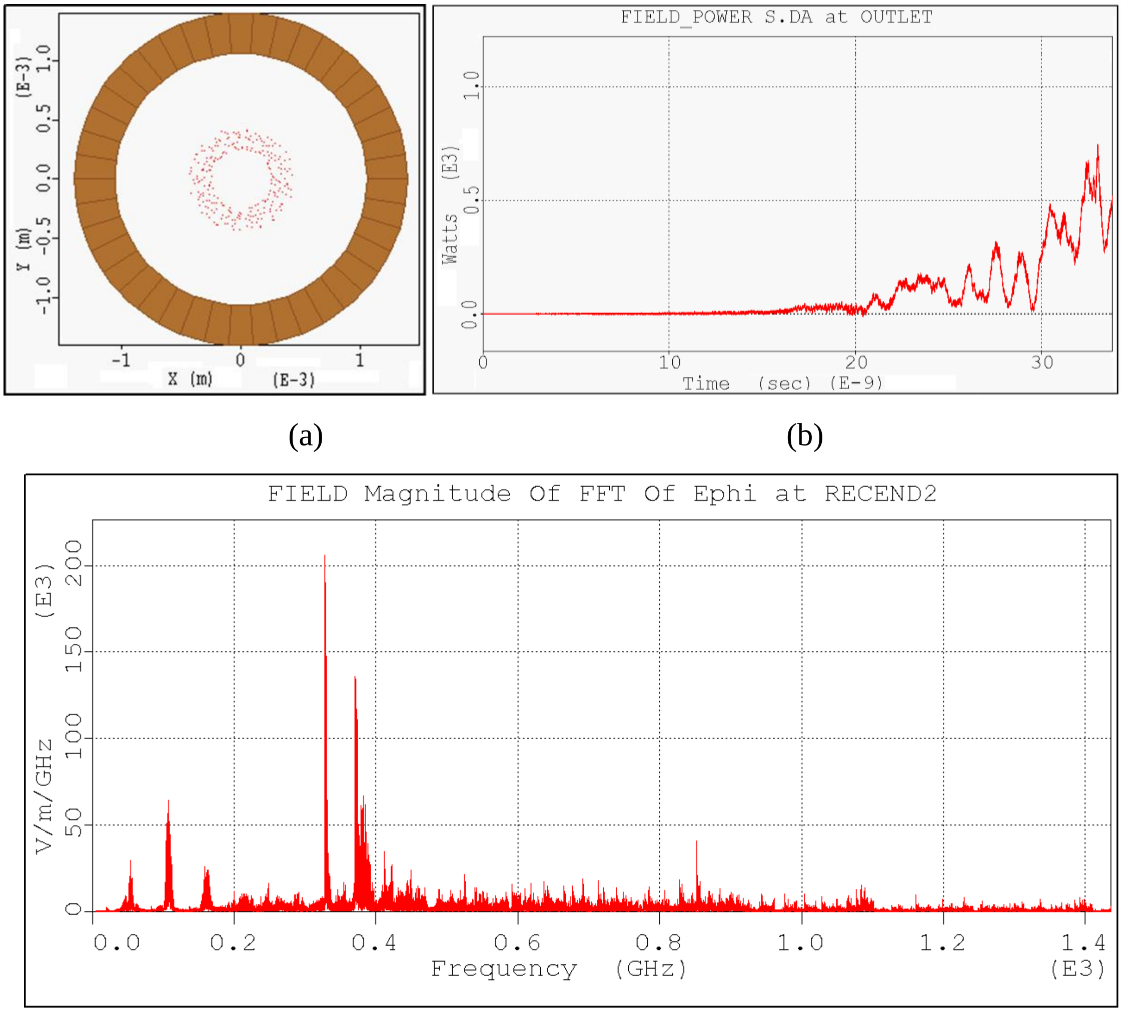

(a) (b)

(c)

Figure 3-19 The gyrotron simulation results with beam thickness and beam spread. (a) the emitter ring with thickness in the simulation; (b) The simulated microwave output power at the end of the output of the gyrotron cavity; (c) the frequency of the simulated output microwaves at the end of output of the gyrotron cavity

In the previous simulation, ideal beam with zero thickness and no beam velocity ratio α spread was used. In order to study the effects of the electron beam spread and beam thickness on the simulation results, a series of simulation were carried out using the 3D particle in cell code MAGIC. In the electron beam simulation, when the beam velocity ratio α increases, the beam spread will increase. For example, the beam velocity ratio spread $\Delta\alpha/\alpha$ is about 10% when the velocity ratio is 1.65, and the beam velocity ratio spread increase to 25% when velocity ratio α reaches 3. Further increase of the beam velocity ratio α would result in a significant increase of the beam spread and the reflection of some beam electrons. For example, the beam velocity spread would reach 45% and beam velocity ratio spread will exceed 30% when the velocity ratio goes to 3.5.

When a 0.1 mm beam thickness and 25% beam spread were set as the input parameters in the simulation, the total output power dropped to ~500 W, and some other competition modes at output were present, especially the competing TE_{61} which became dominant with the output power at design frequency and mode dropping to ~200 W. The results of this simulation can be seen in Figure 3-19. The result indicates that the beam thickness and beam spread has a significant effect on the output of the gyrotron, lowering the gyrotron efficiency and output power. Also there will be competing modes present at the output of the gyrotron which cause less output power in the designed operating mode.

Chapter 4

Cusp Electron Gun

4.1 **Introduction**

The electron gun is an essential and vital component in vacuum electronic devices. All vacuum electronic devices rely on the power from the electron beam produced by electron guns as all the microwave output power is extracted from electron beams. There are various types of electron guns that have been applied in vacuum electron devices giving a large range of current densities and voltages for different applications. Normally they can be classified by the current density it generated, (a) low current electron guns and (b) high current electron guns. Low current electron guns usually refer to a current of less than 20 μA where collective forces can be ignored. These are widely applied in electron microscopes, electron probes and electron spectrographs, etc. Electron guns that can produce an electron beam with a current larger than 10 *mA* are defined as high current electron guns where collective forces have to be taken into account. These electron guns are widely applied in Free Electron Lasers (FEL), microwave sources, accelerators and electron beam welders. For high power microwave sources, high power electron beams are necessary as the output microwave power will always be a portion of the power of the electron beam. To generate a higher power electron beam it often requires the beam voltage and/or beam current to be increased. Also a high quality electron beam is often required to increase the efficiency of the coupling between the beam and the wave. The beam must possess uniform energy with a well-defined beam envelope and beam halo, in addition, it needs to be geometrically stable and also electrically stable as the variation in the electron fluctuations and velocity will cause noise current and produce noise on the output.

For all the various application of electron beams, the first step is to extract low-energy particles from a source and to form them into a beam. The particle source and initial acceleration gaps constitute the injector. Although an injector may represent only a small fraction of the cost and size of a high-energy accelerator, it often presents the most difficult physical and technological problems. The particles move slowly in the first acceleration gap, and the space-charge forces are correspondingly strong. A high quality electron beam source, i.e. cathode, is a fundamental component in order to achieve a high quality electron beam.

4.2 **Cathode**

The cathode is the source of the electron beam and the current density of electron emission from the cathode ranges from milliamperes to tens of amperes per square centimetre of cathode area. J. R. Pierce [133] listed the primary characteristics that an ideal cathode should have:

1. Would emit electrons freely, without any form of persuasion such as heating or bombardment. Electrons would leak off from it into vacuum as easily as they pass from one metal to another
2. Would emit copiously, supplying an unlimited current density.
3. Would last forever, its electron emission continuing unimpaired as long as needed.
4. Should emit electrons uniformly and traveling at practically zero velocity.

Of course, real cathodes have none of these ideal characteristics as the cathode surface changes in time and space rapidly and the electrons emitted have a random velocity in random directions in a real cathode.

In order to withdraw an electron completely from a metal, a potential energy barrier must be overcome. The potential barrier at the interface between the cathode surface and the surrounding vacuum is commonly known as the work function Φ. Most solid materials at ordinary temperatures and pressures are amorphous or crystalline. Constituent atoms, molecules, or ions are arranged in an orderly repeating pattern in crystalline solids. In amorphous solids there are no long-range order positions of the atoms such as common window glass. In a metallic crystal lattice the outer electrons which are called valence electrons are shared by all the atoms in the metal with their orbits overlapping.

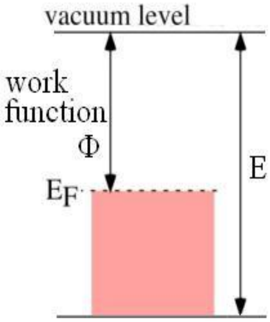

Figure 4-1 Schematic energy level of work function

The valence band is filled with electrons up to Fermi energy (E_F), and they are not bound and are free to conduct current, typically the free electron density in a metal is $10^{23} cm^{-3}$. The work function Φ corresponds to the energy difference between the Fermi energy and vacuum level which is illustrated in Figure 4-1: the work function of a material can be given by the equation $\Phi = E - E_F$. The E is the total amount of energy needed to drive an electron to the lowest free state in vacuum, E_F is the top energy state of an electron in the material. Typical work function values for the metal range from two to five electron volts. These values vary significantly due to the surface condition, and it tends to lower the work function when metals of different work function are joined. Thus, the mechanisms of generating current in vacuum devices can be classed as: 1). Impart sufficient energy to the electrons to overcome the potential barrier; 2). Reduce the barrier height to increase the quantum tunnelling; 3) Combination of these two techniques.

A high quality electron beam source means the cathode can produce high intensity uniform emission, with a long life time. The escape of electrons from the cathode surface is determined by the relative magnitude of the electrons energy. Only those electrons with energies large enough to overcome the surface potential barrier (work function) of the cathode can escape. There are three main modes of electron emission from a solid. Thermionic emission and photoemission rely on supplying electrons with sufficient energy by increasing the cathode temperature or photo-excitation of electrons to overcome the work function of the cathode material Field emission consists of the quantum mechanical tunnelling of electrons through the strong electric-field-narrowed potential barrier at the surface of a metal. The fourth kind of electron emission is from dense plasma on the cathode surface, because plasma is considered to be of zero effective work function.

4.2.1 **Thermionic Cathode**

Thermionic cathodes [134] are by far the most common cathodes applied in the conventional vacuum electron devices. Thermionic cathodes are usually made of low work function and high melting temperature materials and operate together with the Schottky effect—that is by applying electric field on the cathode to reduce the energy required for electron emission, and enhances the emission current. They can produce electron beams of relatively high brightness. At temperatures above absolute zero, some electrons have sufficient energy to escape from the cathode surface, and the number of electrons with sufficient energy to escape increases as the temperature of the cathode rises. The emission of electrons caused by heating of a cathode surface is referred as thermionic emission.

The electron energy distribution in a metallic conductor can be described by the Fermi-Dirac distribution function below [135]:

$$f(E)=\frac{1}{1+e^{(E-E_F)/KT}} \tag{4.1}$$

Where E is the electron energy, K is Boltzmann's constant; T is the cathode temperature in *Kelvin*. As discussed in previous section, only those electrons with energy greater than the sum of the Fermi energy plus the work function ($E \geq \Phi + E_F$) can escape from the cathode surface and make contribution to the current flow from the cathode, and the minimum momentum required for these electrons are:

$$\frac{P_{xc}^2}{2m}=\frac{1}{2}mv_x^2=E_F+\Phi \tag{4.2}$$

Where m is the relativistic electron mass, v_x is the electron velocity at the surface in the perpendicular direction. Assume the number of electrons which has momentum larger than P_{xc} is n_e per unit volume, therefore, the emission current density can be given by the well-known Richardson-Laue-Dushman equation for temperature-limited emission:

$$J = A_0 T^2 e^{-e\Phi/KT} \tag{4.3}$$

The universal constant A_0 is defined as:

$$A_0 = \frac{4\pi meK}{h^3} \approx 1.2\times10^6 Am^{-2}T^2 \tag{4.4}$$

Where h is the Planck constant. It is shown in equation (4.3) that the current varies exponentially with both function and temperature, and by comparison the T^2 term is negligible. The value of A_0 is found to be significantly lower than the theoretical value (about a quarter to a half the value). There are two main reasons. First, the work function which is assumed to be independent of temperature normally varies approximately linearly to the temperature in reality; second, the work function is not constant across the entire emitter surface which will reduce the effective area of the cathode.

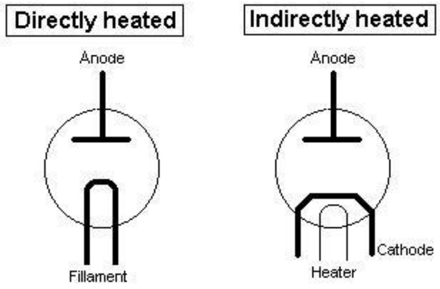

Figure 4-2 The schematic of directly heated cathode and indirectly heated cathode

The cathodes can be directly or indirectly heated in real applications as shown in Figure 4-2. In directly heated cathodes, the heat current passes through the filament which is also the emitter of the cathode. Early cathodes were all directly heated. Directly heated cathodes are fairly efficient, and can reach electron-emitting temperature rapidly. But there are several disadvantages in directly heated cathodes. The structure of the heating filament makes parts of it is closer than other parts, also as the current pass through the filament, there will be voltage drop along the filament, this will makes the electric potential difference along the filament, which will result in unequal emission and loss of efficiency. Another disadvantage occurs when ac current is used as the heating current, the increase and decrease of the current will cause a small increase and decrease of the emitted electrons.

In indirectly heated cathodes, the only function of the filament is to heat the cathode, which is normally built around and covers the filament. The indirectly heated cathodes are relatively large, so they take longer to reach electron-emitting temperature. But once they have been heated up to operating temperature, they do not respond to the small variations in heater temperature caused by the ac heating current, also this cathode can be made equal potential through the entire emitter surface. Most of the thermionic cathodes are indirectly heated in now days. Due to the heat losses, the cathode temperature is lower than the heater temperature. This brings the requirement of a low work function emitter. Thus oxide cathodes [136], dispenser cathodes [137] and scandate cathodes [138] are normally used in indirectly heated cathodes, and these cathodes have a relatively low work function of around 1.2 -2.1 eV [139].

Commercial thermionic cathodes are normally operated at temperatures in the vicinity of 1050 – 1350 K, sizes range from 500 μm to 25 cm and routinely provide up to several A/cm^2 with lifetimes over 40,000 hours. Optimized heater package designs can lead to beam currents of approximately 1 A per watt of heater power.

4.2.2 **Field Emission Cathode**

Another way to extract electrons from a metal surface is by field emission [140]. When a very strong external electric field $(10^6 - 10^9 V/m)$ is applied, the shape of the potential barrier will be modified. The width of the potential barrier at the surface of the metal is reduced due to applied field and the height of the barrier is lower due to the Schottky effect, so that electrons can tunnel through the barrier and escape from the metal even though they do not have sufficient energy to overcome the barrier. Field emission cathodes get a lot advantage such as the potential to achieve extremely high current density with no external power source required (such as a heater, primary e-beam, or intense light source). They can almost instantly work as they do not need any heating time. Field emission cathodes can achieve extremely high-frequency emission modulation. .

Fowler and Nordheim [141] developed the first analytic description of the field emission process by solving a one-dimensional quantum mechanical wave equation. This equation can be used to predict the current density emitted from a metal cathode under an applied electric field. Assume the applied voltage is *V*, the current density J_F can be approximated by:

$$J_F \approx \frac{A(\beta V)^2}{\Phi} e^{-\frac{B\Phi^{3/2}}{\beta V}} \tag{4.5}$$

Where *A* and *B* are approximately constants, and β is the geometric field enhancement factor that includes effects such as the cathode-anode distance and deviations from the purely planar cathode. From the equation, we can find that the current density is very sensitive to the “enhanced” applied voltage. That’s why in practical situations the field-enhanced emission always occurs at some small needle-shaped protrusions or whisker present even on well-polished cathode surfaces. This leads to diode breakdown at low macro-fields with low electron beam currents. In order to overcome this problem, a novel kind of cathode called Field Emission Arrays (FEA) has been developed. The FEA cathode is fabricated specially to have an extremely high density of delicate field emitting points or tips, which can field-emit electrons uniformly and continuously.

By using thin-film deposition of molybdenum and micro fabrication techniques, the cathode incorporated sharp emitters with a closely spaced gated electrode. Very high electric fields can be achieved at the emitter tips with relatively small applied voltages. Figure 4-3 shows a picture of the field-emission micro-tips array. Such tips can be made from carbon fibres, silicon pyramids, and carbon nanotubes. The density of these arrays is typically 10^5-10^6 tips/cm^2. The non-destructive current provided by such an array is limited to the range of many microamperes to a few milliamperes, though the calculated current density at such tips can approach 10^8 A/cm^2. Thus the average current density drawn from such an array lies between a few A/cm^2 to several hundreds of A/cm^2.

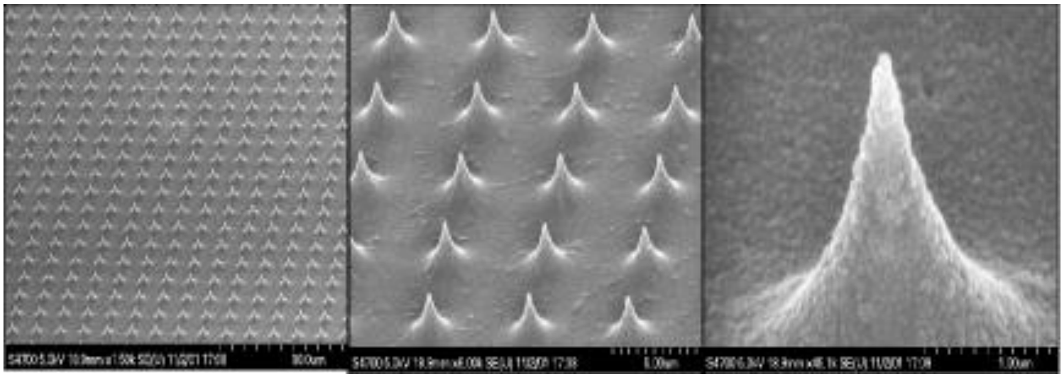

Figure 4-3 Field-emission micro-tips array [142]

4.2.3 **Secondary Emission Cathode**

When electrons with sufficient energy hit a surface, they may cause other electrons to be emitted from the surface. The incident electrons are called primary electrons and the emitted electrons are called secondary electrons. Secondary emission plays a very important role as cathodes in cross-filed tubes, electron multipliers and micro-channel plates.

In a second emission cathode, normally only a small percentage of the electrons are thermionic emitted, others are secondary electrons. Secondary electron yield δ defines the number of emitted electrons per impact electron. With δ significantly larger than 1, namely a single incident electron may liberate many electrons (from several to several thousand [143]) from the cathode. This character of secondary emission makes the secondary emission cathode very attractive as a useful source of free electrons. When an electron strikes the cathode, several situations may happen depending on the nature of the collision, the electron may a) reflect backwards; b) travel deep into the cathode and continue collision with electrons embedded deep in the cathode and some of them will escape from the surface and become secondary electrons. If the incoming electrons continue to penetrate deep into the cathode, the collision can no longer drive the electron out of the surface. The depth of the collision that can cause secondary electrons is called the escape depth of the material. Different materials have different maximum secondary yields, thus increasing the secondary emission yield of material is an active field of research for secondary emission cathodes.

In vacuum electron devices, secondary emission cathodes are normally applied in crossed-field devices. It produces annular beams with current up to several hundreds of amperes at around 40 kV.

4.2.4 Other Cathodes

A photocathode is another emission mechanisms discovered by H. Hertz in 1887 and described by A. Einstein in 1905. It can produce a beam of the highest brightness but are applicable only to short pulse applications. Because this type of cathode operates at room temperature, it simplify the mechanical design of the electron guns, it can also be operated on the high–voltage terminal of an accelerator because the stimulated emitting is coupled through photons rather than by a direct electrical connections. It will be easy to modulate the output electron beam at high frequency by varying the photon flux. Laser-driven photo-cathodes can supply very high-current density and are useful for some pulsed beam applications.

Explosive emission cathodes (EEC) [144] can produce the very high current densities of several kilo amperes per centimetre square. Thus it was widely used as an intense electron source for the generation of high power microwaves (HPM). EECs are simple and easy to use. When high electric field is rapidly applied to the cathode especially those micro-points on the cathode surface which due to field enhancement have an even higher electric field, the cathode material and cathode absorbed gases will be liberated from the cathode surface explode and be ionized. Thus a plasma layer near the surface of the cathode will be formed, and this plasma serves as a virtual free electron source. All types of electron emission mechanisms we mentioned above work with the EEC. The plasma layer induces thermionic emission by heating the cathode surface, secondary emission via ion back-bombardment, and field emission due to the large electric field. And even photoemission due to the photons that are emitted when the electrons and the ions recombined.

Surface plasma cathodes can produce high density electron beam current. Moderately uniform plasma could be created by covering the cathode surface with some insulating materials such as velvet cloth. However they are not suitable for high-brightness beams.

A pseudo-spark cathode is based on the principle of a hollow cathode discharge under a special geometry which is operated at a low pressure of about 50-500 mtorr. It is an axially symmetric self-sustained intense current gas discharge. Pseudo-spark cathodes have been proven to be capable of generating electron beams of adjustable pulse length $(ns \sim \mu s)$, high-current density $(>1kA/cm^2)$, high brightness $(\sim 10^{11} Am^{-2}rad^{-2})$, small beam diameter $(\leq 3mm)$, and high-power density($\sim 10^{10} W/cm^2$) [145].

4.3 Electron Gun Design

After the generation of electrons from the cathode, configurations are needed to extract the electrons from the cathode, accelerate focus the electrons to form the required shape of beam. There are different types of configuration for different types of beams for different applications.

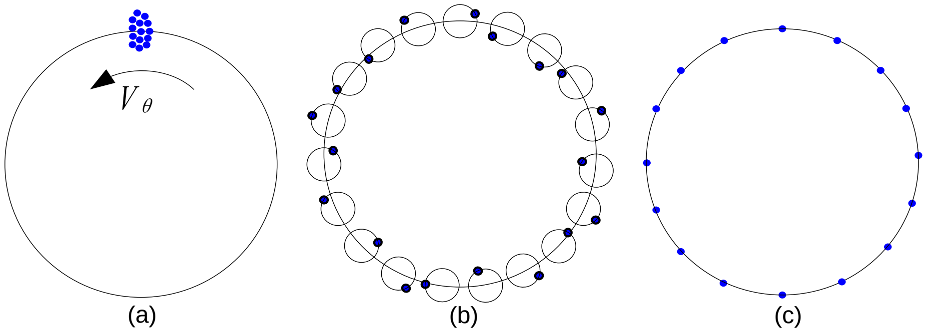

Figure 4-4 Schematic diagrams of the three different electron beams produced by (a) Pierce gun with kicker, (b) MIG and (c) cusp electron gun

There are mainly three types of electron beam used in gyro-devices: 1/ helical electron beam produced by Pierce gun with a kicker, 2/ off-axis encircling electron beam produced by Magnetron Injection Gun (MIG), 3/ axis encircling electron beam produced by a cusp electron gun as shown in Figure 4-4.

4.3.1 **Pierce Gun**

Pierce gun is a classic electron gun design that forms a uniform current density profile for linear devices such as klystrons, TWTs, RF injectors, ubitrons, and free-electron masers. The analytic derivation of Pierce gives a self-consistent solution for a space-charge dominated injector. The procedure predicts the shapes of the accelerating electrodes to produce a laminar beam with uniform current density. Although the treatment holds only for the special geometry of a sheet beam accelerated through an extraction grid, it gives valuable insights into the design of more complex guns. In different applications, different shapes of cross-section electron beams are required. Generally speaking, there are three different shapes of cross-section 1/ Pierce electron guns: 2/ spherical diode electron guns which produce conical electron beam and 3/ annular electron guns.

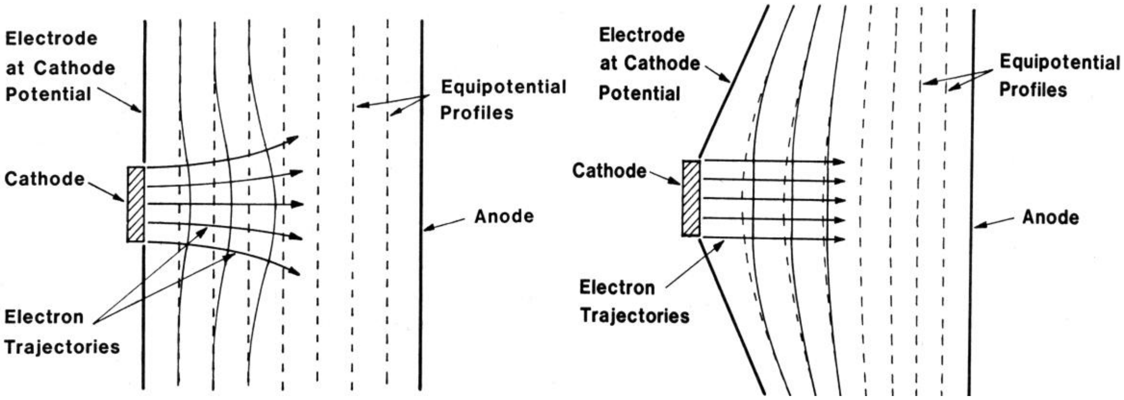

Figure 4-5 Equipotential profiles without (dashed lines) and with (solid lines) electrons in flat cathode (left) and Pierce Gun (right)

In the Pierce gun the particles emerge from the source region with negligible kinetic energy; particles motion in the extraction gap is usually non-relativistic although relativistic Pierce guns have been developed for high power applications; the force from the beam-generated magnetic fields is small; potentials at the source and extractor electrodes are determined by conducting surfaces — the beam exits the anode-cathode gap through a hole in the anode. The Pierce electrode helps to form the parallel or even convergent electron beam.

As shown in Figure 4-5 (left), when electrons are present, as the space charge forces between the electrons are pushing on each other and causing their trajectories to diverge, so the electron trajectories diverge as the electrons move away from the cathode. Thus the equipotential profiles are changed to the right as indicated by the solid lines because of the space charge forces, and the electrons tend to move perpendicular to the new equipotential profiles.

In order to make the electron beam travel in parallel paths, the electrodes adjacent to the cathode are tipped toward the anode to straighten the equipotential profiles as shown in Figure 4-5 (right). It is also possible to generate a convergent electron beam, thus current density will also be significantly increased.

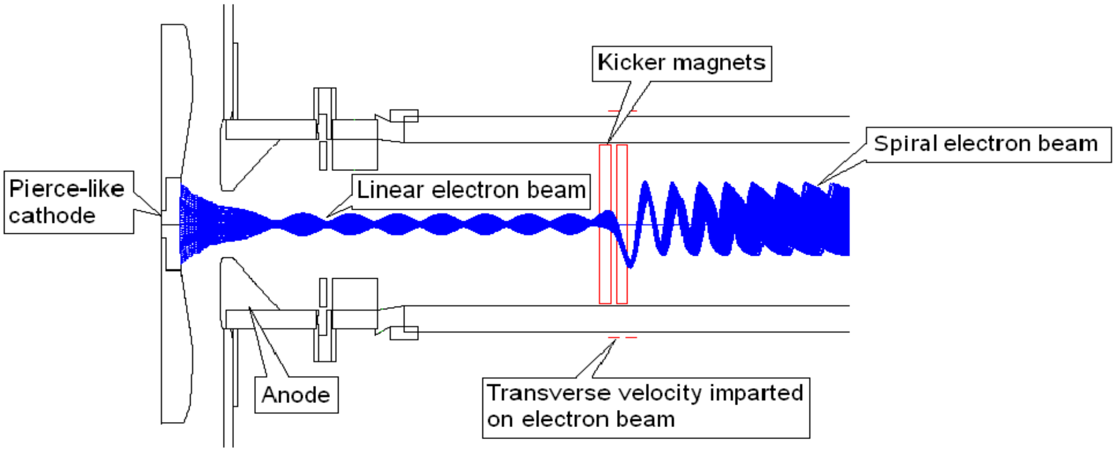

Figure 4-6 Schematic of a Pierce-type electron gun with kicker

When a kicker magnet is added in the Pierce-type electron gun system, the pierce electron gun can produce and spiral electron beam which is helical encircling around the axis. Normally the magnetic kicker produced a pulsed magnetic field which imparts a transverse impulse to the electrons, and the electrons will gain a transverse momentum and start a helical, axis-encircling trajectory as shown in Figure 4-6.

4.3.2 **Magnetron Injection Gun (MIG)**

MIG Gun produces an annular electron beam as shown in Figure 4-7. The electron beam follows a helical trajectory in the applied magnetic field, in which the electron beam cycles in small cyclotron orbits. The potential difference between the anode and cathode produces the electrical field used to accelerate the electrons and extract the electron beam from the electron gun. The applied magnetic field is axially symmetric with its strength increasing smoothly down the tube in a magnetic compression region to the peak magnetic field in the interaction region.

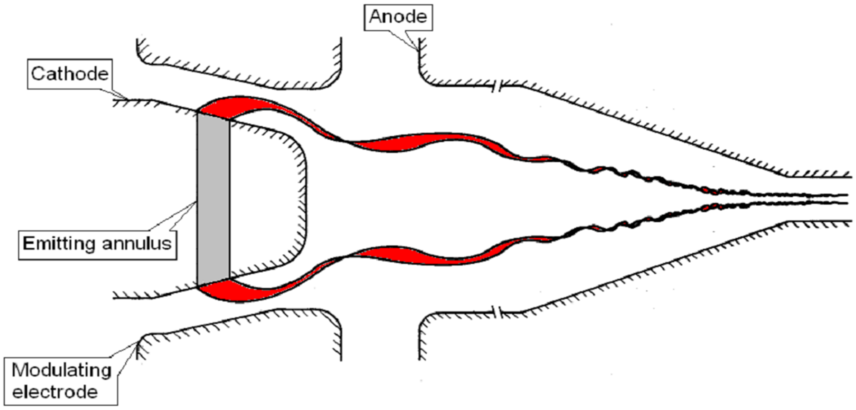

Figure 4-7 Schematic of a magnetron injection gun [146]

MIGs are widely used in vacuum devices such as magnetrons, cyclotron resonance masers and gyro-devices including gyrotrons, gyro-klystrons and gyro-TWTs. A MIG is normally run as a temperature-limited thermionic emitter particularly for high-power and relativistic devices. The MIG has been utilized most extensively for gyro applications as the cathode; where the anode and RF interaction region are very closely co-located with the MIG.

4.3.3 **Cusp Gun**

A cusp electron gun produces an axis-encircling electron beam through a magnetic field reversal just after the cathode. Azimuthal rotation is imparted on the electrons through the conservation of canonical momentum as they pass through the different magnetic field regions. The magnetic field reversal point is called as cusp point.

A Cusp electron gun has a lot of inherent advantages over other electron guns in gyro-devices especially in harmonic gyro-devices. Firstly the cusp electron gun produces an axis-encircling electron beam which has very good mode selectivity in a harmonic gyrotron as it requires the harmonic number *s* equals the wave transverse mode index number *m* for effective beam-wave coupling [147], thus parasitic oscillations can be reduced. The Cusp electron gun can operate in a Continuous Wave (CW) mode. Unlike a Pierce electron gun with a kicker magnet which works with a pulse mode as the kicker magnet is normally operated in pulse mode. Furthermore, due to the high power of the spent electron beam, a cusp electron beam is more suitable for beam energy recovery by using a depressed collector and reducing the energy density on an electron dump. Due to all these advantages the cusp electron gun using a temperature limited thermionic cathode based on a cusp electron gun was chosen in the harmonic gyrotron experiment.

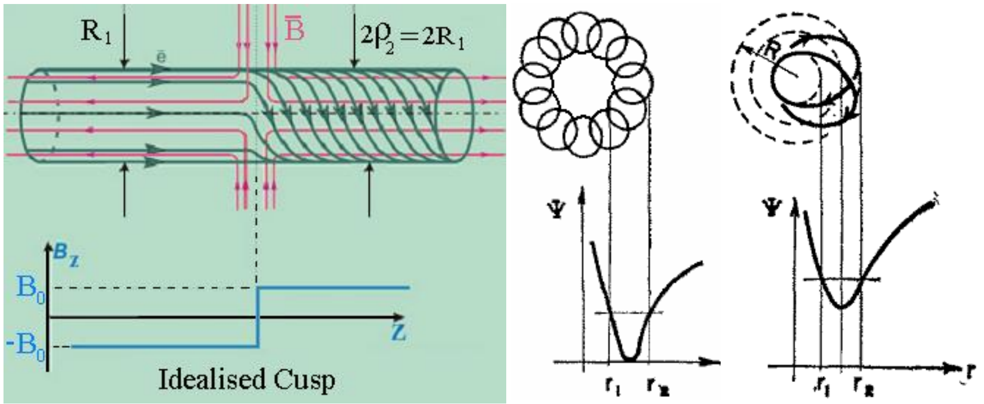

(a) (b) (c)

Figure 4-8 Cusp magnetic field (a) and motion of particles in off-axis-encircling beam (b) and axis encircling beam (c).

In order to describe the cusp electron gun mechanism, the equation of a charged particle motion through an axially symmetric magnetic field $\partial A_\theta / \partial \theta = \partial V / \partial \theta = 0$ is introduced here as below:

$$H = \frac{P_r^2}{2m} + \frac{P_z^2}{2m} + \frac{1}{2m}(\frac{P_\theta - qrA_\theta}{r})^2 + qV \tag{4.6}$$

Where P_r , P_z and P_θ is the canonical angular momentum in the *r*, *z* and θ directions, respectively. A_θ is the Magnetic vector potential in the θ direction. V is the scalar potential. The canonical angular momentum of an electron is a constant of its motion due to Busch’s theorem [148]. This equation can be rewritten in terms of the effective potential $\Psi(r,z,t)$.

$$H = \frac{P_r^2}{2m} + \frac{P_z^2}{2m} + \Psi \tag{4.7}$$

where:

$$\Psi = \frac{1}{2m}(\frac{P_\theta - qrA_\theta}{r})^2 + qV \tag{4.8}$$

If the effect of the accelerating potential V is ignored and instead only the effects of the magnetic field are considered, Ψ is a function only of r as shown in Figure 4-8. In our case, only confined electrons are considered, hence Ψ have at least one minimum, which means there must exist at least one point where:

$$\frac{d\Psi}{dt} = -\frac{P_\theta - qrA_\theta}{mr}(\frac{P_\theta}{r^2} + q\frac{\partial A_\theta}{\partial r}) = 0 \tag{4.9}$$

In order to satisfy this equation, either:

$$\frac{P_\theta - qrA_\theta}{r} = 0 \tag{4.10}$$

or:

$$\frac{P_\theta}{r^2} + q\frac{\partial A_\theta}{\partial r} = 0 \tag{4.11}$$

The angular momentum of the particle can be described as:

$$P_\theta - qrA_\theta = mv_\theta r \tag{4.12}$$

For an off-axis encircling beam: $v_\theta = 0$, which means $P_\theta - qrA_\theta = mv_\theta r = 0$, so it satisfies equation (4.10). Assume the off-axis encircling beam pass through the cusp magnetic field where the magnetic field flux changes sign. These electrons enter the system with a state that $P_\theta = qrA_\theta$; assume the electron beam has an off-axis orbit R, thus:

$$A_\theta = \tfrac{1}{2} rB_z \tag{4.13}$$

Where B_z is the magnetic field component in the z direction. As the electron pass through the cusp electron beam where B_z changed sign, which means A_θ has to change sign as well. Thus equation (4.10) no longer holds. If the particles are still confined then from equation(4.12), v_θ cannot be zero anymore which means the electron beam will become an axis encircling electron beam. This process is illustrated in Figure 4-8. As the electron beam passes through the field reversal, the electron beam trajectory changed into an axis encircling beam, and as the magnetic field increases again, the electron beam radius will shrink again.

4.4 MAGIC Code Simulation

3D PIC code MAGIC was used to simulate and optimize the design of the cusp electron beam source. In the MAGIC code, the cathode is chosen to emit using the thermionic mode emission command, and the work function is chosen to be 1.5 *eV*- the value found for previous cathodes using a tungsten cathode impregnated with barium.

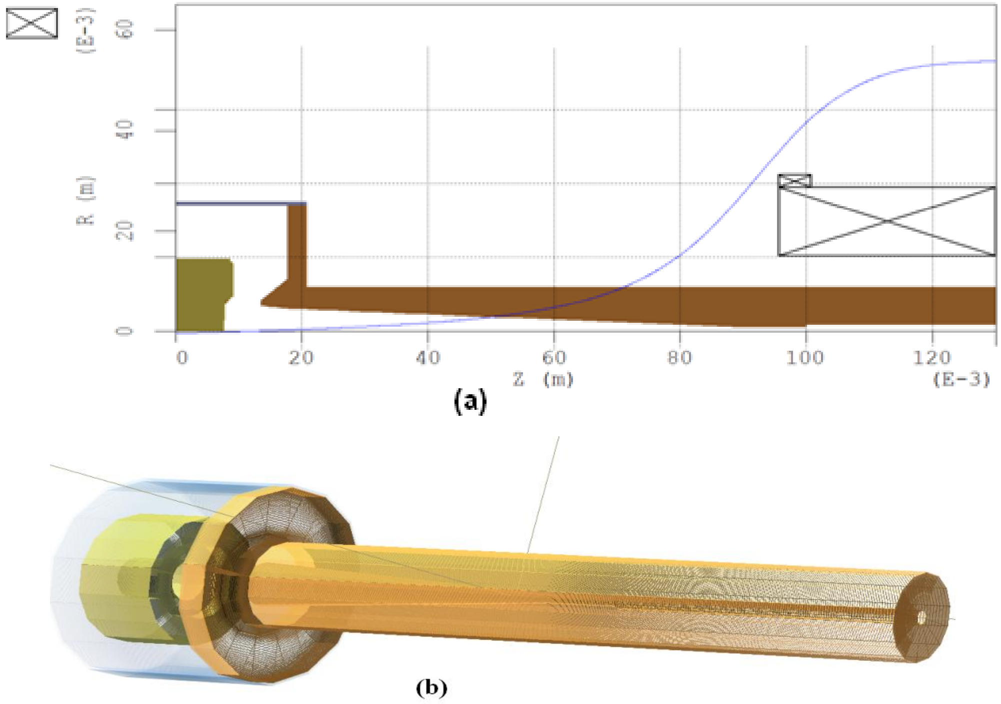

Figure 4-9 the geometry of the cusp electron gun (a) 2D image with magnetic field profile over laid and (b) 3D image

The 2D geometry and 3D image are shown in Figure 4-9 and the magnetic field is overlaid as shown in Figure 4-9 (a) with the cusp point in relation to the geometry of the cathode and anode defined in the diagram. The magnetic field is produced by two solenoids located accordingly to figure 4-9(a). The “reverse” coil that is located behind the cathode has a length of 22 mm, producing a negative magnetic field, and the other solenoid namely the main cavity coil has a length of 225.5 mm producing an positive magnetic field and also producing an uniform positive magnetic field at the downstream region which was also used as the magnetic field for the beam-wave interaction.

Two extra layers of coils were added to both ends of the main solenoid to sharpen the B-field profile of the magnetic field and also reduce the overall turns required to produce such a profile. The diode and gun geometry were optimized to produce a high quality electron beam. The electron beam velocity ratio α is tunable by adjusting the position of the two solenoids [149]. The potential difference applied between the cathode and anode will determine the beam energy.

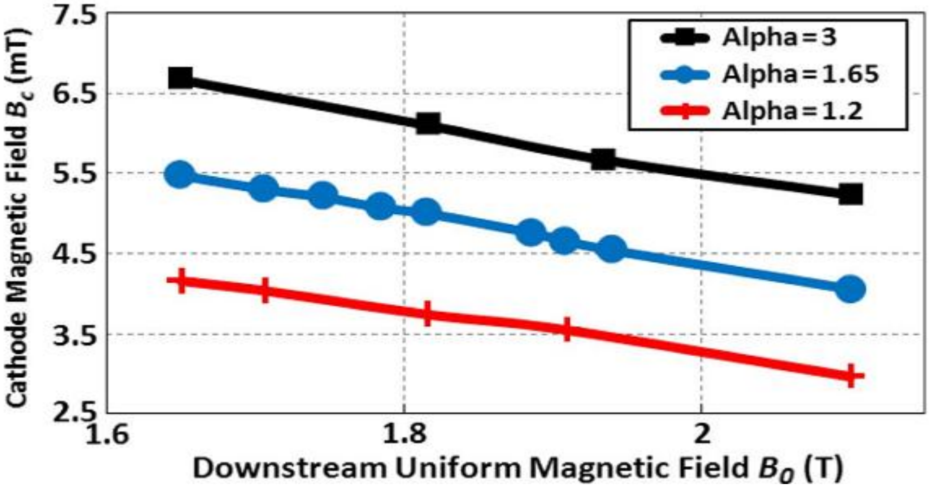

Figure 4-10 Magnetic-field operation ranges for different values of velocity ratio (α) [149]

The parameters of the electron beam were chosen to be as follows: beam energy E = 40 keV with beam current of ~1.5 A, the uniform magnetic field region at the downstream side is 1.7-2.1 T, the beam velocity ratio α is tunable from 1-3. The simulation results of different velocity ratios α are show in Figure 4-10.

The 3D view of the beam trajectories and their projections in the axial and the transverse planes are shown in Figure 4-11 which clearly shows the axis–encircling behavior of the beam.

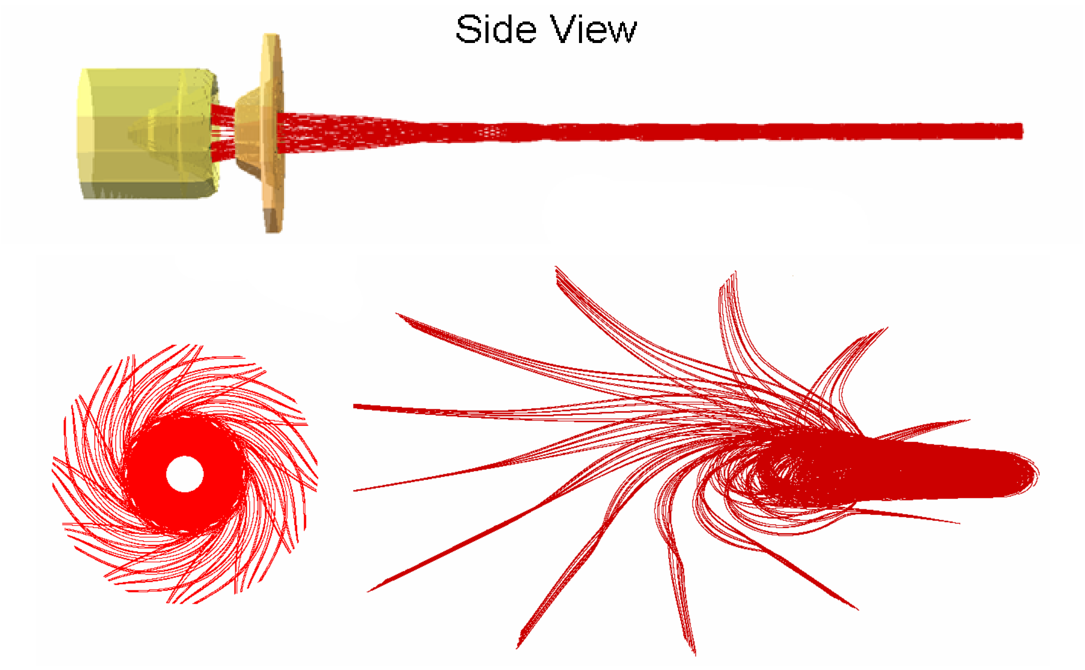

Figure 4-11 the side view and cross section view of the electron beam trajectory

The optimize geometry of the cusp gun including the resultant beam trajectories are shown in Figure 4-12, in which the cusp point has been highlighted. In this simulation, the reverse coil starts at -6cm while the main coil starts at 12.3cm. the electron beam have a velocity ratio α of 3, beam current 1.5 A, beam voltage of 40 kV with an inner radius of 0.27 mm and an outer radius of 0.36 mm. This is consistent with the analytical calculation of the Larmor radius of 0.31 mm.

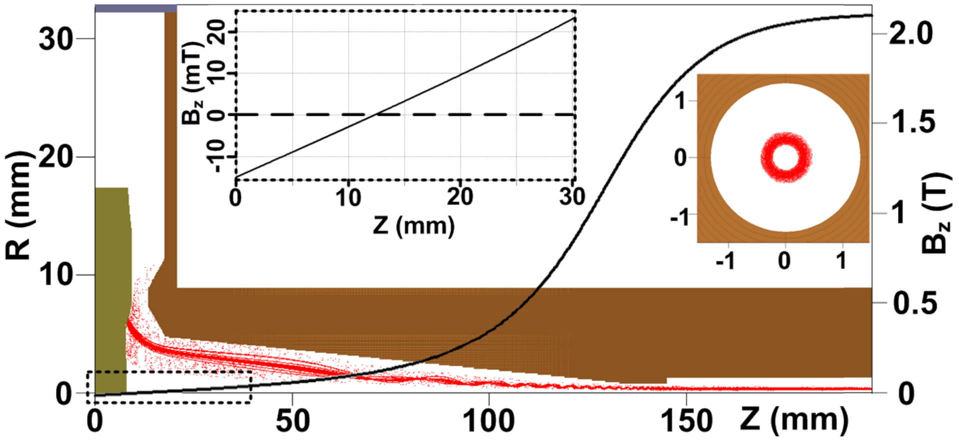

Figure 4-12 Simulated cusp gun and resultant beam trajectories [150]

Chapter 5

RF Component & Diagnostic Design

5.1 Introduction

Cavity design has been discussed in Chapter 3. The fabrication of the cavity as well as the microwave measurement of the cavity carried out using a 325GHz to 500GHz Vector Network Analyser will be discussed. A calibration of the high frequency rectifying crystal millimetre wave detector and cut-off filters used to measure the power and frequency of the radiation generate by the gyrotron are presented in this chapter.

5.2 Cavity Fabrication

The cavity was manufactured using Electrical Discharge Machining (EDM) also known as spark erosion. The EDM process was invented by two Russian Scientists, Dr. B. R. Lazarenko and Dr. N. I. Lazarenko in 1943. The world’s first industrial NC controlled EDM was introduced in 1969 [151]. Electrical discharge machining is a machining method primarily used for hard metals or those that would be very difficult to machine with traditional techniques. EDM typically works with materials that are electrically conductive. There are different types of EDM such as Sinker EDM and Wire EDM;

Sinker EDM [152] sometimes is also referred to as cavity type EDM or Volume EDM. Sinker EDM consists of an electrode and work-piece that are submerged in an insulating liquid typically oil, or less frequently, other dielectric fluids. A voltage is applied between the electrode and the work-piece, as the electrode approaches the work-piece, dielectric breakdown occurs in the fluid forming a plasma channel, and a small spark jump. The sparks usually strike at different times because it is very unlikely that at different locations the inter-electrode space has identical local electrical characteristics which would enable the various sparks to occur simultaneously. These sparks occur several hundred thousand times per second, and each spark will dissipate a tiny portion from the work-piece by melting and vaporizing the work-piece material, then the flushing of dielectric fluid through a nozzle are used to clean out the eroded debris, thereby avoiding a short circuit. Sinker EDM is capable of complex 3D shape manufacture, often with small or odd shaped angles, vertical, directional, helical, conical, rotational, spin and indexing machining.

Wire EDM also known as wire electrical discharge machining (WEDM) or wire-cut EDM. It is a method to cut conductive materials with a thin electrode that follows a programmed path. The electrode is a thin single-strand metal wire, usually brass. The wire feeds from reel to reel and pass through the work-piece, typically occurring submerged in a tank of dielectric fluid such as deionised water. The wire is charged to a voltage very rapidly and when the voltage reaches the correct level, a spark jumps the gap and melts a small portion of the work-piece. Then the de-ionized water cools and flushes away the debris from the gap. The wire is controlled by upper and lower diamond guides that are usually accurate to 0.004 mm, and typical wire diameters range from 0.1 mm to 0.3 mm although smaller and larger diameters are available. WEDM is not typically used to produce complex 3D geometries, instead it is typically used to cut plates and to make punches, tools, and dies from hard metals that are too difficult to machine with other methods.

As in the EDM process, there is no physical contact between the electrode/cutting wires with the work piece, also there are no large cutting forces involved in the removal of the material. So there is very little change in the mechanical properties of the work-piece material, and there is no burrs generated during the cutting. The hardness of the work-piece material has no detrimental effect on the cutting speed which means it can works in large scale cutting especially in WEDM. These properties make WEDM a very good method to manufacture our cavity.

Another way discussed was to simply drill a cavity but the surface finish would be dependent on the drill and the speed of the drill used in the manufacturing process. Also it would be very difficult to drill the cavity of a radius of 1.3mm over a length of 50mm. Due to wobbling of the drill, making it very easy to break the drill and difficulty in aligning the hole by having to cut the cavity in two and drill from both ends it was decided to manufacture the cavity using the spark erosion technique only.

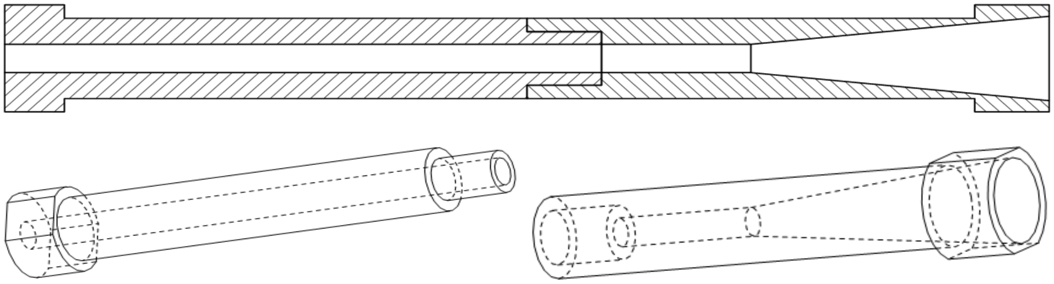

Figure 5-1 section view and the through view of the design of the cavity

The cavity design drawing is shown in Figure 5-1, the flat on both ends of the cavity is the gap where air can pass through while evacuating and venting the system. The picture of the manufactured cavity is shown in Figure 5-2.

Figure 5-2 Picture of the manufactured cavity with scales on it

5.3 **Cold Microwave measurements**

In order to measure the RF properties of the cavity a Vector Network Analyzer was used. A network analyzer is an instrument that is designed to handle the analysis of circuits (networks) in RF engineering. A network analyzer is the most complex and versatile piece of test equipment in the field of RF engineering. It is used in applications in research & development and also for test purposes in production. There are two main categories of Network Analyzers [153]: Scalar Network Analyzer (SNA) and Vector Network Analyzer (VNA). Among them, SNA can only measure the amplitude properties, but VNA can measure both amplitude and phase properties.

5.3.1 Wave Quantities and S-parameters

Wave quantities are used in characterizing RF circuits to distinguish between the incident wave *a* and the reflected wave *b*. The incident wave propagates from the analyzer to the device under test (DUT) while the reflected wave travels in the opposite direction from the DUT back to the analyzer. Figure 5-3 shows a one-port device with its wave quantities which have units of $\sqrt{W}$ (square root of Watt).

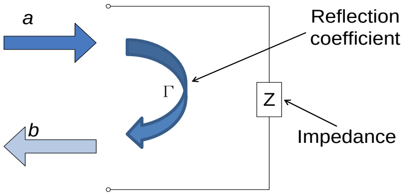

Figure 5-3 One-port device with incident and reflected waves

The power travelling to the one-port device is given by $|a|^2$ and the power reflected is given by $|b|^2$. The reflection coefficient Γ represents the ratio of the incident wave to the reflected wave as $\Gamma = b/a$. Z is the complex impedance of the DUT, with a reference impedance of $Z_0 = 50\Omega$, the normalized impedance $z = Z/Z_0$. The reflection coefficient can be written as:

$$\Gamma = \frac{z-1}{z+1} \tag{5.1}$$

So the normalized impedance z can be drawn in smith chart when the reflection coefficient Γ is measured. In a two-port device, besides the reflection at the two ports, there is also the possibility of transmission in the forward and reverse directions. In comparison to the reflection coefficient, these are called the scattering parameters (S-parameters) as shown in Figure 5-4 as S_{11}, S_{12}, S_{21}, S_{22}.

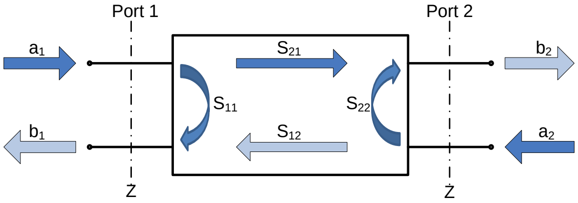

Figure 5-4 Two-port device with its wave quantities

These S-parameters are used to define the ratios of the respective wave quantities. S_{11} and S_{21} are defined as the reflection coefficient on port 1 and the forward transmission coefficient from port 1 to port 2, respectively, under the condition of a reflection free termination $\Gamma = 0$ is used on port 2 (match) and also no incident wave at port 2 which means $a_2 = 0$. These can be defined in the equations below

$$S_{22} = \left.\frac{b_2}{a_2}\right|_{a_1=0} ; \qquad S_{12} = \left.\frac{b_1}{a_2}\right|_{a_2=0} \tag{5.2}$$

For the reverse measurement, a match $\Gamma = 0$ is used on port 1 and also $a_1 = 0$, S_{22} and S_{12} are defined as the reflection coefficients on port 2 and the reverse transmission coefficient from port 2 to port 1, which can also be defined as:

$$S_{11} = \left.\frac{b_1}{a_1}\right|_{a_2=0} ; \qquad S_{21} = \left.\frac{b_2}{a_1}\right|_{a_2=0} \tag{5.3}$$

For more general situation that both ports have an incident wave, the equation can be obtained by the wave quantities and S-parameters from the S-parameter matrix (S-matrix) below:

$$\begin{bmatrix} b_1 \\ b_2 \end{bmatrix} = \begin{bmatrix} S_{11} & S_{12} \\ S_{21} & S_{22} \end{bmatrix} \begin{bmatrix} a_1 \\ a_2 \end{bmatrix} \tag{5.4}$$

5.3.2 **VNA and Cold Measurement Results**

As mentioned previously, a VNA can measure both amplitude and phase angle. The network analyzer generates a sinusoidal test signal that is applied to the DUT as a stimulus signal. The DUT are considered to be linear, and then the response of the DUT will also be sinusoidal. The analyzer will measure the different values for the amplitude and phase of the wave quantities and these values are used to calculate the complex S-parameters. The magnitude of the S-parameter corresponds to the amplitude ratio of the wave quantities and the phase of the S-parameter corresponds to the phase difference between the wave quantities. The VNA has a lot advantages over the SNA such as only a vector network analyzer can perform full system error correction; only vectorial measurement data can be unambiguously transformed into the time domain and so on.

Figure 5-5 The Anritsu ME7808B VNA system

The Anritsu ME7808B VNA system shown in Figure 5-5 was used to measure the RF component. The ME7808B broadband VNA is a high performance measurement instrument that covers the frequency range from 40 MHz to 110 GHz in a single fast sweep. It was built on the advanced technology of the Anritsu Lightning 40 MHz to 65 GHz VNA and the 65 GHz to 110 GHz millimetre Wave (mmW) modules using a unique multiplexing coupler design. It consists of a Lighting 37397D 65 GHz VNA; two millimetre wave modules (3642A series) - extended W band (WR-10) and two 20 GHz ultra-low phase noise frequency sources. With different extended oscillation heads it frequency range of operation can be extended to cover 140-220 GHz (WR-05 heads) and 325-500 GHz (V02.2VNA2-T/R 325-500 GHz high frequency heads).

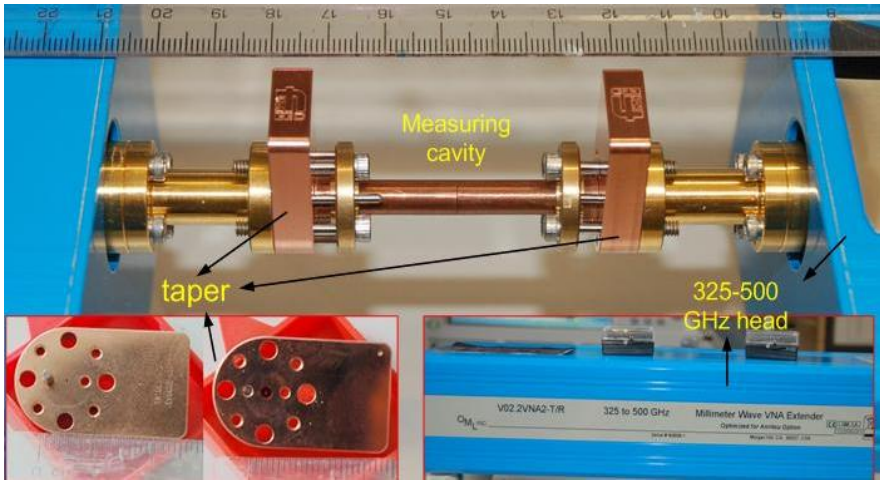

Figure 5-6 The setup of the cavity transmission measurement

The setup of the transmission and phase measurement are shown in Figure 5-6. As the output of the VNA port is a rectangular waveguide, two rectangular to circular waveguide converters were needed at both ends of the VNA output port. The device under test – the cavity was located between these two tapers.

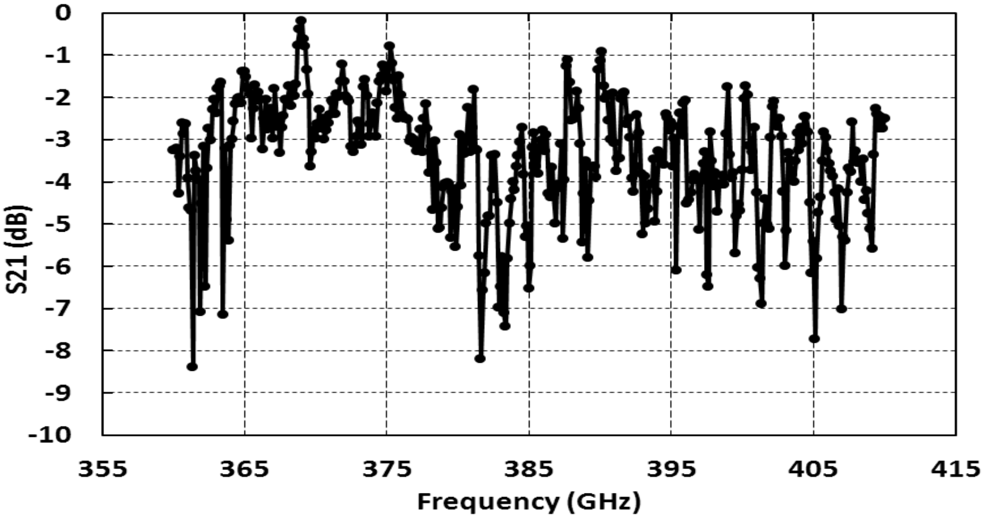

Figure 5-7 The transmission measurement results of the spark erosion made cavity

In the measurement, the output ports of the VNA were taken as the reference plane, and then measure the transmission character of the two tapers without the cavity transmission and then measuring again with both tapers and the cavity present. The transmission characteristics of the cavity can be obtained by comparing these two measurements results.

The transmission characteristic of the spark eroded cavity was measured and the results are shown in Figure 5-7. The average loss of the spark erosion cavity is -4 dB over the frequency range from 360 to 410 GHz. Due to the good performance of the EDM process in fabricating the 2.6 mm diameter cavity the cut-off filters needed for the gyrotron frequency diagnostic were constructed using the EDM process.

Figure 5-8 The picture of 140-220 GHz High Frequency head

The 2.6 mm diameter cavity was also measured using the VNA mainframe but with a different high frequency head operating in the frequency range: 140-220 GHz. The picture of the high frequency head in the 140-220 GHz frequency range is shown in Figure 5-8. The cold test results are shown below in Figure 5-9:

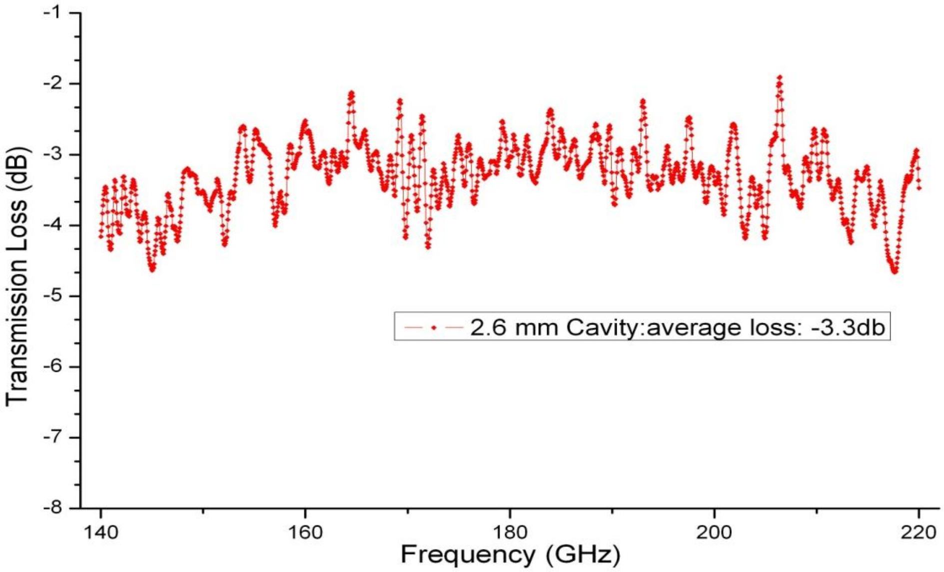

Figure 5-9 Cold test results of the 1.3 mm radius cavity

5.4 **Cut-off Filters Design and Cold test**

Cut-off filters are used in our experiments to determine the frequency of our millimetre wave radiation, as the output frequency is too high to be measured directly without the purchase of an expensive high frequency heterodyne mixer. The cut-off frequency of an electromagnetic waveguide is the lowest frequency an electromagnetic wave will propagate in the waveguide in a certain mode. The cut-off frequency is directly related to the electromagnetic waveguide geometry. The cut-off frequency can be calculated using the free space dispersion relation equation: $\omega = ck$, where $k = 2\pi/\lambda = \sqrt{k_x^2 + k_y^2 + k_z^2}$, k is the wave number, k_x, k_y and k_z are the wavenumber in the direction x, y and z respectively. c is the speed of light and λ is the wavelength. In a waveguide, if we define the wavenumber in the longitude direction as k_z and the transverse direction as k_c then the wavenumber can be written as: $k = \sqrt{k_c^2 + k_z^2}$. So we can get the relationship of the wavenumber with respect to the wavelength as:

$$2\pi \frac{f}{c} = \frac{2\pi}{\lambda} = \sqrt{k_c^2 + k_z^2} \tag{5.5}$$

For the electromagnetic wave to propagate in the waveguide, $k_z^2 \geq 0$. The frequency needs to satisfy the requirement:

$$\frac{2\pi f}{c} = \frac{2\pi}{\lambda} > k_t \tag{5.6}$$

If we define $k_c = 2\pi/\lambda_c = 2\pi f_c/c$, so only the frequency higher than f_c can be propagate in the waveguide. Thus f_c is called as the cut-off frequency and λ_c is called as cut-off wavelength and k_c is the cut-off wavenumber.

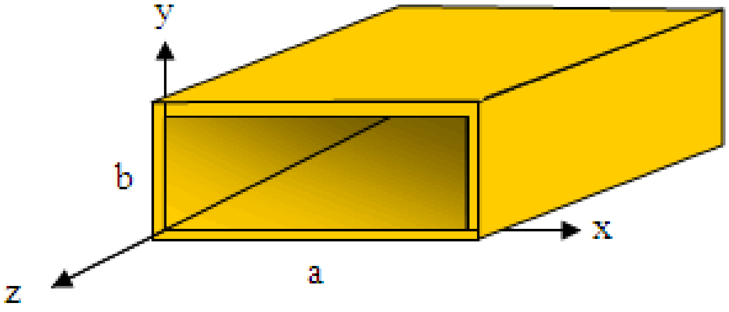

Figure 5-10 the drawing of a rectangular waveguide

For a rectangular waveguide shown as Figure 5-10, the cut-off wavenumber can be calculated using the equation below:

$$k_c = \sqrt{(\frac{m\pi}{a})^2 + (\frac{n\pi}{b})^2} \tag{5.7}$$

Where m is the number of $\frac{1}{2}$ wavelength variation of the field in the "a" direction, and n is the number of $\frac{1}{2}$ wavelength variation of the field in "*b*" direction. "a", "b" are the two sides of the rectangular waveguide, and normally a=2b.

When the fundamental mode TE_{10} is considered, the dimensions of the cut-off waveguide can be calculated using the equation(5.7). In order to measure the frequency of our harmonic gyrotron experiment (for the 2.6 mm diameter cavity and 2.11 mm diameter cavity) a series of different cut-off filters were designed and constructed. The design drawing of the filters produced by AutoCAD are shown in Figure 5-11.

As shown in the picture, the cut-off filter is designed based on a standard G-band waveguide flange. So it can be connected to the microwave detector components such as the horns, attenuators, and rectifying crystal detectors. The cut-off waveguide was 3 mm in length. One side of the waveguide is fixed to the same height as a standard WR-5 (140-220 GHz) waveguide (0.65 mm), while the width of ("a" in Figure 5-11) the cut-off waveguide were varied due to the required cut-off frequency. At both ends of the cut-off waveguide there are tapers as a transition section from the cut-off waveguide to a standard WR-5 waveguide as shown in Figure 5-11.

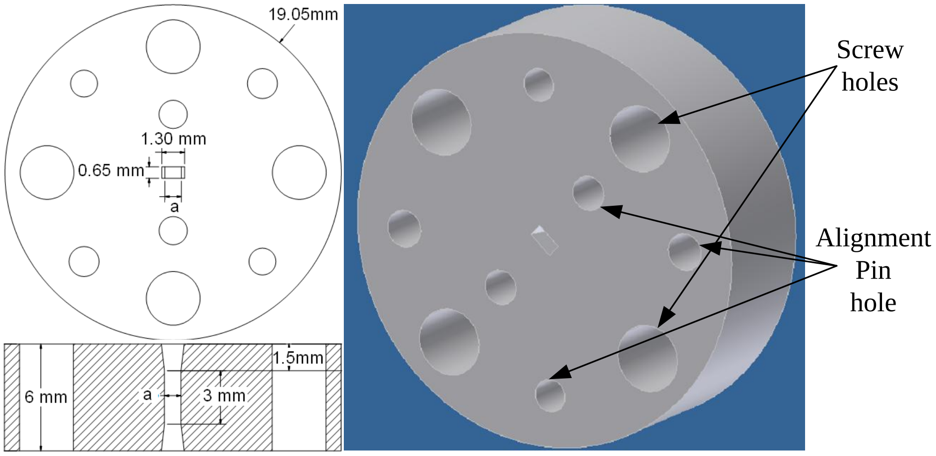

Figure 5-11 The design drawing of the cut-off filters

The dimensions and cut-off frequencies are listed in Figure 5-11. Some of the cut-off filters were measured using the VNA, the measured results and dimension a are listed in Table 5-1. The measured value is slightly larger than the designed value because of the rounded corners in manufacture.

Table 5-1 The waveguide dimension and it's cut-off frequency

a (mm)	Cut-off frequency (GHz)	Measured cut-off frequency
1.388	108	109
1.363	110	113
0.937	160	162
0.833	180	183
0.750	200	201.3
0.577	260	
0.500	300	
0.428	350	

The measurements were performed using the VNA machine by measuring the reflection signal S_{11}. Some of the measured results with a picture of the manufactured cut-off filters are shown in Figure 5-12.

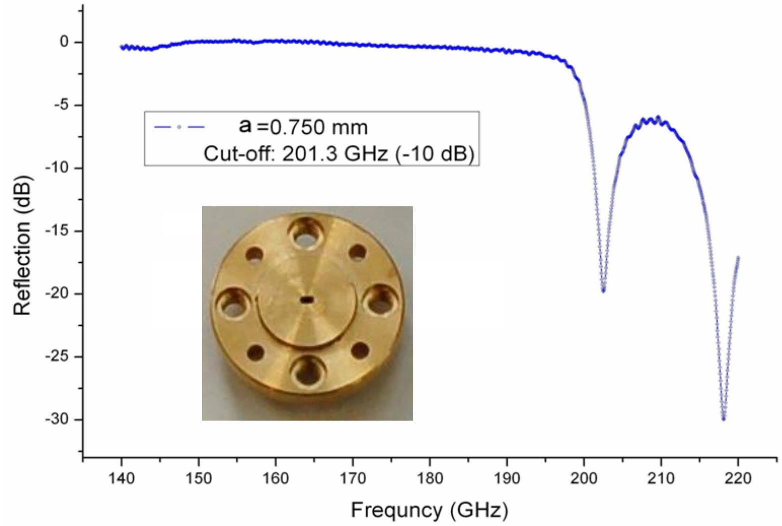

Figure 5-12 the reflection measurement result of one of the cut-off filters and its picture

5.5 Wave-meter Calibration

A wave-meter is another device that can be used to measure the microwave frequencies with very high accuracy. There are three basic kinds of wave-meters: 1/ the absorption, 2/ the reaction, and 3/ the transmission types. The absorption wave-meter is a simple device normally contains a piece of waveguide and a cylindrical cavity with a variable cavity length which are connected to the waveguide by a coupling hole or coupling holes at the E-plane. Most wave-meters are waveguides; however, coaxial types are possible.

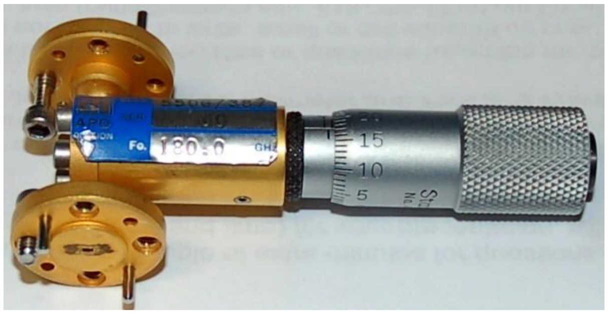

Figure 5-13 A picture of the wave-meter

Shown in Figure 5-13, is a picture of the wave-meter used in the experiment. The cylindrical cavity is a short circuit resonant cavity, which resonates at a half-wavelength. By turning the micrometre, the short circuit end will move and the cavity dimension changes, thus the resonance frequency changes.

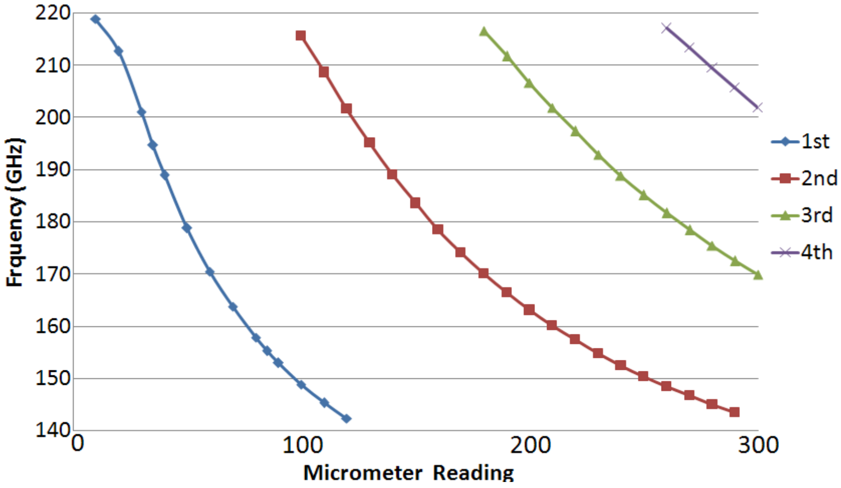

Figure 5-14 The Calibration results of the wave-meter

When the resonance frequency hits the microwave source frequency, there will be a sharp dip at the detector connected to the other end of the waveguide in the wave-meter. Thus the source frequency is measured. Due to the mechanism of operation of the wave-meter, the harmonics of this frequency will have the same affect. The wave-meter has been calibrated using the 140-220 GHz VNA high frequency heads. The results are shown in Figure 5-14.

5.6 Microwave detector and calibration

Rectifying crystal detectors of the point contact type were used to detect the millimetre wave radiation in the gyro-experiments. The detector consisted of a semi-conductor crystal in point contact with a fine metal wire. The sensitivity this type of detector is dependent on the power that incident upon the detector. As shown in Figure 5-15, the detector operated in the “square law” region when low power mm-waves were incident upon the crystal, where the detector's output voltage is proportional to the incident power measured in watts. As Ohm's Law states the voltage should be proportional to the square-root of power. Thus, this region is called the “square law” region. When the incident power increases, the detector’s response will move into the “linear region” where the detector’s output is proportional to the square root of the input power. Further increase of the incident power upon the detector will cause the detector’s response to shift into the saturation region and finally it will destroyed (“burn out”) if the incident power keeps increasing.

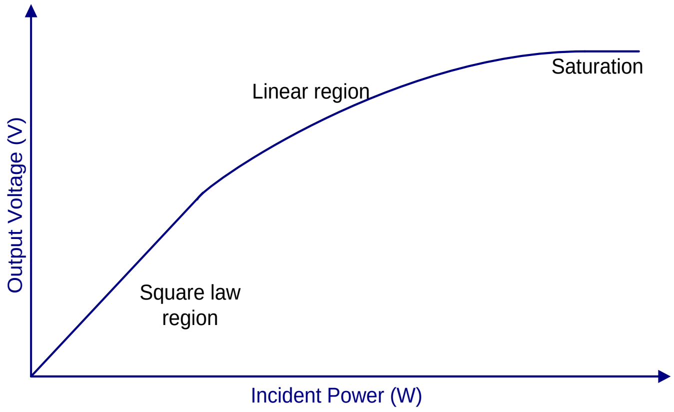

Figure 5-15 The characteristics of the point contact crystal detector

The point contact crystal detector used in the experiments has been calibrated. A schematic drawing of the calibration circuit is shown in Figure 5-16.

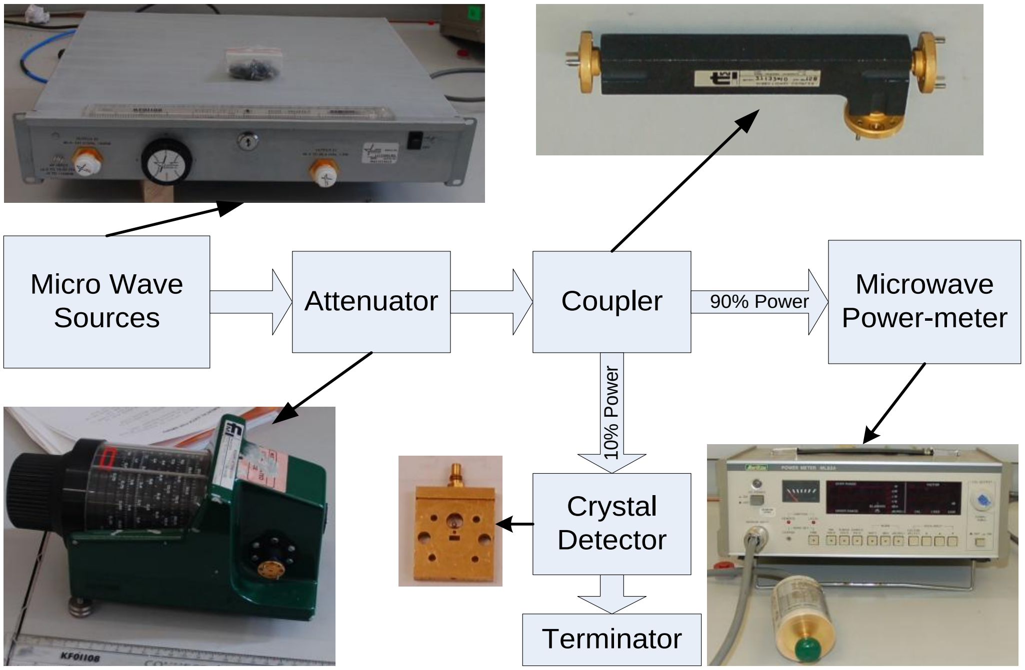

Figure 5-16 The circuit of the crystal detector calibration

The microwave source used in the calibration is a microwave frequency multiplier. When 6 to 10 dBm of power from a microwave sweeper at frequency of 15 GHz to 16.83 GHz range was input to the device, about 19 dBm power at a frequency of 90.0-101.0 GHz at output port 2 or 1.5 W of microwave output at frequency of 90.0-95.5 GHz at output port 2 is generated. An attenuator was used in the calibration. It’s a rotary attenuator with a dynamic range from 0 dBm to -70 dBm which was used to adjust the incident power. The microwave radiation after the attenuator was coupled through a directional coupler in two directions. One of the directions contains 90% of the incident power which was connected to an Anritsu microwave power meter ML83A, with a frequency range from 70GHz to 110 GHz. In the other direction which contains 10% of the incident power the point contact crystal detector was connected followed by a terminator load. The output voltage signal from the crystal detector was then monitored by a high sensitivity digital voltage meter. The calibration was taken at a frequency of 94 GHz. The calibration experimental results are shown in Figure 5-17. The curve at the top-left is the relation between the crystal detector reading and the power-meter reading. The curve at bottom right corner (the small figure at bottom right) is the calibrated response curve which indicates the output voltage reading of the rectifying point contact crystal detector against the incident power on the detector.

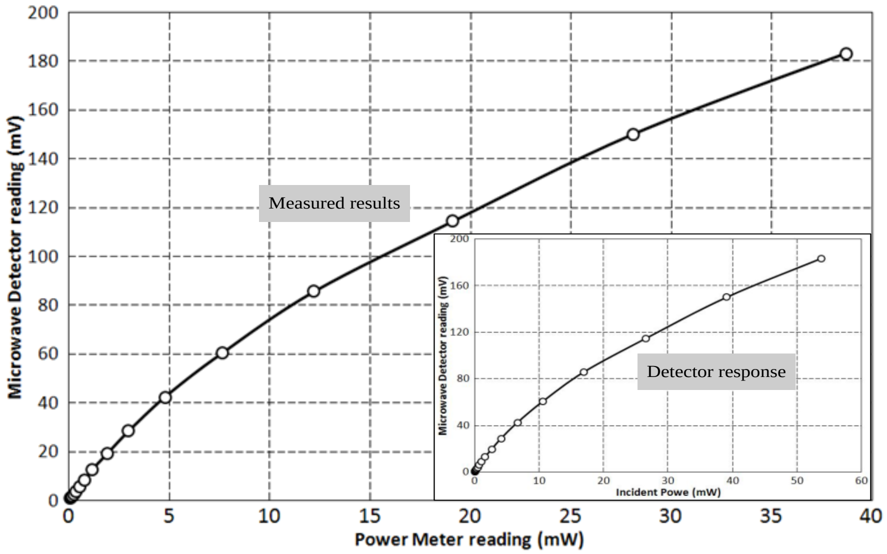

Figure 5-17 The calibration result of the point contact crystal detector at 94 GHz.

The rotary vane attenuator used both in the calibration of the detector and also in the gyro-experiments was calibrated. The other attenuator used in the gyro-experiment was in the form of a micro-meter pin attenuator in the range from 0 dB to -30 dB. Both attenuators are calibrated and the results were shown in Figure 5-18.

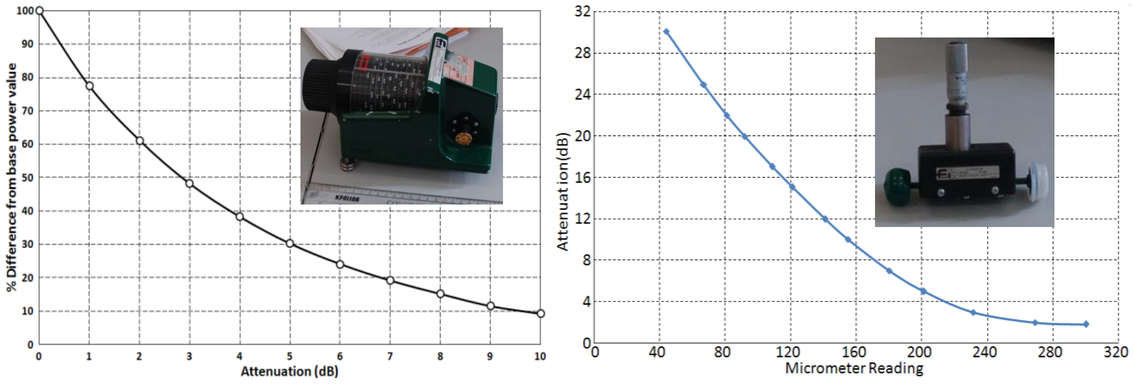

(a) (b)

Figure 5-18 The calibration results of the two attenuators: (a) the rotary attenuator used in crystal detector calibration; (b) the micrometer attenuator used in the gyro-experiment

5.7 **Gyrotron Window**

The process of the beam-wave interaction and production of millimetre wave radiation inside the gyrotron cavity requires a high vacuum. The millimetre wave radiation needed to be transported to the other devices or detectors, thus windows are necessary to seal the vacuum and let the millimetre wave signal pass through with low loss and reflection. It normally consists of one or more layers of dielectric. The window used in the gyro-experiments is a thin single sapphire window as shown in Figure 5-19. The window's dimensions are 15.44 mm in diameter and 1.6mm in thickness, mounted on a standard 34 mm copper gasket sealed vacuum flange.

Figure 5-19 The picture of the sapphire window

The transmission losses of the window have been measured using the W-band VNA heads operating in a frequency range from 75 GHz to 110 GHz. The results of this measurement are shown in Figure 5-20, which were taken using a time domain reflection measurement. The time domain measurement allows location and analyses the millimetre wave properties of the window alone to be considered. Two smooth lossless (or with very low losses) mediums are used at both ends of the window to help make the gate needed for the time domain measurement to be made, and the location of the window can be found using the time domain with the gate set just before and after the window. Operating the VNA in the time domain mode enabled the reflection S_{11} parameter of the reflection profile of the window alone to be measured. The graph shows there is one resonance located at a frequency of 78.3 GHz. There should be another one resonance close to 115 GHz but this cannot be seen due to the limitation in the VNA frequency range (75GHz to 110GHz)). This measurement allows the calculation of the dielectric constant of the window which was calculated to be 12.8. Theoretically there will be a lower reflection at its harmonics, such as the 2^{nd} harmonic at 156 GHz, the 3^{rd} harmonic at 235 GHz, the 5^{th} harmonic at 390 GHz which is the frequency of the Harmonic gyrotron i.e. (154, 195, 236 and 390) GHz. This simple window was therefore suitable for incorporation with the gyrotron experiment. A multi-layer broadband microwave window will be designed for future experiments.

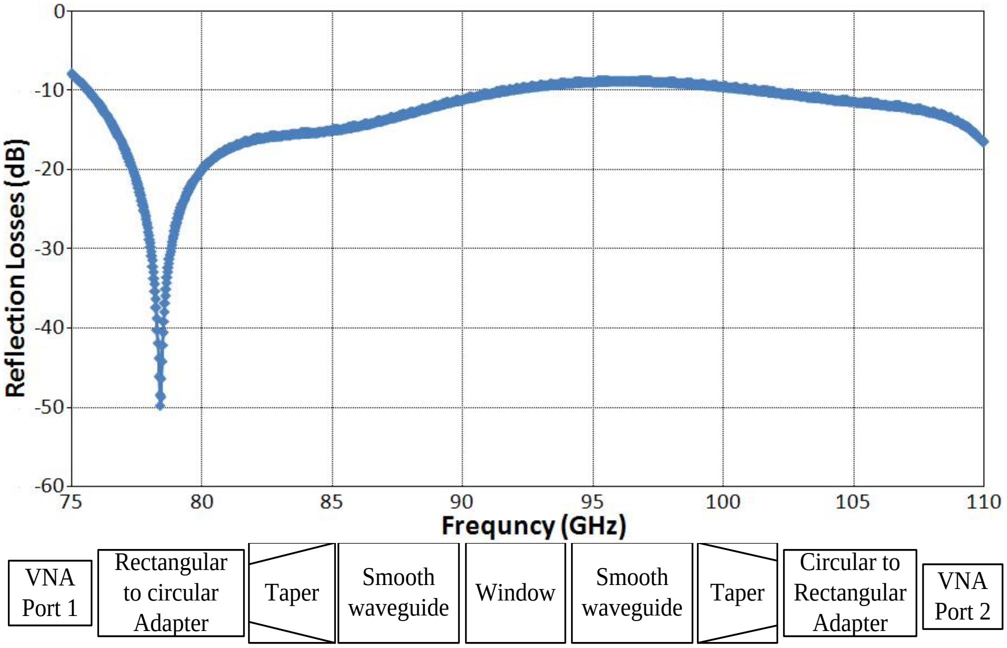

Figure 5-20 The measured S11 parameter of the sapphire window

Chapter 6

Experiment Setup

6.1 Introduction

The Gyrotron experiment will be described in detail in this chapter including the main components such as the high voltage power supply, the solenoids, the cooling and vacuum systems.

6.2 The Vacuum System

The Gyrotron is a vacuum device, so it is important to maintain a high vacuum in the beam-wave interaction region as well as in the electron gun region to prevent the barium aluminate tungsten thermionic cathode from being poisoned. A high vacuum of less than 1 x 10^{-7}mBar is essential when the barium aluminate thermionic cathode is at operating temperature. An ion pump working in conjunction with a turbo-molecular pump backed by a scroll pump was used to maintain the vacuum in the gyrotron experiment. In such a vacuum the electron beam was able to be propagated from the cathode through the cavity while minimising collisions which helps to maintain the beam quality.

The schematic drawing of the vacuum system in the experiment is shown in Figure 6-1.The vacuum system consisted of an ion pump, a turbo pump and a mechanical scroll pump, and two gauges to monitor the vacuum at both the high vacuum part and the lower vacuum part of the system. The high vacuum ion gauge was located close to the electron gun chamber as shown in Figure 6-3. A ceramic insulation pipe was used to electrically isolate the vacuum system from the electron gun which was operated at high voltage.

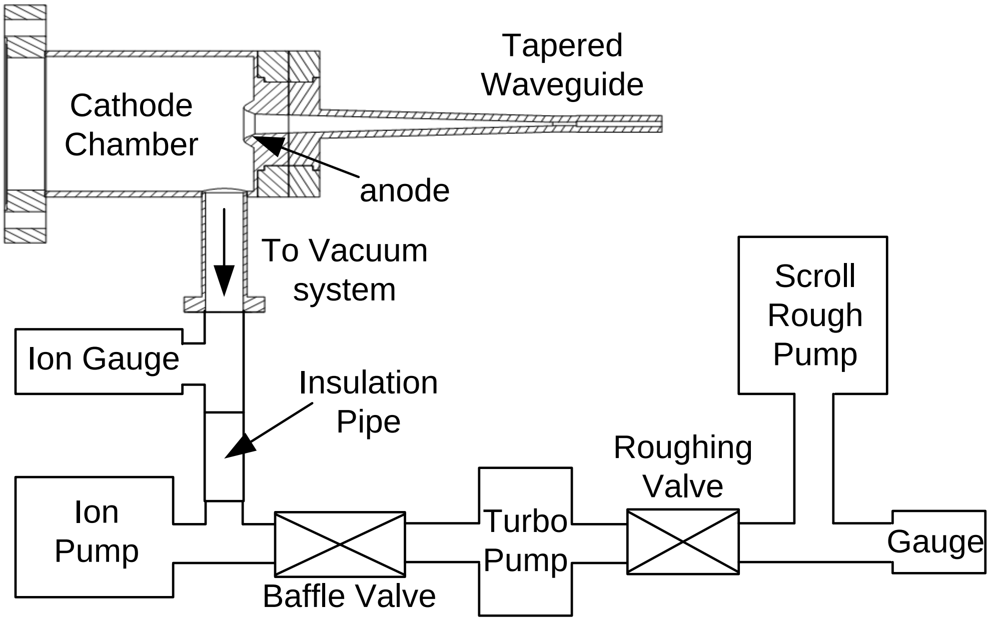

Figure 6-1 the schematic drawing of the setup of the vacuum system

The mechanical scroll pump which operates without the need for lubrication oil was used as the backing vacuum pump for the turbo-molecular pump as the turbo-molecular pump cannot be operated at atmospheric pressure. When in operation, this scroll pump can obtain a vacuum at the outlet of the turbo-molecular pump with a pressure of $\sim 1\times10^{-3}$ mBar, which allowed the turbo pump to be started. When the turbo-molecular pump is at full speed, the vacuum at the cathode chamber reached a pressure of 1×10^{-9} mBar when the thermionic cathode was not activated. As the cathode system needed to be kept at high vacuum, and the turbo-molecular pump could not be easily sealed if there was an unexpected power shutdown an ion pump was also used to maintain the high vacuum in the cathode chamber. One operating procedure adhered to was during the night when no one was around, the baffle valve was closed and only the ion pump was used to keep the high vacuum in the system. Thus the high vacuum environment was sealed even when the turbo-molecular pump and the scroll pump were unexpectedly shut down because of a power cut, as the ion pump was sealed to high vacuum even when it was not in operation. The whole system could still maintain a vacuum pressure in the range of 10^{-7} mBar vacuum when the power was off for a whole day.

6.3 The interlock system

In the lab bay, a lot of work was carried out to make sure the high voltage power supplies, high pressure water system, high current DC power supplies for the solenoids electron gun, etc., were interconnected via a safety interlock system. The interlock system in the lab was an engineering control used to ensure a safe working environment for the scientists working on the experiment. The interlock system earthed the gyrotron and shut down all the power supplies automatically when one single safety requirement was not satisfied. Each safety requirement needed to be satisfied before the power could be switched on and the earth system activated.

For the cooling water and pressure water system, detectors were used to monitor the pressure and flow rate of the water, and only when the cooling specification of the experiment was satisfied by the correct output voltage being registered by the detectors were the power supplies able to be activated. If the water flow rate dropped below a set critical level or temperature increase of the cooling water was too high then the voltage signal to the interlock system decreased resulting in the shutdown of the power supplies and earthing of the experiment. The lab bay in which the gyro-experiments were carried out was enclosed and surrounded by lead in the roof, walls, floor and a movable lead door. The door had a sensor which gave an initialising voltage signal to the interlock system when the door was securely closed.

All the power supplies were connected and interlocked to the safety system cooling and door entry switches. When all the safety check signals were satisfied, the earth of the lab could be lifted. The power supplies were then able to be activated by pressing the power supply on button on the interlock box for about 5 seconds, an audible and visual alarm was initiated in the form of an audible alarm 3 times and the lab HT alarm lighting which informed everyone in the laboratory that the gyrotron was in operation. An emergency stop button was located at the door, and at each power supply system and the interlock box, which when pressed shut down all power supplies and earthed the bay.

6.4 The diagnostic system

In chapter 2 the methods and mechanisms for measurement of the current, voltage and electron beam parameters were discussed. In this section the setup of our diagnostic system will be described in detail.

As the electron beam need to be accelerated to 40 kV, this voltage was too high to be directly measured, hence a voltage divider was required to measure the voltage signal. In the experiments, a resistive voltage divider was designed, built and used to measure the voltage signal that was used to accelerate the beam. The circuit diagram for the voltage divide can be seen in Figure 6-2.

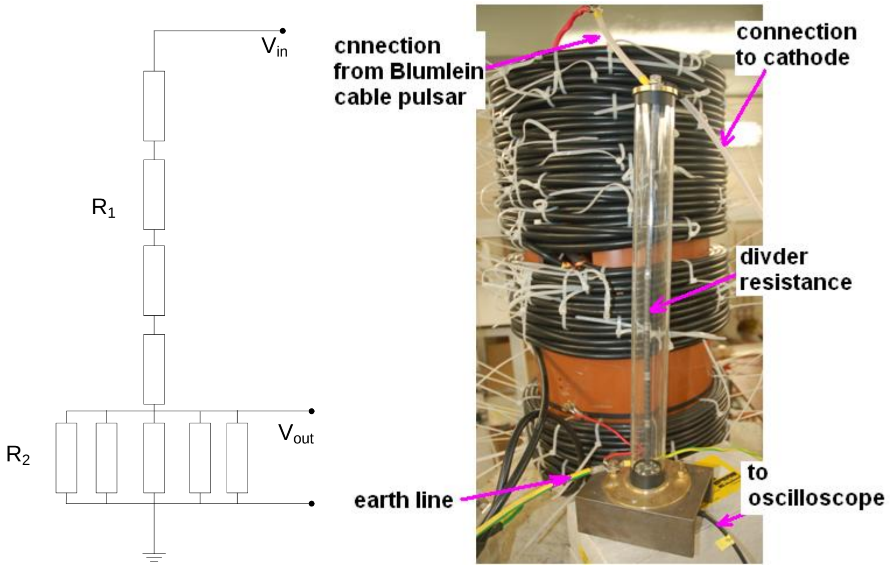

Figure 6-2 The schematic drawing of the electrical circuit of the voltage divider and a photograph of the voltage divider constructed used to measure the voltage generated by the cable pulser.

In the voltage divide, R_1 was made from 7 identical resistors connected in series with a total value of 2714 Ω, R2 was made from 4 resistors connected in parallel with a total value of 2.76 Ω. The division ratio of the voltage divider was $R_2/(R_1+R_2)=1039$, which means for a 40 kV signal, resulted in an output voltage of 38.5 V which could be measured by an oscilloscope with an attenuator.

A Rogowski coil was used to measure the electron gun diode current. The Rogowski coil was located on the earth line connect the cathode chamber which can be seen in Figure 6-3. As all the electrons emitted have to travel back through the earth line, so the diode current can be monitored at this position. The voltage signal from the Rogowski coil was connected to an oscilloscope housed in a shielded screened room through a BNC cable as shown in Figure 6-3.

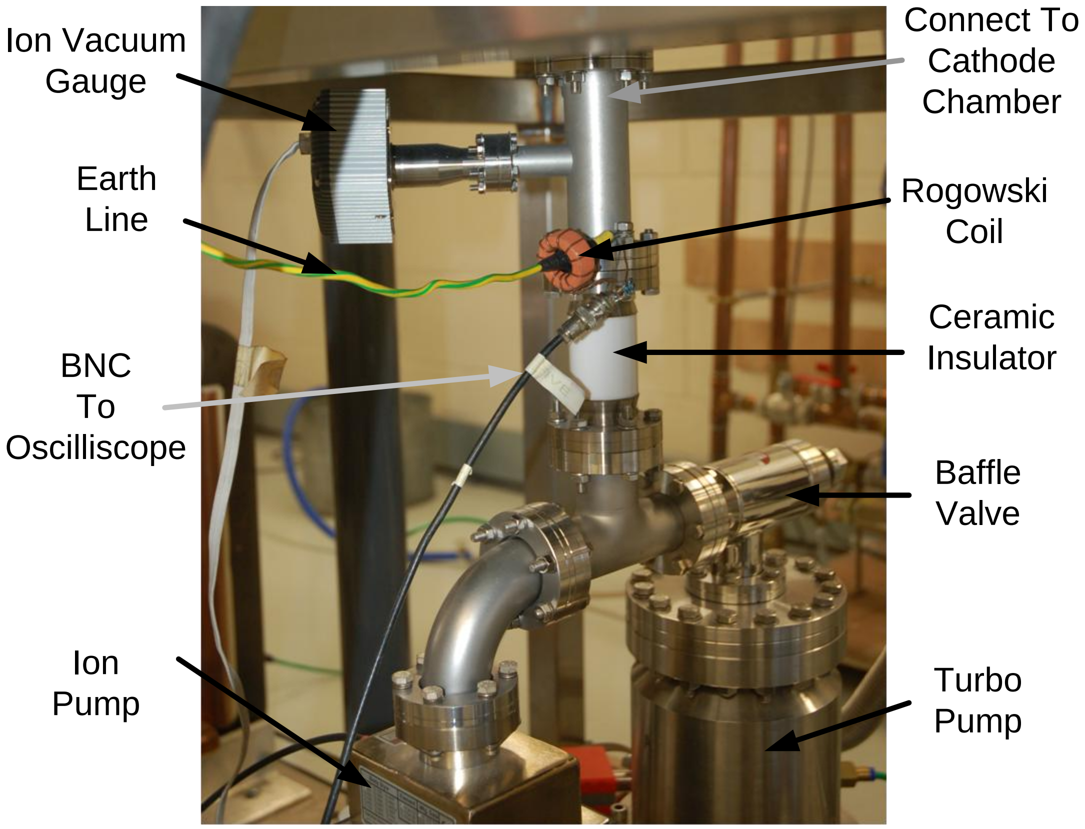

Figure 6-3 The Rogowski coil used to measure the diode current

A Faraday cup was used to measure the transported electron beam that passed through the narrowest diameter part of the cavity (the backstop reflector which is a cutoff reflect with diameter of 1.6 mm and it reflects the microwave radiation back to the cavity and output direction while avoid entering the cathode region) and hence the portion of the beam current that contributed to the gyrotron interaction could be measured. The Faraday cup used in the experiment is very simple which can be seen in Figure 6-4. It is a 4 mm rod with a cup shaped head. To ensure the cup was located along the axis of the beam tube, a ceramic support located at the end of the Faraday cup as shown in Figure 6-4 was used.

Figure 6-4 Picture of the Faraday cup used in the experiment

This faraday cup was isolated from the electron gun system via a ceramic tube which can also be seen figure 6.4. Two 100 ohm resistors were connected in parallel between the Faraday cup and the beam tube of the experiment. Thus after the electron beam hit the Faraday cup, the current passed through the sample resistances to the earth and a voltage signal was generated across the resistors. The BNC cable that connected to both ends of the resistors was used to transmit the voltage signal to the oscilloscope located in an electro-magnetic shielded screened room.

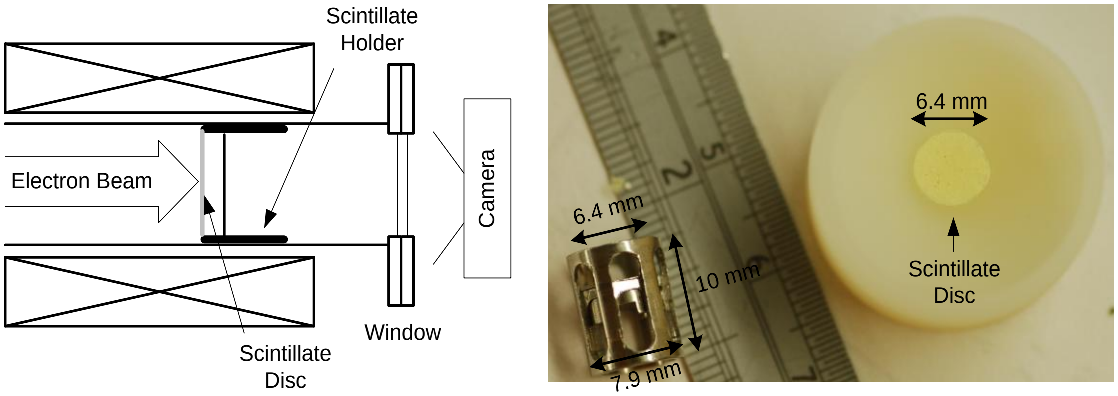

Figure 6-5 The schematic drawing of the scintillator diagnostic and the picture of the scintillator hold and the scintillate disk in the experiment

A scintillator was used to measure the beam profile in the experiments. A very thin layer of scintillate powder was coated on a transparent material. This scintillator was then put in the scintillator holder and placed into the beam tube with the scintillated surface positioned perpendicular to the electron beam as shown in the schematic drawing of the scintillator diagnostic Figure 6-5. The scintillator used in the experiment marked in the picture, has a diameter of 6.4 mm. The stainless structure in Figure 6-5 was used to hold the scintillator. The slot cuts on the scintillator holder are gas channels to enable gas on the inside of the beam tube to be pumped out of the vacuum system during the experiments. Another small annular tight fitting stainless piece located on the inside of the scintillator tube located behind the scintillator, was used to hold the scintillator in position and to assure it remained perpendicular to the direction of beam propagation is shown in the Autodesk drawing, Figure 6-6. The beam tube was sealed by an optically transparent glass window. A digital camera was used to take the pictures of scintillator when the electron beam impacted on the scintillator witness plate diagnostic. The Camera used in the experiments was a Nikon D50 with a Sigma 105 Micro lens.

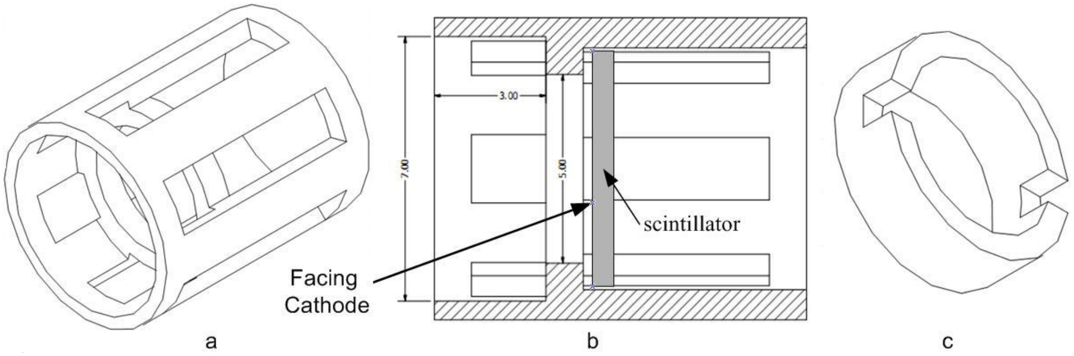

Figure 6-6 The Autodesk drawing of the scintillator holder; (a) the outside holder, (b) the cross section view of the scintillator with the position of the scintillator; (c) the annular shape piece to keep the scintillator in position

6.5 Cathode power supply system

The gyrotron was designed to be able to work under CW, but to reduce the water cooling requirement and to proof the design it was decided to test the experiment in pulse mode of operation. The power supply for accelerating the electron beam was a 40 kV pulse with a width of ~370 ns seconds produced by a stacked double Blumlein pulse generator. This pulse generator consists of two double Blumleins being connected in series. One double Blumlein was an inverting type and the other one is a non-inverting type. Both were made from high voltage co-axial cable by myself assisted by Mr. Liang Zhang and Dr. Wenlong of the University of Strathclyde.

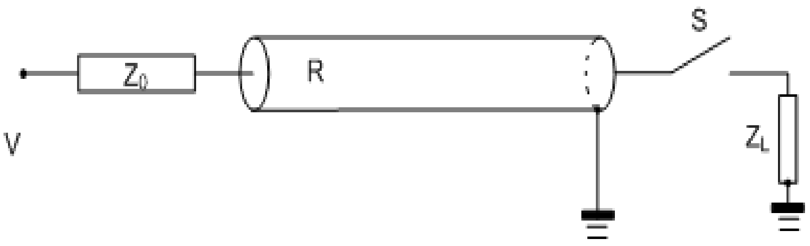

Figure 6-7 The schematic circuit of a pulse forming line

In order to understand the operation of a double cable Blumlein line, a basic understanding of the cable pulse forming line (PFL) is necessary. An effective circuit of the cable pulse forming line can be seen in Figure 6-7, which is a relatively simple concept. When the switch S is open, this system is charged by a DC voltage V through a charging resistance Z_0. Then when the switch is closed the charged cable will discharge with an output V_{out} to the load which has an impedance of Z_L. The output V_{out} of the pulse forming line can be given in equation(6.2), and the pulse length τ is a function of the cable length l_{cab}, and the speed of the wave travelling through the cable v_c.

$$\tau = 2\frac{l_{cab}}{v_c} \tag{6.1}$$

$$V_{out} = \frac{Z_L}{Z_L + Z_0}V \tag{6.2}$$

As we can see from equation (6.2) the output voltage cannot exceed the charging voltage, so in order to gain a large output voltage a Blumlein cable pulsar was used.

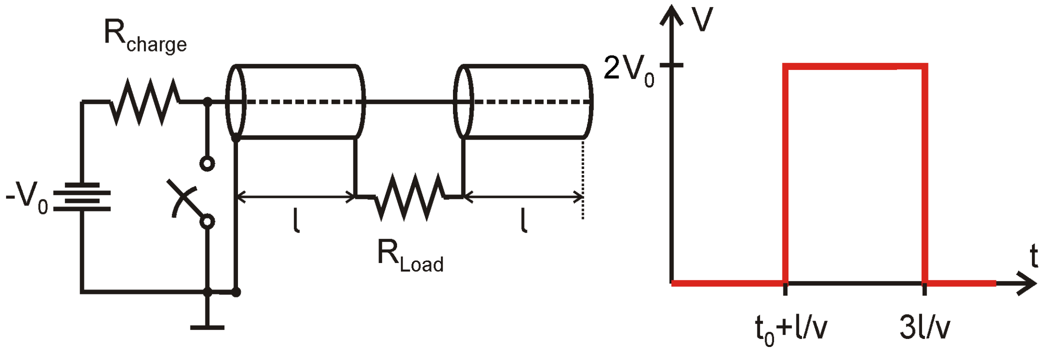

Figure 6-8 The Schematic of a single Blumlein cable pulsar and the pulse it produced

The circuit diagram of the Blumlein pulsar is given in Figure 6-8. The two cables are the same length so the pulse produced on the load can be added and the output voltage V_{out} is given in equation(6.3).

$$V_{out} = \frac{2VZ_L}{Z_1 + Z_2 + Z_L} \tag{6.3}$$

The output voltage can be doubled compared to the PFL, and it is possible to approach almost twice the output voltage compared to the input voltage if $Z_L >> Z_1 + Z_2$ which depends on the resistance of the output load. The impedance between the 2nd transmission lines and the earth will reduce the efficiency of the system and result in a modest reduction in the output voltage. When a third cable with twice the length of the Blumlein cable (Cable 3) were introduced to the single Blumlein setup, then a double cable Blumlein was built as shown in Figure 6-9.

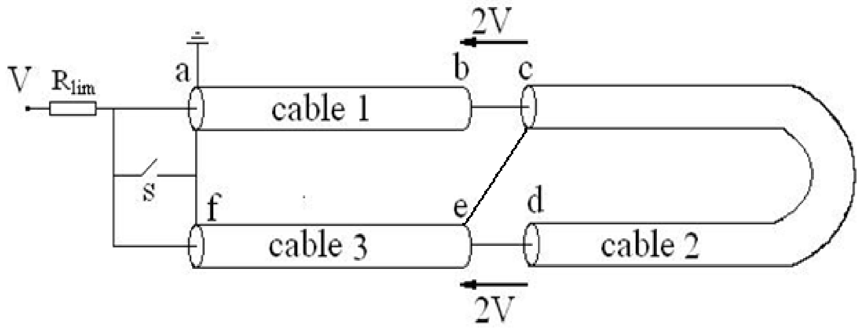

Figure 6-9 The schematic diagram of a double cable Blumlein

For a single Blumlein a voltage of 2V can be produced between points: b-c and e-d. When c and e are connected, a voltage pulse 4V can be obtained between points: b and d. Two types of output from the double Blumlein can be generated depending on the different earth points chosen: the inverted Blumlein which an earth at point b and an output at point d; the non-inverted Blumlein which an earth at point d and an output at b. the inverting and non-inverting Blumlein can generate a -4V and +4V pulses respectively.

An inverting double cable Blumlein was built in the experiments. The schematic diagram of the pulsed power unit is shown in Figure 6-10. A spark-gap switch was used to switch the double cable Blumlein pulsar. The spark-gap switch normally consisted of an arrangement of two conducting electrodes separated by a gap usually filled with gas such as air, N_2, Argon or SF_6. For triggered spark gap switches, there is normally a trigger electrode between the two separated electrodes as shown in Figure 6-11.

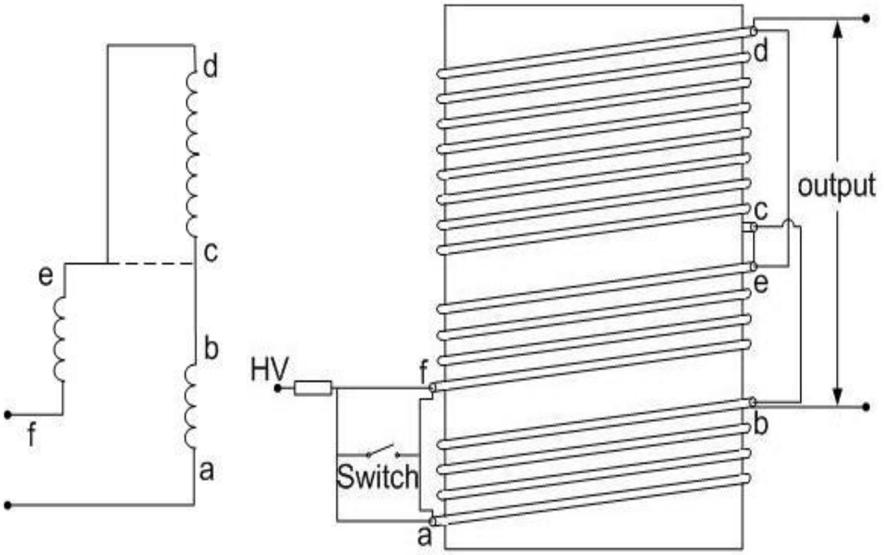

Figure 6-10 The schematic diagram of the double cable Blumlein in our experiments

The voltage V is applied on the two dome shaped electrodes, and the potential between the dome electrode and the mid trigger-plate was adjusted by changing the resister values of R_{b1} and R_{b2} or by the gap distance if there were no such voltage dividing resistance. It can also be operated in self-breakdown mode when there is no trigger pulse applied on the middle plate electrode. The basic mechanism of the spark gap switch is: the high voltage V is applied on the two dome-shaped electrodes, when a trigger pulse is applied to the trigger electrode in the middle, which will change the electrical field in the gap between the electrodes. For example if the trigger pulse is positive, the electrical field between the trigger plate and the earth dome will increase sharply and reaches to the break down voltage. Thus the gap is discharged and the electric field between the charging dome electrode and the trigger plate (now earth) will increase sharply as the whole voltage V is applied to these two electrodes and it will exceed the self-break down voltage, so it will break down, thus the switch will be conducting and close.

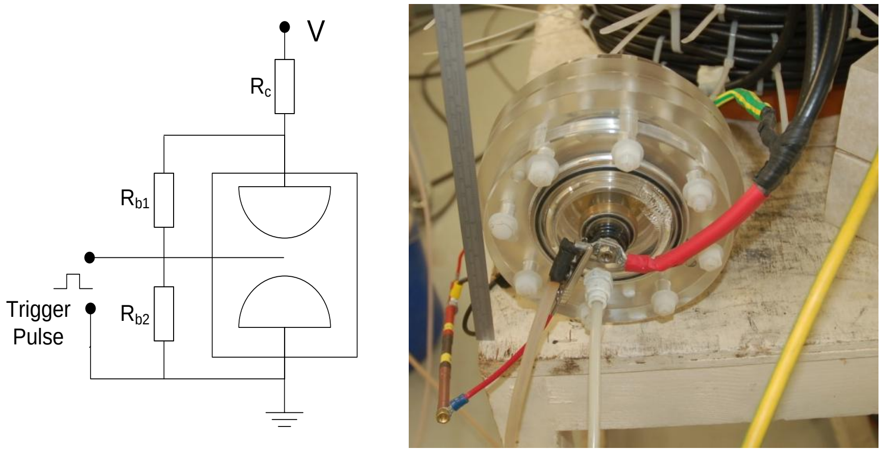

Figure 6-11 The electrical circuit diagram for a mid-plan triggered spark gap switch and the picture of the spark gap switch used in our experiments

The spark-gap switch used in the experiment is shown in Figure 6-11, the voltage dividing resistance values are R_{b1}=250 MΩ, and R_{b2}=200MΩ. This gap switch was operated without a trigger pulse in a self-break down mode. The gap of the three electrodes can be adjusted in order to obtain a stable breakdown voltage which also allowed the production of a suitable pulse used to drive the cusp electron gun.

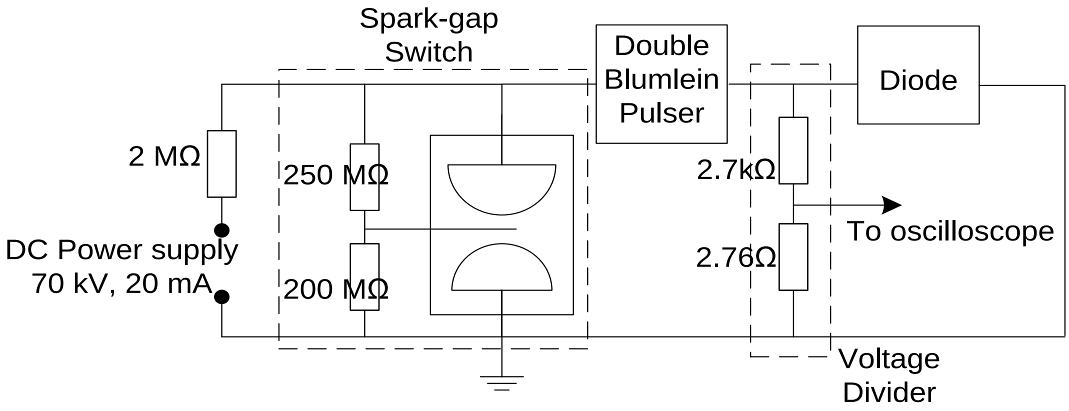

Figure 6-12 The schematic drawing of the power supply used for the cathode diode

The whole power system for accelerating the electron beam including its diagnostic systems can be seen in Figure 6-12. The power supply used to charge the double cable Blumlein pulsar was a 70 kV, 20 mA Glassman DC high voltage power supply. This was used to charge the double cable Blumlein pulsar through a 2 MΩ resistor.

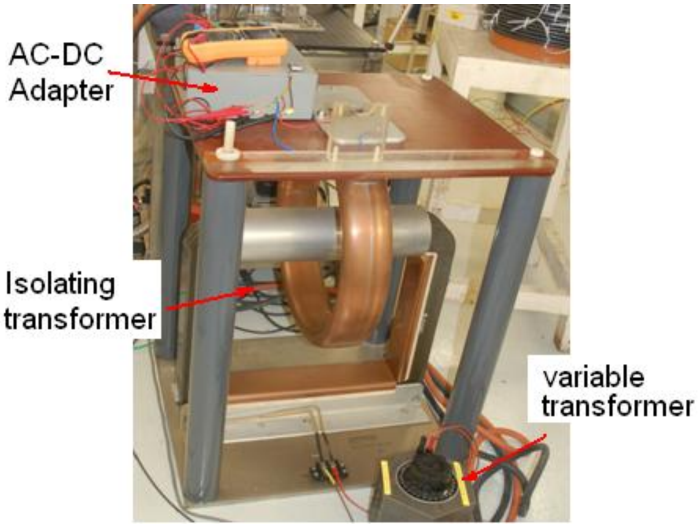

Figure 6-13 The power supply for heating the cathode

As the cathode used in our experiments was a thermionic cathode, a heating current was required to heat the cathode to its working temperature of around 1050℃. The resistance of the cathode heating coil was measured to be ~1 Ω with the heating current generated by a DC power supply as AC current would result in a changing of the magnetic field at the cusp point in the cusp gun. The cathode heater power supply was isolated from the double cable Blumlein pulsar by an isolating transformer with more than 40 kV isolation capabilities. The high voltage which drives the electron gun was therefore isolated from the heater coil preventing damage of the heater and cathode. A picture of the power supply system used for heating the cathode is shown in Figure 6-13. The variable transformer at bottom right was used to adjust the input voltage to the isolating transformer in the centre of the picture, which was used to adjust the heater power and temperature of the cathode. An AC-DC converter was used at the output of the isolating transformer before the current flowed through the heater coil. A voltage meter and current meter were used to monitor the voltage and current driving the heater coil.

6.6 Solenoid Design and Test

In our gyrotron experiment, the cusp electron gun and the two solenoids are very important to the success of our experiment. In order to achieve CW operation of our gyrotron, these solenoids needed to be operated DC and produce a uniform region of magnetic field that was long enough for the beam-wave interaction cavity, and the magnetic field needed to be as higher than our designed B-field requirement of 2.13 T.

Table 6-1 solenoid parameters

Maximum Magnetic Field	~2.16T
Layers	14 in centre and 16 at both end
Turns/Layer	103
Average Diameter	5.68 cm
Current required for Maximum B-field	~270 A

In order to optimise the design of the solenoids both the Matlab code and the 3D PIC code MAGIC were used. Due to the requirement of the magnetic field (both in amplitude and width), a model of the solenoid was built including number of turns, layers and the driving current. The power deposited in the solenoid and the result heat generated and also the requirement of cooling system were calculated. These calculated results were used to revise the model of the solenoids until the magnetic field amplitude required for the gyro-experiments, the size of the solenoid and cooling requirements were optimised for CW operation. The design results are show in Table 6-1.

The wire used in building the solenoid was 2.2 mm by 2.2 mm square copper wire which had varnish coating insulation on the surface. The main solenoid has 14 layers, and each layer have 103 turns. Two layers of extra copper were added at both ends of the solenoid to sharpen the magnetic field profile, and each extra layer had 15 turns of wire. The approximate length of the wire needed for this solenoid was 285m, calculated using the MATLAB code. The resistance of the solenoid was calculated using the equation:

$$R = \frac{L \cdot \rho}{A} \tag{6.4}$$

where ρ is electrical resistivity of the wire material in this case copper and A the cross-section area of the wire. The current requirement for the maximum magnetic field can be obtained through Amperes law:

$$I \approx \frac{B}{\mu_0 N} \tag{6.5}$$

Where N is the turn density of the solenoid, thus the power of the heat produced by the solenoid can be calculated using $P = I^2 R$. The calculated results are shown in Table 6-2.

Table 6-2 Magnetic field and heating power produced by the main solenoid

B-field (T)	1.65	1.82	2.16
Resistance (Ω)	0.99	0.99	0.99
Voltage (V)	209	226	267
Current (A)	211.4	228.84	270.1
Power (kW)	44.3	51.9	72.2

Though in MAGIC simulation, a solenoid with small average radius produces an electron beam with the highest quality by using a small cross-sectional area, but as the cross-sectional area decreases the resistance of the solenoid will increase and this will cause an increase of the heating power. The optimal wire size was found to be 2.2 mm varnished square wire when all factors were taken into consideration.

To achieve such a high magnetic field, a high current is required to flow through the copper windings of the solenoid which means there will be large amount of heat produced in the solenoids. Thus, an efficient cooling system is required for the solenoid especially when in DC operation. Two solenoids were used in the experiments to produce the cusp magnetic field, mounted in together in series but with an opposite direction of magnetic field in each solenoid. Strong forces therefore existed between these two solenoids during the experiments, thus a firm supporting jacket was required to hold and position the two solenoids without blocking the cooling water channel into the solenoids.

In order to cool down the enormous heat produced by the solenoid, a large amount of water was needed to flow through the solenoid removing the heat from each layer and single turn of the coil. A 0.4 mm gap was designed between each layer of the coils, and by using square wire; the water channel between the layers enabled a smooth flow of water to pass through the gap between each layer increasing the surface area of the contact of the wire with the cooling water. When the cooling water pressure was 3 Bar, simulation shows the temperature rise of the water was about 30°C at 2.16 T. The configuration of the coil is shown in Figure 6-14. The reverse coil was configured the same way although it was much shorter in overall length.

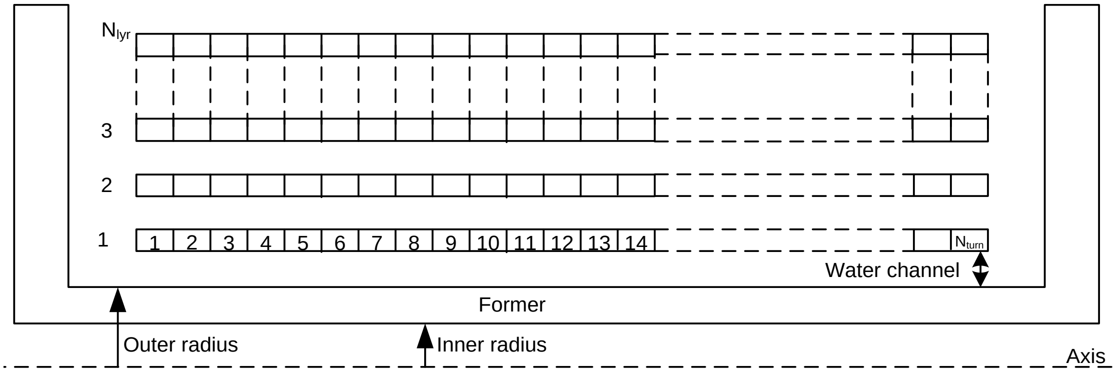

Figure 6-14 The configuration of the winding in both the cavity and reverse coils

The attracting forces were calculated using a simple model consisting of thin coaxial circular coils in air [154] as shown in Figure 6-15. Where R_I, R_{II} are the average radius of these two solenoid, a, b are the solenoids' length respectively. and c is the distance between the two coils from their centre point. The calculated force is about 800 N. Apart from this force; each turn inside the solenoid also experiences an electromagnetic force.

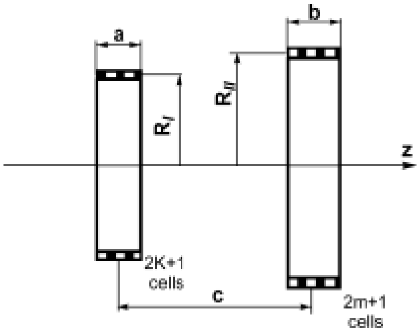

Figure 6-15 The configuration of two thin wall solenoids

To prevent the solenoid from deformation or shifting in position, the cavity solenoid former was machined from a solid piece of stainless steel so the deformation and weakening of welding could be avoided. Furthermore, strong structures are required at both ends of the solenoid to support the coils without blocking the water channel. The water channel gap supports are needed to hold and to prevent the coil from shrinking, and this support needs to have a minimal effect on the water channels and its ability to efficiently pass water. Thus, nylon wire with a diameter of 0.5 mm was used between each layer of the coils and also the channel between the coils and the former. These wires went straight through the solenoid from one end to the other end, and each end was tied to the supporting structure at both ends of the solenoid. .

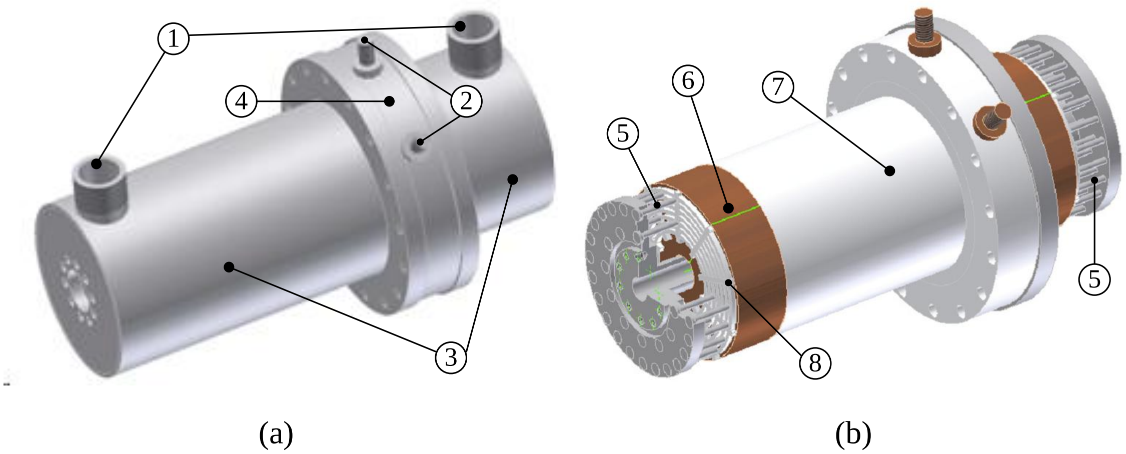

(a) (b)

Part list: (1) water pipe connection; (2) electrode; (3) Outer former; (4) Nylon insulate; (5) Clevis pins; (6) Coils; (7) Nylon Insulator; (8) Polycarbonate Mesh

Figure 6-16 The designed cavity solenoid (a) solenoid in former, (b) solenoid structure inside former with cut-view at left end

The distance between each wire is kept to be around 10 mm in order to keep a ~10 mm wide uniform cooling channel between the coil layers and also between the coil and the former. Thicker wires were deliberately chosen when winding the coils; for it is found that the nylon wires will be compressed by approximately 0.1 mm. Clevis pins were used to hold the horizontal position of the whole coil, and also to keep the input and output water channel for cooling the main solenoid. As the strong force produced by the coils may damage the varnish insulation layer, in order to keep the solenoid insulated from the metal clevis pins, two 4 mm thick polycarbonate meshes were used at both ends of the solenoid which had channels machined of the surface for passing water through the meshes. The design of the main solenoid in shown on the Autodesk Inventor drawing, Figure 6-16.

When finished winding the solenoid, the two ends of the wire were then connected to two copper electrical connectors (2) in Figure 6-16. These two electrodes sit inside a nylon insulator were used to connect the DC current power supply to the coils. Rubber O-rings were used between the electrode caps and the nylon to seal the water. The picture of the main solenoid during the winding process is shown in Figure 6-17. Nylon wires that were used to form the cooling channel can be seen in the picture.

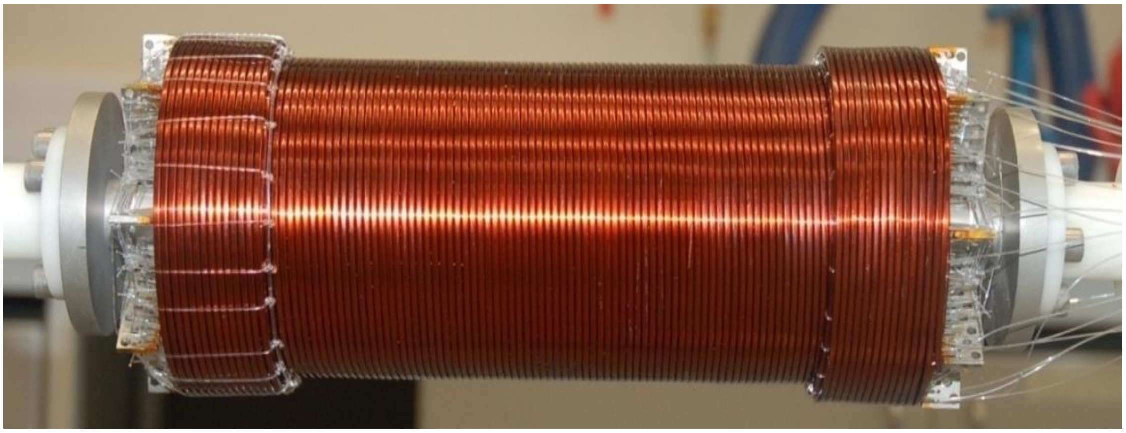

Figure 6-17 the main solenoid during winding process

The reverse coil used at the cathode side to produce the negative magnetic field required for the cusp electron gun was designed in the same way as the main coil. It contained 4 layers coils with 10 turns per layer. The maximum magnetic field produced was about 68 mT at a current of 200 A. Approximately ~2.8 kW of heater power will be produced at the maximum working point, which means its cooling requirement was much less compared to the main solenoid, and the cooling water pressure used was about 1.5 bar. The reverse coil parameters are shown in Table 6-3:

Table 6-3 The reverse coil parameters

Magnetic Field (mT)	50.8	61.8	68
Current (A)	170	181	200
Power (kW)	2.0	2.3	2.8

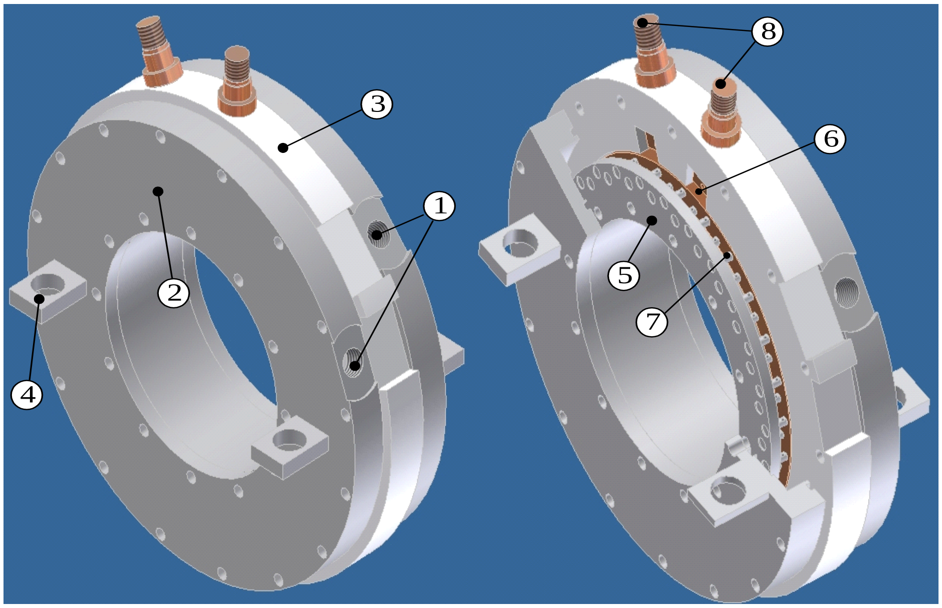

(a) (b)

Part list: (1) water pipe connection; (2) Outer former; (3) Nylon insulator; (4) connection to mounting system; (5) Inner former; (6) Coils; (7) Clevis pins; (8) Electrodes

Figure 6-18 The design of the reverse coil by Autodesk Inventor, (a) solenoid in former, (b) solenoid structure inside former with cut-view at left end

The same 2.2 mm square varnished wire was used to wind the solenoid; the average diameter of the reverse coil is about 16 cm. The water channel between the layers was supported in the same way as in the main coil by 0.5 mm thick nylon wire. These wires are tied to a drilled hole which was machined horizontally through the clevis pin. The resistance of the reverse coil was 0.7 Ω .

The design structure of the reverse coil in Autodesk Inventor was shown in Figure 6-18. Part 4 in the picture was used to connect with the 3 axis mounting system which allows the position of the reverse coil during experiments to be adjusted. Instead of polycarbonate meshes a plastic cap was put on the top of the clevis pins to insulate the coils from the pins.

The constructed main solenoid and reverse solenoid with water cooling connections can be seen in Figure 6-19. Both solenoids are located on their own 3-aixs adjustable mounting systems, so the position of these two solenoids can be adjusted and locked during the experiments.

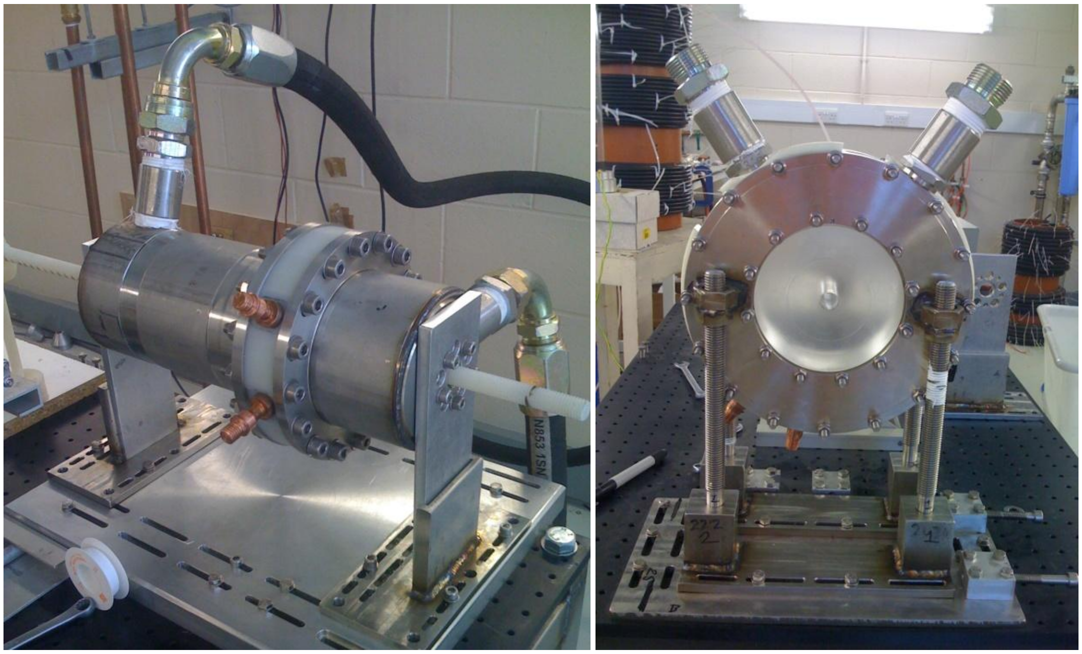

Figure 6-19 the constructed main solenoid (left) and reverse solenoid (right) mounted on a 3-axis adjustable mounting system

6.6.1 Cooling system of the two solenoid

As the main solenoid produces a large amount of heat during experiments, a sophisticated cooling system was required. As we mentioned previously, about 3.5 bars of water pressure was applied between the main solenoid water hose, and about 1.5 bars of water pressure was applied on the reverse coil. The water needed to pass through water filters before it passed through the solenoids, to avoid the possible debris in the water blocking the gap between the layers of the solenoid as the gap between each layer of coils of wire was only 0.4 mm. Two water filters were used in parallel to ensure the water flow rate through the filter system. The diameter of the water connections for the main solenoid was 2 inches, and 1 inch for the reverse coil to ensure enough water flow and no pressure losses due to the changing of pipe dimensions.

The water cooling system is shown in Figure 6-20. After passing through the filters, the cooling water was split into two so the reverse solenoid and main solenoid can be cooled separately. A ball value was used at the branch pipe that goes into the reverse coil to control the water flow into the reverse coil as the reverse coil requires much less water flow than the main solenoid. Two pressure gauges were installed at each branch of pipes before the cooling water goes into the solenoids, so the water pressure at the reverse coil and main solenoid can be monitored independently. Behind each of the pressure gauges there is a flow rate meter to measure the flow rate inside the water pipe, and ensure enough water fluid was passing through the two solenoids. Two temperature detectors were mounted at the output pipes of the two solenoids, separately, to monitor the temperature of the cooling water after passing through the solenoids.

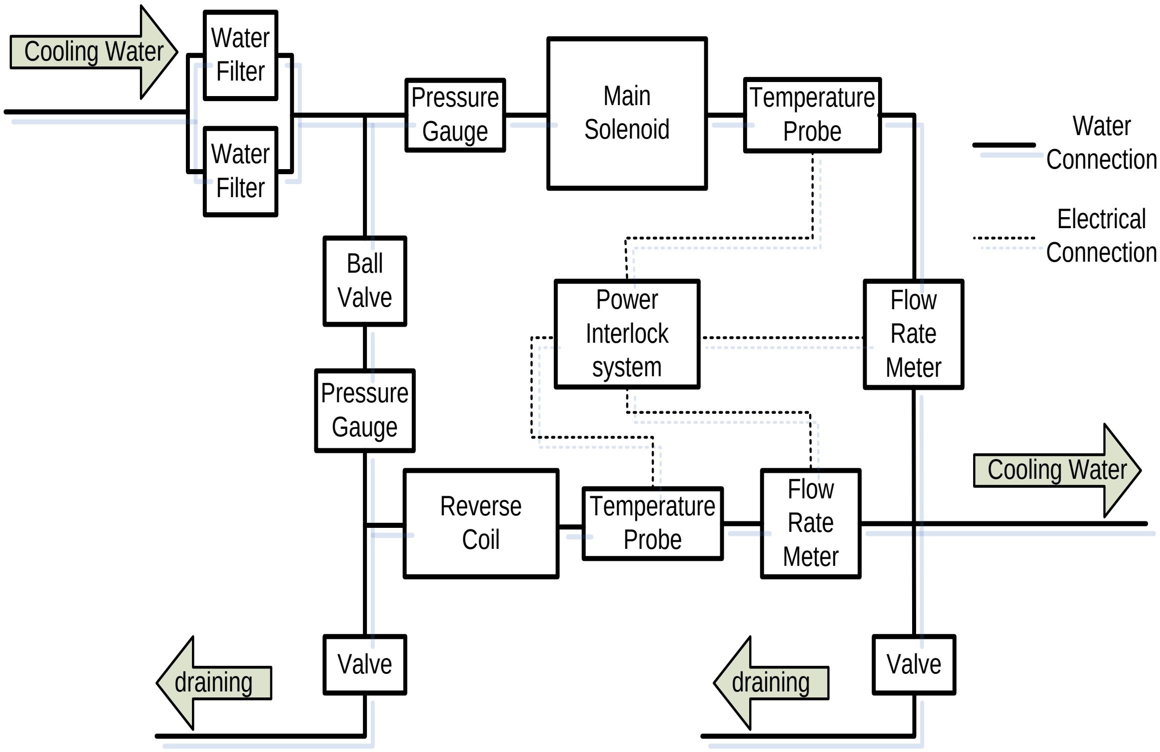

Figure 6-20 The schematic drawing of the water cooling system

Both the temperature probes and the water flow rate meters at the reverse coil water pipe and the main solenoid water pipe were connected to the power supply interlock system. So if the cooling water temperature goes higher than the threshold temperature or the water flow is lower than the given minimum value, the electrical power to the solenoids will be switched off to protect the solenoid from overheating and any further system damage. All interlocks needed to be initialised in the on state before the power supply system to the experimental bay could be turned on.

6.6.2 Power supply for the Solenoids

For the main solenoid it requires a maximum current of over 270 A, and as the resistance for the main solenoid coils are ~1Ω at room temperature, the power supply output voltage was more than 270 V at a current of over 270A. Each single NADA power supply in our lab had a maximum current and voltage rating of 300 A at 70 V. In order to produce enough power to drive the main cavity solenoid, 5 NADA power supplies were connected in series. Each single NADA power supply was also connected to the power interlock distribution board which automatically shut down the power supplies if any problem was encounter with the cooling system or engineering control interlocks for the experimental area. The schematic drawing of the power system and a picture of the power supply for the main solenoid are shown in Figure 6-21.

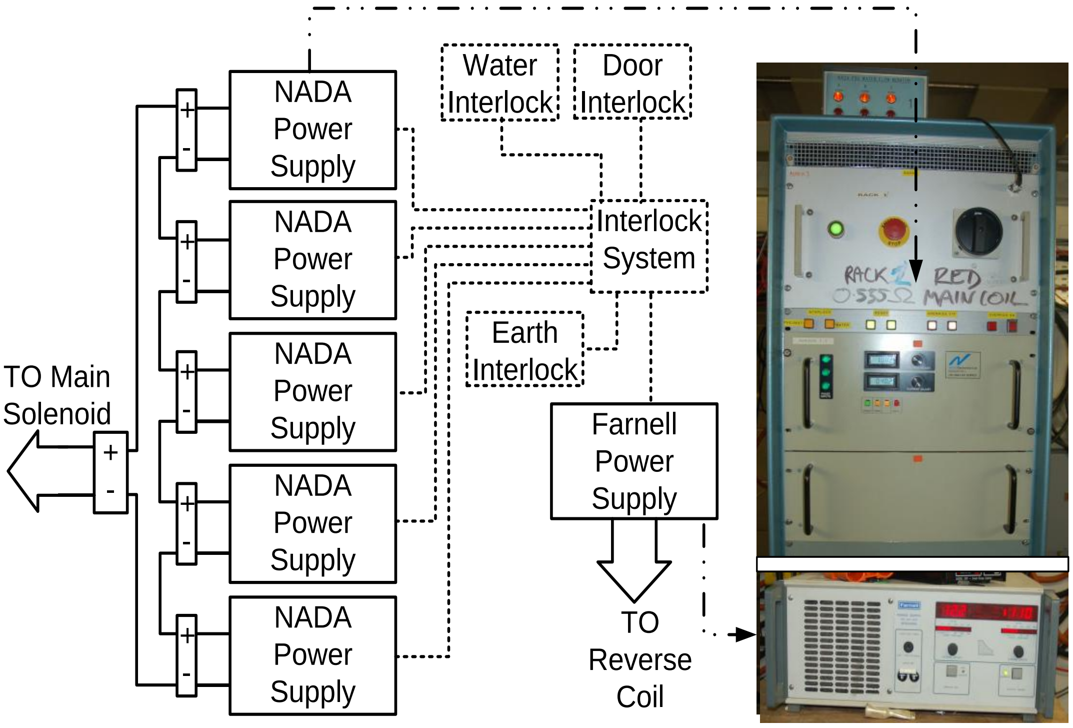

Figure 6-21 Power supply system for the two solenoids

The NADA power supply system are also cooled by water, both the cooling water system and the NADA power system are connected to the interlock which will shut down the power supply automatically if anything goes wrong with the system. The reverse coil was powered by a Farnell power supply which an output voltage of 30 V at a current of 200 A. The picture of the Farnell power supply is also shown in Figure 6-21.

6.6.3 Solenoids performance

The solenoids were tested and measured before being used in the CUSP gun beam formation and Gyro-experiments to verify how well the designed magnetic field profile of the solenoid matches measured magnetic field profile. A Gauss-meter with an axial Hall probe was used to measure the magnetic field.

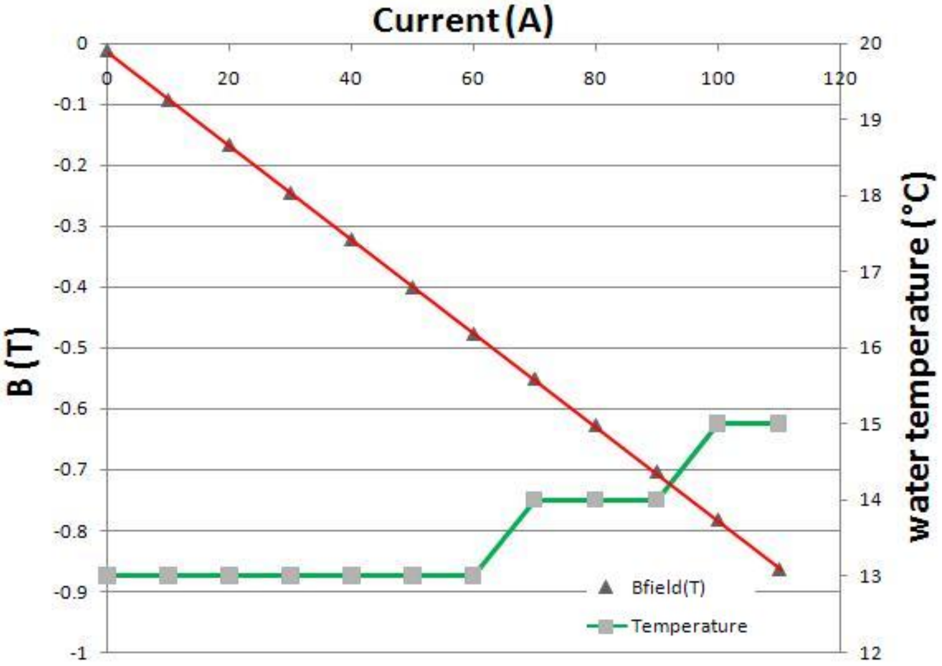

Figure 6-22 The relationship between the solenoid magnetic field, cooling water temperature and current of the main solenoid

Firstly, the Hall probe was put in the centre of the main solenoid along its axis (basically at the maximum magnetic field point), then the solenoid current was increased and the magnetic field increase measured as a function of the solenoid current. The cooling water temperature after it passed through the solenoid was monitored. The results of this measurement are shown in Figure 6-22. From the picture we can see the increase of the magnetic field with the increase of current is very linear in agreement with theory, and the temperature increase at 100 A was only 2 degrees. In further experiments, the current was increased to 250 A, and the temperature increase was about 10 degrees.

The probe was kept on the axis of the main solenoid and moved slowly to measure the magnetic field profile along the axis of the solenoids. The results are shown in Figure 6-23.

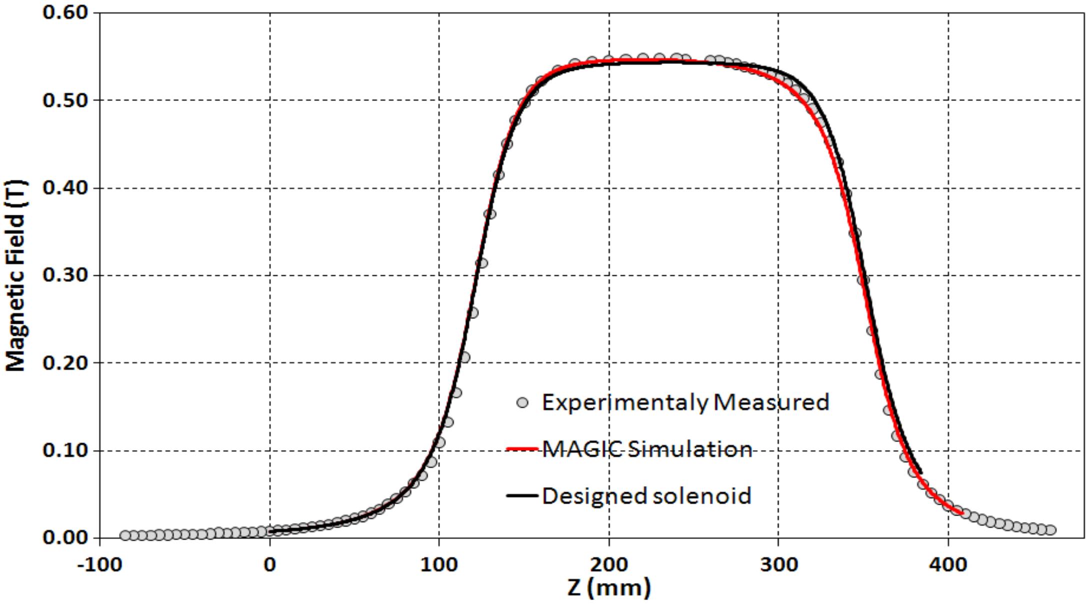

Figure 6-23 The magnetic field of the main solenoid along its axis

This measurement is taken at a driving current of 70 A and the maximum B-field was ~0.54 T. It was found that the measurement profile agreed very well on the left side (cusp gun side), but the measured results at the right side (output and windows side) was slightly lower and not so flat compared to the designed solenoid profile. After checking the solenoid again, it was found that the last extra layers of coils at the right end of the solenoid were wound in the wrong direction. Thus it almost cancelled the other extra layers contributions, and caused the magnetic field profile to be lower and drop of faster than the designed profile. Therefore, another simulation with the coils in the winding configuration used in the experiment was taken (shown as the red curve in Figure 6-23), and in this case it was found to be in good agreement with the measured profile. As in agree with the design principles the experimental cusp region on the left side of the profile was in good agreement with our designed profile, and the length of the flat-top region (+/- 1% of the maximum value) was ~10 cm and was of sufficient length to incorporate the whole gyrotron interaction region.

The magnetic field profile of the reverse coil was measured in the same way as the main solenoid, and is shown in Figure 6-24. This measurement is taken at a driving current of 100 A (black dot is the measured point). The green curve is the simulation results of the reverse coil at a driving current of 92 A. As can be seen in the figure 6.24, these two magnetic profiles are in very good agreement. The difference in the two currents from 100A to 92A is caused by the power supply system of the reverse which had an output current of about 8% less than the value displayed on the Farnell power supply readout.

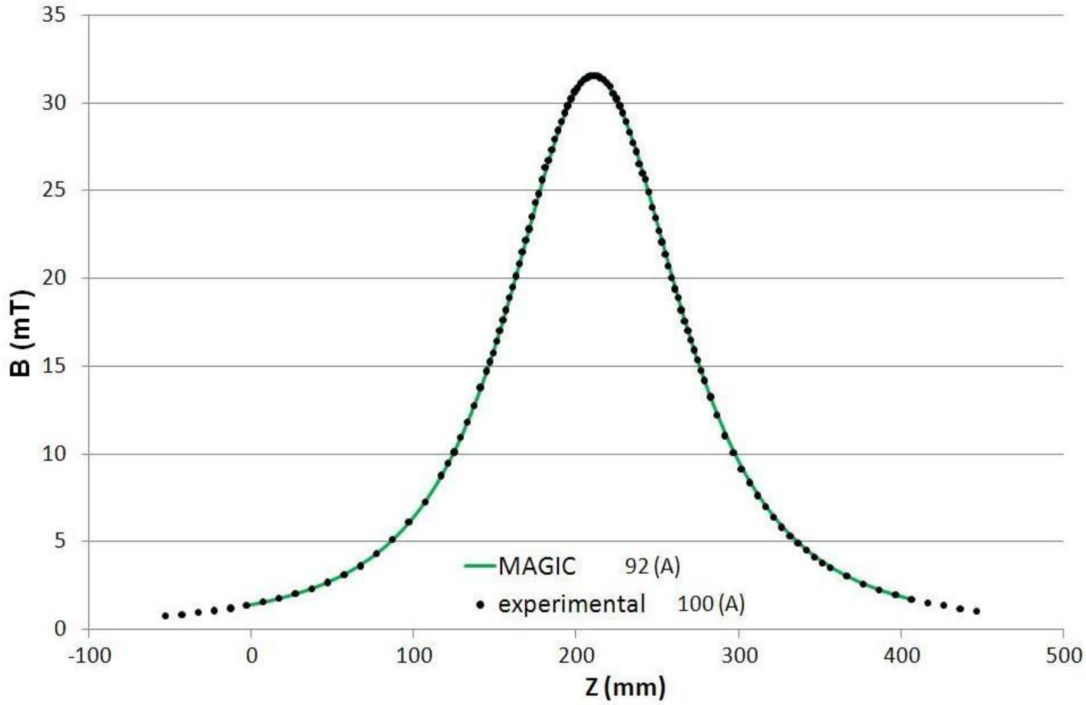

Figure 6-24 The measured magnetic field of the reverse coil with its simulated results

6.7 Experiment setup overview

A schematic drawing of the whole experimental setup is shown in Figure 6-27, and a picture of our electron beam and gyro experiments are shown in Figure 6-25 and Figure 6-26 respectively.

Figure 6-25 The picture of the gyro-experiment bay

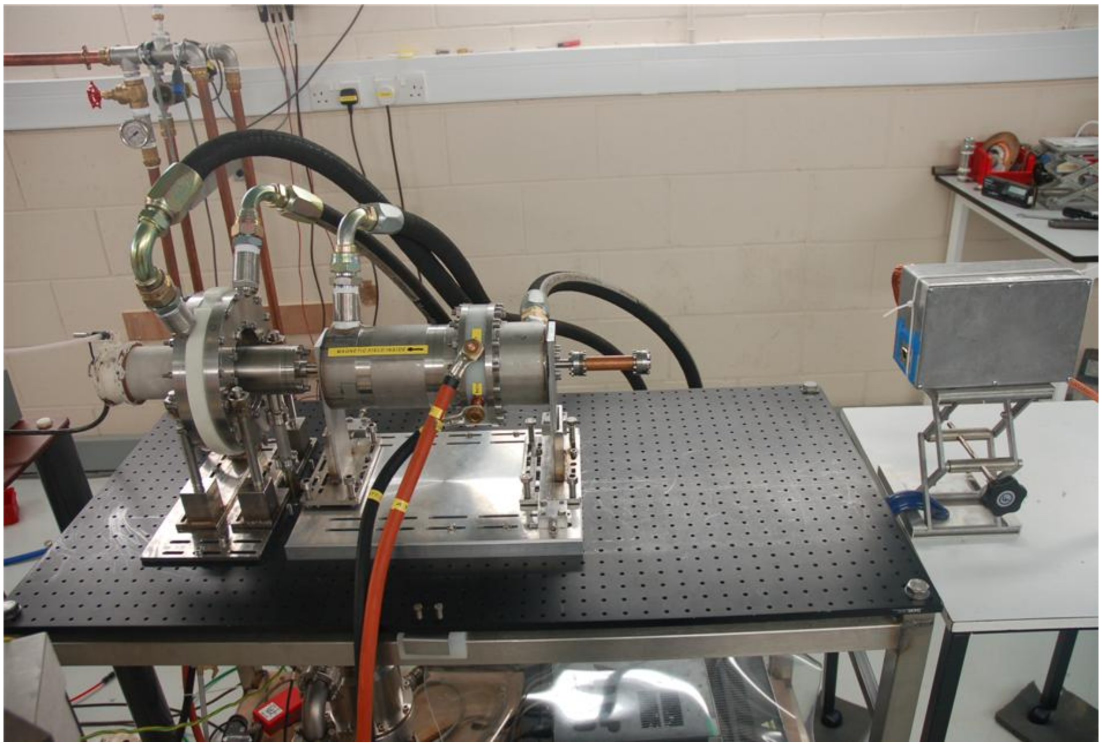

Figure 6-26 The setup of the Gyro-experiments

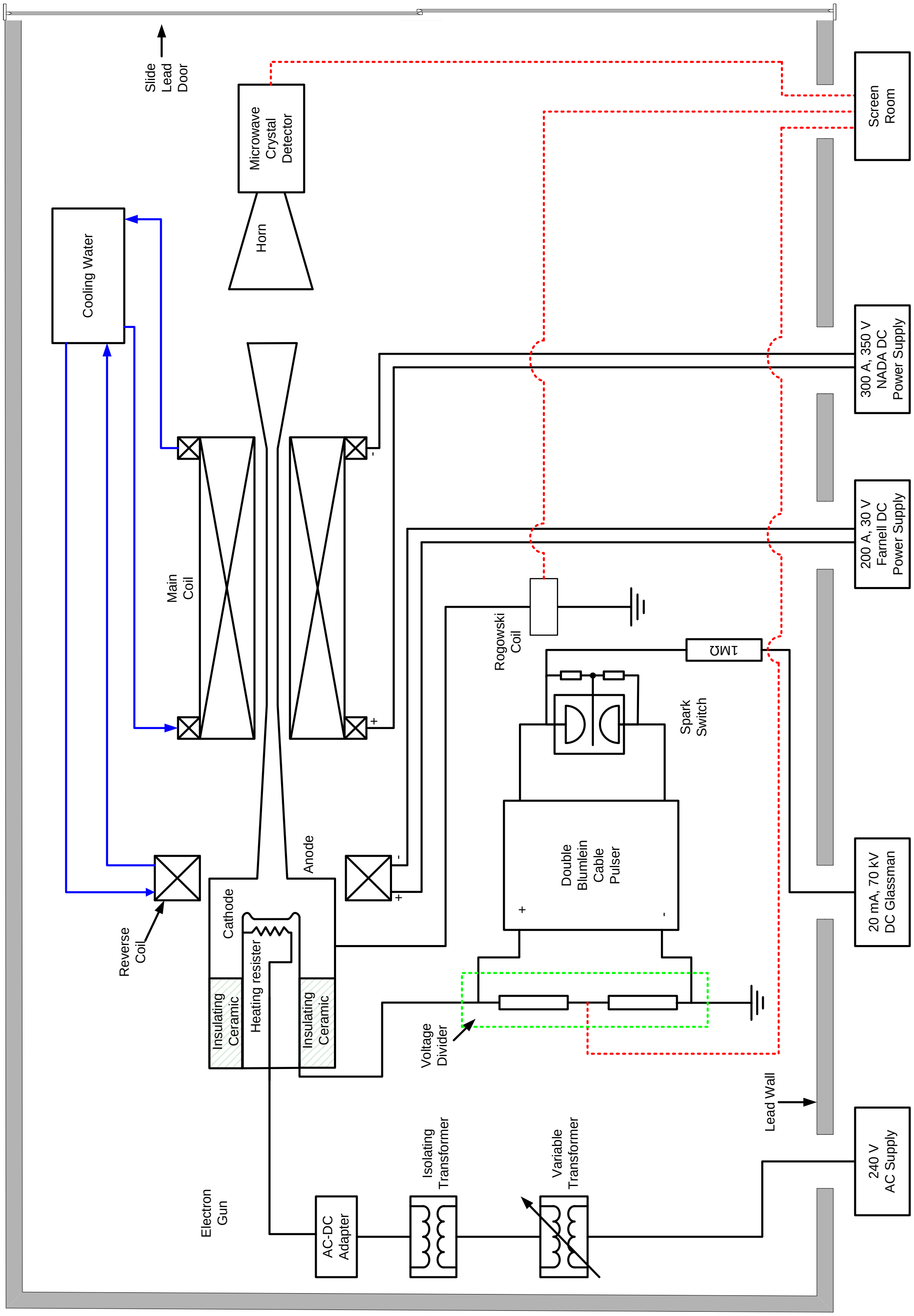

Figure 6-27 The Schematic drawing of the setup in the Gyro-experiment bay

Chapter 7

Experimental Results

7.1 Introduction

In this chapter, the experimental results will be presented, including all the cusp beam and gyrotron millimetre wave measurements. In the gyro-experiment, the electron beam and beam quality are very important. As the simulations show in chapter 3, the electron beam parameters would affect the interaction efficiency and mode competition. Such problems in the gyrotron operation are especially serious for the high harmonic gyrotron which requires relatively higher velocity ratio α in the beam for better mode selection and efficiency. Thus the electron beam experiment will be presented first in this chapter including the power supply diagnostic results. The harmonic gyrotron experimental results are also presented.

7.2 Beam Experiment Result

As mentioned in previous chapters, the electron beam used in the gyrotron simulation in chapter 3 is 40kV, 1.5A axis encircling electron beam. To accelerate the electron beam, a 40 kV power supply is required. This high voltage was provided by a double Blumlein pulser with a self-break down spark gap switch in the experiments. By adjusting the gap distance of the spark gap switch, the self-breakdown voltage of the switch was set to be ~12.8 kV. When this voltage was applied to the switch i.e. the double cable Blumlein pulser was charged to this voltage, the spark gap switch would breakdown, and a voltage pulse would be produced at the output of the pulser driving the cusp electron gun. The parameters of the voltage pulse are important to the beam parameters such as beam energy, velocity spread, and alpha spread. A voltage pulse with a slow rise time and varying voltage during the pulse width will cause the electron beam with varying energy and velocity.

The pulse voltage signal produced by the double Blumlein pulser when connected to the electron gun is shown in Figure 7-1. The rise time of the pulse is ~40ns; the average voltage applied to the cusp electron gun is ~40 kV and the pulse width is ~400ns. The fluctuation of the voltage amplitude in the flat-top region is ~5% from the average voltage. The voltage pulse is slightly higher than 40 kV when not connected to the cathode producing an average voltage of 44 kV. There was about 10% voltage amplitude drop when the double Blumlein pulser was connected to the cathode load, this is because the capacitive resistance of the electron gun system to which the pulser connected. This changing voltage will cause the change of the beam energy and shifting the resonant point, and also the shape of microwave radiation pulse, especially at high harmonic operation.

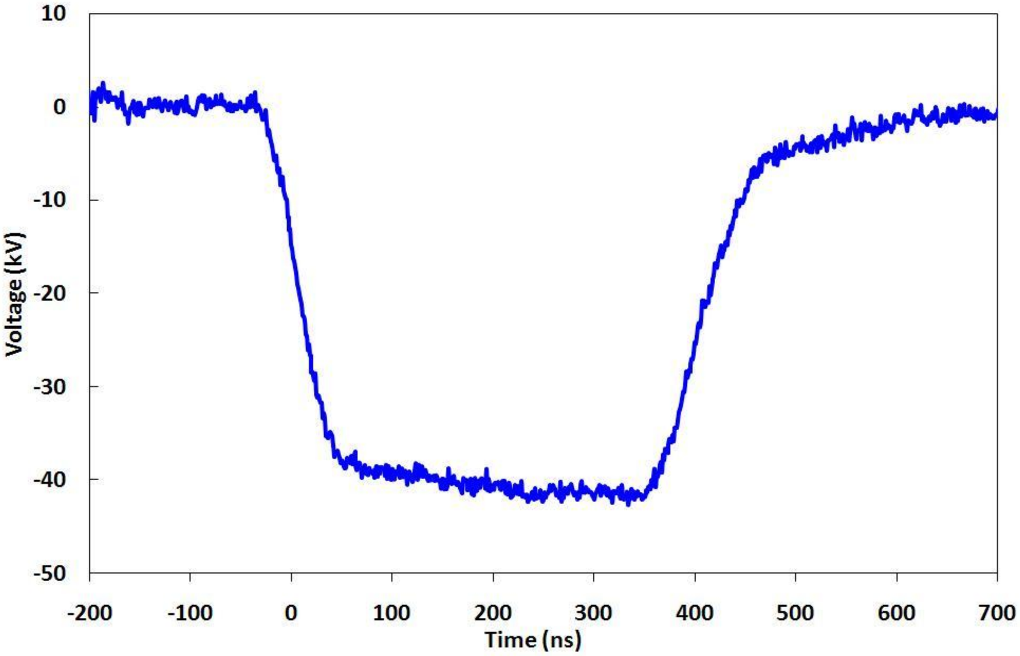

Figure 7-1 The voltage pulse produced to accelerate the electron beam by the cable pulser

The first series of experiments were to measure the beam current and cathode emitting current. The cathode emitting current was measured by a Rogowski coil located at the earth line of the electron gun chamber, as all the electrons emitted from the cathode surface will finally hit the beam tube wall or the Faraday cup and then go back to the earth line of the electron gun. The beam current was measured by a Faraday cup in the centre of the beam tube when the gyrotron cavity was removed.

The cathode emitting current was measured by firing several shots when the cathode was at room temperature (without applying heating power to the cathode), with several shots recorded as background signals from the Rogowski coil and Faraday cup. These background signals were very stable which enabled them to be used as a reference measurements of zero cathode emitting current. The heating power to the thermionic cathode was then applied to the cathode and when it reached operating temperature, the signals from the Rogowski coil and the Faraday cup were recorded again using a digital storage oscilloscope. The cathode emitting current and the beam current were measured by subtracting the background signal from the signal recorded when the cathode was a full operating temperature. The recorded Rogowski coil signals are shown in Figure 7-2.

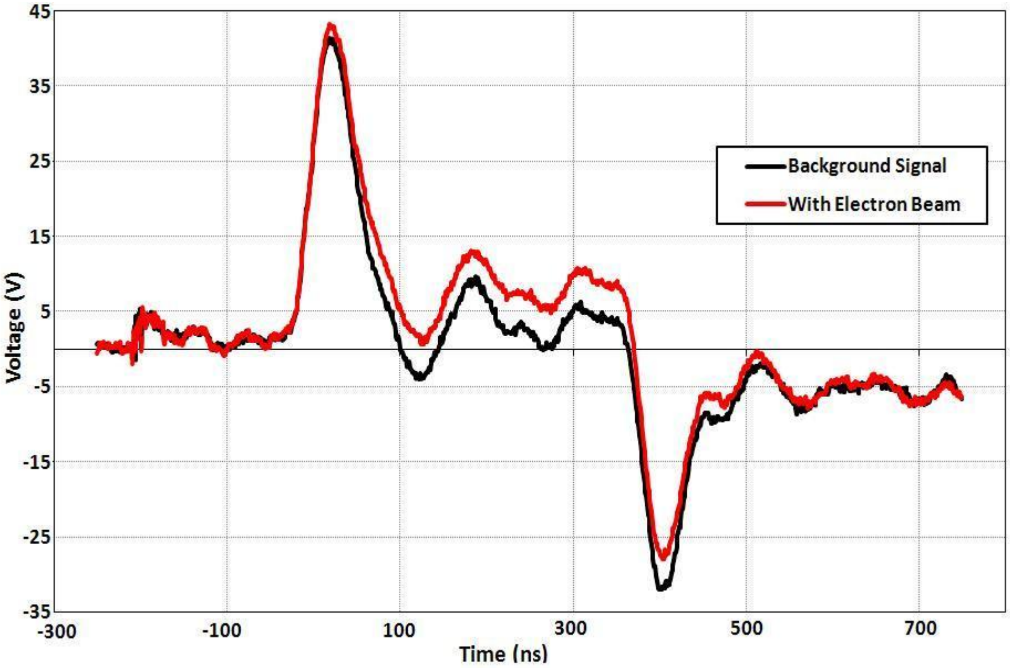

Figure 7-2 The recorded Rogowski coil signals in the experiments.

The black curve in the picture is the background signal, and the red curve is the Rogowski coil signals when cathode is at operating temperature. The two big pulses at start and end of the signals (~0 ns and ~400 ns) were displacement current signals at the rise and fall time of the driving voltage pulse. The cause of the displacement current is that the electron gun diode acts as a capacitive load with capacitance C_d. When the voltage pulse is applied to the diode the builds up of voltage between the cathode and anode results in a large amount of displacement current which is needed to charge this capacitor. For the same reason, there will be a large amount of displacement current required to discharge the capacitive diode when the pulse falls. The amplitude of the displacement current is proportional to the capacitance of the diode and the ratio of the charging voltage pulse.

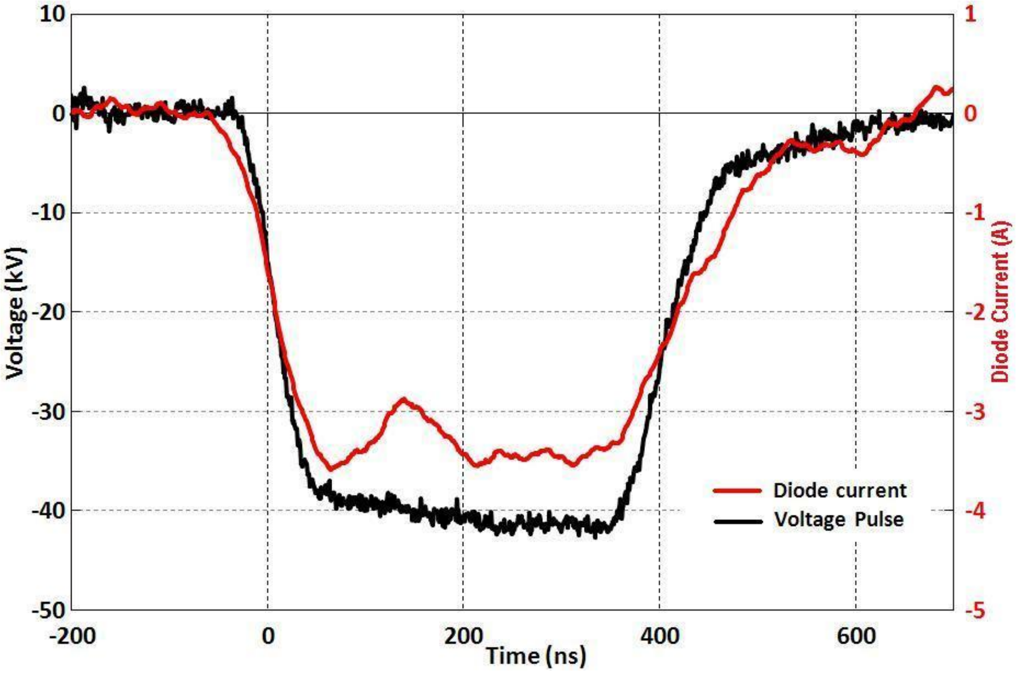

Figure 7-3 The diode current pulse with the beam voltage pulse

The displacement current does not correspond to the real cathode emitting current which can be measured by subtracting the background signal produced by the Rogowski coil from the signal when the electron beam is present. The cathode emitting current signal with respect to the driven voltage pulse is shown in Figure 7-3. The red curve is the diode current signal (the subtraction of the two Rogowski signals with average background signal) and the black curve is the voltage pulse. These two signals are in very well correlated in time.

By changing the heating power of the cathode, the change of the cathode emitting current with the heating power can be found as shown in Figure 7-4 . It can be seen from this picture that the emitted current is linear to the heating power, which means the cathode is operated in the temperature limited regime.

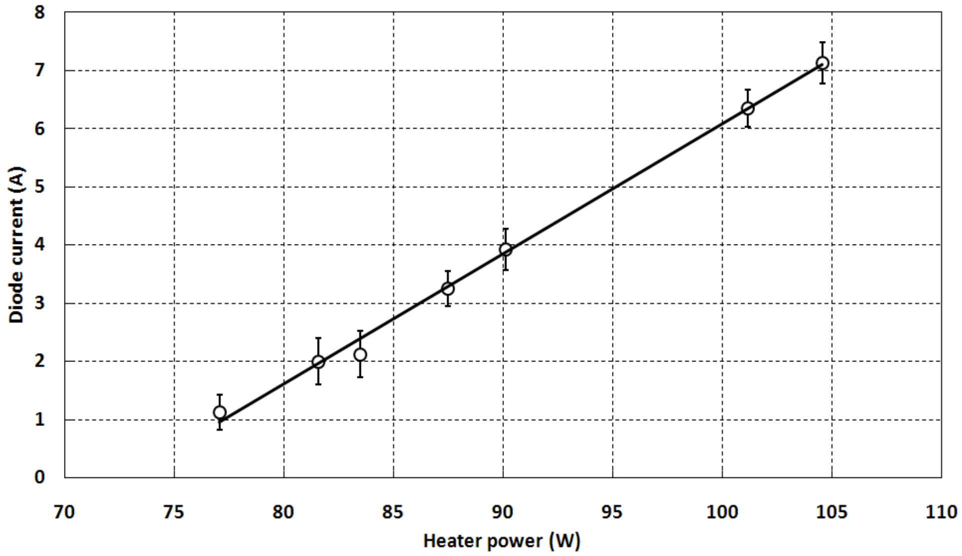

Figure 7-4 The cathode emitting current changes with the cathode heating power

The transported electron beam current that passes from the diode through to the interaction region was measured by the Faraday cup. The transported electron beam is the beam that contributes to the gyrotron interaction. The Faraday cup was positioned at end of the flat magnetic field (within 5%) region near the output. The transported beam current was not only dependent on the cathode emitting current, but also dependent on the magnetic field of the electron gun. When there was no cathode heating current no cathode emitting current was measured and hence no beam current was transported to the gyrotron interaction region. If the cathode emitting current is unchanged, the transported beam current was found to be sensitive to the change of the magnetic fields of the two solenoids. Normally, the main coil magnetic field was kept constant and the transported beam current will increase with the decrease of the reverse solenoid magnetic field until the loss of the cups. Namely, the transported electron beam current increases with the decrease of velocity ratio α at the same main magnetic field.

When magnetic fields of the two solenoids were set to the same as the simulated value i.e. within the designed velocity ratio α range, the transported electron beam current increased with the cathode emitting current. But the change was very slow when the cathode emitting current exceeded 2 A with the transported current of 1.4 A. The beam current was still limited below 1.6 A when the cathode emitting current exceeded

8 A. A typical transported electron beam current pulse is shown in Figure 7-5. The electron beam current was~1.5 A with less than 4% variation at the flat region and same width as the voltage pulse. The maximum beam transport ratio recorded was 96% at a cathode emitting current of ~1.8 A.

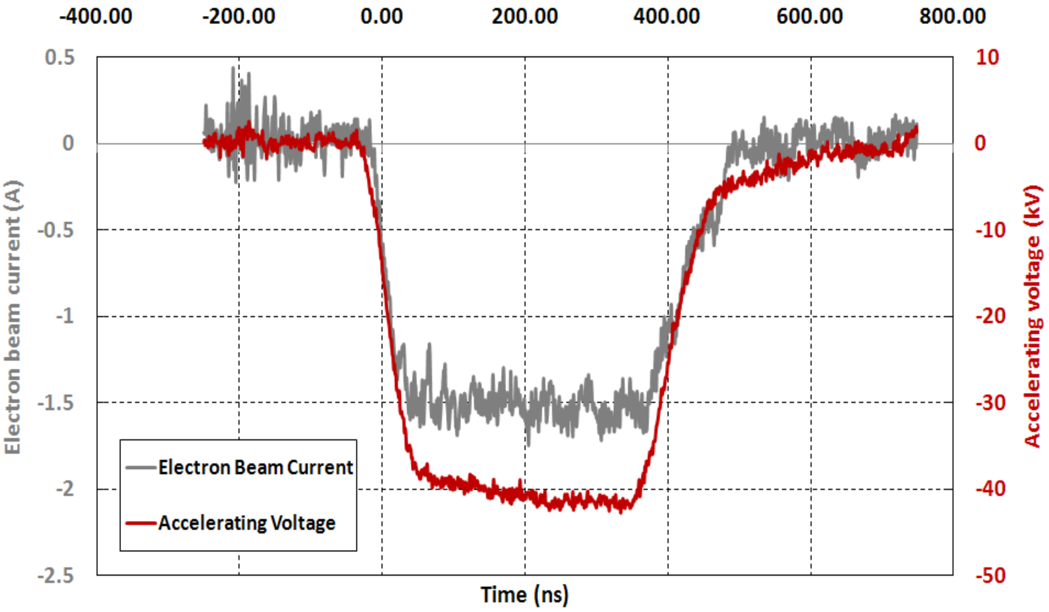

Figure 7-5 The transported electron beam current and the driven voltage pulse

The electron beam profile was recorded using a scintillator mounted perpendicular to the electron beam inside the beam tube. The scintillator was placed at position Z_2 as shown in Figure 7-6. It was about 11.5 mm inside the beam tube from the outside edge of the window’s flange and located at the falling edge of the magnetic field (~90% of the maximum magnetic field).The axial position of the scintillator of 11.5 mm was chosen as it was the minimum distance required for the micro-lens used in camera to take the pictures of the light emission from the scintillator.

From the profile of the electron beam, information can be obtained very directly such as whether the beam is an axis-encircling beam or a solid beam, beam radius and position, etc. The setup of the scintillator has been discussed in detail in Chapter 6. As the diameter of the electron beam is less than 1 mm from the simulated results a micro-lens was used to take the picture with a Nikon D50 digital camera. The micro lens camera takes a 1:1 imagine of the object in the photo. As the electron beam is pulsed, in order to record the image, the camera was set in bulb mode while taking the picture of the scintillator. Namely, the shutter of the camera is kept open during the experiment. The shutter switch was opened and closed using a remote controller.

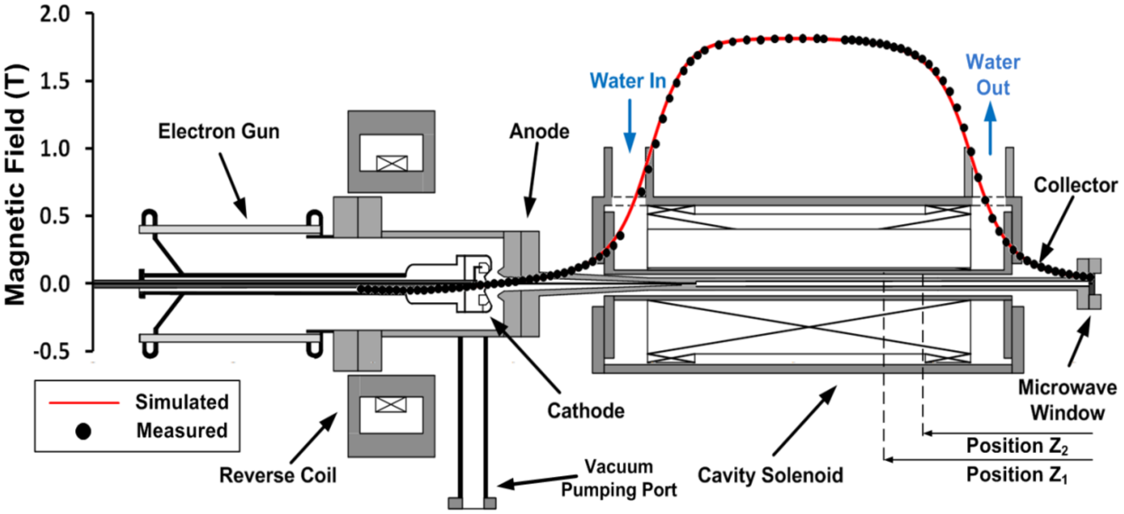

Figure 7-6 The Schematic drawing of the setup of the electron beam experiments

As usual, a background signal was recorded when the beam was unable to be formed in the cusp gun and transported through the interaction region, by having the cathode heater at operating current and accelerating voltages applied to the electron gun, but no beam image was recorded by the camera when current was not supplied to the solenoids. In contrast a typical electron beam picture recorded when the two solenoids generate magnetic fields is shown in Figure 7-7.

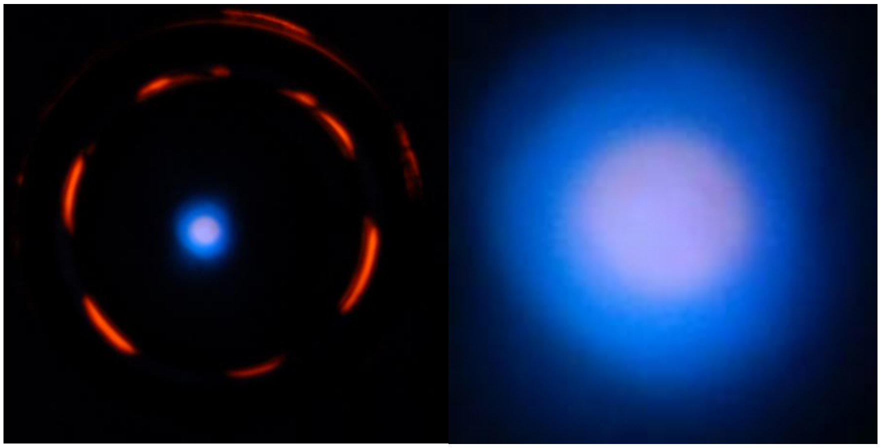

Figure 7-7 The scintillator image recorded by the camera (left) and the enlarged beam image (right)

The left image is the full picture taken by the camera. The orange coloured ring is light from the hot cathode passing through the scintillator holder which was used as a dimension reference for the electron beam. The outside orange ring is the gap between the scintillator holder and the beam tube, the inner orange ring is the 6 slot channels that were made for vacuum pumping the scintillator. The blue circle is the electron beam picture as the scintillator powder used in this measurement gave blue light when the electron beam impacted in the copper disk of the scintillator. It can be seen clearly from the picture that the blue ring showed evidence of an annular shaped electron beam which means an axis encircling electron beam was formed.

The beam radius, and beam position inside the electron beam can be obtained from the scintillator photos. From the diameter of the electron beam, beam voltage and the magnetic field at the measured location, the velocity ratio of the electron beam at the scintillator position can be calculated. By changing the reverse coil current, different scintillator pictures were obtained with different beam radius, which indicates different velocity ratio alpha. Processing this picture by mapping the blue light component, another picture with better contrast was obtained as shown in Figure 7-8.

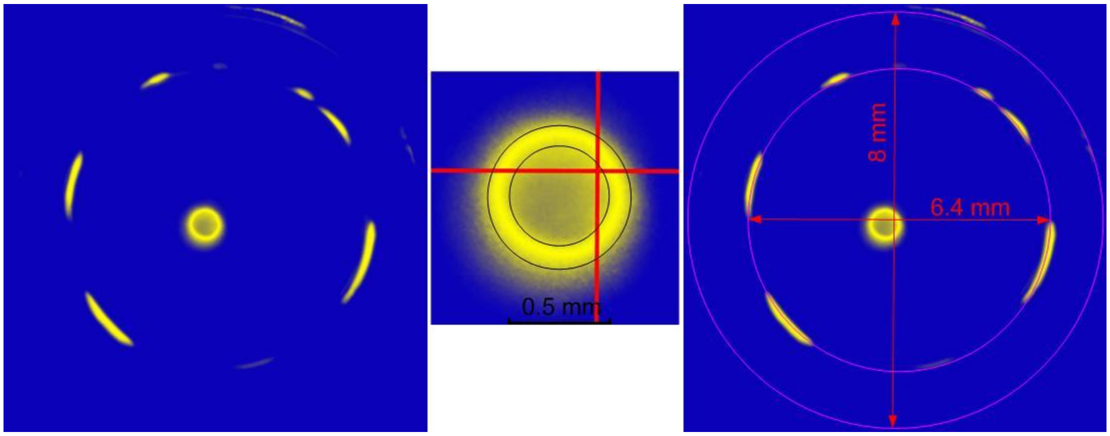

Figure 7-8 The process of getting the beam information from the electron beam picture

In these pictures, only the blue component of each pixel point remained. By measuring the outside scintillator rings' dimension, the dimension of the picture was calculated as shown in Figure 7-8. The dimensions of the two outside rings, the gap between the scintillator holder and the beam tube, and other the 6 slot channels that made for vacuum pumping of the scintillator were known to be 8 mm and 6.4 mm respectively. Calculation shows that the sizes of the two rings are in good agreement with each other in the picture.

The beam size and beam radius can be calculated from the picture (for example, the outer ring of the electron beam has a diameter of 0.76 mm, and the inner ring has a diameter of 0.5 mm). From these parameters and the location of the scintillator in the measurements, the average beam alpha can be calculated. When the electrons are encircling in the magnetic field, the velocity component perpendicular to the magnetic field ($v_\perp$) and the electron circling radius r, magnetic field B are related by equation:

$$v_\perp = \frac{eB}{\gamma m_0} r \tag{7.1}$$

where, γ is the Lorentz factor and can be calculated from equation (7.2).

$$\gamma = 1 + \frac{eV}{m_0 c^2} \tag{7.2}$$

V is the accelerating voltage measured to be 40 kV in the experiments, the magnetic field B can be calculated from the main solenoid current and the position of the scintillator; average r can be calculated from the outer ring and inner ring diameter obtained from the beam image. Thus the electron perpendicular velocity can be calculated. The total velocity v of the electrons can be calculated using the Lorentz factor γ given by equation (7.3).

$$v = c \cdot \sqrt{1 - (\frac{1}{\gamma})^2} \tag{7.3}$$

As $v_{\|} = \sqrt{v^2 - v_\perp^2}$, thus the velocity ratio α at the scintillator position can be obtained through $\alpha = v_\perp / v_{\|}$. The scintillator lies in position Z_2 in Figure 7-6 where the magnetic field is only 90% of the maximum magnetic field. In order to get the beam velocity ratio α value at the gyro-interaction point while the gyrotron cavity were put inside the beam tube, or namely, at the maximum magnetic field (as position Z_1 in Figure 7-6), a series simulations were carried out using the 3D PIC code MAGIC. In these simulations, an electron beam with the same parameters as measured were produced at position Z_2, thus the beam parameter at position Z_1 could be obtained from the simulation.

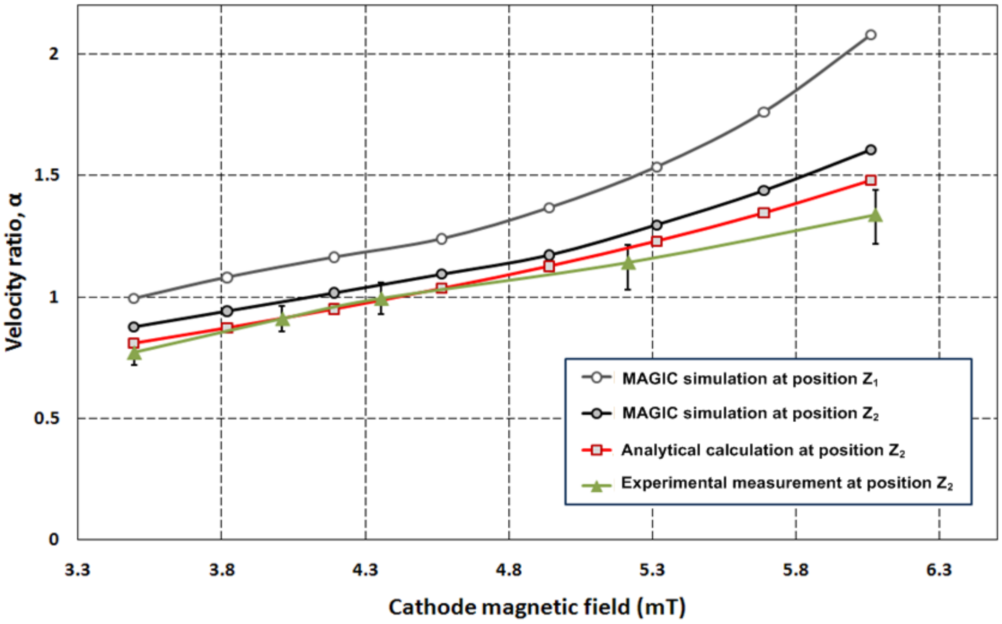

Figure 7-9 The measured velocity ratio α valued at position Z_2 compared with the simulated, and analytical calculated velocity ratio α at position Z_2 and corresponding simulated velocity ratio α value at position Z_1.

By changing the reverse coil and main coil current, different velocity α can be obtained. Due to the limitation of the reverse coil power supply, the maximum measured velocity ratio α at position Z_2 is 1.34, with a corresponding velocity ratio α of 1.56 at position Z_1. The measured velocity ratio α value at position Z_2 was compared with the simulated and analytical calculated velocity ratio α value at position Z_2 and corresponding simulated velocity ratio value at position Z_1 are all shown in Figure 7-9. They were in good agreement with each other.

7.3 Gyrotron Experiment

A harmonic gyrotron experiment was carried out for the 2.6 mm diameter cavity. The microwave signal was measured by a crystal detector as mentioned in Chapter 5. The illustrated picture of the experimental setup is shown in Figure 7-10. The detector was connected after a W-band horn with a W-band attenuator, and then followed by a load to terminate the millimetre wave radiation. The whole detector system was put in a metal box for RF shielding and minimise background noise. A double shielded BNC cable delivers the detector signal to the oscilloscope in the screen room outside the experimental bay. The detector was placed at the far-field of the output taper about 110 mm away, with ~ 20° angle with respect to the axis of the output taper.

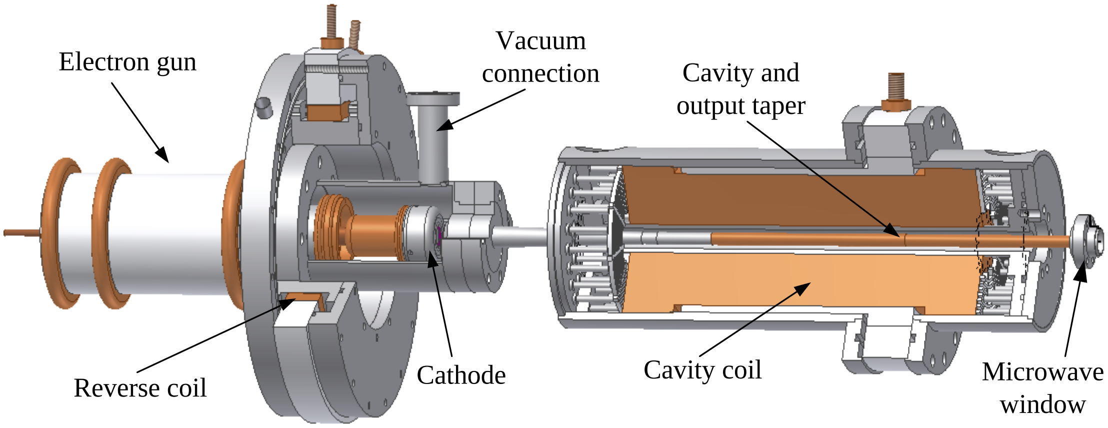

Figure 7-10 The illustrative picture of the harmonic gyrotron experimental setup

As the harmonic gyrotron was designed to work at different harmonic numbers at different magnetic fields, we started with the second harmonics. In the first round of experiments, the detector used in the experiment was PJ crystal detector, no: SN99, 2801, which gave a negative signal when receiving millimetre wave radiation. Millimetre wave output signals were observed at a cavity coil current of 266 A to 269 A on the reading of Ampere meter on the cables to the solenoids (260A to 263A on the power supply), with the reverse coil current in the range from 206 A to 216 A. These correspond to a cavity magnetic field of 2.074 T ~ 2.097 T, and a reverse coil magnetic field from 66.0 mT to 69.1 mT. Namely, millimetre wave output was observed at a beam velocity ratio from 1 to 3.

A typical millimetre wave signal observed is shown in Figure 7-11. Millimetre wave radiation was generated at 269 A in the main coil and 214 A of current in the reverse coil while the beam current was ~1 A. The resonance point was found to be sensitive to the voltage pulse. It can be seen that the resonance point is very close to the calculated resonance point in chapter 3, and has a very good agreement with our design and calculated value. The magnetic field in this experiment is a little higher than expected due to the voltage pulse (average 41 kV) being slightly higher than the design value of 40 kV. The gyrotron performance was optimized by slightly changing the main coil and reverse coil current. The strongest millimetre wave signal was recorded by the detector of more than 200 mV at a cavity coil current of 266 A with a reverse coil current of 212 A.

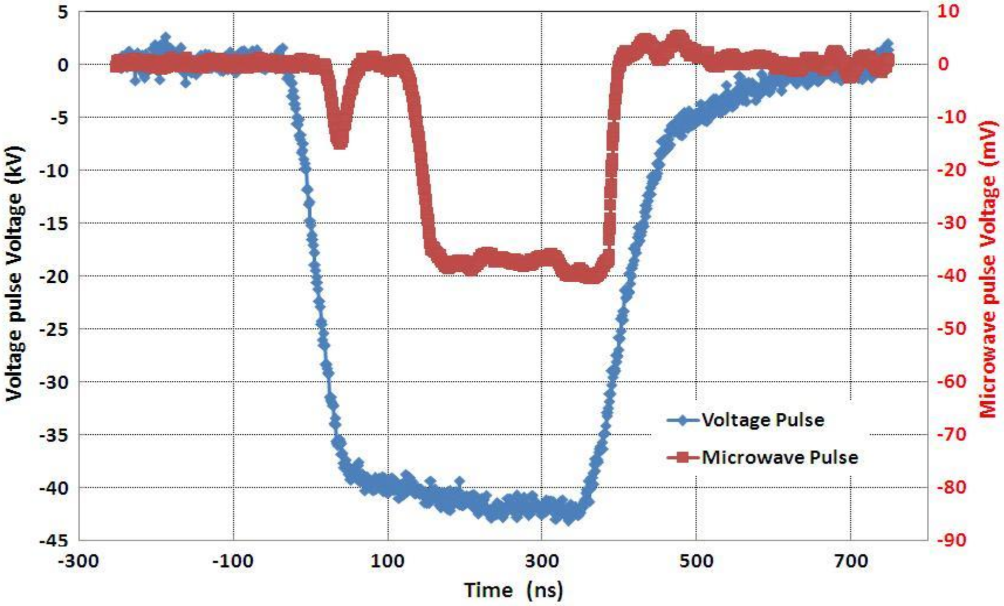

Figure 7-11 Measured microwave signal and voltage pulse

In the second round of experiments, the detector was changed to NJ crystal detector SN: 135.2701 (which gave 1/3 of the voltage output signal at the same incident power at 95GHz compared to the PJ crystal detector), which gives a positive signal when millimetre wave radiation is incident on the detector. The gap of the self-break down gap-spark switch was adjusted to lower the cathode driving voltage and the magnetic field of the resonance point was reduced. Optimized millimetre wave output were observed at a main coil current of 264 A (Ampere meter reading), and a reverse coil current of 210 A, which corresponded to a main cavity magnetic field of 2.06 T.

The observed millimetre wave signal is shown in Figure 7-12. Cut-off filters were used to measure the frequency of the millimetre wave pulse. The full millimetre wave pulse could still be observed after propagation through the 106 GHz cut-off filter which was positioned in front of the detector, an obvious decrease in the amplitude of the millimetre wave pulse could be observed when the 108 GHz cut-off filter was placed in front of the detector. No millimetre wave signal was obtained when the 110 GHz cut-off filter was put in front of the detector, which meant the millimetre wave frequency was in the range of 108 GHz to 110 GHz. The millimetre wave frequency observed was very close to the calculated frequency of the 2nd harmonic at 112 GHz. The slight difference may be caused by the error in the diameter of the cavity when in manufacture or the expansion of copper cavity at high temperature. Calculation shows if the diameter of the gyrotron cavity changes from 2.60 mm to 2.64 mm then the frequency of the 2nd harmonic will drop to 109 GHz with the 2nd harmonic resonance point shifting to 2.08 T from 2.09 T.

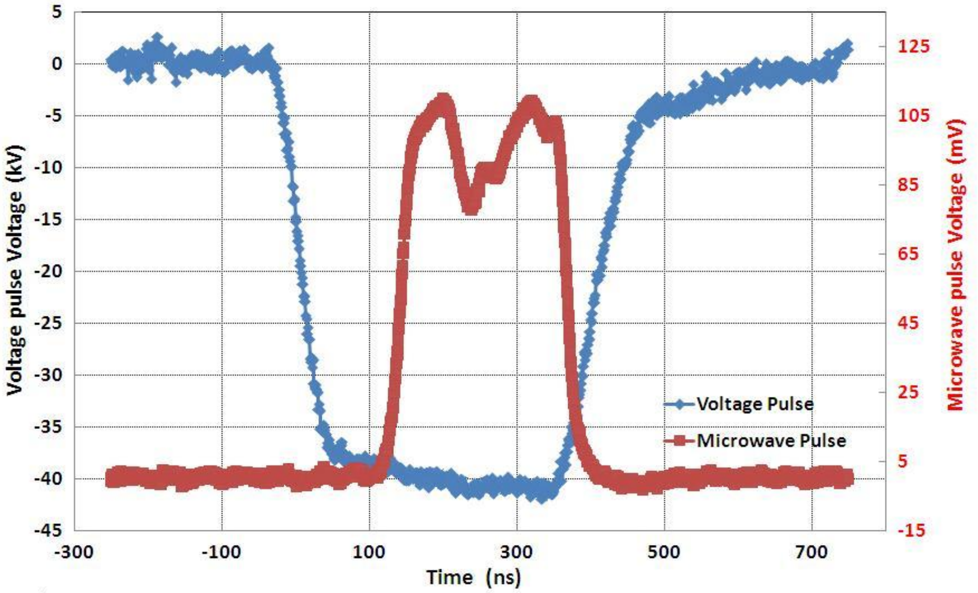

Figure 7-12 The positive microwave signal measured by the detector

A good agreement was found with the experiment results and the calculation in chapter 3, and this has verified the design of the 2nd harmonic gyrotron. The resonance cavity magnetic field range of the harmonic gyrotron is very small (less than 0.02 T at 2nd harmonic), and also it is very sensitive to the beam voltage. If the beam voltage pulse were reduced to 38 kV, the main cavity magnetic field of the 2nd harmonic resonance point would shift to 2.02 T (258 A). A power cut in our lab one night damaged the vacuum of the gyrotron system and the cathode was exposed to the air overnight. This caused the poisoning of the cathode, and stopped the experiment in search of the 3rd, 4th, and even higher harmonic gyrotron interactions. This experiment will be delayed to the future work when the thermionic cathodes are replaced.

7.4 Summary

In this chapter, the results of the cusp beam experiment and harmonic gyrotron experiments are presented. In the beam experiment, a 40 kV 400 ns voltage pulse with a ~320 ns flat top and 40 ns rise and fall time was produce to drive the electron beam emitted from cathode. More than 1.5 A of current were measured by the Faraday cup at different velocity ratio α values from 1-3. The profile of the electron beam captured by a scintillator diagnostic demonstrated that the beam produced by the cusp gun is an axis encircling electron beam. Also, the dimensions of the measured beam which in conjunction with the measured beam current and voltage enable the beam alpha to be ascertained was in very good agreement with the simulated velocity ratio α value.

In the harmonic gyrotron experiments, 2nd harmonic radiation was observed by crystal detectors. Cut-off filters were used in the experiment, and the radiation frequency was determined to be in the frequency range of 108~110 GHz. The resonance point and frequency of the millimetre wave radiation were in very good agreement with the calculations presented in chapter 3. The pursuit of 3rd, 4th and even higher harmonic radiation will be carried out in the future after the acquisition of the detectors in the 200-400 GHz frequency range.

Chapter 8

Conclusion & Future Work

8.1 Introduction

In this chapter, the achievement of this project by now will be concluded, and then the research needed to be carried out in the future with some possible improvements in the experiment will be discussed.

The aim of this project was to design a high harmonic gyrotron. As has been demonstrated in the previous chapters, the following achievements were made and the main goal of the project satisfied as summarized below

1. Design of harmonic gyrotron cavities, (a) 2.11 mm diameter 7th harmonic cavity and (b) 2.6 mm diameter 2nd, 3rd, 4th, and 5th harmonic cavity.
2. Manufacture of these gyrotron and setup the experiment infrastructure.
3. Beam experiments and harmonic gyrotron operation.

8.2 Gyrotron Design

Two gyrotron cavities with different diameters have been designed, the following consideration were taken into account in the design of the two harmonic gyrotron cavities.

1. Resonant frequencies and relative mode with respect to the cavity diameter.
2. The Q factor of the two cavities were calculated and the starting oscillation thresholds for mode competition in the gyrotrons
3. Output taper design along with mode conversion considerations in the output taper.

4. Manufacture method and comparisons by millimetre wave measurements.
5. Beam spread and thickness effect on the gyrotron interaction

By solving the small signal theory equations, the dispersion and growth rate curve were obtained for the gyrotrons and the parameters for the interaction such as the resonant frequencies, relative mode, cavity size and interaction magnetic field. The cavities Q factors have been studied with the changing of the cavity length and output angle. The Q factors were chosen carefully to suppress the unwanted mode interaction in the gyrotron but satisfy the starting oscillation threshold requirement for the designed mode. The mode conversion at the output taper has been considered in the designing with the 6 degree, 10 mm output taper causing less than 10% mode conversion to other modes.

The 3D PIC code MAGIC was used to simulate the interaction of the high harmonic gyrotron. For the 2.11 mm diameter gyrotron, about 600 W of output power was predicted at the design frequency of 390 GHz and the design TE_{71} mode at the 7th harmonic. When 0.1 mm beam thickness and 25% beam velocity ratio spread were considered in the simulation, it was found that the total output power will drop to ~500 W. and competing modes were found at the output, especially the competing TE_{61} mode. It became slightly dominate at the output, causing the output power at the design frequency and mode to drop to ~200 W.

The gyrotron cavity was manufactured in two different ways: spark erosion and drilled. The cold millimetre wave measurements using the high frequency VNA shows that the spark erosion cavity has a lower transmission loss than the drilled cavity. The transmission curves of the cut-off filter manufactured by spark erosion were measured and the construction technique was shown to be of high accuracy..

8.3 Beam and Gyrotron Experiments

The platform for the cusp electron gun and gyrotron experiment were built up including the vacuum system, water cooling system and the power supply system and tested A double Blumlein pulser was built to produce a 40 kV, 400 ns width pulse to drive the electron beam. The power supplies for cathode heating and for driving the solenoids were also commissioned. Two water cooling DC solenoids were built for the cusp electron gun and successfully operated. The main solenoid has been operated at DC under 269 A of current producing approximately 2.1 T magnetic field. A series of diagnostic systems was designed and constructed to measure and monitor the parameters during of the experiment such as: voltage divider for high voltage measurement, cooling water temperature and fluid monitors, Faraday cup and scintillator for beam measurements.

The cusp electron gun has been tested, experiment results shows that the electron gun has a good agreement with our design, and satisfied our requirement. The data that the cathode emitting current changes with the cathode heating power demonstrated the cathode is operating in temperature limited regime. More than 1.5 A of transported beam current was measured at different beam velocity ratio α and under different main coil magnetic fields. The change of the transported beam current with the change of beam velocity ratio at the same cathode emitting current has been measured. The profile of the electron beam obtained by the scintillator proved the form of the electron beam to be of an annular shape. From the beam profile, the velocity ratio α, beam thickness and beam spread can be calculated. All the results were in good agreement with our design values.

Successful harmonic gyrotron experiments were carried out with a millimetre wave pulse observed at the 2nd harmonic resonance point of the 2.6 mm harmonic gyrotron cavity. The frequency of the radiation has been measured by cut-off filters, and the millimetre wave radiation measured to be in the range of 108 GHz -110 GHz. The results of the frequency and resonance point have a very good agreement with our analytical calculation.

8.4 **Future Work**

Harmonic gyrotrons provide an alternative way to approach the terahertz region with moderate magnetic field and relatively high power and has been studied around the world. The 2nd harmonic gyrotron experiment has proofed our design and calculation of the gyrotron. In the future, the crystal detectors and accessories will be acquired for investigation at these higher frequencies. The acquisition of a power meter will enable the power of the millimetre wave radiation in this frequency range to be measured.

A broadband window will be designed in the future. The single layer sapphire window has resonant transmission only at single frequency and its' harmonics. This is ok for the proof of principle experiment presented in this thesis. A multi-layer broad band window is under design which will be useful for the harmonic gyrotron and will improve the performance of the harmonic gyrotron. The pursuit of the 3rd, 4th, and even higher harmonic resonance radiation of the 2.6 mm harmonic gyrotron will be carried out in the future, including measurement of the power, frequency, and radiation pattern. Also, the attainment of the 7th harmonic gyrotron using the 2.1 mm gyrotron cavity will be carried out after further experiments with the 2.6 mm harmonic gyrotron.

A corrugated gyrotron structure for the harmonic gyrotron has been analytically studied and presented in the 2008 IRMWW conference. The idea of a corrugated gyrotron should have better mode selection inside the gyrotron and improve the efficiency of the gyrotron. In the future, a new version of the 3D PIC MAGIC code which has parallel calculation capability will enable the simulation of the corrugated gyrotron structures in high harmonic operation at high frequency. More studies will be carried out to proof the idea.

Reference

1. J. Clerk Maxwell, F.R.S, A Dynamical Theory of the Electromagnetic Field, *Philosophical Transactions of the Royal Society of London* 155: 459–512. 1986.

2. Faraday, Michael, Experimental Researches in Chemistry and Physics. London: Richard Taylor and William Francis. pp. 81–84, 1859.

3. Hertz, H.R. "Ueber sehr schnelle electrische Schwingungen", *Annalen der Physik*, vol. 267, no. 7, p. 421-448, May 1887.

4. E. J. Nichols and J. D. Tear, Joining the infrared and electric wave spectra, *Astrophys. J.*, vol. 61, pp. 17–37, 1925.

5. R. W. McMillan, “Terahertz imaging, millimeter-wave radar,” in Advances in Sensing with Security Applications, J. Bymes, Ed. Springer Verlag, pp. 243–268, 2006.

6. Peter H. Siegel, Terahertz Technology, *IEEE Trans. on Microwave Theory and Techniques*, Vol. 50, No. 3, March 2002.

7. Eric T. Mueller, Terahertz Radiation: Applications and Sources, *The Industrial Physicist*, Aug/Sep, 2003.

8. Antonio C. Torrezen, Seong_Tae Han, Michael A. Shapiro, etc. CW Operation of a Tunable 330/460 GHz Gyrotron for Enhanced Nuclear Magnetic Resonance, *IRMMW-THz*, C.A, Pasadena, USA, 2008.

9. V.S. Bajaj, C. T. Farra, M. K. Hornstein, etc. Dynamic nuclear polarization at 9T using a novel 250 GHz gyrotron microwave source, *Journal of Magnetic Resonance* 160, pp. 85-90, 2003.

10. R. G. Griffin and T. F. Prisner, High field dynamic nuclear polarization – the renaissance, *Phys. Chem. Chem. Hys.*, 12, 5737-5740, 2010.

11. Alexander Borak, Toward Bridging the Terahertz Gap with silicon-based Lasers, *Science*, vol 308, 29 April, 2005.

12. Jean-Baptiste Masson, Martin-Pierre Sauviat, Jean-Louis martin, and Guilhem Gallot, Ionic contrast terahertz near-field imaging of axonal water fluxes, *Applied Physical sciences,* Vol.103, no.13, March , 2006.

13. X-C Zhang. Terahertz wave imaging: horizons and hurdles. *Phys. Med. Biol.* 47, 3667–3677, 2002.

14. AG Davies, EH Linfield and M B Johnston. The development of terahertz sources and their applications. *Phys. Med. Biol.* 47, 3679–3689, 2002.

15. N. C. Luhmann and W. A. Peebles, Instrumentation for magnetically confined fusion plasma diagnostics," *Rev. Sci. Instrum.*, Vol. 55, no.3, pp. 279-331, Mar. 1984.

16. D. L. Brewer, K. W. Kim, L. Zeng, Y. Jiang, etc. "Integrated reflectometer-interferometer system for plasma density profile measurement," *Plasma Phys. Controlled Fusion*, Vol. 40, No.9, Sept. 1998.

17. Teruo Saito, Takashi Notake, Yoshinori Tatematsu, etc, Development of a Sub Terahertz High Power Pulse Gyrotron for Collective Thomson Scattering, *IRMMW-THz*, C.A, Pasadena, USA, 2008.

18. D. leisawitz, et al., Scientific motivation and technology requirements for the SPIRIT and SPECs far-infrared/submillimeter space interferometers, *in Proc. SPIE*, vol. 4013, Munich, Germany, Mar. 29-31, 2000.

19. D. Canet, et al., *J. Mol. Biol.* 330, 397-407, 2003.

20. C. W. Robertson, PhD Thesis, Dept. of Phys., Uni. of Strathclyde.

21. QinetiQ, 100 GHz Millimetre Wave.

22. M. C. Gaidis, Space-based applications of far infrared systems, *8th Int. terahertz Electron. Conf.,* Darmstadt, Germany, Sept. 28-29, pp.125-128, 2000.

23. T. Idehara, T. Saito, I. Ogawa, etc., The potential of the gyrotrons for development of the sub-terahertz and the terahertz frequency range-A review of novel and prospective applications, *Thin Solid Films,* Vol. 517, Issue 4, 31 December, pp. 1503-1506, 2008.

24. *Technology Review*, 10 Emerging Technologies that will change your world, Feb, 2004.

25. E. R. Mueller, J. Hesler, T. Crowe, etc. Widely-tunable laser sideband THz source for spectroscopy & LO applications, *12th Int. Space THz Tech. Symp., San Diego, CA, Feb*, 14-16, 2001.

26. Qing Hu, Benjamin S. Williams, etc, Terahertz Quantum Cascade lasers and electronics, http://www.rle.mit.edu/media/pr146/pr146_ch29_Hu.pdf

27. A. Barkan, F. K. Tittel, and D. M. Mittleman, Linewidth and tuning characteristics of Terahertz quantum cascade lasers, *Optics letters*, Vol. 29, No.6, March 15, 2004.

28. Michael C. Wanke, Christopher Nordquist, Christian L. Arrington, etc, Integration of Terahertz Quantum Cascade Lasers with Lithographically Micromachined Waveguides, *IRMMW-THz 2008, C.A, Pasadena*, USA.

29. T. Aellen, S. Blaser, M. Beck, etc, Continuous-wave distributed feedback QC lasers on peltier cooler, *Applied Physics Letters*, vol. 83, pp. 1929-1931, Sept 2003.

30. T. J. Kulp, etc., The application of quasi-phase matched parametric light sources to practical infrared chemical sensing systems, *App. Phy. B*, vol 75, 317-327.

31. Yisa Rumala, The Quantum Cascade Laser: Will it be the Mid and Far Infrared Laser of the Future? The York Scholar, V. 3(fall 2006), available on: http://www-personal.umich.edu/~yisrum/QCLpaper.pdf

32. M. C. Nuss and J. Orenstein, Terahertz time domain spectroscopy (THz-TDS), Millimeter-Wave Spectroscopy of Solids, G. Gruener, Ed. Berlin, Germany: Springer-Verlag, 1997.

33. E. R. Brown, K. A. McIntosh, K. B. Nichols, etc., Photomixing up to 3.8 Thz in low-temperature-grown GaAs, *Appl. Phys. Lett.*, Vol. 66, no. 3, pp. 283-287, Jan. 1995.

34. S. Verghese, K. A. Mcintosh, and E. R. Brown, Highly tunable fiber coupled photomixers with coherent terahertz output power, *IEEE Trans. Microwave Theory Tech.*, vol. 45, pp. 1301-1309, Aug. 1997.

35. E. R. Brown, Milliwatt THz Average Output Power from a Photoconductive Switch, *IRMMW-THz*, C.A, Pasadena, USA, 2008.

36. T. H. Ning, History and future perspective of the modern silicon bipolar transistor, *IEEE Trans. Electron Devices,* Vol. 48, pp. 2485-2491, Nov, 2001.

37. Miguel Urteaga, dennis Scott, Sundararajan Krishnan, Yun Wei, etc, G-Band (140-220 GHz) Inp-Based HBT Amplifiers, *IEEE Journal of Solid-state Circuits*, Vol. 38, No. 9, Sept, 2003.

38. George I. Haddad, and Robert J. Trew, Microwave Solid-State Active Devices, *IEEE Trans. on Microwave Theory and Techniques*, Vol. 50, No. 3, 2002.

39. H. Eisele, Recent advances in the performance of InP Gunn devices and GaAs TUNNETT diodes for the 100-300 GHz frequency range and above, *IEEE Trans. on Microwave Theory and Techniques*, vol. 48, no. 4, 2000.

40. L. Ozyuzer, A. E. Koshelev, C. Kurter, etc. Emission of Coherent THz Radiation from Superconductors, *Science*, Vol. 318, 21, Nov, 2007.

41. G. P. Gallerano, S. Biedron, Overview of Terahertz Radiation Sources, *Proceedings of the 2004 FEL Conference,* pp216-221, 2004.

42. Tarhan Rana, Graphene Terahertz Plasmon Oscillators, *IEEE Transactions on Nanotechnology*, Vol.7, No.1, Jan, 2008.

43. R. Tauk, F. Teppe, S. Boubanga, etc. Plasma wave detection of terahertz radiation by silicon field effect transistors: Responsivity and noise equivalent power, *Appl. Phys. Lett.* 89, 2006.

44. H. A. H. Boot and J. T. Randall, Historical notes on the cavity magnetron, *IEEE Trans. Electron Devices*, vol. ED-23, pp. 724-729, July 1976.

45. R.A Cairns, and A. D. R. Phelps, Generation and applications of high power microwaves, Co-published by SUSSP Publications and Institute of Physics Publishing, 1996.

46. A.S.Gilmour. Jr. Microwave Tubes, Artech House, Inc. Dedham, 1986.

47. Alan Reddish, Microwave tubes in their maturity, IEE, IEE London, 22-3 Oct, 1984.

48. Levi Schachter, John A. Nation, Slow-wave amplifiers and oscillators: A unified study, *Phys. Rev A.* Vol. 45, No. 12, June 1992.

49. Hyoung S. Kim, Han S. Uhm, Head Effect of Modulated-electron Beam on cavity excitation in Klystrode, *Journal of the Korean Physical Society*, Vol. 42, Feb. 2003.

50. G.S. Nusiovich, M. Walter, J. Zhao, Excitation of cackward wars in forward wave amplifiers, *Phys. Rev. E*, Vol. 58, No. 5, 1998.

51. W. M. Black, R. K. Parker, R. Tobin, etc. A Hybrid Inverted Coaxial Magnetron to Generate Gigawatt Levels of Pulsed Microwave Power, IEDM, 1980.

52. S. Riyopoulos, Nonlinear self-consistent theory for crossed-field devices, *Phys. Rev. E*, Vol. 47, No. 4, 1993

53. L. Sivan, Microwave Tube Transmitters, Chapman & Hall, London, 1994.

54. A. Zolfghari, P. Mac Gibbon, B. North, Comparison of Klystron and Inductive output tubes (IOT) Vacuum-electron Devices for RF Amplifier service in Free-Electron Laser, *Proceedings of EPAC*, Luzern, Switzerland, 2004.

55. J. Jacob, New Developments on RF Power Sources, *Proceedings of EPAC*, Edinburgh, Scotland, 2006.

56. Manfred Thumm, Lambert Feher, Millimeter-wave-sources Development: Present and Future, *8th International Conference on Microwave and High Frequency Heating*, Bayreuth, Germany, 2001.

57. Armand Straprans, Earl William Mccune, Jack A. Ruetz, High-Power Linear-Beam Tubes, *Proceedings of the IEEE*, Vol.61, No.3, March 1973.

58. J.A. Nation, D. Shiffler, L. Schachter, etc. High Power Travelling Wave Tube Amplifiers for RF Accelerators, *EPAC*, 1990.

59. Richard Cousin, Jean Larour, Jacques Gardelle, etc., Gigawatt Emission From a 2.4-GHz Compact Magnetically Insulated Line Oscillator (MILO), *IEEE Trans. on Plasma Sci.*, Vol. 35, No. 5, 2007.

60. Alexander N. Vlasov, Anatoly G. Shkvarunets, John C. Rodgers, etc. Overmoded GW-Class Surface-Wave Microwave Oscillator, *IEEE Trans. Plasma Science*, Vol. 28, No. 3, 2000.

61. R. Lawrence Ives, Microfabrication of High-Frequency Vacuum Electron Devices, *IEEE Trans. Plasma Sci*. Vol 32, No. 3, Jun. 2004.

62. S. Bowater, D Findlay, D. Wilcox, RF Tube comparisons and other requirements, ppt in RF ‘Basic technology’ bid RAL, 23rd Feb. 2005.

63. Alexander N. Korolev, Sergei A. Zaitsev, Ivan I. Golenitskij, etc. Traditional and Novel Vacuum Electron Devices, *IEEE Trans. On Electron Devices*, Vol. 48, No. 12, Dec. 2001.

64. Siegel, P.H., H. Manohara, C. Marrese, A. Husain, J. Hone, J. Xu, and B. Chang, Design and Fabrication of a 1200 GHz Nanoklystron, in Proceedings, *9th International conference on THz electronics, Charlottesville,* VA, Oct 2001.

65. Robert E Miles.Joan Garcia, John R Fletcher, D Paul Steenson, etc., Modelling of Micromachined Klystrons for Terahertz Operation, *8th International Cofnerence on Terahertz Electronics, Darmastadt,* Germany, 2000.

66. Steven H. Gold, Review of High-power microwave source research, *Rev. Sci. Instrument*. 68(11), 1997.

67. S. P. Bugaev, V. A. Cherepenin, V. I. Kanavets, etc. Investigation of Millimeter-wavelength-range Relativistic Diffraction Generator, *IEEE Trans. Plasma Sci*. 18, (1990): 518.

68. Bruce E. Carlsten, Steven J. Russell, Lawrence M. Earley, etc. Technology Development for a mm-Wave Sheet-Beam Traveling-Wave Tube, *IEEE Trans. Plasma Science*. 33(1), pp. 83-95, 2005.

69. Ives, L., J. Neilson, M. Read, M. Caplan, C. Kory, R. Witherspoon, and S. Schwartzkopf, Terahertz Backward Wave Oscillators, Conference Digest, *International Conference on Infrared and Millimeter wave*, pp.225-226, 2002.

70. Seong-Tae Han, Kyu-Han Jang, Jin-Kyu So, Low-Voltage operation of Ka-band Folded Waveguide Traveling-Wave Tube, *IEEE, Trans. Plasma Science*, VOl. 32, No. 1, Feb., 2004.

71. Gun-Sik Park, Hyun-Jun Ha, Woo-Kyoung Han, Investigation of Folded Waveguide TWT, *25th International Conf. on Infrared and Millimeter Waves*, 2000.

72. G. Dohler, D. Gallagher, and J. Richards, Millimeter Wave Folded Waveguide TWTs, *Vacuum Electronics Annual Review Proceedings*, p. V.15, 1993.

73 A. J. Theiss and D. B. Lyon, Litton High-Power Ka-Band TWTs for Airborne Radars, *IEEE Aerosp Electron. Syst*. Mag., vol. 10, p.33 , 1995.

74. Hyun-Jun Ha, Sun-Shin Jung, Gun-Sik Park, Linear Theory of a Folded Waveguide Traveling-Wave Tube, *Journal of the Korean Physical Society*, Vol. 34, No.3, 1999.

75. J.H. Booske, W. J. Lee, S. Gallagher, etc. Microfabricated TWTs as high power, wide band sources of THz radiation.
http://www.engr.wisc.edu/ece/faculty/booske_john/THzmVEDTWTpaper.pdf

76. Alexander N. Vlasov, Anatoly G. Shkvarunets, John C. Rodgers, etc. Overmoded GW-Class Surface-Wave Microwave Oscillator, *IEEE Trans. Plasma Science*, Vol. 28, No. 3, 2000.

77. I.V. Konoplev, A. W. Cross, P. MacInnes, W. He, etc. Free-electron maser based on a cavity with tow- and one-dimensional distributed feedback. *App. Phys. Lett.* Vol. 92, 2008.

78. I. V. Konoplev, L. Fisher, K. Ronald, A. W. Cross, etc. Surface-field cavity based on a two-dimensional cylindrical lattice, *App. Phys. Lett.* Vol, 96. 2010.

79. Hai Zhang, Jianguo Wang, Changjiang Tong, etc., Numerical studies of powerful terahertz pulsed generation from a super-radiant surface wave oscillator, *Phys. of Plasma*, Vol. 16, 2009.

80. Steven H. Gold, Review of high-power microwave source research, *Rev. Sci. Instrument*. 68(11),1997

81. Lawson, W., J. Cheng, J.P.Calame, etc, High-power operation of a three-cavity X-band coaxial gyroklystron, *Phys. Rev. Lett*. Vol. 67, 520-523.

82. Ngo, M., B. G. Danly, R. Myers, D. E. Pershing, etc. High-power millimeter-wave transmitter for the NRL WARLOC radar, *Proceedings IEEE IVEC*, New York, 2002.

83. G. S. Nusinovich, M. Walter, Theory of the inverted gyrotwystron, *Phys. Plasmas* 4(9), Sept, 1997.

84. Blank, M., B. G. Danly, and B. Levush, Experimental demonstration of a W-band (94GHz) gyrotwystron amplifier, *IEEE Trans. Plasma Sci*. 27, pp. 4205-411, 1999.

85. Blank, M., K. L. Felch, B. G. James, etc. Development and demonstration of high-average power W-band gyro-amplifiers for radar applications, *IEEE Trans. Plasma Sci.* 30, pp. 865-875, 2002.

86. Lawson, W., P. E. Latham, J P. Calame, Et al. High power operation of first and second harmonic gyrotwystrons, *J. Appl. Phys*. 78, pp.550-559, 1995.

87. Bratman, V. L., A. W. Cross, G. G. Denisov, et al., High-gain wide-band gyrotron traveling wave amplifier with a helically corrugated waveguide, *Phys. Rev. Lett.* 84, pp. 2746-2749, 2000.

88. Denisov, G.G., V.L. Bratman, A. D. R. Phelps, etc. Gyro-TWT with a helical operating waveguide:New possibilities to enhance efficiency and frequency bandwidth, *IEEE Trans. Plasma Sci*. 26, pp.519-518, 1998.

89. Cooke, S. J., and G. G. Denisov, Linear theory of a wide-band gyro-TWT amplifier using spiral waveguide, *IEEE Trans. Plasma Sci*. 26, pp. 519-530, 1998.

90. Bratman V L, Cross AW, Denisov G G, He W, Phelps A D, Ronald K, Samsonov S V, Whyte C G, Young A R. High-gain wide-band gyrotron traveling-wave amplifier with a helically corrugated waveguide. *Phys. Rev. Lett.*, 84(12), pp. 2746–2749, 2000.

91. V. L Bratman, Vacuum Electron Sources of Terahertz Radiation, *IRMMW-THz* 2006, Shanghai, 2006.

92. A. N. Korolev, S. A. Zaitsev, I. I. Golenitskij, etc, Traditional and novel vacuum electron devices, *IEEE Trans. Electron Devices*, vol. 48, no12, dec 2001.

93. Zaytsev, N> I., T. B. Pankratova, M. I. Petelin, etc. Millimeter and submillimeter-wave gyrotrons, *Radio Eng. Electron. Phys*. 21, 103-107, 1974.

94. Kisel, D. V., G. S. Korablev, V. G. Navel' Yev, etc. An experimental study of a gyrotron operating at the second harmonic of the cyclotron frequency with optimized distribution of the high fregqency field. *Radio Eng. Electron. Phys*. 19, 95~100, 1974.

95. Idehara, T., I. Ogawa, S. Mitsudo, etc., Development of frequency tunable medium power gyrotrons as submillimeter wave radiation sources, *IEEE Trans. Plasma Sci*. 27, 340-354, 1999.

96. M. Yu, Glyavin, A. G. Luchinin, and G. Yu. Golubiantnikov, Generation of 1.5-kW 1-Thz Coherent radiation from a gyrotron with a pulsed magnetic field, *Phys. Rev. Lett.* 100, 015101, 2008.

97. Sirigiri, J. R., M. A. Shapiro, and R. J. Temkin, Experimental Results from the MIT 140 GHz quasiopitcal Gyro-TWT, *Conference Digest of 27th IRMMW*, Setp, 2002.

98. B Piosczyk, G Dammertz, O Dumbrajs, etc., A 2 MW, 170 GHz coaxial cavity gyrotron –experimental verification of the design of main components, *3rd IAEA Technical Meeting on ECRH Physics and Technology in ITER*. 2005.

99. B. Piosczyk et al., Towards a 2 MW, CW, 170 GHz coaxial cavity gyrotron for ITER, *Fusion Eng. And Design*, 66-68, pp. 481-485, 2003.

100. I. V. Bandurkin, V. L. Bratman, G. G. Denisov, etc. New Schemes of High-harmonic Gyro-devices with Frequeny Multiplication, *IRMMW-THz 2006*, Shanghai, 2006.

101. A. V. Savilov and G. S. Nusinovich, On the theory of frequency-quadrupling gyroklystrons, *Phys. Plasmas*, 14, 053113, 2007.

102. Ilya V. Bandurkin, Vladimir L. Bratman, Yuriy K. Kalynov, etc, Terahertz High-Harmonic Gyrotrons and Gyro-Mulitipliers, *IRMMW*, Pasadena, C. A. 2008.

103. Luchini, H. Mots, Undulators and Frree-Electron Lasers, Clarendon Press, Oxford, 1990.

104. Mark Lee, Michael C. Wanke, Searching for a solid-state Terahertz Technology, *Science*, 6, vol. 316, April 2007.

105. J. D. Lawson, “The Physics of Charged-Particle Beams”, Oxford University Press, 2nd edition, Oxford, 1988.

106. Lapostolle P M, “Possible emittance increase through filamentation due to space charge in continuous beams”, *IEEE Trans, Nucl. Sci*.NS-18, pp.1101-1104, 1971.

107. Y. J. Chen, T. J. Fessenden, Improvements on the Accuracy of Beam Bugs, UCRL-JC-130426.

108. J. Cooper, On the High-frequency Response of A Rogowski Coil, Plasma Physics, *Journal of Nuclear Physics*, Part C, Vol. 5, pp, 285~288, 1963.

109. D. A. Ward, J. La, T. Exon, Using Rogowski Coils for transient current measurements, *Engineering Science And Education Journal*, June 1993.

110. Liao Jingsheng, Guo XiaoHua, Luo Cheng, etc, Studies of Rogowski Current Transducer for Low Amplitude Current, *CCECE-CCGEI*, Montreal, May/Mai 2003.

111. Thomas R.T, High impulse voltage and current measurement, *IEEE Trans Voltage and Measurement.* Vol.19, No.2, pp 112~117, 1970.

112. Pellinen, D. and Staggs V, A technique to measure high-power electron beam currents. *Rev. Sci Instr*, Vol.44, 1973.

113. John D.Ramboz, Machinable Rogowski Coil Design and Calibration, *IEEE Trans. Instrument and Measurement*., Vol.45, No.2, 1996.

114. P N Murgatroyd, A K Y Chu, G K Richardson, etc. Design Note, Making Rogowski Coils, *Meas.Sci. Tech.* 2, 1991.

115. L. D. Landau, E. M. Liftshitz, and L. P. Pitaevskii, Electrodynamics of Continuous Media, Pergamon: New York, 1984.

116. Gian Luca Orlandi, Spatial coherence in the transition radiation spectrum, *Optics Communication* 267, pp322-334, 2006.

117. T. Nakazato, M. Oyamada, N. Niimura, etc., Oberservation of Coherent Synchrotron Radiation, *Phys. Rew. Lett*. (63) 12, 1989.

118. T. Nakazato, M. Oyamada, N. Niimura, etc. Spectrum of Coherent Synchrotron Radiation, *Particle Accelerator Conference,* San Francisco, CA, USA, 1991.

119. Zaytsev, N. I., T. B. Pankratova, M. I. Petelin, and V. A. Flyagin, Millimeter and submillimeter-wave gyrotrons, *Radio Eng. Electron. Phys*. 21, 103-107, 1974.

120. T. Idehara, I. Ogawa, S. Mitsudo, Y. Iwata, S. Watanabe, Y. Itakura, K. Ohashi, H. Kobayashi, T. Yokoyama, V. E. Zapevalov, M. Y. Glyavin, A. N. Kuftin, O. V. Malygin and S. P. Sabchevski, *IEEE Trans. on Plasma. Sci*., 32, No. 3, 903, 2004.

121. Q. S. Wang, D. B. McDermott, C. K. Chong, C. S. Kou, K. R. Chu and N. C. Luhmann, Jr, *IEEE Trans. on Plasma. Sci.,* 22, No. 5 608, 1994.

122.Q.S. Wang, H. E. Huey, D. B. McDermott, Y. Hirata and N. C. Luhmann. Jr, *IEEE Trans. Plasma Sci*, 28, No. 6, 2232, 2000.

123. Victor L. Granatstein and Igor Alexeff, High Power Microwave Sources, Artech House, INC., 685 Canton Street, Norwood, MA 02620, 1987.

124. K. R. Chu, and Anthony T. Lin, Gain and Bandwidth of the Gyro-TWT and CARM Amplifiers, *IEEE Trans. on Plasma Sci*. Vol. 16, No. 2 April 1998.

125. K. R. Chu, Adam T. Drobot, Harold Hwaling Szu, and Phillip Sprangle, Theory and Simulation of the Gyrotron Traveling Wave Amplifier Operating at Cyclotron Harmonics, *IEEE Trans. on Microwave Theory and Techniques*, Vol. MIT-28, No.4, April 1980.

126. K. R. Chu, The electron cyclotron maser, *Rev. of Mod. Phys.*, Vol. 76, Apr., 2004.

127. V. E. Zapevalv, Yu. K. Kalynov, A. N. kuftin, etc., Low-Q cavites for high-power gyrotrons, *Radiophysics and Quantum Electronics*, Vol. 37, No. 3, 1994.

128. T. H. Chang, C. H. Li, C. N. Wu, and C. F. Yu, Exciting circular TEmn modes at low terahertz region, *Applied Physics Letters*, 93, 111503, 2008.

129. Melissa K. Hornstein, Vikram S. Bajaj, Robert G. Griffin, et al. Second Harmonic Operation at 460 GHz and Broadband Continuous Frequency Tuning of a Gyrotron Oscillator. *IEEE Trans. on Electron Devices*, Vol 52, No. 5, May 2005.

130. M. V. kartikeyan, E. Borie, M. K. A. Thumm, Gyrotrons, Springer-Verlag Berlin, 2004.

131. D. B. Mcdermott, N. C. Luhmann, Jr., A. Kupiszewski and H. R. Jory, Small-signal theory of a large-orbit electron-cyclotron harmonic maser, Phys. Fluids 26(7), July 1983.

132. L. Ludeking, D. Smithe, T. Gray, Introduction to MAGIC, Mission Research Corporation, Virginia, 2003.

133. A.S.Gilmour. Jr. Microwave Tubes, Artech House, Inc. Dedham,1986.

134. Thomas, R. E., J. W. Gibson, G. A. Hass, and R. H. Abrahms. “ Thermionic Sources for High-brightness Electron-beams.” *IEEE Trans. Plasma Sci*. 15,1987.

135. Bube. R. H, “Electrons in Solids”, Longman, London, 1978.

136. Al-Ajili, A. N. H., A. K. Ray, J. R. Travis, S. N. B. Hodgson, etc., Thermal decomposition and electrical conductivity of oxide cathode emission materials, *J. Mater. Sci.: Mater. Elect.* 11, 489, 2000.

137. Cortenradd, R. A. W. Denier van der Gon, H. H. Brongersma, etc. Surface analysis of thermionic dispenser cathodes, Appl. Surf. Sci. 191, 153, 2002.

138. Li, J., S. yan, W. Shao, Q. Chen, and M. Zhu, Investigation and application of impregnated scandate cathodes, Appl. Surf. Sci. 215, 49, 2003.

139. Robert J. Barker, J. Booske, Neville C. Luhmann, Jr. and Gregory S. Nusinovich, Modern Microwave and Millimeterwave Power electronics, IEEE press, A John Wiley & Sons, INC., Publication, USA 2005.

140. Zhu, W. (ed.), Vacuum Microelectronics, Wiley-interscience, New york, 2001.

141. Flower, RT. H., and L. nordheim, Electron emission in intense electric fields, Proc. R. Soc. A 119, 173, 1928.

142. M.Hajra, C. E. Hunt, M. Ding, o. Auciello, etc, Effect of Gases on the Field Emission Properties of Uncd-coated Silicon Field Emitter Arrays, *J. Appl. Phys.*, vol. 94(6), pp. 4079-83, 2003.

143. Kim, W. S., W. Yi, S. Yu, etc., Secondary electron emission from magnesium oxide on multi-walled carbon nanotubes, *Appl. Phys. Lett.* 81, 1098, 2002.

144. Guozhi Liu, Jun Sun, Hao Shao, Changhua Chen and Xiaowei Zhang, Research on an improved explosive emission cathode, *J. Phys. D: Appl. Phys*. 42, 2009

145. Huabi. Yin, Pseudospark Discharge and Cherenkov maser experiments, PhD Thesis, University of Strathclyde, Glasgow, 1998.

146. David Rowland, “A Cusp Gun for Gyro-Devices”, PhD Thesis, University of Strathclyde, Glasgow, 2008.

147. K. R. Chu, Theory of electron cyclotron maser interaction in a cavity at the harmonic frequencies, *Phys. Fluids*, 21, pp. 2354-2364, 1978.

148. A. S. Gilmour, Jr., Principles of Travelling-Wave Tubes, Artech house, Boston, 1994.

149. C. R. Donaldson, W. He, A. W. Cross, et al., “Design and numerical optimization of a Cusp-Gun-Based Electron Beam for Millimetre-Wave Gyro-Devices”, *IEEE Tran. Plasma Sci*. Vol.37, No. 11, 2009.

150. F. Li, W. He, A. W. Cross, et al., “Simulation of a ~390 GHz 7th Harmonic Gyrotron using a large orbit electron beam”, *J. Phys. D: Appl. Phys.* Vol. 43, No. 15, 2010.

151. http://www.charmillesus.com/newsroom/literature/Agie/EXPERIENCE%2024.pdf.

152. Antonie Descoeudres, Characterization of electrical discharge machining plasmas, These EPFL, no. 3542, 2006.

153. Michael Hiebel, “Fundamentals of Vector Network Analysis,” Rohde & Schwarz GmbH & Co. KG, 5, Germany, 2005.

154. Slobodan I. Babic and Cevdet Akyel, “Magnetic Force Calculation Between Thin Coaxial Circular Coils in Air,” *IEEE Trans. Magnetics*, Vol. 44, No. 4, pp. 445-452, April, 2008.

Appendix

ARTICLES & PUBLICATIONS:

Journal papers

- F Li, W. He, et al., "Design and Simulation of a 390 GHz 7th Harmonic Gyrotron using a large orbit electron beam", *J. Phys. D: Appl. Phys.*, 42, 155204, (2010).
- C. R. Donaldson, W. He, A. Cross, A. D. R. Phelps, F. Li, et al; "Design and numerical optimization of a cusp gun based electron beam for millimetre wave gyro-devices", IEEE *Trans. Plasma. Sci.*, 11, pp.2153-2157, (2009).
- C.R. Donaldson, W. He, A. Cross, F. Li, et al: "A cusp electron gun for millimetre wave gyrodevices", *Appl. Phys. Lett.*, 96, 141501, (2010).
- W. He, C. R. Donaldson, F. Li, et al.: W-Band Gyro-devices Using Helically Corrugated Waveguide and Cusp Gun: Design, Simulation and Experiment", *Terahertz Science and Technology,* Vol. 4, No. 1, March (2011).

Conference papers

- F Li, et al., "the simulation of an high power 390GHz large-orbit harmonic gyrotron", *IEEE International Vacuum Electronics Conference (IVEC),* Volume 808, pp. 169-172, Monterey, CA. (2008).
- F. Li, et al., "The Design of a 390 GHz gyrotron Based on a Cusp Electron Gun", *33rd international Conference on Infrarad, Miliimeter And Terahertz Waves (IRMMW-THz),* Pasadena, CA, (2008).
- C. R. Donaldson, et al., "A 10 kW W-Band Gyro-BWO using a Helically Corrugated Waveguide", *33rd international Conference on Infrarad, Miliimeter And Terahertz Waves (IRMMW-THz)*, Pasadena, CA, (2008).
- C. R. Downaldson, et al., "A W-band gyro-Bwo using a helically corrugated waveguide", *IEEE International Vacuum Electronics Conference (IVEC)*, pp. 93-94, (2008).

- W. He et al., “Experiment of a high power W-band gyro-BWO using a helically corrugated waveguide”, *International Conference on Infrared, Millimeter and Terahertz Waves (IRMMW-THz),* (2009)
- F. Li, et al., “The design of a 390 Ghz gyrotron based on a cusp electron gun’, *2nd UK/Europe-China Workshop on Infrared, Millimeter and Terahertz Waves (IFMMW-THz*), p.85, (2009)
- W. He, et al., “Design simulation and experiment of a cusp electron beam for millimetre wave gyro-devices,” IEEE Vacuum Electronic Conference (IVEC), pp. 517-518, (2009)
- W. He, et al., “W-band gyro-devices using helical interaction waveguides and cusp guns”, *2nd UK/Europe-China Workshop on Infrared, Millimeter and Terahertz Waves (IFMMW-THz*), p.96, (2009)
- F. Li, et al., “The design of a 390 GHz gyrotron based on a cusp electron gun", *International Conference on Infrared, Millimeter and Terahertz Waves (IRMMW-THz),* pp. 1-2, (2010).
- L. Zhang et al., “Simulation of a four-stage depressed collector for a W-band Gyro-BWO”, *International Conference on Infrared, Millimeter and Terahertz Waves (IRMMW-THz),* pp. 1-2, (2010).
- W. He et al., “A W-band gyro-TWA using a helically corrugated waveguide,” *International Conference on Infrared, Millimeter and Terahertz Waves (IRMMW-THz),* pp. 1-2. (2010)
- C.R. Donaldson et al., “Experimental demonstration of a W-band gyro-BWO using a helically corrugated waveguide”, *International Conference on Vacuum Electronics Devices (IVEC),* pp. 1-2, (2010).
- W. He et al., “W-band Gyro-devices using helical interaction waveguides and cusp guns”, *Proceedings of the 3rd China-Europe Workshop on MM-Waves and Thz,* pp. 54-57, (2010).
- C.R. Donaldson et al., “Experimental demonstration of a W-band gyro-BWO using a helically corrugated waveguide”, International Conference on Infrared, Millimeter and Terahertz Waves (IRMMW-THz), pp.1-2, (2010).

- C. R. Donaldson, et al., “Updates of a W-Band Gyrotron-BWO experiment Based on a Cusp Electron Gun”, *38th IEEE International Conference on Plasma Science and 24th IEEE Symposium on Fusion Engineering (ICOPS & SOFE)*, Chicago, USA. (2011)